



UNIVERSITY OF  
BIRMINGHAM

# ***Improving Productivity of an Electron Beam Melting System Using Ti – 6Al – 4V***

***EngD Thesis***

By

**Riccardo Tosi**

**Supervisor: Professor Moataz Attallah**

**Supervisor: Professor David Ian Wimpenny**

A thesis submitted to the University of Birmingham for the Engineering Doctorate degree  
in the faculty of Metallurgy and Materials, May 2019.

UNIVERSITY OF  
BIRMINGHAM

**University of Birmingham Research Archive**

**e-theses repository**

This unpublished thesis/dissertation is copyright of the author and/or third parties. The intellectual property rights of the author or third parties in respect of this work are as defined by The Copyright Designs and Patents Act 1988 or as modified by any successor legislation.

Any use made of information contained in this thesis/dissertation must be in accordance with that legislation and must be properly acknowledged. Further distribution or reproduction in any format is prohibited without the permission of the copyright holder.

## Synopsis

The electron beam melting system is a unique powder bed technology used to manufacture high value components for different applications. Titanium alloys are conventionally used to produce additive manufacturing parts in several industrial sectors due its mechanical and geometrical characteristics. This demonstrates an increasing interest in this system. However, limits on productivity are pushing the market to improve the process of additive manufacturing (AM) parts into real production. The aim of this thesis is to gain a fundamental understanding of the Arcam A2XX system and its characteristics in order to explore new approaches for improving productivity.

This thesis explores fundamental studies of Ti - 6Al - 4V alloy manufactured with an electron powder bed fusion (E-PBF) system using a standard configuration, hardware reduction, and advanced methods to decrease the manufacturing time and its impact in production. All the studies include a metallurgical investigation of the parts, mechanical properties and an overall analysis of the components manufactured.

A standard build was first investigated to capture the E-PBF A2XX system behaviour and its build characteristics. After a fundamental study investigation, the hardware was modified to better understand the flexibility of the standard system. An “adaptonic chamber” was manufactured to reduce the amount of powder required during the build. This optimised the chamber volume, which generated benefits such as time saving and machine turnaround. Subsequently, two advanced manufacturing techniques called “in-situ shelling” and “hybrid manufacturing” were explored in order to understand whether the production time capturing un-melted powder in a shell to post treat could be reduced, and to include the starting plate as part of the final component respectively. Time and cost were monitored to measure productivity. Further research is recommended to gain deeper insight into the techniques successfully explored in this thesis.

## Contents

Synopsis.....	II
Acknowledgments.....	VII
Presentation and Publication.....	VIII
List of Abbreviations and Symbols .....	IX
List of Figures .....	X
List of Tables.....	XVI
Chapter 1: Introduction.....	1
1.1 Thesis Introduction.....	1
1.2 Aims and Objectives .....	1
1.3 High Productivity in AM .....	2
1.4 Thesis Outline.....	3
1.5 The Engineering Doctorate Degree .....	4
Chapter 2: Literature Review .....	5
2.1 Introduction .....	5
2.2 Electron Beam Melting by Arcam.....	6
2.1.1 E-PBF System .....	7
2.1.2 Heat Dissipation .....	7
2.1.3 Pre-heating Method .....	9
2.1.4 Melting Method .....	10
2.1.5 Scanning Theory .....	12
2.1.6 Defects in E-PBF .....	13
2.1.7 Inspection Methods .....	15
2.1.8 Post Processes .....	18
2.3 Powder for E-PBF .....	22
2.4 Materials Available in E-PBF.....	27
2.5 Ti - 6Al - 4V in E-PBF .....	28
2.4.1 Ti - 6Al - 4V Behaviour during the E-PBF Process.....	28
2.4.2 Ti - 6Al - 4V Solidification in E-PBF .....	30
2.4.3 Ti - 6Al - 4V Mechanical Properties in E-PBF .....	35
2.6 Parts Location and Build Control.....	37



2.7 Advance Hardware Configuration .....	38
2.8 Shelling Design for Manufacturing.....	40
2.9 Hybrid Manufacturing .....	41
2.10 Production with Additive Manufacturing .....	43
2.9.1 Market Overview.....	43
2.9.2 AM Benefits against Conventional Machining .....	45
2.9.3 Productivity and Cost in AM.....	47
2.11 Literature Review Summary & Gaps .....	48
2.12 Thesis Chapters Identified Through Literature Review.....	50
Chapter 3: Experimental Methodology.....	51
3.1 Introduction .....	51
3.2 Experimental Development .....	52
3.3 A2XX Electron Beam Melting Settings per Experiment.....	53
3.4 Melting Strategies .....	54
3.5 Materials .....	55
3.6 Powder Characterisation.....	56
3.7 Samples Preparation .....	57
3.8 Micro-Hardness measurement .....	58
3.9 Archimedes Test.....	58
3.10 Optical Microscopy.....	58
3.11 Scanning Electron Microscope (SEM) .....	59
3.12 X-ray CT and $\mu$ -CT .....	59
3.13 Mechanical and Fatigue Testing.....	60
3.14 Hot Isostatic Pressing .....	62
3.15 Starting Plate Preparation.....	63
Chapter 4: Heat Distribution Changes in a E-PBF Build Chamber .....	64
4.1 Introduction .....	64
4.2 Experimental Procedure.....	65
4.2.1 Experimental Work and Build Preparation .....	65

4.3 Results and Discussions.....	67
4.3.1 Powder Analysis .....	67
4.3.2 Microstructure Analysis .....	69
4.3.3 Contamination Issues .....	73
4.3.4 Micro-Hardness Properties .....	75
4.4 Conclusion .....	78
Chapter 5: Development and Analysis of the Pre-Sintering, Solidification, and Build Integrity of an Adaptronic Chamber .....	79
5.1 Introduction .....	79
5.2 Experimental Procedure.....	80
5.2.1 Machine.....	80
5.2.2 Design Conceptions .....	81
5.2.3 Hardware.....	82
5.2.4 Parameters Development .....	84
5.2.5 Powder Analysis .....	84
5.2.6 Preheat 1 influence - Case Study .....	86
5.2.7 Experiment Set-Up .....	87
5.3 Results and Discussions.....	88
5.3.1 Microstructural Investigation.....	88
5.3.2 Material Analysis .....	90
5.3.3 Micro-Hardness Properties .....	92
5.3.4 $\mu$ -CT Analysis of Pre-Sintered Powder .....	93
5.3.5 $\mu$ -CT Investigation of Tensile Bars .....	95
5.3.6 Mechanical Properties .....	97
5.3.7 Fatigue Tests .....	102
5.3.8 Chambers Comparison .....	105
5.5 Conclusion .....	106
Chapter 6: In-Situ Shelling in E-PBF .....	109
6.1 Introduction .....	109
6.2 Experimental Procedure.....	109
6.2.1. Parts and Build File Preparation.....	109
6.2.2. Hatching Parameters and Machine Settings .....	111

6.3. Results and Discussions.....	113
6.3.1 Post Analysis Procedure .....	113
6.3.2 Optical Microscope Porosity Measurements.....	115
6.3.3 Microstructural Behaviour after HIP Treatment.....	117
6.3.4 Mechanical Properties .....	124
6.3.5 Manufacturing Time Calculation.....	129
6.4 Conclusion .....	130
Chapter 7: Hybrid Manufacturing in E-PBF .....	131
7.1 Introduction .....	131
7.2 Experimental Procedure.....	132
7.2.1. Substrate Preparation .....	132
7.2.2 Software and Parameters .....	135
7.2.3 DOE Preparation of the Substrates .....	135
7.3 Results and Discussions.....	137
7.3.1 Parts Manufacture .....	137
7.3.2 Starting Plate Post Analysis .....	138
7.3.3 Microstructural Characteristics.....	141
7.3.4 Beam Focus Influence .....	144
7.3.5 Micro-Hardness.....	147
7.3.6 Tensile Properties.....	148
7.4 Conclusion .....	157
Chapter 8: Conclusion and Future Work.....	158
8.1 Conclusion .....	158
8.2 Future Work .....	160
References.....	165

## **Acknowledgments**

I would like to take this opportunity to express my gratitude to Prof. David Wimpenny (Manufacturing Technology Centre - MTC) for his continuous support as my supervisor during the past 8 years since I moved to the UK. He has supported my development both personally and scientifically and I am very grateful for this.

I would also like to express my appreciation to Prof. Moataz Attallah (University of Birmingham - UoB), who has supported me to explore and gain a deeper understanding of the metallurgical world. His passion and patience have motivated me throughout this journey.

A special thanks is dedicated to my colleagues. Emmanuel Muzangaza's (MTC) technical support has been key to developing this thesis. Our shared passion for AM technologies has provided me with much inspiration. Yijun Liu (MTC) has also supported me in understanding complex metallurgical topics, taking the time to really understand what I needed.

A wonderful team have worked on reviewing this thesis, which has helped to make it more readable. Thank you to all who have dedicated their time to it (Han L, Jen N, And T, Nic C, Dai A, Ste H).

I feel very privileged for the support of everyone at the MTC (from the office to the workshop), the University of Birmingham and the funding received from the EPSRC (Engineering and Physical Sciences Research Council) and MTC. I would like to thank everyone who has given me the opportunity to complete this piece of work.

Last but not least, a massive thank to the continuing support of my family. They only know how much love and support they are able to give me.

**Riccardo Tosi**

## **Presentation and Publication**

International conferences contribution:

- Microstructural changes in Ti - 6Al - 4V at different thermal conditions using Electron Beam Selective Melting process (Material Science & Technology conference, Columbus, Ohio, US, 10/06/2015).
- E-PBF, Adaptronic Chamber (Electron Beam Additive Manufacturing conference, Nuremberg, Germany, 27/04/2016).

Journal:

- C. L. A. Leung, R. Tosi, E. Muzangaza, S. Nonni, P. J. Withers, P. D. Lee. 'Effect of preheating on the thermal, microstructural and mechanical properties of selective electron beam melted Ti-6Al-4V components', Materials & Design, Volume 174, 15 July 2019.

## List of Abbreviations and Symbols

Al: Aluminium  
ALM: Additive Layer Manufacturing  
AM: Additive Manufacturing  
BCC: Body Centre Cubic  
C: Celsius  
CAD: Compute Aided-Design  
DED: Direct Energy Deposition  
DOE: Design of Experiments  
E-PBF: Electron Powder Bed Fusion  
FEA: Finite Element Analysis  
g: grams  
GA: Gas Atomized  
HCF: High Cycle Fatigue  
HCP: Hexagonal Close Packed  
HIP: Hot Isostatic Pressing  
HV: Vickers Hardness  
IR: Infrared Radiation  
L-PBF: Laser Powder Bed Fusion  
mm: millimetre  
MTC: Manufacturing Technology Centre  
NDE: Non-Destructive Evaluation  
PA: Plasma Atomised  
PBF: Powder Bed Fusion  
PRS: Powder Recovery System  
PSD: Particle Size Distribution  
SEM: Scanning Electron Microscope  
SLS: Selective Laser Sintering  
SS: Stainless Steel  
UTS: Ultimate Tensile Strength  
T: Temperature  
Ti: Titanium  
V: Vanadium  
X-CT: X-Ray Computer Tomography  
XRD: X-Ray Diffraction  
 $\mu$ -CT: X-Ray Micro-Tomography  
Kg: Kilogram  
~: Approximation  
 $\varnothing$ : Diameter  
2D: Two Dimensional  
3D: Three Dimensional

## List of Figures

Figure 1. 1: Thesis structure .....	3
Figure 2. 1: EBSM system with main parts integrated (left) [16]. Electron gun and chamber details (right) [17]. .....	6
Figure 2. 2: Log-file of a typical layer cycle in E-PBF. ....	8
Figure 2. 3: Heat dissipation theory [26].....	9
Figure 2. 4: E-PBF preheating theory and current calculation (a) [29], sintering behaviour of preheated powder particles (b, left [17] – right [31]).....	10
Figure 2. 5: E-PBF heating and melting on the top, and a schematic of beam movement at the bottom (just for A2 series machine) [21]. ....	11
Figure 2. 6: SF related to the melt pool (left), pool interaction between layers (right) [27]. ....	12
Figure 2. 7: Relation between speed and thickness [26]. ....	13
Figure 2. 8: Process and gas induced porosity observed through optical microscope [39]. ....	14
Figure 2. 9: Infrared image captured using an in-situ thermal camera [48]. ....	16
Figure 2. 10: An example of $\mu$ -CT X - Y section of an AM part [55]. ....	17
Figure 2. 11: Semi-sintered powder cake after completing a build [32]. ....	18
Figure 2. 12: Three main characteristics which effect the final product performance of finished parts [61]. ....	19
Figure 2. 13: Microstructural and mechanical behaviour before and after and HIP cycle [63]. ....	20
Figure 2. 14: Powder production methods [80]. ....	23
Figure 2. 15: HDH powder (a), gas atomised powder (b), plasma atomised powder (c), plasma rotating electrode powder (d) [82]. ....	24
Figure 2. 16: Influences to consider in metal powders [84]. ....	25
Figure 2. 17: Materials tested using E-PBF systems, 2016 review [93]. ....	27
Figure 2. 18: Three stages condition during and microstructural formation in a typical Ti - 6Al - 4V E-PBF cooling rate [98]. ....	28
Figure 2. 19: Phase transformation changes achieved at different holding T [100]. ....	29
Figure 2. 20: Schematic diagram of fusion boundary on E-PBF [109] (a). Variation of thermal gradient and growth rate along the solidification area [114] (b). Physical effect of a schematic beam deflected from left to right [115] (c). ....	31
Figure 2. 21: Simulation of powder spreading and layers melting in E-PBF [117]. ....	32
Figure 2. 22: example of $\beta$ phases generated in a Ti - 6Al - 4V part manufactured by E-PBF [121]. ....	33

Figure 2. 23: Morphology characteristics of Ti - 6Al - 4V Kroll's etched microstructure achieved in E-PBF [98]. .....	34
Figure 2. 24: Widmansteatten microstructure achieved using different volume energy [111]. ....	35
Figure 2. 25: Mechanical properties of Ti - 6Al - 4V parts manufactured using different approaches [127]. .....	36
Figure 2. 26: Fe - Ti intermetallic structure captured with a SEM between the base/build interface (a), Fe and Cr contamination in the first few hundreds microns (b) [119]. .....	37
Figure 2. 27: Reduced kit (a), cooling time comparison with the original chamber (b) [133]. .....	39
Figure 2. 28: Shell with lose semi-sintered powder before (left) and after (right) HIP consolidation [139]. .....	41
Figure 2. 29: Combined fabrication of Ti - 6Al - 4V and pure Copper [148]. .....	42
Figure 2. 30: Total service and product revenue of AM [1]. .....	44
Figure 2. 31: Three axis model of considering a part to be manufactured (left), when AM should be considered in production [166]. .....	47
Figure 3. 1: Beam trajectories upon layers where contour and hatch melting are noticed [171]. ..	55
Figure 3. 2: Microtomography system set up at the European Synchrotron Radiation Facility (a), reconstructed image of powder particles at the beginning of sintering (b) [185]. .....	60
Figure 3. 3: Tensile bar characteristics represented in mm. ....	61
Figure 3. 4: Typical E-PBF Ti - 6Al - 4V tensile curve (a), fatigue machine used for the tests (b). ....	62
Figure 3. 5: Example of a Ti - 6Al - 4V cycle performed during a HIP cycle [187]. .....	63
Figure 4. 1: 13 Samples generated by E-PBF using Ti - 6Al - 4V. ....	66
Figure 4. 2: 13 blocks after the manufacturing, they are attached on a 316 SS substrate. The reused plate shows drawings which have need cleaned before the current build. ....	67
Figure 4. 3: SEM pictures of PA 45 - 106 $\mu$ m powder batch used for the build. ....	68
Figure 4. 4: Polished powder analysis with low (a) and high magnification (b) captured by OM. .	68
Figure 4. 5: Equiaxed and columnar grains investigation on the bottom of the A3 specimen observed by OM. ....	70
Figure 4. 6: Mid (a) and edge (b) pictures of A3 specimen taken with SEM. ....	70
Figure 4. 7: Comparison of specimens with different preheating strategy, along the building direction, analysed by OM. ....	71
Figure 4. 8: Polarised OM prior $\beta$ grain boundaries analysis on the bottom (A) and on the top region (B) of the A3 specimen X - Z cross section. ....	72
Figure 4. 9: $\alpha$ lath comparison between a sample built at the edge of the preheat region (A1) and a specimen built in the middle of the cake. ....	73



Figure 4. 10: SEM and XRD analysis of contaminated area located at the bottom of specimen A3. ....	74
Figure 4. 11: Contamination amount from the bottom of the material up to 80 $\mu\text{m}$ . ....	75
Figure 4. 12: Micro-hardness graph which captures the trend line of each specimen analysed. ..	77
Figure 4. 13: A3 core and edge micro-hardness comparison graph. ....	77
Figure 5. 1: Project development diagram.....	80
Figure 5. 2: Arcam A2XX (a), and its standard starting plate (b). ....	81
Figure 5. 3: Original A2XX 3D hardware (a), manufactured chamber (b) new chamber design options (c - d - e). ....	82
Figure 5. 4: New adaptronic chamber 190 x 190 mm (a), reduced powder hopper sheets (b), reduced powder outlet opening (c), rack teeth reduction to 220 mm (d).....	83
Figure 5. 5: Gas atomised powder from TLS, surface (a) and section (b) characteristics. ....	84
Figure 5. 6: Hall flow, apparent density, and PSD curve analysis of GA powder supplied by TLS. .	85
Figure 5. 7: GA powder morphology analysis captured using a Malvern G3 Morphology system.	86
Figure 5. 8: preheat 1 lines observed during the process. ....	87
Figure 5. 9: Reduced length powder spreading (A), new 190 x 190 mm adaptronic chamber cake (B). ....	88
Figure 5. 10: Cylinders manufactured during the adaptronic chamber build (a), “low preheat” samples cut and Kroll’s etched (b), “standard preheat” porosity sections (c), porosity comparison average between preheat conditions d), columnar main $\beta$ -grains observed along the build direction in the standard preheat sample under polarised OM (e). ....	89
Figure 5. 11: Z - X SEM low preheated section (a), X - Y section of a high preheat part (b). ....	90
Figure 5. 12: EDX analysis of a standard manufactured samples with related spectrum elements. ....	91
Figure 5. 13: Micro-hardness performed along X - Z direction. ....	92
Figure 5. 14: 2D slice of the reconstructed volume in Y - Z direction of cans made with high (a), standard (b), and low (c) preheating strategy. ....	93
Figure 5. 15: Pore and pack density quantification.....	94
Figure 5. 16: Quantitative analysis of packing density and its variables captured in each condition. ....	94
Figure 5. 17: Comparison between the physical parts and CAD file. ....	95
Figure 5. 18: Prospective images of randomly selected tensile bars analysed by $\mu$ -CT for porosity investigation.....	96
Figure 5. 19: Pores analysis performed by $\mu$ -CT of the 3 pre-heat conditions investigated.....	97

Figure 5. 20: Tensile bars, cuboids for fatigue and microstructural analysis, and 3 mm $\varnothing$ x 3mm shells manufactured on each experiment condition (a), necking region of S - 1 tensile sample (b). .....	97
Figure 5. 21: Chart of the three different preheat conditions. ....	99
Figure 5. 22: SEM surface fracture analysis of L - 1 (a - d), S - 1 (b - e), H - 1 (c - f). ....	99
Figure 5. 23: L - 2 surface fracture captured by SEM with lack of fusion and porosity highlighted (a), crack propagation point with un-melted powder (b), lack of fusion with non-fused powder particle (c). ....	101
Figure 5. 24: Stress concentration edges in a cylindrical pore (a), high stresses edges in an elliptical pore (b) [204]. ....	102
Figure 5. 25: Post HCF image of high preheat #2 (a), and low preheat #3 specimens (b). ....	103
Figure 5. 26: SEM fatigue surface fracture of standard preheat #1 (a) and its crack initiation site (b). High preheat #2 (c) and a localised pores region (d). ....	104
Figure 5. 27: SEM image of low preheat #3 sample. Crack propagation site (a) with non-consolidated powder particles (b). ....	105
Figure 6. 1: CAD model of the shell (a) and its internal X - Z section (b). ....	110
Figure 6. 2: Materialise Magics file made for the build (a), with a representation of the cylinders main body (b). Tensile bar with encapsulated powder from the middle to the top region; supports are shown at the bottom of the cuboid (c). ....	111
Figure 6. 3: Energy density distribution in relation to the line energy (a). SF values used during the experiments (b). ....	113
Figure 6. 4: Cylinders and tensile specimens with supports after the build (a). Archimedes' test equipment used to test the samples before and after the HIP cycle (b). Samples #16 shrank after being HIPped (c) and porosity localised on the top surface of loose powder samples (d). ....	114
Figure 6. 5: OM porosity associated to BF (a), and its relation between weight and porosity (b). .....	116
Figure 6. 6: OM etched X - Z section of sample #2 (a), #5 (b), #9 (c), #13 (d). X-CT scan of loose powder shell in sample #16; X - Z (e), and X - Y (f) orientation. ....	117
Figure 6. 7: Influence of BF and energy density distribution on porosity [33, 213]. ....	117
Figure 6. 8: Values (a) and equations (b) used for calculating the shell core (c) using an Archimedes test rig. ....	118
Figure 6. 9: Shrinkage comparison between optical 2D and Archimedes' 3D analysis after a thermal HIP cycle (BF - SF). ....	119
Figure 6. 10: OM 2D mosaic X - Z section of sample #5 (a), #8 (b), and #15 (c) after being HIPped. .....	119

Figure 6. 11: OM X - Z microstructural sections of #15 shell and core (a), and a close OM image of a void compaction happened after HIPping in sample #4 (b).....	121
Figure 6. 12: SEM bottom shell / core interface of #15 (a) and #16 (b).....	122
Figure 6. 13: $\alpha$ lath average measurement of sample #5 (a - d), #8 (b - e), and #15 (c - f) before and after HIP treatment.....	123
Figure 6. 14: Average measurement if $\alpha$ lath width between different manufacturing conditions. ....	124
Figure 6. 15: Micro-hardness measurement before and after HIPping and indents location. ....	125
Figure 6. 16: HIPped region of a tensile specimen before being machined (a). 2D drawing of an in-situ shelling tensile bar (b), and the interface between HIPped powder and E-PBFed region (c).	126
Figure 6. 17: In-situ shelling mechanical properties. ....	126
Figure 6. 18: SEM surface fracture of tensile sample #1 (a), with a crack initiation region (b), and its ductile fracture (c). Tensile sample #2 surface fracture (d), with a crack initiation region and particles debonded (e), and its ductile fracture (f). ....	128
Figure 6. 19: Time Vs OM porosity Vs shrinkage of each condition manufactured.....	129
Figure 7. 1: E-PBF starting plate with 4 different substrate conditions (a). SEM region of the starting plate microstructure (b). Y - Z SEM section of peened surface and its plastic deformation length (c). Preliminary DOE studies to capture the laser re-melted region of DOE 2, and a Y - Z OM section of variable 7 and its ~86 $\mu$ m re-melted region (d). ....	133
Figure 7. 2: DOE 1 substrate design with cube designation numbers (a), Magics snap shot of the starting plate with substrate treatments and cuboids location before the E-PBF build (b). ....	136
Figure 7. 3: DOE 2 substrate design with tensile bar descriptions (a), Magics 3D snap shot of 40 mm starting plate and tensile bars location before the E-PBF build (b). ....	137
Figure 7. 4: 48 cuboids manufactured on a Ti - 6Al - 4V substrate, lack of fusion observed.....	137
Figure 7. 5: SEM pictures of shot peened C1 substrate (a), laser re-melted region on sample D1 (b), bended substrate after being stress relieved during the build cycle where substrate was cut and overlaid (c).....	140
Figure 7. 6: OM region between substrate and deposited region of the etched B2 cube. ....	142
Figure 7. 7: OM sample C1 X - Z plane section (A), SEM lack of fusion from sample C1 section (B), OM EB penetration and microstructure from the laser remelted D3 substrate (C), OM mosaic of etched D2 part (D).....	143
Figure 7. 8: Fusion zone of bottom left X - Z A2 sample section (a), laser re-melted bottom left X - Z D1 sample section (b), central fusion interface of sample C3 (c) and C1 (d) with main $\beta$ -grains growing through the fusion zone.....	144

Figure 7. 9: Close image of half of the cuboids analysed during the BF investigation (a), A2 top line scan measurement captured with OM (b). SEM cross section pictures of A1 (c), A2 (d), and A3 (e) top surface with relative overlap measurements. ....	145
Figure 7. 10: BF influences measured in the build. ....	146
Figure 7. 11: Equispaced 200 g micro-hardness indents.....	147
Figure 7. 12: 200 g HV micro-hardness indentation average value and trend line captured from the AMed region to the substrate.....	148
Figure 7. 13: Schematic of the tensile bars and their characteristics manufactured (left); DOE 2 completed build with all tensile specimens manufactured on 40 mm thick Ti - 6Al - 4V starting plate (right).....	149
Figure 7. 14: Tensile bars values compared to ASTM F2924 – 14 standard [106] (a). Horizontal (b), vertical (c), and vertical in-situ shelling HIPped (d) tensile bars before being machined. Hybrid vertical #3 tensile bar machined and tested (e). ....	151
Figure 7. 15: SEM tensile surface fracture analysis of hybrid horizontal #1 sample. Full image of the AMed part on the substrate (a). Allows show the porosity generated during the AMing of the material and the crack initiation of the specimens (b). Different axial load relative to the pores (c). ....	152
Figure 7. 16: SEM fractography of hybrid vertical # 1 surface fracture sample (a) and its crack initiation pore (b). Hybrid vertical # 2 surface fracture sample (c) and its ductile dimpled surface (d). ....	154
Figure 7. 17: OM X - Z cross section of #4 (a), intersection lines between the solidify E-PBF and HIP areas and the substrate (b), microstructure at the interface region between the consolidated powder and the substrate (c).....	156
Figure 7. 18: SEM fractography of hybrid in-situ vertical # 1 surface fracture sample (a) and its ductile behaviour (b). ....	156

## List of Tables

Table 2. 1: Details of the experimental chapters explored in the thesis. ....	50
Table 3. 1: Experimental stages and their characteristics (SF is related to speed function). ....	52
Table 3. 2: Parameters and settings used during the experimental chapters. ....	53
Table 3. 3: Powder chemical composition required in Ti-6Al-4V (element % - ASTM F2924). ....	55
Table 3. 4: Powder characterisation analysis requirements by ASTM standards. ....	57
Table 3. 5: SEMs description and location. ....	59
Table 3. 6: CT systems and settings (set.) used to analyse the samples. ....	60
Table 3. 7: Mechanical tests settings (set.) performed. ....	61
Table 4. 1: Parameter setting used during the E-PBF build. ....	65
Table 4. 2: Shown the flowability of the powder captured with Hall Flow technique. ....	69
Table 4. 3: Pre-setting of the micro-hardness system using different loads. ....	76
Table 4. 4: Micro-hardness average calculated from the bottom to the top side of four different specimens. ....	76
Table 5. 1: Preheat 1 main settings. ....	87
Table 5. 2: Preheat conditions used for the trials. ....	88
Table 5. 3: Mechanical properties results. ....	98
Table 5. 4: Roughness surface captured on the top region of the E-PBFed specimens. (*) no failure happened before $10^7$ cycles. (+) failure outside the gauge region. ....	102
Table 5. 5: Conventional Vs adaptronic chamber comparison. ....	106
Table 6. 1: Themes used during the experiment. (*) Standard MTC settings. ....	111
Table 6. 2: SF table with related speed and energy density. ....	112
Table 6. 3: OM 2D % porosity observed in the specimens with related BF and SF. ....	115
Table 7. 1: Surface roughness (Sa) captured in different surface condition and starting plate thickness. ....	134
Table 7. 2: E-PBF hatch settings used during the hybrid builds. ....	135
Table 7. 3: Summary of findings observed in the substrates and their conditions. ....	141
Table 7. 4: Tensile bar results. * Indicates if the specimen broke outside the middle 50 % of the gauge length. + Indicates if the specimen broke outside of the gauge length. ....	150

## **Chapter 1: Introduction**

### **1.1 Thesis Introduction**

Due to rising demand and expectations of the Additive Manufacturing (AM) market, manufacturers, end users, research institutes, and universities are continually working to increase productivity in AM industries to bring them to the next level. The literature suggests that AM can achieve worldwide growth of 38% by 2020 (The Wohlers report) [1]. This thesis presents fundamental studies and advanced manufacturing methods to produce additive manufactured parts using Ti - 6Al - 4V powder loaded into an E-PBF system. The process is commonly used for single or low production batches which normally manufacture components available on the market. Decreasing the total part weight, optimising the part or assembly design, and increasing mechanical properties are the main objectives targeted using an E-PBF technology. In order to achieve that, different approaches are investigated and analysed to better understand the AM impact on future production. Reducing or improving conventional production with the use of unconventional manufacturing methods can achieve optimised part production, which benefits productivity in AM and its impact in the market. These experiments are indirectly connected where metallurgical and mechanical properties were observed and compared to the conventional strategies now used in E-PBF.

### **1.2 Aims and Objectives**

The aim of this doctorate is to explore ways to increase productivity in AM, specifically using an A2XX E-PBF system from Arcam through advanced methods of manufacturing. These targeted a reduced lead time in part production, consequently generating benefits for manufacturing. The improved productivity in E-PBF should be approached from different angles such as having control of the build behaviour, understanding how the software and hardware work, and exploring advanced techniques to manufacture parts.

The objectives are focused on understanding the potential options available to improve production using an E-PBF system. Different methods are investigated to better understand the machine and its limits, in addition to an exploration of manufacturing options. The objectives can be summarised as:

- Fundamental E-PBF studies - build behaviour
- Adaptable build chamber - hardware and software configuration
- Advance build strategies - hybrid manufacturing and in-situ shelling techniques

Detailed explanation of the aims and objectives, gaps in research and novelties are highlighted in Table 2. 1.

### **1.3 High Productivity in AM**

Since AM systems were introduced to the market in the 1980s [2], they were mainly used for prototypes and low part manufacturing. Today, production is one of the hottest topics discussed in AM due its complexity and the challenges involved in moving the technology forward. For this reason, manufacturers and end users are trying to reach the next level of development by targeting different methods and approaches to push AM systems into real production [3, 4].

Advanced techniques of manufacturing and hardware solutions for medium and high part production are currently being explored and developed. Issues relating to productivity are mainly related to the cost of manufacturing AM components, its production rate, the cost calculation that needs to be done before starting part production and the readiness level which is directly related to investing in an AM production chain.

Multiple technologies are considered to raise productivity of high value components. These include automatic powder recovering systems, larger platforms, automated systems and manufacturing stages, integrated inspection and cleaning systems, and many other advanced and new additive techniques. The need to improve current systems is heavily under development, a rush against

time to the best AM technology available to switch from conventional manufacturing to customised production is under consideration from end users.

## 1.4 Thesis Outline

This thesis and its associated studies aim to improve the production rate using Ti - 6Al - 4V alloy using an ARCAM A2XX system. The path developed during the thesis is summarised in Figure 1. 1.

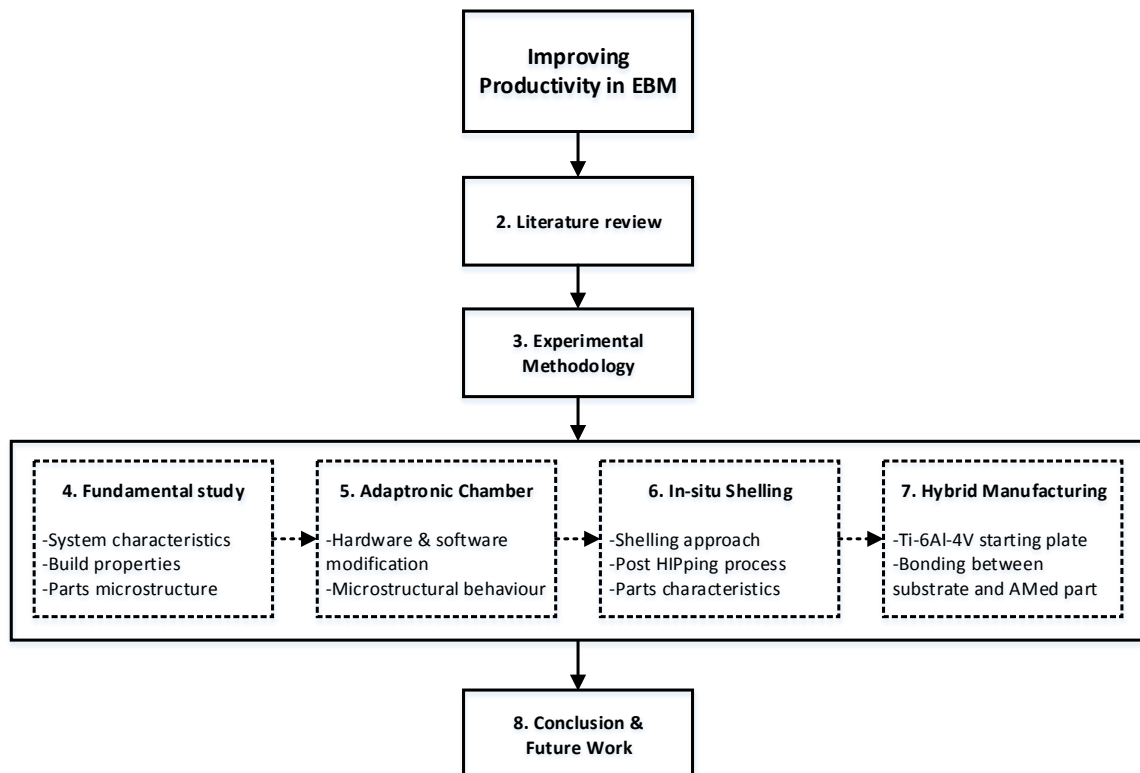


*Figure 1. 1: Thesis structure.*

It explores the fundamentals of the technology, advanced manufacturing approaches with related research evaluations, and provides a final conclusion. The chapters can be summarised as follows:

- Chapter 2 includes a review of the electron beam powder bed technology and the characteristics of the parts manufactured with it. A general literature review of Ti - 6Al - 4V alloy and its development and structure using an E-PBF system is provided. Its use and



applications in industry, the market, and its productivity status are reviewed to better understand the current state of AM and any gaps in knowledge.

- Chapter 3 explains the systems and methodology applied in this thesis. Approaches and methods used during the development of the experiments are described, and machines and fundamentals are listed and summarised.
- Chapters 4 to 7 demonstrate the experimental investigations carried out in this study. Machine fundamentals, hardware and software modification, and new ways to improve manufacturing are explored (further details can be found in Table 2. 1 and are summarised at the beginning of each experimental chapter).
- Chapter 8 provides a review of the investigations carried out during this thesis and concludes the results achieved during the experiments. It also provides recommendations for further research.

## **1.5 The Engineering Doctorate Degree**

The EngD degree is a four-year programme principally delivered by the Manufacturing Technology Centre (MTC) and the University of Birmingham (UoB), and is sponsored by the Engineering and Physical Science Research Council (EPSRC) and the MTC.

The background of this thesis was developed with support from the MTC and UoB. Both supported the progression of the entire doctorate. Its duration was 4 years, plus an additional year for writing. This included taught modules with a weight of 120 credits distributed between management and professional development skills, contextual skills, and advanced technical skills delivered at the University of Birmingham, the University of Nottingham and Loughborough University. The skills acquired during this doctorate focused on improving management and technical skills for the delivery of the main research projects.

The doctorate was delivered as a part of the AMAZE project (Additive Manufacturing Aiming towards ZeroWaste and Efficient Production of High-TechMetal Products) which was financially sponsored by the Seventh European Frame Programme (FP7).

## **Chapter 2: Literature Review**

### **2.1 Introduction**

As a result of aims and objectives described in the previous chapter, a tailored literature review was required to understand the current state of the E-PBF technology.

Powder bed methods use a layer-by-layer approach to build-up parts directly from a computer-aided design (CAD) file; a controlled heat source is used to consolidate the shape required on each layer. Industries have shown an interest in AM technologies due to their ability to generate near-net shape parts without the use of dies or heavy machining, reducing material waste and lead-time. Despite having relatively low production rates, small production and prototypes made with expensive materials, AM processes have generated interest in several high value sectors, such as medical, space, and aerospace [5, 6, 7, 8].

Electron beam melting, and its ability to fuse powder particles by deflecting accelerated electrons by electromagnetic coils [9], has the advantage of manufacturing 3D shapes not achievable using conventional methods. Due to continuous improvements to the system and the need from industries to improve productivity, several pushes in production planning from both users and manufacturers is currently in progress [10].

This literature review sequentially introduces the E-PBF machine with its heating strategies and melting characteristics, process and post process approaches, and powder and materials available for the system. Afterwards, an overview of Ti - 6Al - 4V properties and its characteristics when manufactured with an E-PBF system are analysed to provide an overview of the mechanical and microstructural characteristics of a component manufactured within an E-PBF system.

After a general literature review of the process and post-process methods, and material properties of Ti - 6Al - 4V, a literature review was conducted to introduce the experimental chapters and the current status of productivity in AM. A summary and gaps are listed at the end of the chapter, where a table providing a summary of experiment can also be found.

## 2.2 Electron Beam Melting by Arcam

Electron beam technology was first patented by Steingerwald Karl Heinz in 1952 [11]. After the first layer-by-layer development at the Swedish' Chalmers University of Technology in Gothenburg in 1995, the first Electron Beam Melting (E-PBF) system was launched by Arcam AB (founded in 1997) at EuroMold in 2002 [12].

Nowadays, Arcam AB is currently supplying three different systems; Arcam Q10, Q20, A2X with a build envelope from 7200 cm<sup>2</sup> to 15200 cm<sup>2</sup> and four different types of powder: Ti - 6Al - 4V, Ti - 6Al - 4V ELI, Titanium Grade 2 and Cobalt-Chrome ASTM F75, and Inconel 718 [13, 14, 15].

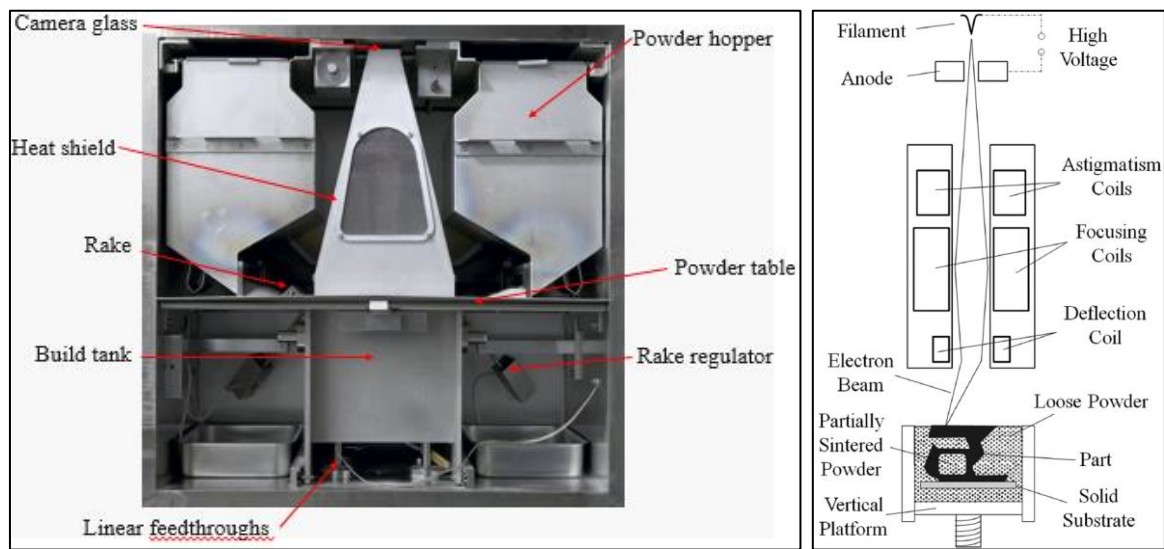


Figure 2. 1: EBSM system with main parts integrated (left) [16]. Electron gun and chamber details (right) [17].

As shown in Figure 2. 1, the electron beam system is manufactured with an electron beam gun, where a tungsten single crystal filament is heated to an extremely high temperature ( $T$ ) and electrons are released. An electrical field accelerates the electrons to half the speed of light; then, they are focused by electromagnetic coils located at the end of the gun [18]. Three electron magnetic lenses, known as coils, are installed inside the gun which sequentially correct the astigmatism of the beam, the beam spot size, and the X - Y deflection of the beams [19]. The electrons selectively melt each layer of metal powder spread on the table with the desired geometry. High preheat  $T$  and vacuum chamber help to eliminate impurities and results in high strength properties of the material; maintaining a high build  $T$  provides great properties and low residual stress in the part.

### 2.1.1 E-PBF System

Having defined the melting theories used in an E-PBF system, other variables must be considered during the manufacturing of the parts, such as scanning strategy, powder distribution, platform lowering, and a controlled vacuum environment [20].

Having a controlled vacuum environment of  $10^{-4}$  -  $10^{-5}$  mbar the electromagnetic lenses move inertia-free electrons, speeding them up to  $10^5$  m/s in the designed envelope, with the ability of allowing almost immediate jumps from one point to another [21]. A minimal amount of helium is used to prevent smoke events that are caused by the electrostatic charge [22] which may result in powder jumping and eventually build termination.

The powder is spread on a Stainless Steel (SS) plate with a rake which moves in the left to right direction for fetching/picking up the powder from the gravity chambers located on the sides. The first layer of powder is spread on top of the preheated starting plate, which is usually SS. Afterwards, the bed is going down to a preselected layer thickness, normally between 50 and 150  $\mu\text{m}$  [21], which is usually selected from the morphology of the powder and the melting strategies defined for the build. Saying this, most of the components inside the E-PBF machine are manufactured using SS due its very high non-magnetic properties (permeability close to 1 [23]) that permit no attraction fields, which may disturb the trajectory of the electrons when shot.

Powder flow is facilitated inside a vacuum system, where tap and apparent density are the main characteristics for having good flowability properties; satellites and small particles can considerably reduce the flow and increase potential instabilities during the process. Gas atomised powder with a size between 45  $\mu\text{m}$  - 106  $\mu\text{m}$  is normally used from the E-PBF community.

### 2.1.2 Heat Dissipation

E-PBF systems work using an elevated T inside the vacuumed chamber. Several advantages such as flowability in weld and reduced contaminant pick-up of build material (due to oxygen environment control) are beneficial during the manufacturing of the parts [24].

The surface T differs between materials. Ti - 6Al - 4V has a suggested range of  $\sim 720$  °C (650-850 °C), which should be maintained in a constant condition whilst the melting and equilibrium is taking place. As a result, the amount of introduced energy equals the conducted or radiated energy. As shown in Figure 2. 2 (log-file), to maintain a stable T, both preheating and melting are set to match the heat balance required for the process per layer [25].

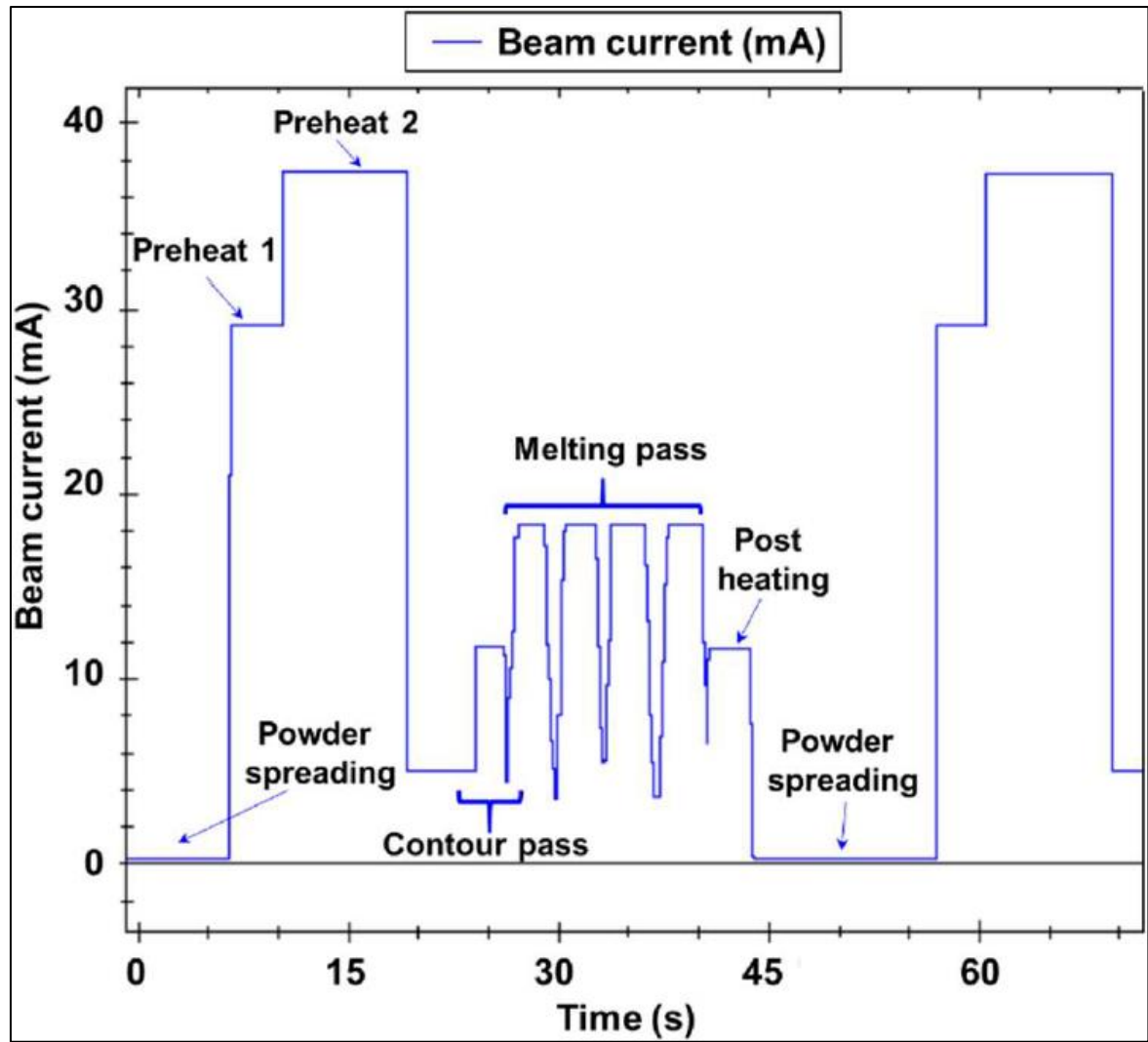


Figure 2. 2: Log-file of a typical layer cycle in E-PBF.

Figure 2. 3 shows that major heat losses are through radiation of the top surface and through the sintered powder from the surrounding surface of the part and base plate [26, 27]. Only the top surface is kept at the  $T$  required to melt the layer, which has a tendency to raise up upon layers. The rest of the part will be at variable  $T$ . There is a tendency for increased  $T$  along the build which can occur due the heat released from the surfaces previously melted.

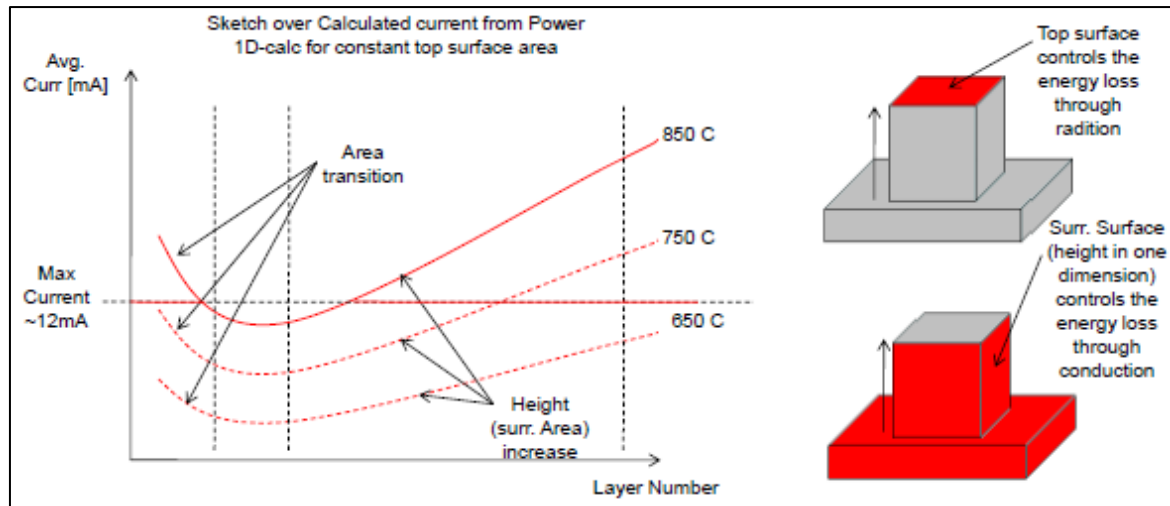


Figure 2. 3: Heat dissipation theory [26].

### 2.1.3 Pre-heating Method

After the powder has been spread on the table, a preheating scan is performed in order to raise the T and to semi-sinter the powder layer. An energy buffer is used for maintaining the overall energy consumption for all process steps. The beam is defocused during pre-heating phase in order to heat up the material without melting it [28].

The intention of the first preheated area is mainly to increase the T (substrate/previous melted layer and powder particles) and to maintain the overall energy consumption at the same level after each layer. Preheating 2 has the intention of heating up the powder circumventing the part with an additional preheat sequence. During the preheating phases a calculation is automatically generated through a pre-defined equation inside the software. All models loaded for the process step are included in the calculation. Its goal is to maintain a constant surface T during the build by adapting the power according to the geometries of the parts.

The two pre-heating steps used before the melting phase are known as preheating 1 (“jump safe”), and preheating 2 (“melt safe”). Figure 2. 4 (a) shows the random order of waves generated during the preheating 1; an equation is automatically calculated to calculate the energy density in order to obtain an equal energy distribution to all surface. The second preheating preheats the powder circumventing the parts with an additional preheat sequence. It is normally calculated using the average current for the reference area and the calculated average current for an arbitrary area which is obtained by scaling this value with area/reference area [29]. Sintered powder, also known as “cake”, resumed in Figure 2. 4 (b) shows how the powder sinters together from the surfaces in

contact generating a compacted structure to resist the high velocity impact of the electron beams [30, 31].

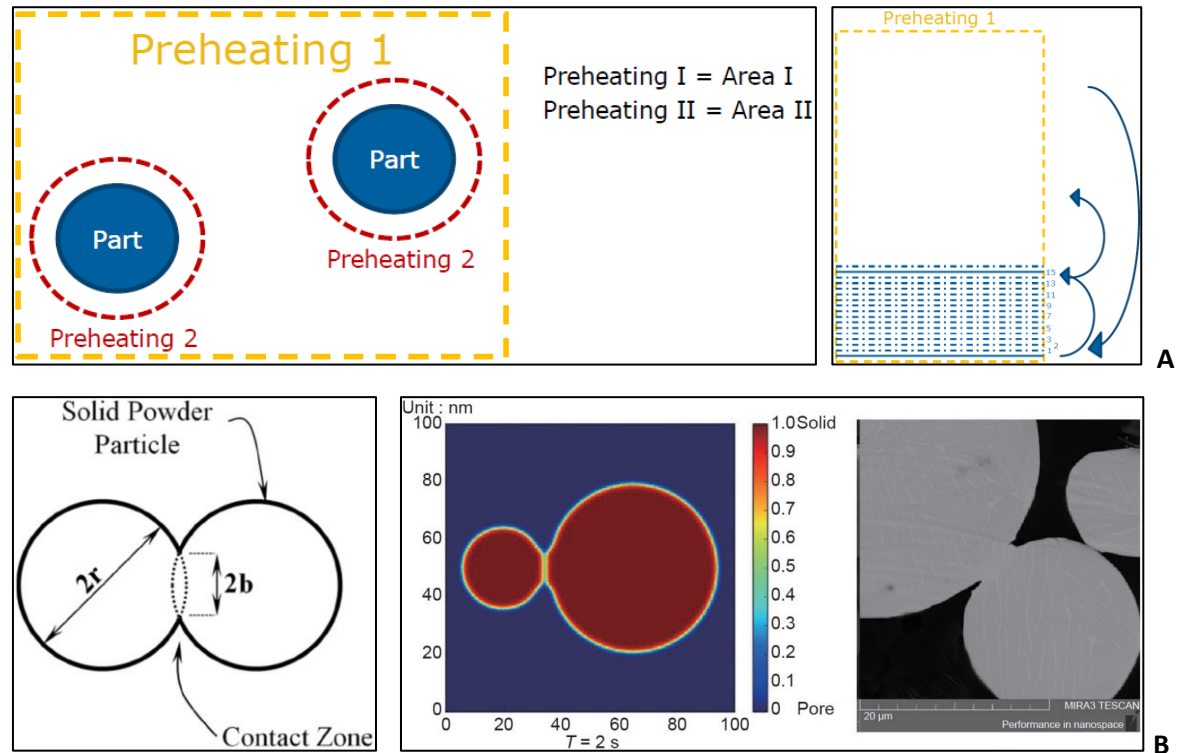


Figure 2. 4: E-PBF preheating theory and current calculation (a) [29], sintering behaviour of preheated powder particles (b, left [17] – right [31]).

Sintering powder together during the preheat stage allows the powder to electrically charge up, increasing the heating  $T$  of the particle. This phase helps to avoid powder blowing away and smoking during the process. Furthermore, an increase in wetting ability between particles and the holding resistance occurs during this phase which facilitated the impact of the high power refined beam [32].

#### 2.1.4 Melting Method

The preheating phase is used to increase the surface  $T$  of the material helping the melting phase, it controls the amount of power that will be used for melting. The calculation generated will allow the E-PBF to maintain a constant surface  $T$  during the build by adapting the power according to the geometries of the model.

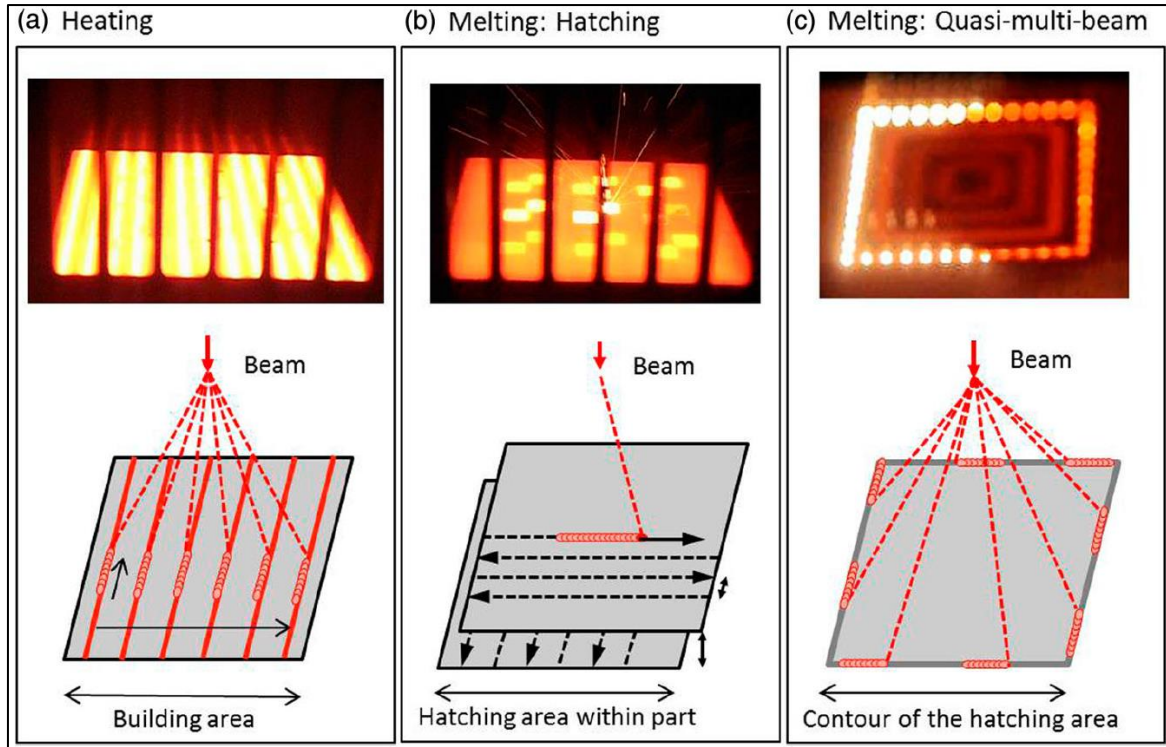


Figure 2. 5: E-PBF heating and melting on the top, and a schematic of beam movement at the bottom (just for A2 series machine) [21].

Figure 2. 5 show different settings of the system during the melting stage. The function of contours and hatching are the principal methods used for a melting strategy. Contour technique melts the periphery contour of the geometry; the beam jumps and shifts between each spot with a given displacement and overlap. The interior area is then melted during the hatch phase, allowing it to solidify the inner geometry using the settings automatically calculated from the parameter settings. A zig-zag strategy is commonly adopted to melt the powder particles with parameters set prior to the build in the A series machine.

A simplify equation is used to calculate the energy density ( $\text{J/mm}^3$ ) that is normally achieved with the following equation [8, 33]:

$$E = \frac{P}{v \times d \times t}$$

Where  $E$  is the energy density,  $P$  the beam power,  $v$  the scan speed,  $d$  the hatch spacing, and  $t$  is the layer thickness. This is used to estimate the energy achieved during the melting and consequent melting strategies and microstructure development.



### 2.1.5 Scanning Theory

In order to generate a correct melt pool size, four main variables are considered during the process:

- Current;
- Speed function (SF) number;
- Scan length;
- Physical properties, such as thermal conductivity, surrounding T etc.

The SF number will set the required melt pool size: the larger the SF the smaller the melt pool size, and vice versa. The calculations of SF s are the same for contour and hatch which are dynamically controlled in order to keep the same melt pool across the melted region [34]. As shown in Figure 2. 6, the hatching SF number will be much higher to achieve the same melt pool size since the line offset and scan length will provide extra heat from adjacent scan lines. During the hatching, no adjustments exist for different scan lengths and therefore the melt pool size will vary slightly depending on this. The metallization of alloying elements will depend upon the SF where a too low value can give aluminium loss in Ti - 6Al - 4V whereas a too high number will give insufficient melting (lack of fusion) [26].

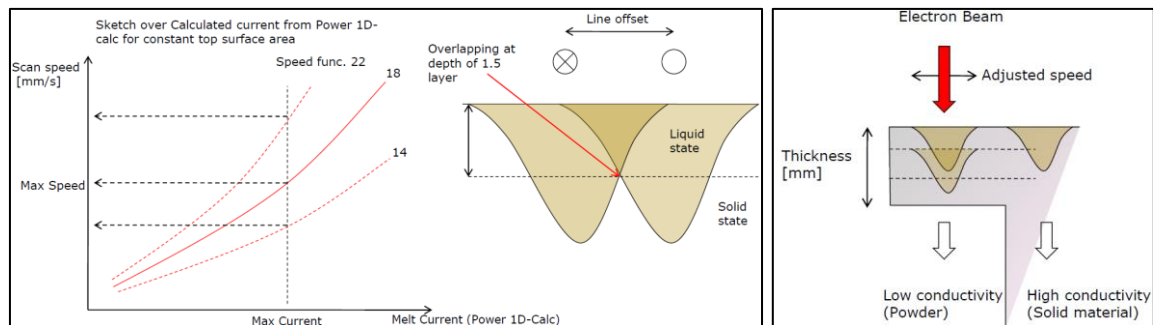


Figure 2. 6: SF related to the melt pool (left), pool interaction between layers (right) [27].

For areas on the geometry that are close to the contour, the melt hatch pattern will introduce more energy per area and also face the melt pool from the adjacent scan line. Therefore, the calculated speed from the SF needs to be adjusted according to a function with the following input variables:

- Speed (calculated from the SF);
- Distance (distance from the contour/turn-point);
- Material properties, such as thermal conductivity for material, powder size etc.

The compensation will only take place when leaving the turn point and not heading towards it. The compensation will be larger but shorter as the incoming speed from the SF gets higher. In contrast to the thickness function the turn point function has no trade-off between melt pool size and surface T and therefore the adjustment can fully be controlled through the speed (Figure 2. 6). The compensation from the turn-point function will superpose the compensation from the thickness function and the SF [26].

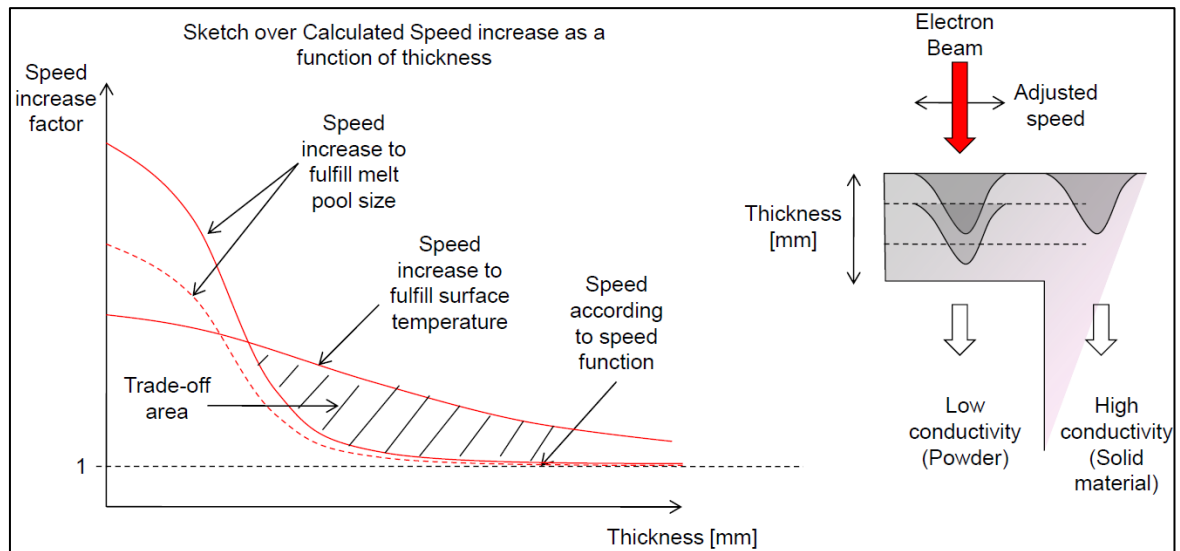


Figure 2. 7: Relation between speed and thickness [26].

### 2.1.6 Defects in E-PBF

Optimized parameters plus stability and repeatability can sometimes be a challenge with E-PBF systems. Consistencies between builds is considered an important step to improve and to guarantee reliability during production. Different types of defects are observed in E-PBF, which can be critical for the manufacture of high spec components where post treatment and inspection methods are used to pass the final conformity standards.

Several defects could be found during a layer-by-layer build due to predictable and unpredictable reasons; some defects are not impacting on mechanical properties, others result in potential fatal failure, some mean that parts should be post treated to become tolerated defects. Standards as ISO/TC261, ASTM F2792, ASTM Committee F42 (and many others) are continuously under review to guarantee international partnership agreements on overall standards for AM.

Porosity is a common issue observed in most powder bed fusion (PBF) technologies. Commonly observed in as spherical and elongated geometries (Figure 2. 8), pores can significantly impact crack growth and fatigue performance of parts [35]. Located in the layers, on the external surface,

and between adjacent layers, pores have different shapes and sizes [36]. They are normally observed as voids or gas pores trapped during the fabrication of layers, where un-melted powder (lack of fusion) can be noticed.

Due to the E-PBF's high preheated T cycle, residual stresses 0.03 mm below the surface are considered nearly to zero [35] and cracks generated during a rapid cooling are minimal. However, delaminations and cracks can be noticed as a consequence of lack of energy density, electron beam shifting issues, poor hardware or powder regulation issues, and non-optimised parameters. Lack of fusion and surface finish condition are considered a high impact defect for mechanical and fatigue performance [37].

In addition, other defects phenomena which may cause defects can appear during the interaction between the powder particle and the melting phase. Ejections as vaporised metal from the melt pool, metallic vapours blowing away non-melted particles, and powder repulsion due electrostatic charging were observed by Liu at al. [38] and Sames at al. [39] as potential causes of defects during the manufacturing of parts. Metallisation can also be a source of contamination if not promptly mitigated [40].

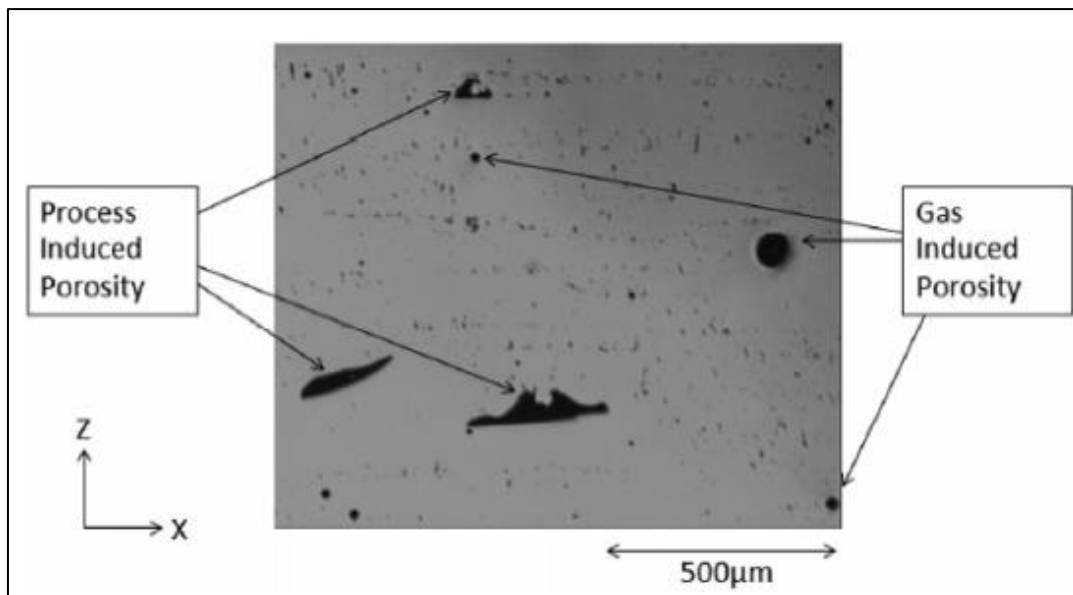


*Figure 2. 8: Process and gas induced porosity observed through optical microscope [39].*

Lately, several PBF investigations on part inclusion and contamination were observed [41]. They can reduce mechanical properties and consequentially generate catastrophic failures. Powder contamination, uncleaned AM system, and external unknown substances may generate critical

issues to in service components, which means that build preparation plays an important role during the manufacturing.

Close loop repairing methods are now under investigation, where in-situ analysis could perform a repairing strategy directly during the live build. At this stage of metal PBF systems, just observation and data analysis are captured, where beam spot, size, and T are used as feedback data for post process and analysis [36].

### **2.1.7 Inspection Methods**

Considered as a key technological barrier [42], quality in AM parts is essential for the manufacture of end use parts. In-situ and non-destructive post analysis inspection methods are used to understand the quality of the parts manufactured with an E-PBF system. Due to inspection complexity, part requirements and application field, several checks need to be done to ensure the quality of the components compared to conventional manufacturing methods [43].

Acquisition of live data for a close-loop monitoring system, highlighted as a key barrier during the roadmap workshop on measurement science for metal-based AM systems [44], is classified as having a critical role for non-destructive evaluation (NDE). Targets to build it right the first-time, development and updated AM standards and process model, validated and specified post processing methods of inspection, and structural health monitoring [45] are all under investigation. In order to define and certify these methods, several projects with worldwide partners are, or were, funded to push the technology forward [46].

Compared to the A2XX, the new Arcam Q-series offers in-situ visual/thermal inspection methods like LayerQam [47, 48], where a camera is used to capture live high-resolution 2D pictures of the manufactured layers in order to spot live issues (such as cracks, voids, defects) and to reconstruct the final 3D shape for a post comparison with the CAD file. Another advanced method, the X-Ray detector, is currently being used to check smokes occurring during the live build. In the future, the same filter could be used to detect more data such as chemical composition, defect size, microstructure development using secondary and backscattered electrons deflected from the impacted surface [40].

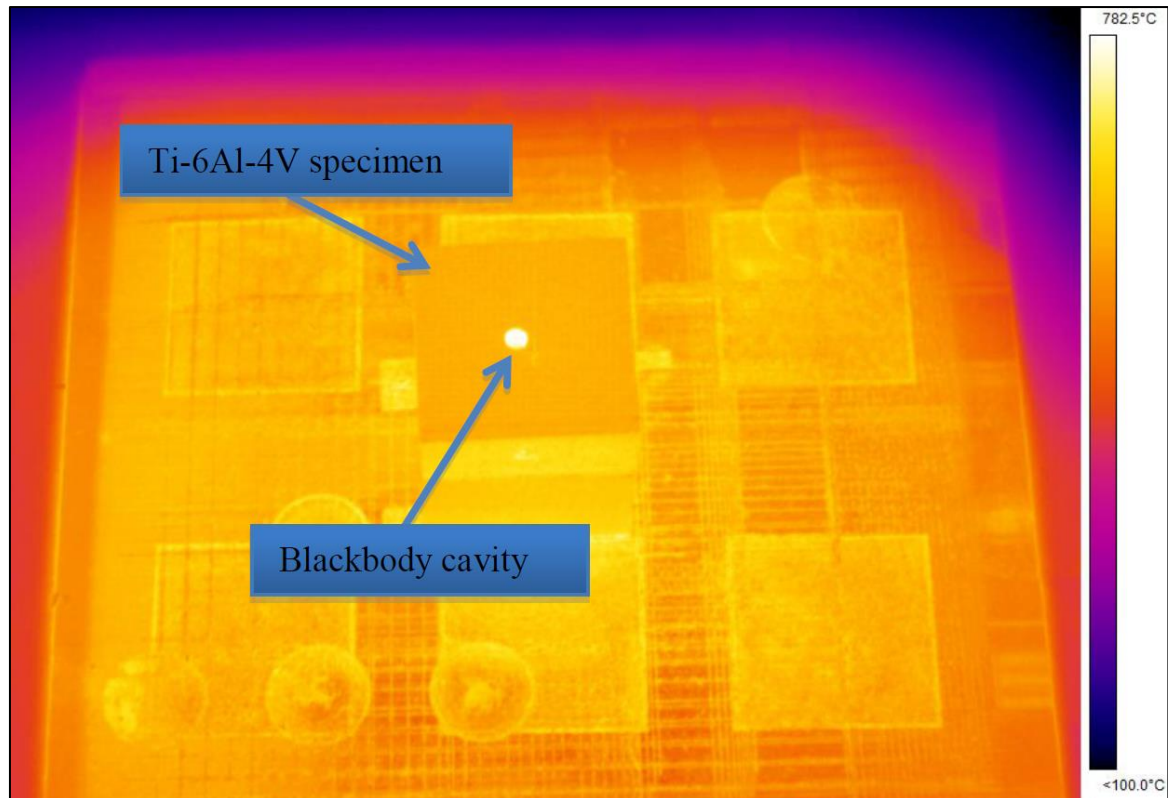


*Figure 2. 9: Infrared image captured using an in-situ thermal camera [48].*

Cheng et al. [49] used a near infrared radiation (IR) camera with low, medium, and high heat calibrations to collect thermal measurements during the process which was used for final element validation (Figure 2.10). During the experiment, preheated 25 – 50 microns powder was trapped inside a shell and post measured with a  $\mu$ -CT (X-Ray Micro-Tomography) system to understand the powder behaviour and to detect its thermal conductivity.

Several inspection methods in different stages are used to certify the part quality. Having mentioned the in-situ options currently available in an Arcam E-PBF machine, other inspection techniques are performed since the parts have been removed from the 'cake'. Post analysis methods can be compared to better understand the porosity and cracks of the specimen manufactured. Conventional optical microscopes (OM) are used to capture 2D sections of the specimens, where voids are shown. Then post processed software, such as Sherlock [50] and ImageJ [51], are automatically or manually operated to capture the porosity.

Other non-destructive methods are also used to define superficial cracks or internal density / porosity [52]. The Archimedes test [53] can be used to detect the volumetric mass density of the specimen in order to detect potential internal porosities. Eddy Current and liquid penetrant inspection are commonly used to investigate superficial cracks and defects [54]. Advance acoustic

emission processes (i.e. ultrasonic tank) are also used to detect porosity, even if settings and post process can be very complex to set-up and analyse.

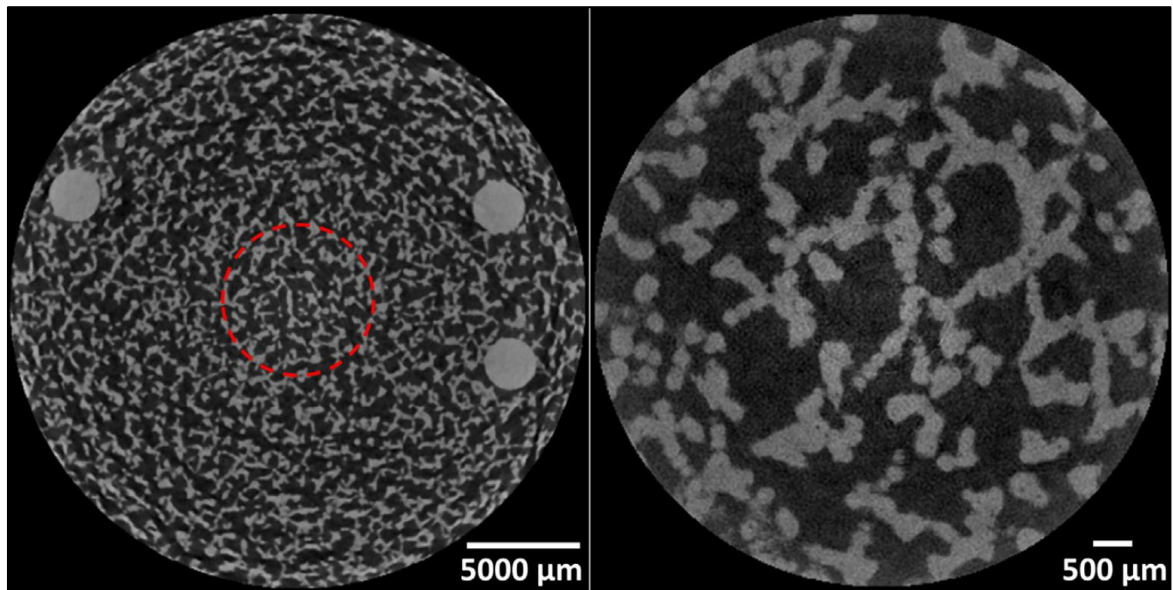


*Figure 2. 10: An example of  $\mu$ -CT X - Y section of an AM part [55].*

Due to the high performance, resolution, and data output, X-CT (X-ray Computer Tomography) and  $\mu$ -CT have recently been used to perform non-destructive morphological post inspection on AMed parts [55] (Figure 2.10). The complexity of capturing machine settings and performing post image segmentation [56] make the technique expensive and time consuming to perform. Despite that, post analysis X-CT studies are performed to investigate the porosity and cracks located inside parts. The scanning resolution available is related to the voxel size of the machine used that represent the minimum resolution achievable with the system used; also the thickness of the specimen has an impact to final resolution. Tamas-Williams et al. [57] used a  $\mu$ -CT system 2.1  $\mu$ m voxel size resolution, where a minimum pore size of 5  $\mu$ m was captured. This post processing data has several acquisition limitations, such as the approximation of resolution for pores below the resolution range. Despite that, advantages of using an NDE scanning technology compared to the conventional cross-sectional methods were observed [58]. Issues such as time and being operator dependent are the main limitations observed during for this technique.

Hou et al. [34] managed to optimize the E-PBF parameters after post analysing the sample using an X-CT system. An automatic image segmentation method was used to scan all the images captured using an in-house developed script.

### 2.1.8 Post Processes

Post processing in this context describes the processes that are taken in treating an E-PBF part post manufacture. Treatments such as Heat Treatment or Hot Isostatic Pressing (HIP) are not discussed.

As a consequence of the preheating stage the powder is 'semi-sintered' together, producing what is known as a "cake" (Figure 2. 11). The cake is typically separated using a blasting system which blows the powder through a high pressure gun to the component located inside an enclosed box. The impact of the shot powder helps to remove the semi-sintered cake attached to the manufactured parts. Normally, most of the powder gets detached from the specimens and collected into recycling boxes located beside the powder recovery system (PRS). Afterwards, the powder is recovered completely, refreshed with other powder, or scrapped. The process provides protection for the operators and grades the powder into useable quantities whilst separating out very fine powder and large agglomerates not suited for the E-PBF process.

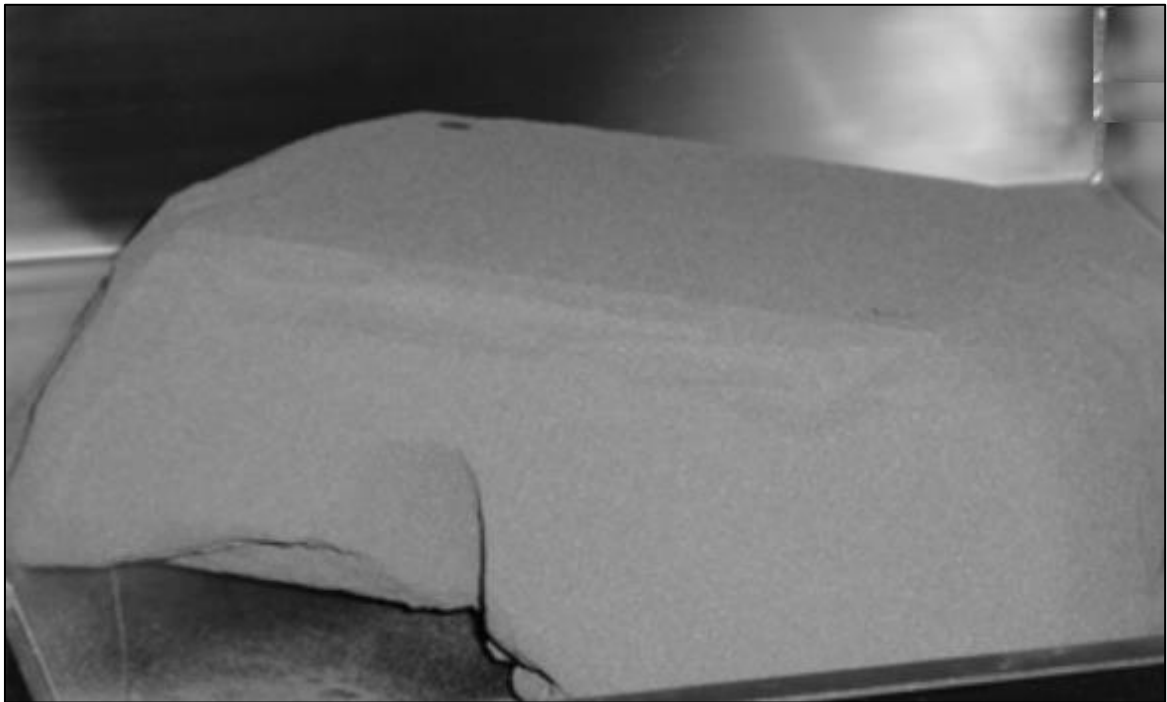


*Figure 2. 11: Semi-sintered powder cake after completing a build [32].*

In the E-PBF context, the dry abrasive blasting principle consists of projecting a mixture of blast media and compressed air onto a semi-sintered powder cake at high velocity to retrieve solid parts encased within the powder cake. The powder cake disintegrates into powder that is recycled for further use. To be efficient and reliable, this process calls for the best possible reproducibility of operating conditions. It is therefore recommended to carry out abrasive dry blasting using



controlled pressure and for a time that does not induce contamination and residual stresses on the part surfaces.

Complex internal holes and features, such as cellular structures, limit and restrict the effectiveness of the removal of the sintered powder [59]. Distinct, and also combined, methods for removing the stuck powder from internal featured have been tested. The limitations of accessibility and physical properties of the semi-sintered cake are still a strong limiting factor when processing line-of-sight limited and complex E-PBF structures [60].

Following part-breakout as described above, the E-PBF part usually has support structure that is attached to the part and does not form part of the component. This support structure is removed using hand tools by skilled operators. This manual process is prone to error and limitations, especially for complex structures. Incorrect support structure removal can lead to part damage, generation of cracks or inadvertent removal of part structures that are in effect not support structures.

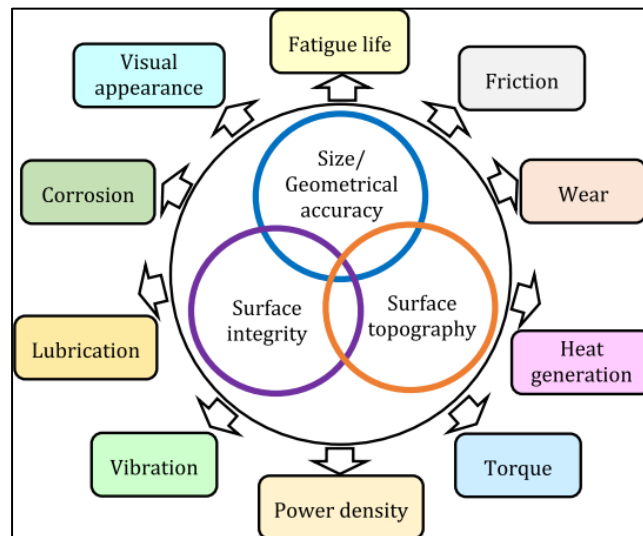


*Figure 2. 12: Three main characteristics which effect the final product performance of finished parts [61].*

All post process techniques are characterised from the starting condition of the material, where the initial roughness and the amount of material to be removed both have an important impact on the final polished part and the approach adopted. The superficial roughness of the part can be related to several factors, however, the main drivers are related to the powder size distribution and layer thickness used during the build [62]. Figure 2. 12 shows three starting conditions that effect the final performance of the manufactured component and the impact on its life cycle [61].



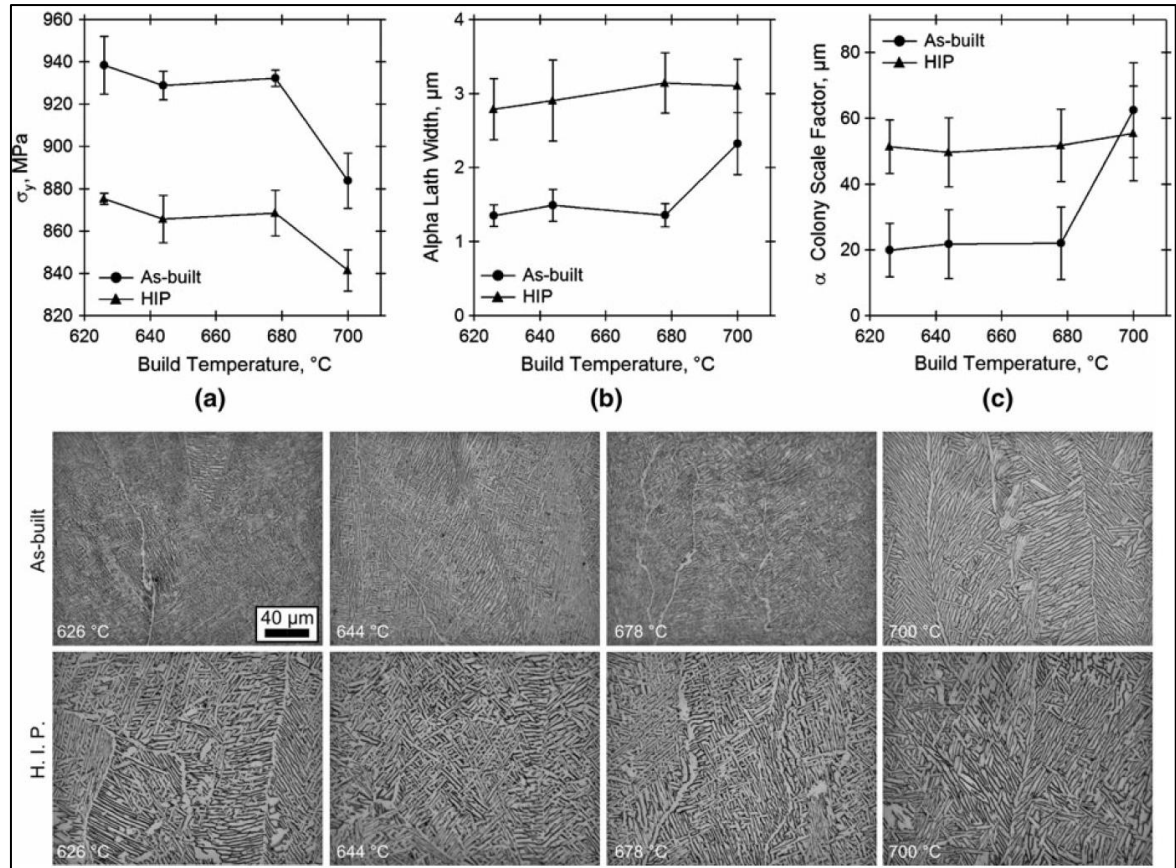


Figure 2. 13: Microstructural and mechanical behaviour before and after and HIP cycle [63].

Depending on the cycle, properties needed, and end user request, heat treatments are conventionally used to post process AMed parts [64]. HIP is a post heat treatment method normally used to post relieve residual stresses and reduce the internal porosity of the part generated during the manufacture process. The high isostatic pressure during a thermal cycle (a standard cycle at Bodycote in Brussels is around 1000 bar under argon,  $\sim 920$  °C per 2 h for Ti - 6Al - 4V [8]) reduces porosity originally located inside the component after the build. A HIP cycle changes the properties of the material, impacting on the mechanical properties, reducing yield tensile strength (TS) and ultimate tensile strength (UTS). However, in most cases, it improves elongation properties, due to the reduction of pores and an increase in the size of alpha lath in Ti - 6Al - 4V [65]. Nevertheless, it is dependent on the build microstructure morphology of the part before HIP treatment [63] (see Figure 2. 13), and the HIPping settings [66].

Bahbou and Ackelid [67] tried different HIP settings with samples with different porosities observing that mechanical properties decrease with the increase in T during a Ti - 6Al - 4V cycle. However, increasing the pressure and decreasing the standard T of 920 °C should close the porosity whilst maintaining high mechanical properties due to the minimal growth of alpha lath.

In addition to the HIPping solution, many other heat treatments are available to modify and tailor the structure after the manufacture of an AM part. Galarraga et al. [68] performed several post heat treatments of Ti - 6Al - 4V manufactured via E-PBF with several studies from above and below  $\beta$  transus, different cooling rates, and different heat treatment solutions, showing different tailored solutions to post process the component.

Other post processes can be performed to improve both the mechanical and surface properties of parts which can be divided into contact systems and non-touch devices:

- Laser re-melting or polishing can alter the surface chemical composition compared to the standard as build properties [69], where an oxide film can be obtained if the treatment is performed in a non-oxygen controlled environment, causing a surface tension that may decrease shear and tensile strength [70]. However, an increase in wear resistance and micro-hardness compared to a standard built surface has been observed [71].
- Shot peening treatment enhances the hardness, compressive yield strength, wear resistance, surface roughness [72] and fatigue [73] of most ALM materials. Depending on the initial surface roughness, a great reduction in roughness can be achieved. Improvement in fatigue performance has also been observed [35]. However, equal surface treatment can be an issue.
- Mass finishing, if in ideal conditions, can result in a part with a surface roughness below  $>0.5 \mu\text{m}$ . As a contact method, it can have many influences on mechanical properties, such as increasing fatigue life as a result of compressive surface stresses generated during the process. Other benefits such as reduced friction, wear resistance, corrosion and torque output can be achieved during this process [74]. Nevertheless, a substantial amount of material can be removed from the surface, which may generate tolerance and assembly issues.
- The removal of the material, either through conventional machining or abrasive finishing, allows for the elimination of defects on the AMed surface, improving the fatigue life by an average factor of about 4 [75]. However, other defects are formed during the near-surface removal which can also decrease the life of the component. Both techniques, depending on the starting condition of the part, the material, and methodology, can achieve a roughness below  $>1 \mu\text{m}$ .
- Electro polishing, using an electrochemical solution, minimises the surface dirt and micro roughness, thus improving the adhering properties and consequently the surface

cleanless. The low-impacting process allows for the treatment of fragile parts [76]. However, it can be costly and time consuming.

The abovementioned techniques and approaches need to be considered according to the final product characteristics which are needed in order to meet defined specifications. The various methods currently available are providing different options for post processing of components. Combined and customised methods are also implemented to maximise properties and performance of the parts. Well defined methods or standards are not in place yet; experience and conducting tests can be the solutions to evaluate the best approach to use.

### **2.3 Powder for E-PBF**

Considered as one of the key elements of a successful build, high-purity metal powder can be manufactured in different ways (Figure 2. 14), with different shapes and qualities. Powder atomisation is the most common method for manufacturing powder in AM. Several methods can be used in powder production, such as gas atomisation, water atomisation, plasma atomisation, rotating electrode process (REP), plasma rotating electrode process (PREP), and centrifugal atomisation. New approaches using cheap and rough powder are currently under investigation like hydride-dehydride (HDH) and granulation-sintering-deoxygenation (GSD) [77] where benefits such as cost-savings of manufacturing the powder were observed [78].

Plasma Atomized (PA) technology was patented in the early 1990s [79] and commercialised a few years later, and Gas Atomized (GA) technology is the most widely used powder production method in the E-PBF technologies. Due its ability to both melt and atomize rod fed material into the converging plasma/gas jets, PA and GA can be used to produce ceramic-free Ti alloys. The PA technology has the ability to achieve a very high molten T and cool slowly enough to guarantee an optimum spherodisation level.

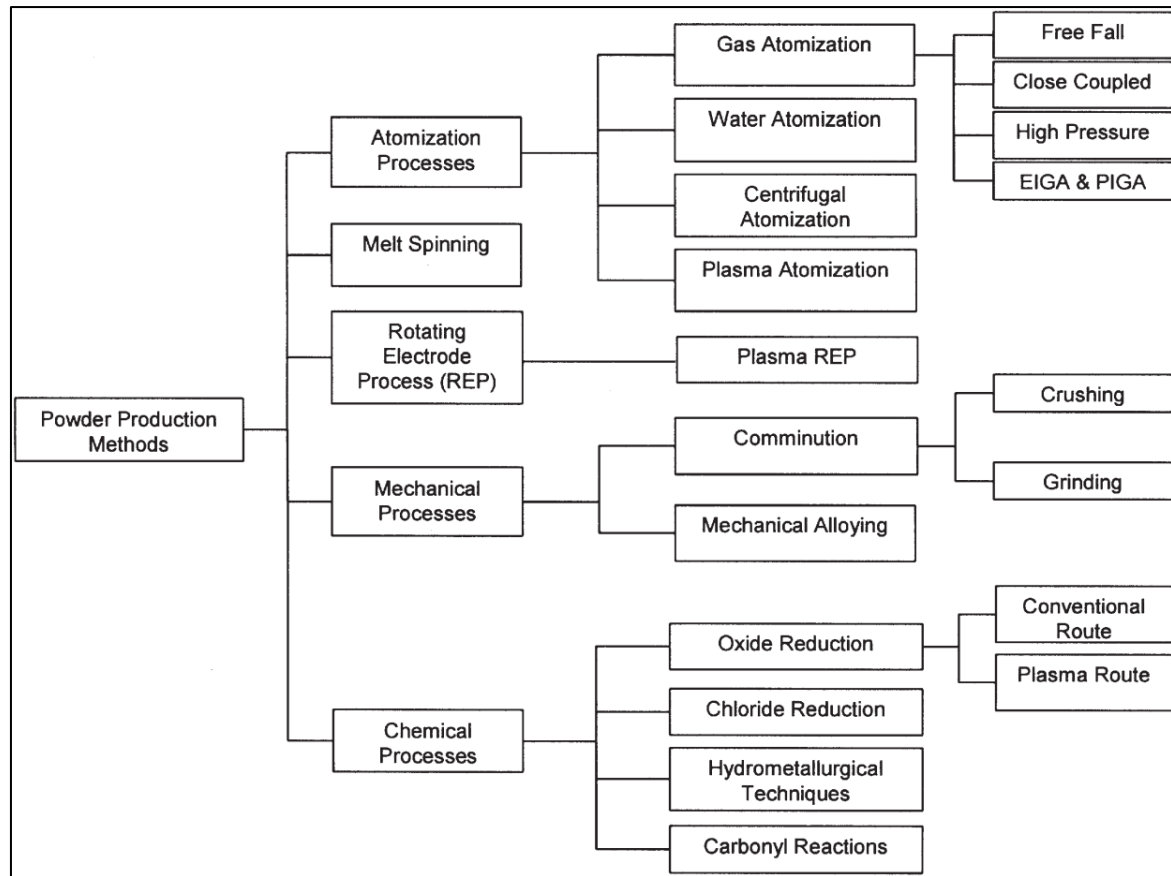
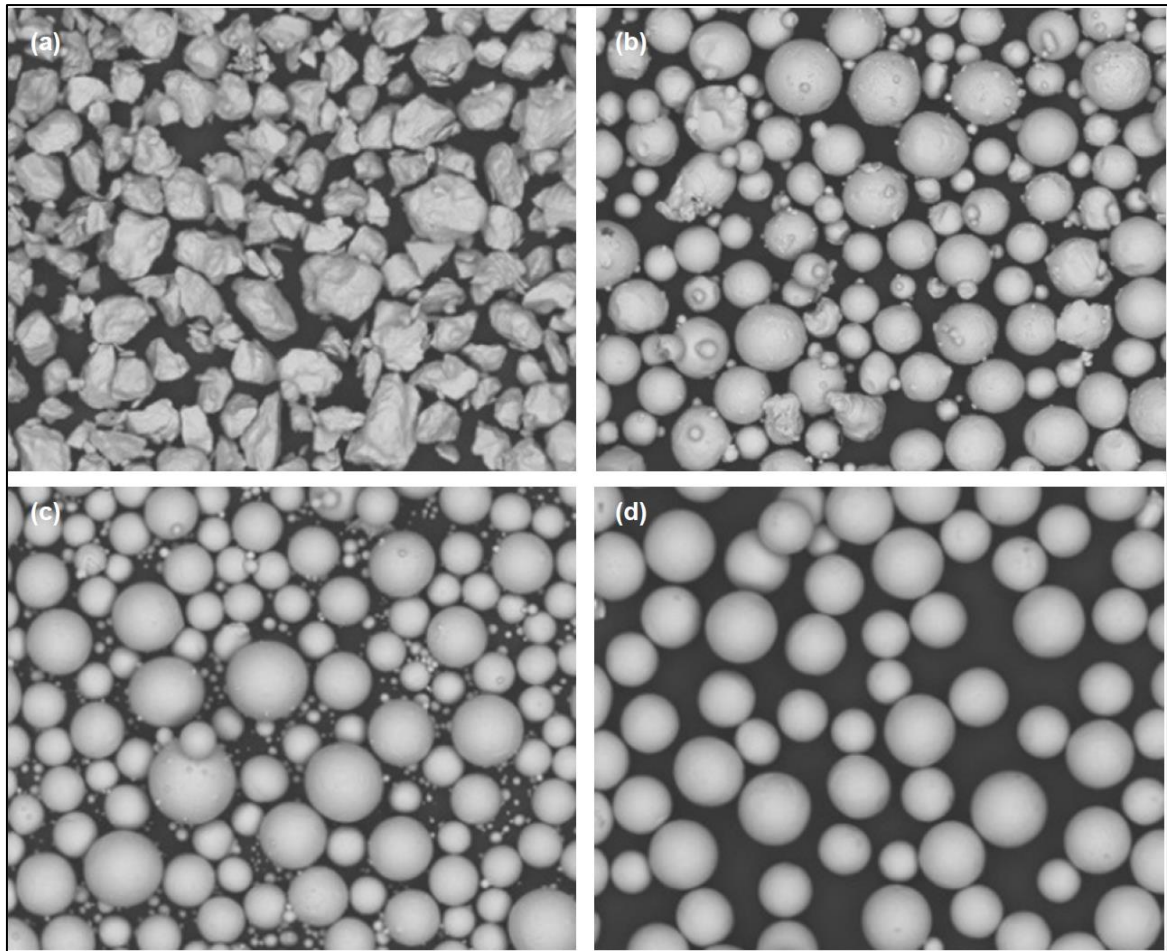


Figure 2. 14: Powder production methods [80].

Compared to the other atomisation techniques, PA solution achieves high T for high melting point metals. Reactive materials as Titanium are also treated. Particle size distribution (PSD) production range is from 0 to 250 microns; the common size used for the E-PBF process is 45 - 106 microns in diameter, which is 50 % of the cumulative distribution (layer thickness is around 70 microns for an A2XX Arcam system). Low oxygen, high purity, excellent flowability, high apparent and tap density are the features that make PA an optimum solution for E-PBF technology [81]. However, its cost is considerably higher than most of the other powder options.



*Figure 2. 15: HDH powder (a), gas atomised powder (b), plasma atomised powder (c), plasma rotating electrode powder (d) [82].*

Clayton et al. [83] demonstrated through four case studies the relationship between powder properties and performances in AM processes, where benefits such as powder life-cycle management were noticed. However, multiple characterisation methods need to be completed in order to better understand the characteristics to apply to the desired machine.

Several analyses should be considered and performed to capture the status of the powder and its characteristics as shown in Figure 2. 16. In order to have a full understanding of the powder, analysis such as chemical composition, flowability, morphology, packing density, particle size distribution (PSD), static angle of repose (AOR) [78] and others can be evaluated at any time during the lifetime of the powder, which can be done after a build (when it is fresh) or after storage.

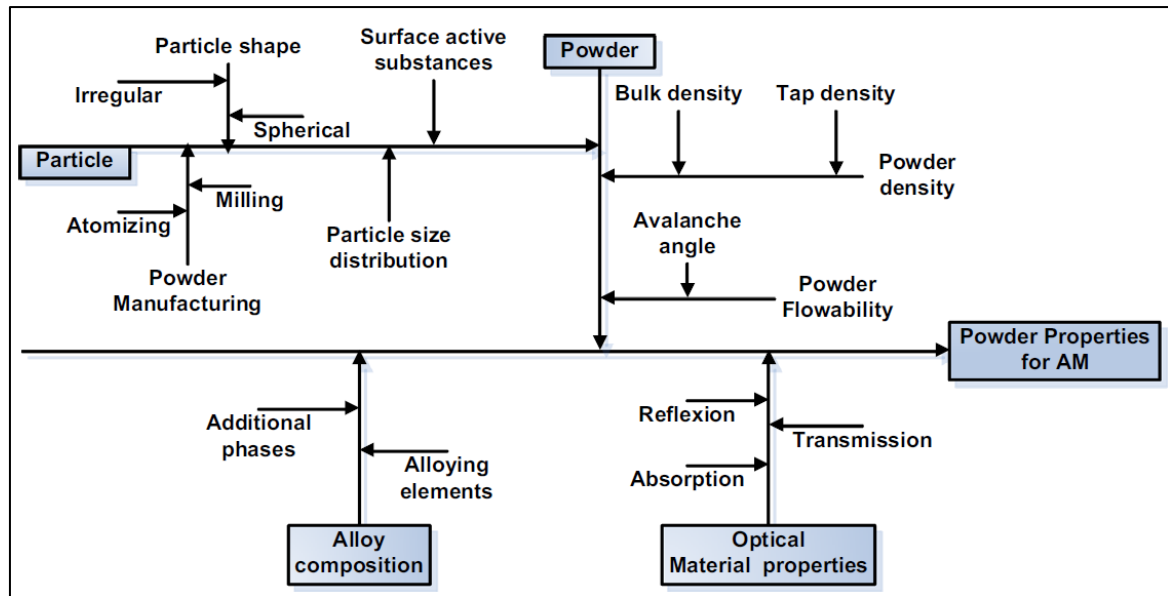


Figure 2. 16: Influences to consider in metal powders [84].

An important variable to consider in PBF is related to powder handling, where potential contamination, shape modification and atomic structure changes need to be considered during the pre- and post- process. Most of AM manufacturers and suppliers noticed that the characteristics of virgin powder can change during storage; studies suggest keeping virgin and used powder inside a limited oxygen container. Seyda et al. [85] noticed coarsening and an increase in flowability of used powder particles. No standards are in place for powder storage at the moment; several institutions, powder manufacturers and end users are working together in order to define a suitable method to store powder in order to maintain the characteristics required. One of the common problems during powder storage is the oxide generated on the powder surface or handling powder in atmosphere which reduces the charged behaviour of the particle. The oxide layer may generate surface resistivity to charging with a successive accumulation of energy and a consequent 'smoke'. Cordero Z. C. et al. [86] noticed that smoke is mainly observed during the preheat phase when the powder gets initially charged. It was also observed that smoke caused by oxidized particles can be reduced by modifying beam speed, increasing powder particle size, and bed T. By changing these variables, a reduction in smoke was observed.

Moisture should also be kept away from powder particles as it can change flowability and metallurgical behaviour. A drying process, normally in a heated oven, is used before performing any powder characterisation tests as it is useful to prevent having moisturised parts during tests.

There are no powder size or layer thickness restrictions in E-PBF. Manufacturers tried different combinations in the past defining a suitable range for E-PBF, which is quantifiable from 25 to 150

$\mu\text{m}$  for spherical powder. Powder compaction and flowability are critical to a successful build. Karlsson et al. [62] tried two different combinations of layer thickness (50 and 70  $\mu\text{m}$ ) using different PREP powder size fractions (25 - 45 and 45 - 100  $\mu\text{m}$ ). The combination of these variables resulted in similar bulk structures between builds and a slightly higher peak-to-valley ratio on the surface build with finer powder due the number of un-melted particle on the surface. However, by optimising the E-PBF settings for small particles it is possible to achieve a better surface resolution and resulting properties, such as build mechanical properties. Manufacturing time was not considered during these experiments.

Traceability is another hot topic in AM where tracking the powder and its quality become an issue if an articulate process is not in place. The issues are related to the production point of the powder, dispatch to the manufacturing site, storage procedure and location, loading and unloading process, recycling and re-store of the powder [87]. Every abovementioned step has the risk of lost or unknown traceability and potential oxide and contamination, even more so when the powder enters a powder bed system. All AM manufacturers, from powder suppliers to system developers, are currently working to ensure that there are secure methods of powder traceability and handling systems, through standards or advance methods, in order to increase the reliability and quality along the entire powder chain [82].

Nowadays the distribution of powder is mainly via third party suppliers. The reason is connected to the quality of the powder guaranteed from the third party suppliers compared to the atomiser companies who only produce and dispatch powder in large quantities [88]. Companies such as Avio-Aero [89] and Arcam (both part of GE Aviation Business) tend to manufacture their own powder in order to manage quantities and quality. Manufacturing powder can be a difficult process which requires experience and knowledge. Otherwise, companies such as LPW Technology [90] supply AM powder bought from powder manufacturers; if required by the customer, they perform in-house analysis to ensure that the powder sold to the customer satisfies the requirements by providing certificates of tests performed before the dispatch.

Different costs can be found in the powder market, according to the type of powder, the powder manufacturers, and the powder distributor. As mentioned, another variable can be related to the amount of powder ordered, where discount can be achieved with large volumes. Other high volume AM part production companies decide other strategies, such as building in-situ atomizers [91] close to the manufacturing facility, or buying atomizing companies [92], which are used to manufacture the powder required for production. Saying that, there are no fixed prices for powder; lots of variables need to be considered before getting a final estimation. Normally, high quality



powder, like PA powder, has a higher cost compared to non-spherical powder with low flowability. However, the rising demand of powder in the worldwide market should allow for the decrease in market price and potentially increase in the powder quality, in addition to the push to the manufacturers to customise the production to focus on AM processes and needs. Typically, atomized titanium powder has a starting cost from around £100 / Kg.

## 2.4 Materials Available in E-PBF

Several materials are available in the E-PBF market, where Ti - 6Al - 4V is the most common, followed by In 718 and Ti - Al. Many materials were simulated, tested and developed with standard Arcam chambers or using reduced kits, where the alloys field has high influence due the characteristics of the materials and their electric conductivity. Also special materials with high electric and thermal conductivity, such as copper, or other materials with superconductive properties were tested.

C. Körner, as shown in Figure 2. 17, reviewed the state of the materials developed before May 2016 by E-PBF, where the limitation of material conductivity drove the development selection to alloys, plus a few exceptions, such as pure titanium, copper, and niobium [93]. Nevertheless, tailored materials can be developed according to the characteristic of the E-PBF system [94, 28].

Material	Properties	References
Alloy group	Alloy	
Co-Cr-Mo	Co-26Cr-6Mo-0.2C	Microstructure, carbide distribution, defects, mechanical properties, components 41,42
	Co-28Cr-6Mo-0.23C-0.17N	Microstructure, texture, in-situ heat treatment, anisotropic mechanical properties, creep properties 43,44
Cu	Pure Cu	Electric and thermal conductivity, Yield strength 12,45-47
Fe	Pure Fe	Microstructure, mechanical properties 48
	316L	Microstructure 14,49
	H13	Microstructure, injection mould inserts 50-52
Nb	Nb	Microstructure 53
Ni	IN625	Microstructure 18
	IN718	Microstructure, texture 19,32,36
	IN718	Grain structure, texture, mechanical properties 25,34,37
	IN718	Residual stresses 15
	CMSX-4	Microstructure, heat treatment 16
	Rene142	Microstructure 54
Ti	Pure Ti	
	Ti-6Al-4V	Microstructure, mechanical properties 26-28,31,35,55
	Ti-6Al-4V	Texture 33,35
	Ti-6Al-4V	Roughness 38-40
TiAl	Ti-48Al-2Cr-2Nb	Microstructure 13,56
	Ti-47Al-2Cr-2Nb	Microstructure 57,58
	Ti-45Al-7Nb-0.3W	Microstructure, selective evaporation, compression strength 7
Open-Cellular materials	Ti-6Al-4V	Mechanical properties, surface effects, permeability 59-64,63,65-76
	Fe/stainless steel	48,77
	TiAl/In625	Open-cellular structures, mechanical properties 78
	CoCr	64
	Cu	47

Figure 2. 17: Materials tested using E-PBF systems, 2016 review [93].



Developments like cellular lightweight materials [95, 96] were under investigation as a result of the ability of the E-PBF to build parts without the necessity of supports that need to be removed, and part stability from the sintering of the cake. However, the sintered powder is difficult to remove from the cellular structure compared to laser powder bed fusion (L-PBF) due the pre-sintering level of the powder that is achieved during the preheating stage.

Due to its properties of working under vacuum and shooting electrons, the E-PBF system has a high potential for the development of new materials or for the combination of multiple materials. Machine limitations and low interest from manufacturers are now limiting a push in development and funding opportunities.

## 2.5 Ti - 6Al - 4V in E-PBF

### 2.4.1 Ti - 6Al - 4V Behaviour during the E-PBF Process

Considering Titanium as an allotropic material element which has two different crystal structures that are dependent on T. Hexagonal Close Packed (HCP) and Body Centre Cubic (BCC) are respectively referred as alpha and beta phases. Below the T of 883 °C, known as beta transus, pure Titanium has a HCP  $\alpha$  phase structure. Whereas, above the beta transus T, the structure change to BCC structure [97].

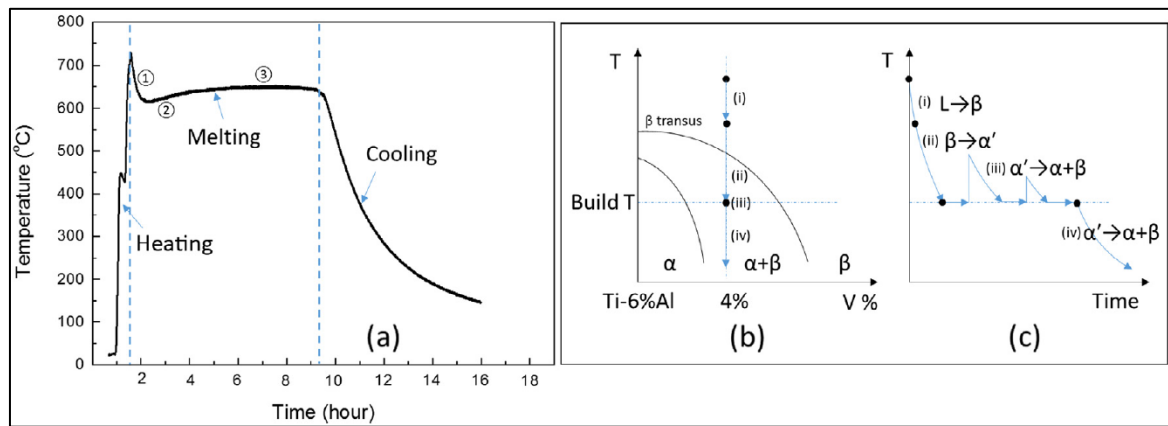


Figure 2. 18: Three stages condition during and microstructural formation in a typical Ti - 6Al - 4V E-PBF cooling rate [98].

BCC  $\beta$  phase transformation to HCP  $\alpha$  phase in pure titanium and titanium alloys can occur by controlling the nucleation or martensitically, cooling rate and alloy composition influence the growth process.  $\alpha$  and  $\beta$  relationship was firstly studied by Burger, it proved the transformation from a BCC crystal structure to 12 hexagonal variants [99].

Figure 2. 18 (a) shows a standard cycle achieved during an E-PBF build where the T is captured from the thermocouple installed on the bottom of the starting plate. Tan et al. [98], estimating the heat loss during a build, explained the microstructural evolution represented in Figure 2. 18 (b) and (c) where prior  $\beta$  grains (i) are formed from the liquid phase, then  $\alpha'$  martensite is formed (ii) due the rapid cooling achieved from above  $\beta$  transus to the build T (iii) where the material is near isothermal annealed with a consequent transformation from  $\alpha'$  martensite (iv) to  $\alpha$  colony and basket wave plus  $\beta$  rods.

The cooling rate achieved in E-PBF is also connected to the percentage of phases developed inside the microstructure which are related to the mechanical properties and microstructural behaviour. Figure 2. 19 shows a studies related to the percentage of  $\alpha$  phase percentage achieved at different cooling rate using different holding T [100]. These values can be connected to the cooling rates achieved in a different location of the build or to the cooling rate of the component itself and its location.

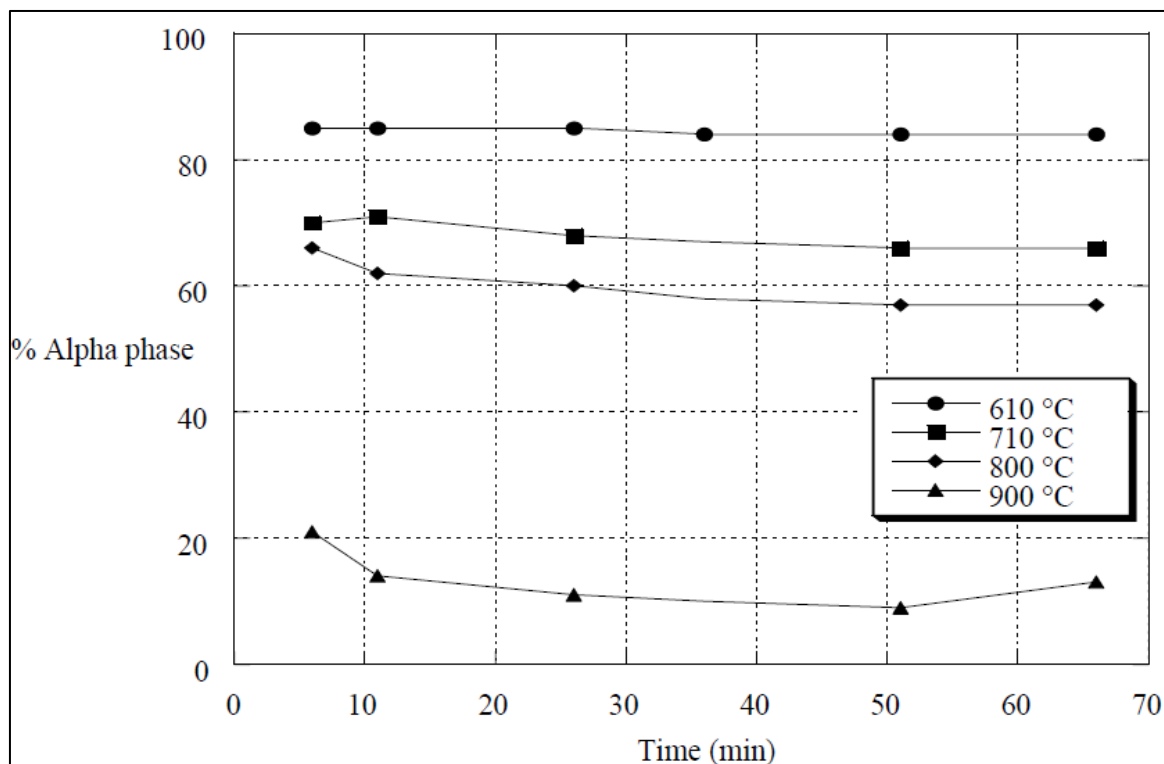


Figure 2. 19: Phase transformation changes achieved at different holding T [100].

The T transformation occur in  $\beta$  phase allow to finalise the microstructure of  $\alpha + \beta$  titanium alloys. Different cooling rate permit the transformation of the microstructure in different configurations, it allows to change the mechanical specification related to the end use of the material. Inside  $\alpha + \beta$  alloys category, Ti - 6Al - 4V is certainly the most sold titanium alloy [101, 99]. Balanced properties

plus the numerous developments and tests performed guarantee a deep understanding of the morphology and microstructure of the material built in E-PBF.

Stabiliser elements, as Al and V, effect  $\alpha$ -stabiliser,  $\beta$ -isomorphous stabiliser,  $\beta$ -eutectoid stabiliser, and strengthening elements help to reinforce the crystal structure of the material. Martensite ( $M_s$ ) is found in alloys which are rapidly cooled from the  $\beta$  or  $\alpha + \beta$  phase generating a martensitic form of  $\alpha$  phase, denoted  $\alpha'$ . Martensitic formation has a much less evidenced strengthening effect [102], and its existence in E-PBF Ti - 6Al - 4V still debatable [98, 103, 104].

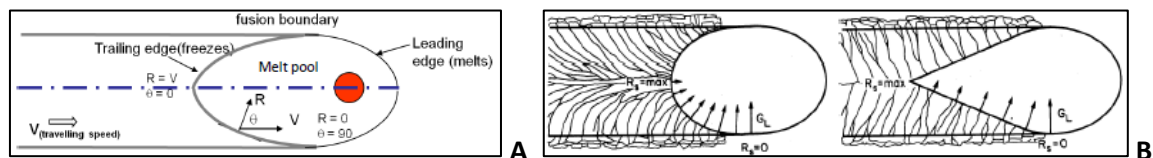
Donachie [105] indicated that with a T above 427 °C titanium pick up oxygen and nitrogen from the atmosphere causing a decrease in mechanical properties as brittle fracture and poor elongation. But at the same time, a minimum level of oxygen needs to be maintained for the atomic characteristics of the material. From the ASTM 2924 - 14 Ti - 6Al - 4V standard [106] a maximum level of 0.2 % of oxygen is allowed inside AM Ti - 6Al - 4V components.

#### 2.4.2 Ti - 6Al - 4V Solidification in E-PBF

Several variables such as melt pool, growth rate, undercooling, T gradient, travel speed and Titanium composition drive the final microstructure of a solidifying melt pool in AM and welding [107, 108, 109, 110].

E-PBF has various settings that can be changed during the set-up of the build. Focus offset, beam speed, number of scan repetitions in preheating phase, beam overlap, and beam current are the main variables normally considered during a parameter investigation. Studies revealed that tailored microstructure is also a possibility, tweaking some sets of parameters [111, 112].

The solidification rate, also known as growth rate, is the proportion at which the liquid/solid interface in the melt pool is generated. The travel speed of the heat source is directly related to the solidification rate which has a significant impact on the final microstructure [113, 109, 114].



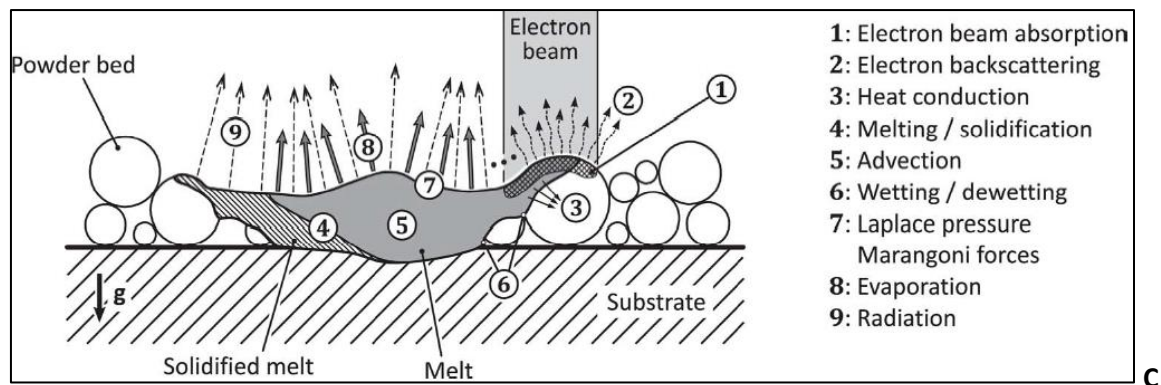


Figure 2. 20: Schematic diagram of fusion boundary on E-PBF [109] (a). Variation of thermal gradient and growth rate along the solidification area [114] (b). Physical effect of a schematic beam deflected from left to right [115] (c).

Figure 2. 20 (a) shows the theoretical relationship between heat source rate and solidification boundary [109, 114]. It is noticeable that the melt pool shape is changing from an elliptical to a narrower shape by raising the travelling speed. Differences in thermal gradient have a different impact on solidification of the material, in fact it changes with the variation of the traveling speed. Elliptical are formed at low and moderate speed, instead tear drop shaped are noticeable at high speed rate (b). The complete phase, from the impact of the electron to cooling, is represented in Figure 2. 20 (c), where the powder particles are melted and consolidated through the electron beam shifted on the top of a spread layer of powder.

Observing the bottom side of a part manufactured in E-PBF, two starting strategies are normally used for the beginning of the build of a component: built directly on the starting plate or manufacture the parts from supports. The difference of nucleation and solidification of the bottom region can be influenced by the technique adopted. Having a component growth using supports can generate cracks during the supports removal with different nucleation areas depending on the support location. Starting the build from the substrate can generate changes in properties on the bonding region according to the material of the substrate and stabiliser that can be transferred during its re-melting phase. In both cases, a base nucleation with equiaxed grains is normally observed.

A simulation of layer evolutions is represented in Figure 2. 21 by Rausch et al. [116], where an electron beam is consolidating the first layer on loose spread powder. A T gradient bar shows the heat impact of the electron beam and the consolidation of the layer, consequentially more powder was spread on the top of the molten region in order to carry on with the consequent melting of the powder particles and the partial re-melting of the previous layer. After 30 layers is noticeable

a T above 900 °C, which is higher than the preheating T. This assumption has been reported in various microstructural investigations, where main  $\beta$ -grains have the tendency of increasing average width along the build direction.

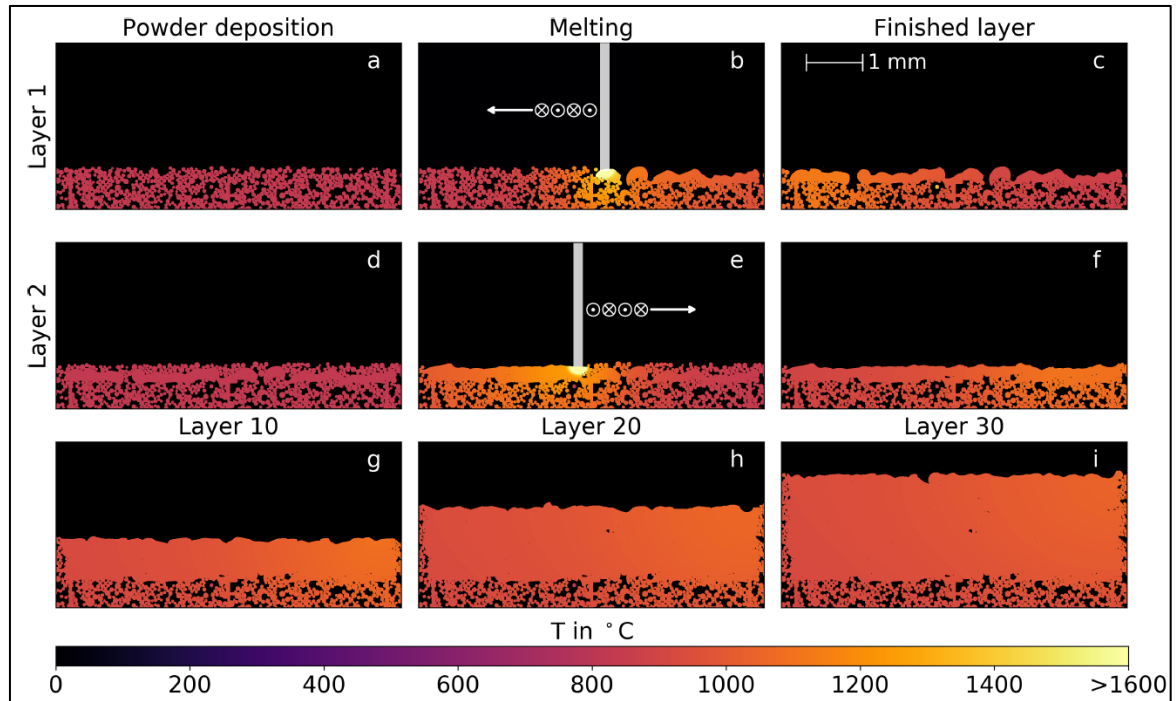


Figure 2. 21: Simulation of powder spreading and layers melting in E-PBF [117].

From the side of the build region, nucleation occurs from partially melted powder particles close to the powder bed which solidify and nucleate. Successively, a spread and melted layer of powder partially re-fuse the bottom substrate generating an epitaxial re-growth of the previous fused layer [118, 119], it generate a fine columnar  $\beta$ -grain slightly curved from the outer powder region to the inner region along the building direction of the component. After the outer grain consolidation, columnar inner main  $\beta$ -grain are observed growing mainly along the  $\langle 001 \rangle$  direction even if some grains tend to rotate to an angled direction due the following of the thermal gradient generated from the beam scan direction [63].

Going half millimetre inside the solid structure in Z direction, due better stability during the cooling phase, solidified vertical prior  $\beta$ -grain grow between layers, where size and length are mainly represented from the settings and the cooling rate used. Reported from many articles in literature [120], the formation of course main random distributed columnar prior  $\beta$ -grain appear during the re-melting phase in the build when the previous layer gets partially re-melted and, during the re-solidification of the alloy, allow  $\beta$  phase growing along the building direction between layers.

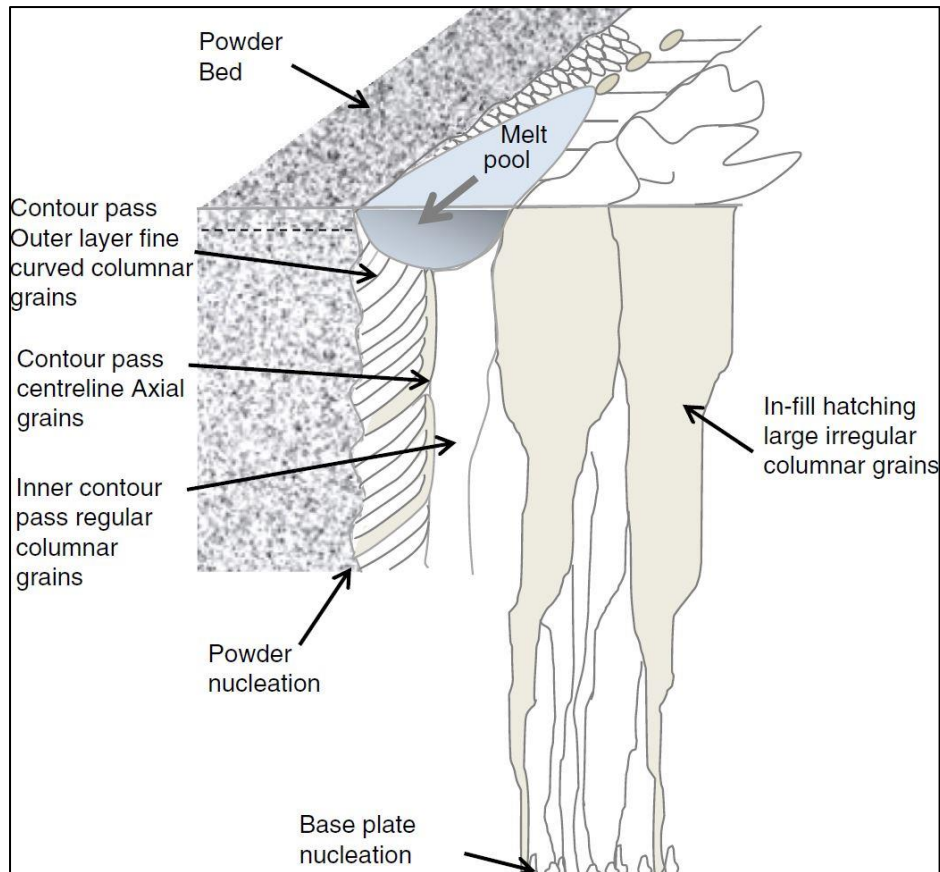
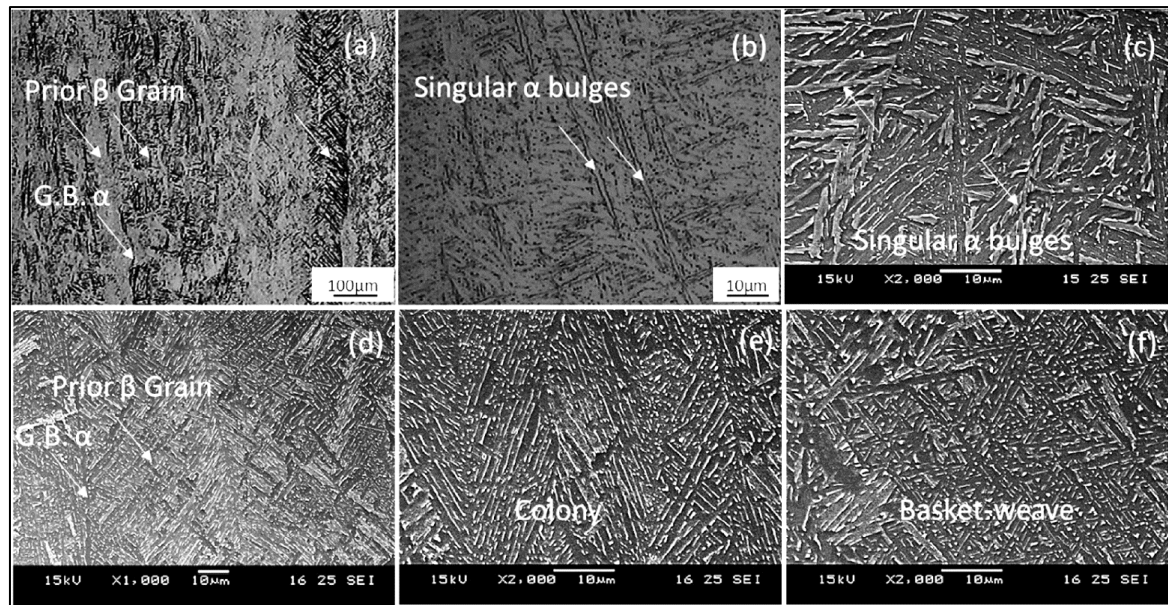


Figure 2. 22: example of  $\beta$  phases generated in a Ti - 6Al - 4V part manufactured by E-PBF [121].

On top of the columnar grain growth description, A.A. Anthonysamy et al. observed in 2013 [121] five different types of  $\beta$ -grains in different locations of the structure. A picture from their studies (Figure 2. 22) schematically represents the regular and irregular columnar prior  $\beta$ -grains which grow along the build direction. In the central region they are generally formed from small randomly shaped grains (base plate nucleation) where the main columnar grains are formed to successively grow along Z direction. On the surface area, different grains are formed with an angle due to nucleation of powder particles which epitaxially re-grow from a partially re-melted area; the tilted geometry can be re-conducted to the cooling region from the side to the centre of the melt pool track.





*Figure 2. 23: Morphology characteristics of Ti - 6Al - 4V Kroll's etched microstructure achieved in E-PBF [98].*

A summary of the main microstructural characteristics is summarised in Figure 2. 23 where columnar prior  $\beta$  grain are growing along the Z direction in  $\alpha$  grain boundaries in a common  $\alpha/\beta$  duplex microstructure (a – d). Sandwich  $\beta/\alpha/\beta$  structure with singular  $\alpha$  bulges could be found (b – c). Lamellar colony and basked-weave  $\alpha$  phase and like-rod  $\beta$  phase is observed in most of the Ti - 6Al - 4V structure (e – f) [98]. The linear X-Y section is represented to casually distributed equiaxed grains located on the entire surface. Refined shaped are noticed close to the surface area with a random crystallographic orientation.

In E-PBF, most of the structure is subjected to columnar prior  $\beta$  grains outlined by  $\alpha$  grain boundaries constructed with  $\alpha + \beta$  basket-wave (Widmanstätten) and colony morphology developed in prior  $\beta$  grains microstructure without formation of  $\alpha'$  [122, 98]. Literature suggests that with a cooling rate of  $>410 \text{ K s}^{-1}$  the formation of  $\alpha_m$  start to appear from a T as high as  $800^\circ\text{C}$  [122] to  $575^\circ\text{C}$  [104], but an annealing treatment decompose the  $\alpha'$  structure into  $\alpha$  as shown by Gil Mur at al [123] above  $700^\circ\text{C}$  which is occurring during the Ti-6Al-4V preheating cycle in E-PBF. Different preheat condition below  $700^\circ\text{C}$  showed a partial decomposition of  $\alpha'$  with a consequent increase in Yield strength and a decrease in alpha lath width. However, Lu at al. [122] observed plates or martensitic needles ( $\alpha'$ ) in the top region of the component due the high cooling rate occurred in the final top layer which suite the rapid Ti-6Al-4V martensitic cooling rate.

Scanning strategies and parameters development can influence the structure of the part manufactured in E-PBF. Studies from Scharowsky at al. [111] Figure 2. 24 show the microstructure

evolution changing the volume of energy delivered during the melting phase where scan speed and volume of energy are influencing the microstructural formation and the consequent mechanical properties of the material. Studies confirmed similar results where changing the main settings changes of microstructure were considered as a potential way to tailor the grain evolution with the consequence of changing the mechanical properties [124, 125, 126].

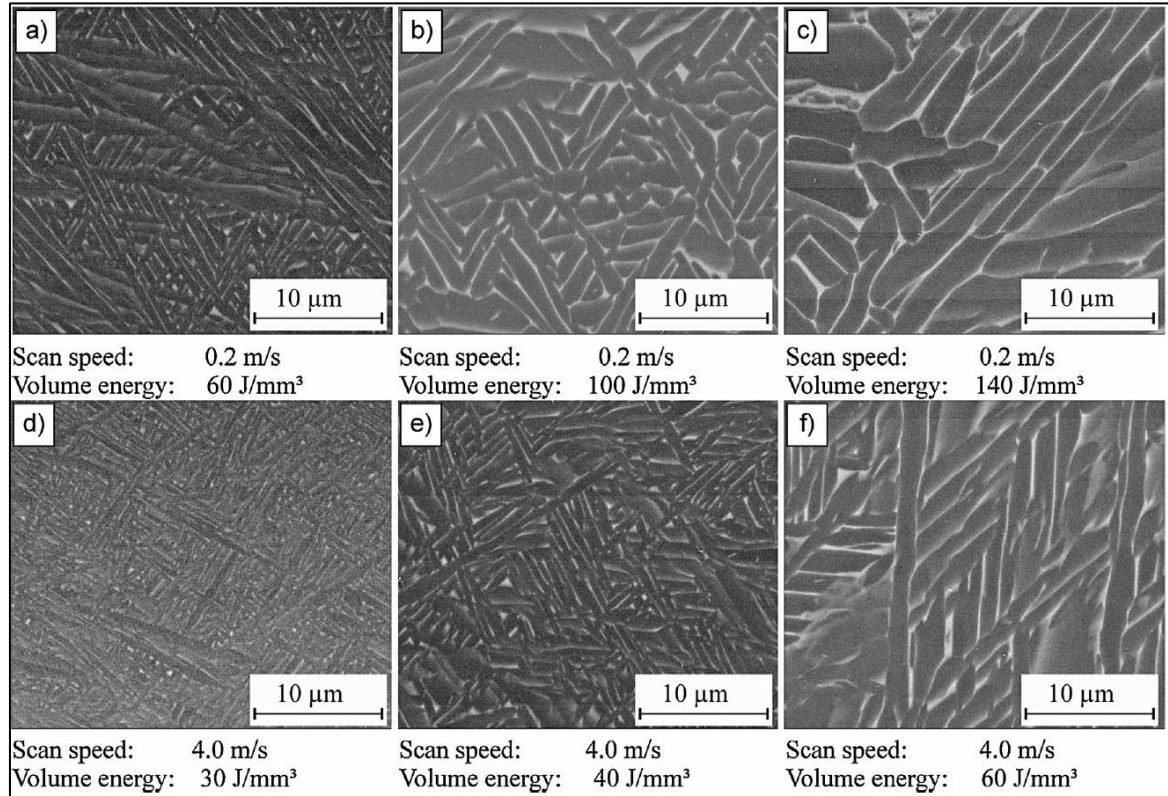


*Figure 2. 24: Widmansteatten microstructure achieved using different volume energy [111].*

### 2.4.3 Ti - 6Al - 4V Mechanical Properties in E-PBF

Given that several studies and case studies have been carried out and analysed, it is possible to say that in most of cases an AMed part has better characteristics than a cast component [126]. Figure 2. 25 shows a cross comparison of mechanical properties of parts manufactured using different processes, where all the AM solution have better properties than the conventional cast, forged or wrought material.

Minimum mechanical properties were defined by the ASTM F2924 - 14 standard [106] where the main specifications need to satisfy a minimum value of 895 MPa for Ultimate Tensile Strength (UTS), a Yield Strength of 825 MPa, and an elongation of 10 %. A range between 895 and 955 °C with a pressure of 100 MPa is suggested for a HIPping cycle.



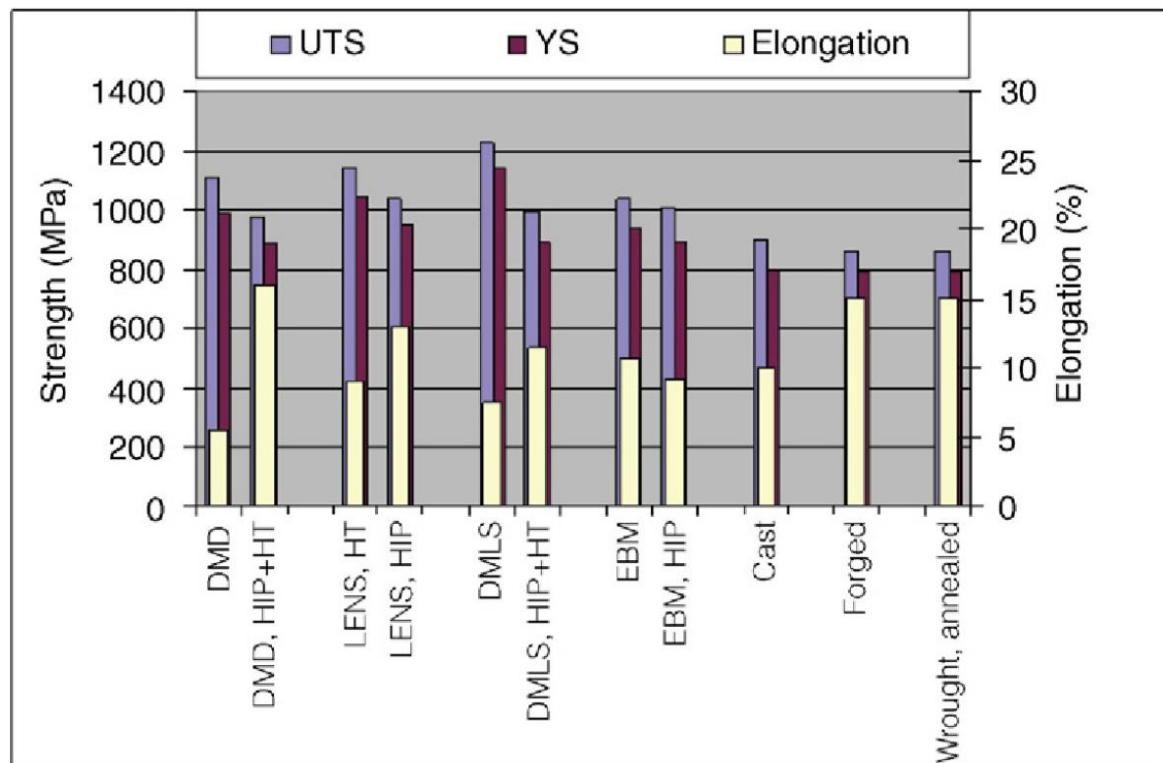


Figure 2. 25: Mechanical properties of Ti - 6Al - 4V parts manufactured using different approaches [127].

Investigations were performed using different T during the preheat stages stage, which is considered one of the key understandings for material development. P. Drescher, H. Seitz [28] defined a link between the preheating stage and the final metallurgical properties, where changing the preheating T was possible to modify  $\alpha$  lath thickness.

As mentioned in paragraph 2.1.8 other different solutions are used to post process the manufactured component in order to improve mechanical properties and improve its characteristics. However, it is relevant considering the impact of the E-PBF on the material, where loss of material can be observed in low boiling point materials as aluminium. A. Klassen at al. [115] evaluated potential methods to reduce the aluminium lost during a build of Ti - 48Al - 2Cr - 2Nb, where the line energy was identified as the key parameter for affecting vaporisation. It was observed how evaporation of stabilisers can be reduced through a reduced energy density, where a refined beam, a decrease in energy density, and a reduced scanning line offset end up to less heat and a consequent reduction in material evaporation and increase in mechanical properties.

With reference to the potential atomic losses during the melting stage, several studies were conducted on recycling properties of powder used. They considered when the powder can be reused before losing the composition required from the material, before losing its properties. H.

Tang et al. [128] observed that recycling powder directly affects the atomic and mechanical properties of the material, recycling Ti - 6Al - 4V conduct to an increase of oxygen and a progressively loss of V and Al content. Manufacturers normally add fresh powder to the used one in order to balance back losses achieved during the process.

## 2.6 Parts Location and Build Control

An important influence for a successful build pass through the influence of the parameters used during the build. Nevertheless, some variables as part location in the X-Y plane and location of the part during the build (Z axis) can play a critical role for the completion of a build.

Mechanical properties, surface roughness, and microstructure can potentially change depending on the location and height of the specimen inside the chamber. Nevertheless, Hrabec and Quinn [129] performed horizontal tensile bars at different Z-height with either manual or automatic mode in order to capture the mechanical properties and microstructural behaviour of parts built along the Z direction. They observed a minimal change in micro-hardness,  $\alpha$  lath thickness, UTS and YS, and oxygen content. Rapid cooling from the side of the build compared to the centre was hypothesized due to higher mechanical properties of parts located close to the build edges.

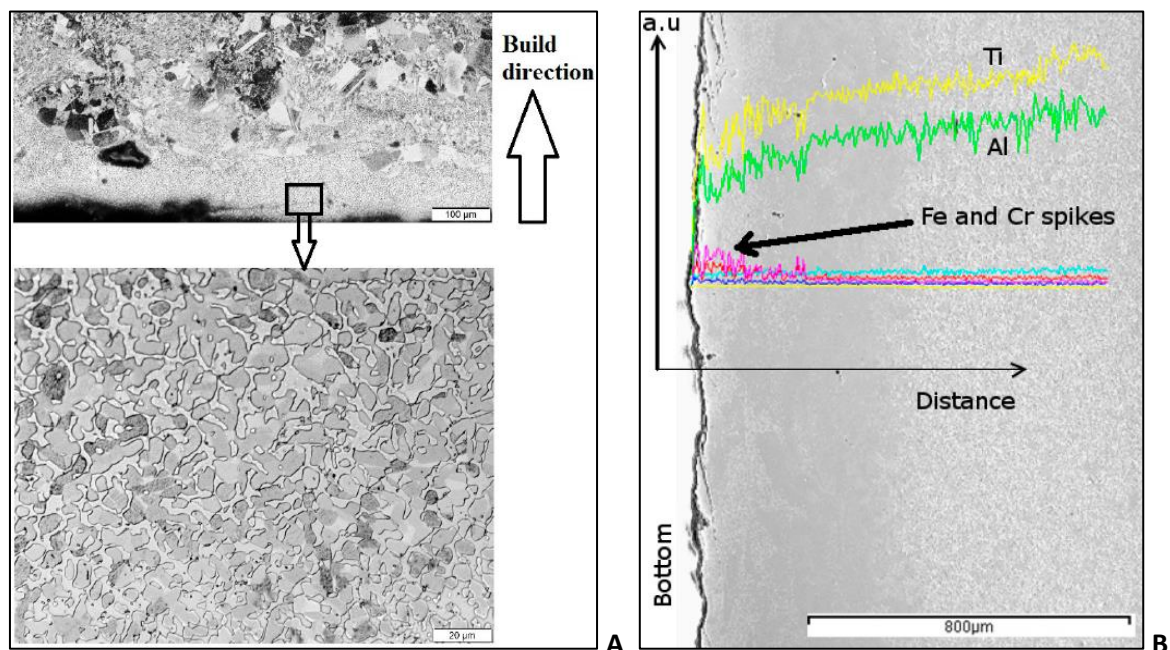


*Figure 2. 26: Fe - Ti intermetallic structure captured with a SEM between the base/build interface (a), Fe and Cr contamination in the first few hundreds microns (b) [119].*

Contamination from the starting plate was noticed by Mohammad et al. [119] and Al-Bermani [63] where a Fe - Ti intermetallic structure was observed across the starting plate/build region as shown

in Figure 2. 26 (left). Fe and Cr spikes were noticed (Figure 2. 26 - right) in the diluted interface region when the SS substrate re-melts during the melting of the first few layers deposited.

Changes in preheat T were explored by Al-Bermani et al. [63] during a prior  $\beta$ -phase reconstruction investigation. By modifying the preheat T from 625 °C to 700 °C, a difference in  $\alpha$  lath size was observed; by decreasing the preheat T an increase in mechanical properties was noticed due a higher cooling rate after melting and a consequent refinement of  $\alpha$  lath size.

## **2.7 Advance Hardware Configuration**

Due to the continuous request for new materials and the need to improve the process of manufacturing parts [130], some E-PBF users decided to modify the standard machine hardware to allow a smaller build, with a consequent balance of powder needed. Changing the standard configuration has an impact on the machine settings to suit the new envelope.

One of the first reduced kits, called Minivat, was presented at the Characterization of Minerals, Metals and Materials conference in 2013, where S. Gaytan et al. [131] redesigned the standard square A12 Arcam 250 x 250 x 330 mm chamber to two types of cylindrical vat of 70 Ø x 100 mm and 120 Ø x 100 mm in length, respectively, in order to minimize the amount of powder needed for a small build. The purpose of the study was to optimise the parameters for Nb, Ti- and Ni- based alloys in a reduced kit. A rake modification was also completed in order to collect the powder directly using a movable hopper installed on the rake itself. This allowed a minimum amount of powder for the build with no need to modify the standard existing hoppers. The development reduced the material needed for a small build and time of manufacturing; however, no material development approaches were disclosed.

Subsequently, North Carolina State University developed a reduced kit for an E-PBF A1 system [132] in order to perform with a wide range of new materials. To achieve this, reduced chamber and hoppers where manufactured, and a new rake system with a funnel to deliver the material was mounted on the powder bed surface (where the raking occurred). The characteristics of the powders were captured and analysed in order to develop a new set of parameters needed for a development strategy approach, where beam speed, beam focus (BF), and beam power where the initial parameters considered. Materials such as Copper, Niobium, Nickel and Titanium based, Nitinol, Metal Matrix Composites, Lunar Regolith, Beryllium Alloys, Tools Steel, different grades of Aluminium were investigated.

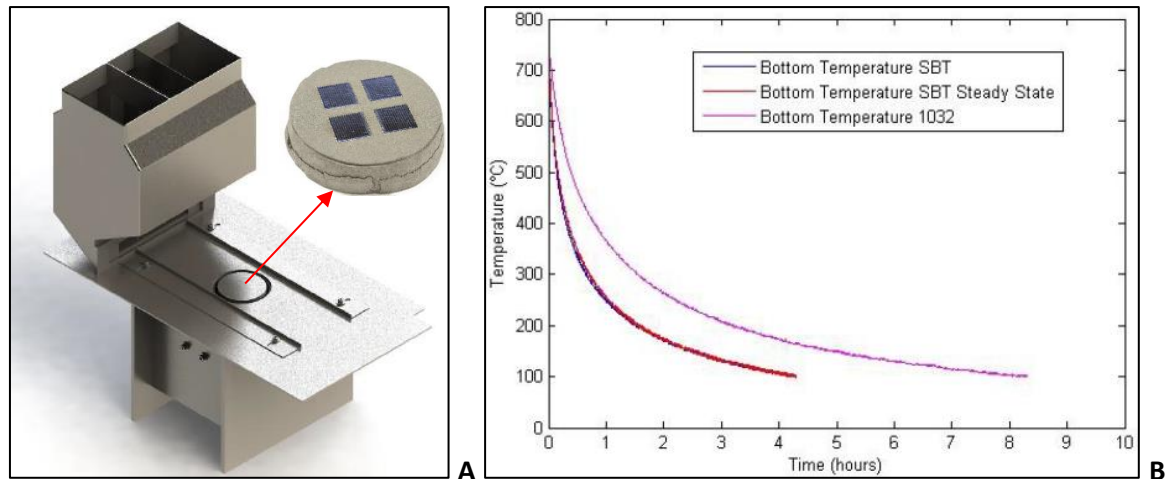


Figure 2. 27: Reduced kit (a), cooling time comparison with the original chamber (b) [133].

Furthermore, Jon Wright et al. [133] manufactured a small Arcam A12 build tank with an inner chamber diameter of 110 mm, a reduced hopper volume using inserts, and parallel guides to direct powder to the build area, which was reduced to a 1/8<sup>th</sup> of the original chamber volume. A comparison between cooling time indicated that faster cooling is achieved with the reduced kit due to an increased irradiate/dissipate surface area to volume ratio as showed in Figure 2. 27. The abovementioned factor raised the issue of the shorter the time between preheat repetitions, which helped to stabilize the T and decrease smokes generated by the lack of charging. Having developed the standard rules and settings for Ti - 6Al - 4V, the authors managed to develop pure Tungsten for fusion applications. No studies where published on the influence of cooling rate on the microstructure and time of manufacturing.

In addition to the abovementioned case studies, other manufacturers are attempting to have more flexibility over the E-PBF process. Several limitations, such as lock settings and machine insurance are preventing users from modifying the system configuration and its settings. However, the need to develop new potential E-PBF materials pushed research institutions, like universities and research centres, to develop new reduced chambers that can be exploited by end users.

Another benefit of having a customised chamber is related to the production environment. Remembering that powder can be reused a certain number of times, and preheating an over needed area increases the time needed for completing a layer, having a customised chamber closed to the shape of the part/s to build can significantly reduce the time of manufacturing, powder handling requirements, and potentially the cost of manufacturing. In addition, a reduced amount of powder needed for a build has the advantage of decreasing the initial investment of powder.

## 2.8 Shelling Design for Manufacturing

In order to reduce porosity level and lack of fusion, post treatments are considered to result in a better microstructural stability, improving the properties of the parts by reducing porosity, lack of fusion, and potential reduce crack initiations. As a well-known process, the HIP method has been used to improve fatigue properties of cast parts [134]. Several AM manufacturers rely on a post HIP cycle to improve the mechanical characteristics of the components and their performance during use by applying a high T at a defined pressure for a fixed time in order to reduce the defects in a part.

One of the first studies was conducted by Ronald Knight and Joseph Wright [135] where shell cans were manufactured by selective laser sintering (SLS) and were HIPped after the production. The authors produced parts with fully dense skin with loose imbedded powder, which were then solidified throughout a HIP treatment. The approach was used to lower the cost and increase productivity during the manufacturing of replacement parts urgently needed and to make spare components.

A hybrid approach was adopted by Qiu et al. [136] who made Ti - 6Al - 4V canisters using a L-PBF system, where AMed tooling filled with Ti - 6Al - 4V powder and prepared to the final HIPping stage were produced. A finite element analysis (FEA) prediction was used to calculate the initial shape and the shrinkage. It was shown that L-PBF is suitable to predict distortions and to make HIP tooling resulting in a homogenous bonding interface between Ti - 6Al - 4V powder and solid shell.

More studies were investigated [137, 138], canister parts were designed for L-PBF, where trapped powder was located inside a shell. After post HIP treatment it was noticed that the loose powder solidifies completely inside the structure, the results showed high quantity residual pores that were evenly distributed in the shell core due the argon gas trapped during the manufacturing process.

Another study showed in Figure 2. 28 was recently performed on E-PBF fabricated shells by Alexander Leich et al. [139] where loose Ti - 6Al - 4V powder was captured inside a square shells with different skin thicknesses. They noticed that manufacturing a shell for HIP with a wall thickness below 1mm can result in failure during the HIPping treatment due surface leaks. No other shell geometries were tested. The consequent post analysis conducted by Karin Frisk et al. [140] showed the shrinkage occurred after a HIP treatment, the microstructural properties between skin and core interface and its characteristics. No pores were visible after the HIP treatment, with good bonding interface between the shell and the loose powder captured inside the core. A standard equiaxed Ti - 6Al - 4V post HIP structure was observed in the core region.

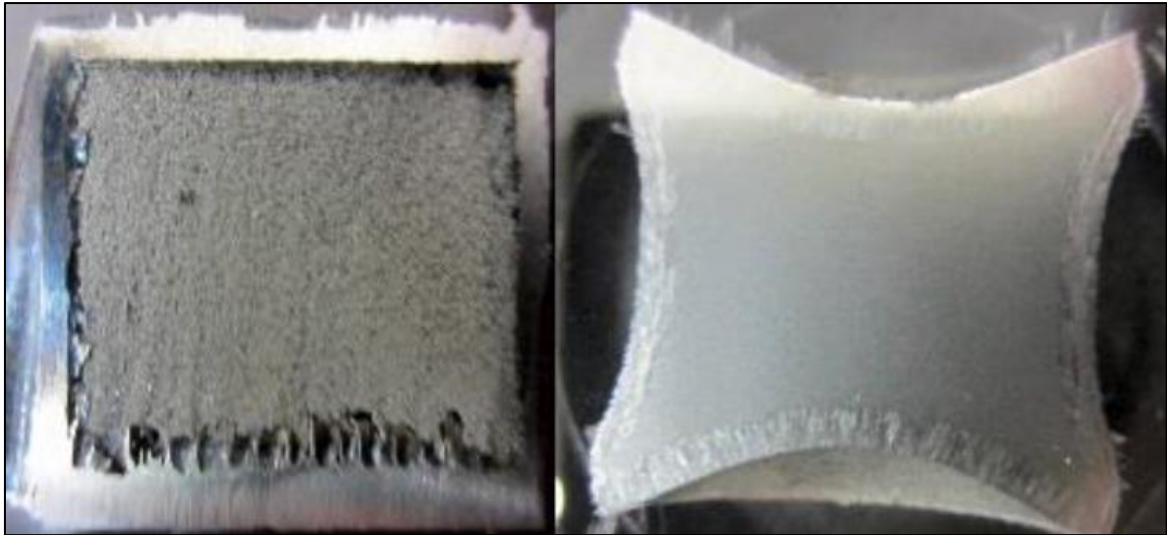


*Figure 2. 28: Shell with loose semi-sintered powder before (left) and after (right) HIP consolidation [139].*

No real case studies or advanced investigations have been mentioned in the literature so far; further studies on trapped powder inside a shell or optimized loose powder design should be considered. This technique can reduce time of manufacturing due a reduction in layer melting time. Distortions that result after HIP shrinkage should be considered during the design of the component. As tested by Qui et al. [136], a simulation can be useful to predict the distortion in order to compensate during the design of geometries.

## **2.9 Hybrid Manufacturing**

Nowadays, increasing productivity is one of the main areas of investigation in AM. This is mainly focused on improving the flexibility and decreasing the cost. In order to achieve this, new manufacturing approaches and new materials are at the centre of the intensive investigations from the AM community. Nevertheless, defining a suitable method which provides flexibility in an enclosed process like the E-PBF is a challenge. Several methods, such as using cheap powder for manufacturing, customising the build envelope, increasing the layer thickness, improving the melting strategies, varying the settings during the process were all tested to understand the flexibility of the machine and its potential advantages.

AM users already explored the subject using multiple materials and combining different processes, from a conventional milling machine with a direct energy deposition (DED) system [141], to combining multi materials within a single E-PBF build [142], using an AMed component or part as



a starting plate [143, 144], or joining an E-PBF manufactured part with another Ti - 6Al - 4V component through linear friction welding [145], and repairing existing parts [146, 147].

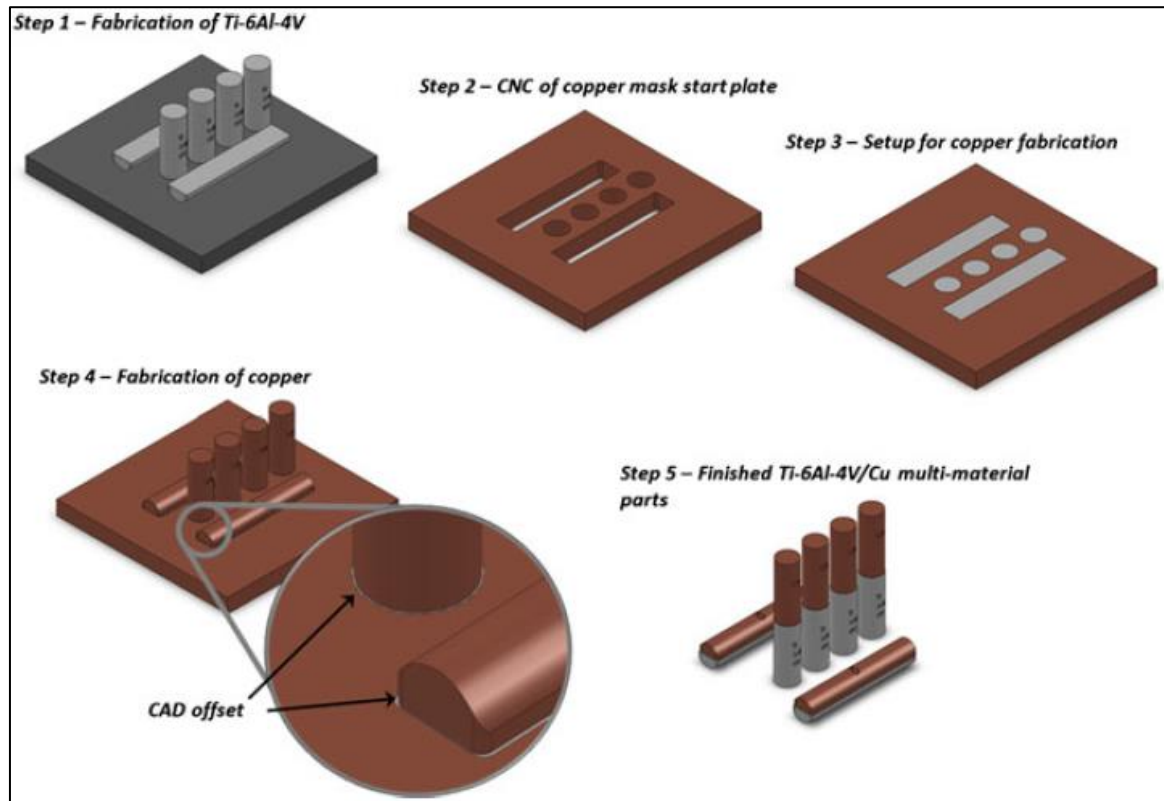


*Figure 2. 29: Combined fabrication of Ti - 6Al - 4V and pure Copper [148].*

A multi-material metallic structure, investigated by Terrazas et al. [148], was explored using Ti - 6Al - 4V AMed parts and pure copper. They achieved multi-material tensile bars, manufacturing the first half of the Ti - 6Al - 4V tensile bars with a standard starting plate, then manufacturing the second half of the tensile bars using a copper mask where the Ti - 6Al - 4V half tensile bar where integrated as shown in Figure 2. 29. Then a final copper build was performed on the top of the titanium components generating full horizontal and vertical multi-material tensile bars. A microstructural investigation showed strong bonding in the transition zone. This technique demonstrated the flexibility of building on top of existing parts using a conventional machine adapted to the final goal of the experiment, which opens up several possibilities such as adding material to existing or worn parts or manufacturing multi-material components.

Using the above approach, a “stop and go process” was performed by Hossain et al. [149] at El Paso University. Using several manufacturing steps, an imbedded sensor was manufactured through 6 steps and 2 builds to enclose an alumina sensor inside a Ti - 6Al - 4V part manufactured by E-PBF. They managed to build on the top side of a previously manufactured AMed part in E-PBF,

levelling it with the starting plate and building up the final sealing part which sealed the part to a mono block component. This advanced approach shows the benefit of encapsulating an external component inside a part manufactured inside the E-PBF in two stages, where an external component sits inside the machine during a build.

Mandil et al. [150] investigated ways to build on top of End-Of-Life parts using an E-PBF system. The authors used a Ti - 6Al - 4V starting plate for a build in order to check the interface between the AM part and the substrate. Using standard E-PBF settings, they noticed strong bonding between the interface and the possibility of building new interfaces into an existing solid flat part.

The ability to manufacture features onto existing parts, and the use of different materials, can provide a new range of manufacturing opportunities for E-PBF. The starting plate can be used as an integrating part of the component, or a real part can be used as a starting plate. More studies can be performed in this area in order to satisfy customer requirements and advance manufacturing solutions.

## **2.10 Production with Additive Manufacturing**

### **2.9.1 Market Overview**

It is too premature to say that AM will replace the conventional manufacturing methods, but it is realistic to observe that the AM market is becoming a real alternative for the production of high value parts, complex geometrical structures and shapes. Several worldwide companies have already invested large sums to increase production using additive solutions. An example is coming from GE who is massively investing in the AM market [151], buying machine manufacturers, powder suppliers, and AM companies in order to make parts from its LEAP engine.

The current market competition in AM is pushing down the price which helps to reduce barriers like business strategies and product development. Other drivers are connected to the reduction of equipment and running costs, manufacturing time, and machine stability, which means that end users are more comfortable to invest capital in AM capabilities. Figure 2. 30 shows continuous growth from 4% in 2003 to 51.3% revenue of the total service and products in the past 12 years with an estimated capital of \$2.65 billion in 2015 [1].



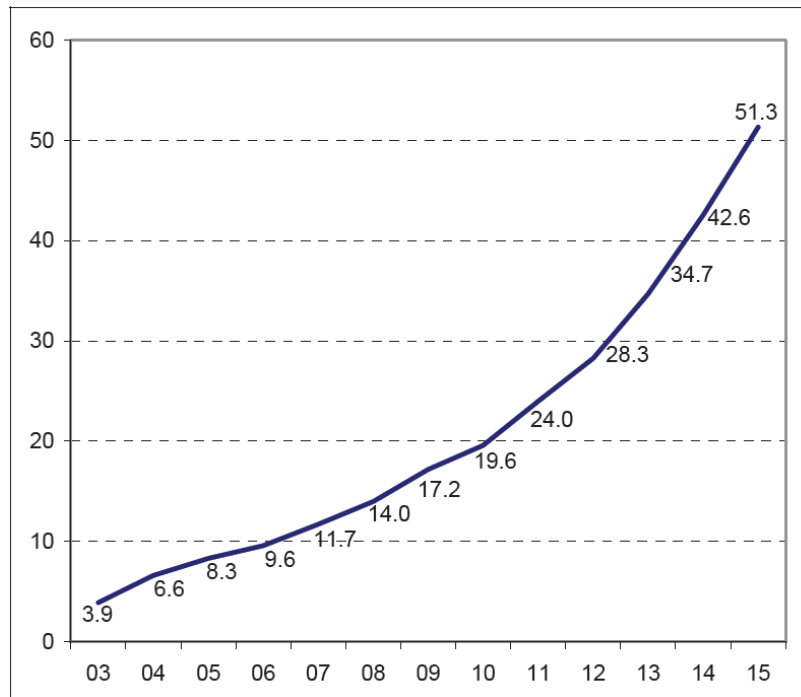


*Figure 2. 30: Total service and product revenue of AM [1].*

Saying that, various components can be manufactured using an E-PBF system, the sector more involved on producing E-PBF parts is medical and aerospace. Due its characteristics of stress-free parts [35], optimised geometry, low needs of supports and anchors during a build, E-PBF systems has changed the way parts are manufactured.

Avio Aero, who are part of GE Aviation, using A2X systems from Arcam, produced titanium aluminide (Ti - Al) jet engine turbine blades with a maximum length of 350 mm. Verretti said that the material is 50 % lighter than the previous nickel-based alloy solution, generating a potential 20 % weight saving of the entire low pressure turbine [152]. Avio Aero ordered 10 E-PBF machines in December 2015 [153] which prove a future full production investment using a PBF technology [154].

Rolls-Royce, with the support of the MTC, manufactured the current biggest AM parts available in the market, which is an engine baring surrounded by 48 vanes AMed as well installed into an A380 flying test bed [155].

Adler Ortho Group in Italy is manufacturing Ti - 6Al - 4V acetabular cups and prosthetic joints, and distributed more than 10,000 units in the orthopaedic market in 2009 [156]; they have now improved the production to different HIP and knee prosthesis with the possibility of purchasing a custom-made implant directly manufactured using patient CT-scans or X-Rays [157]. Since 2015,

Beijing AK Medical had the licence from the Food and Drug Administration for selling the first AM-manufactured implants in China [158].

The mentioned examples of manufacturing companies and what they produce around the globe shows an increase in trust and consequent investment into the AM sectors. Production is slowly moving in the additive area, where customers with different backgrounds and size can be pulled into the market. The constant evolution of systems, knowledge and interest is resulting in increased investment in the area.

### **2.9.2 AM Benefits against Conventional Machining**

Production in AM can generate multiple advantages over conventional methods of manufacturing. In order to move to this way of manufacturing, users need to see benefits in production, cost, value, and responsiveness. There are several examples of where AM can have benefits in production:

- The reduction or elimination of the need for tooling can reduce the cost, lead time, and consequently improve the time to market.
- The current market situation means that there is a need to change/adapt the product released to the market with a rapid change or balance between production and demand, whilst avoiding risks or waste. Having a flexible and tool-less manufacturing provides a fast approach to the product manufactured with the advantage of customisation depending on the needs of the customer and market.
- AM has the ability to manufacture near-net-shape components which helps to reduce the machining cost and time faced using conventional approaches, having the improve, as called in aerospace, the buy-to-fly ratio [159].
- Depending on the component and its use and the high complexity shapes achieved with AM, reduction in the assembly of parts can be made [160]. This can have benefits, such as a reduction in the inventory and assembly line needed for the final component, which gives immediate advantages in documentation, production management, inspection, and an overall reduction in production cost. All the mentioned benefits are also connected to the environmental impact achieved during manufacturing, which still under investigation by the AM community.

After considering some potential advantages achieved using AM technologies, it is necessary to also consider the disadvantages and challenges observed using an AM approach:

- One of the biggest limitations faced nowadays in AM is connected to the high cost of the systems. Machine depreciation is divided between part production and its service life; it is possible to calculate depreciation with different cost models developed according to the company and its viewpoint. The cost calculation of parts manufactured using an AM system represents an important variable to be included and calculated during the cost evaluation of the component. The variables mentioned are the first things to consider during a business case study on AM, then a realistic cost justification needs to be in place. This can be done by comparing the current way of manufacturing with the new AM strategy defined. Conventional methods have years of cost calculation experience with well-known approaches.
- The raw materials, such as powder or wire, that AM machines use, have a high impact on cost. Due to cost and amount of raw material needed for a build, it is still an expensive variable to consider.
- Throughput limitation and slow turnaround time are important limitations to be considered with AM systems. In fact, few machines available in the market have the ability to have a continuous build, such as the VXC800 system from Voxeljet [161].
- Quality and repeatability of parts has always been a hot topic in the AM community. Normally, high value components, such as those for medical and aerospace industries, need to go through rigorous quality control inspections to certify and validate the part which normally needs to pass high requirement standards. The key to unlock this limitation and push the technology forward is focused on generating new standards which are currently underway. ASTM International Committee F42 [162] on AM and ISO Technical Committee 261 [163] are focused on establishing new guidelines to follow in the next few years.

Other challenges and benefits are the design for additive manufacturing and design freedom achievable during the drawing phase. Lightweight and lattice (which include mesh and cellular design) structures are used to improve mechanical properties and to reduce total weight of parts; focused studies are normally required to define which changes can be done to optimise components [164]. Benefits can be seen at different levels, such as combining performance with functionality, reducing manufacturing time and environmental impact, reducing costs and the number of parts [160]. Conversely, quality considerations, constrains of manufacturing and post processing should be considered at the early stage of design, which can be a challenge for designers. Edwards et al. [35], observed that traditional specimens are not enough to predict the

real properties of a component AMed; additional mechanical and fatigue tests focused on the design and properties of the component where suggested.

One of the most serious difficulties faced in the AM is the “traditional attitude” of producers and organisations who are not flexible or happy to change the approach and way of manufacturing components. In fact, modifying the way of manufacturing involves risks and challenges compared to traditional, functional methods. Publishing case studies that evaluated the approaches and show the benefits of AM technologies may change this perspective.

### 2.9.3 Productivity and Cost in AM

The media and experts speculate about the great impact of AM from a market production prospective. There are challenges in predicting the evolution of the technology and the variables involved in cost calculations [165]. Other popular ideas refer to the number of parts to be produced, the complexity of shapes achievable, the difficulties in running an AM system, and the capital investment required [166] (Figure 2. 31). All these assumptions can be a starting point to generate a business model and a potential production investment using additive solutions.

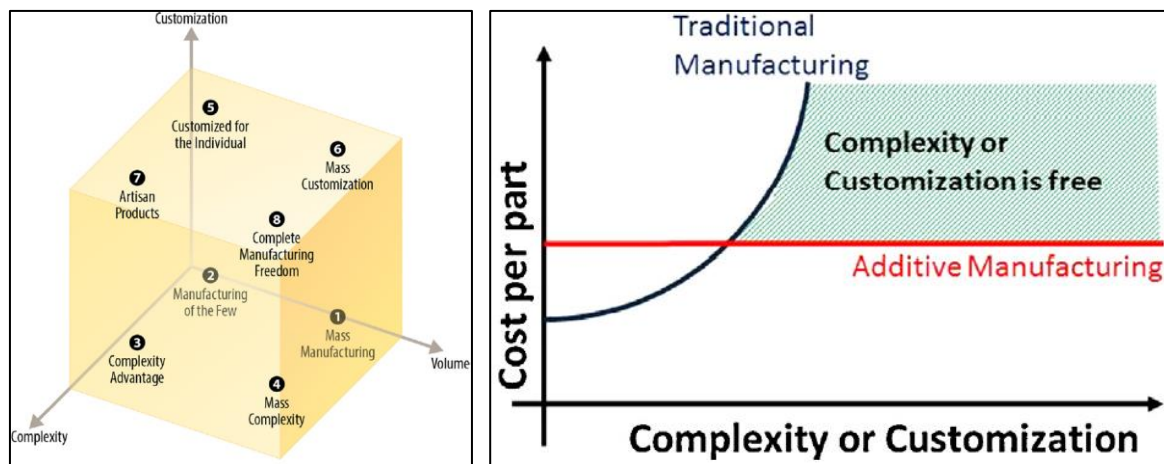


*Figure 2. 31: Three axis model of considering a part to be manufactured (left), when AM should be considered in production [166].*

In 2003 Huang et al. [167] suggested three main aspects where the technology has impact: environment and energy consumption, physical well-being and health, improvement opportunities in current supply chains. In addition to these aspects, more radical challenges are faced, such as managing variants and variables in the AM scenario, including which strategy to adopt for the manufacture of a layer-by-layer part and its characteristics. Another important variable is

connected to the quantity of parts required for production, which influences the business model and its future projection.

Observing the challenge from a different prospective, key aspects should be considered during production with AM systems: optimisation from conventional components can be a route to generate a case study with several advantages, not only cost and time. Weller et al. [168] considered an alternative approach to the economic model in AM. In fact, they used four different AM strengths to push the development into a layer basis technology: free customisation and flexibility, high complexity, combined design for assembly, and versatile machines. Considering the abovementioned approaches used in AM, advance and customised case studies can be calculated to justify additive technologies.

A sensible way of manufacturing in a production environment is related to the sustainable perspective of the technology, the market is currently pushing towards decreased primary energy supply and CO<sub>2</sub> emissions. Due to the immature state of the technique, a full picture is difficult to define even if the AM systems have potential to decrease the sustainable impact occurred during manufacturing [169]. Bourhis et al. [170] suggested a predictive model of consumption where not just the AM machine was considered, but all the parts and needs for production including the pre and post process needed for a complete cost and process estimation.

## **2.11 Literature Review Summary & Gaps**

Having reviewed the literature relating to the E-PBF machine, its software and hardware, advance manufacturing methods, Ti - 6Al - 4V manufactured with an E-PBF, and future impact of AM, it is possible to state and consider the following points:

- The E-PBF systems, and AM solutions in general, are offering excellent mechanical properties (better than several traditional manufacturing approaches) and important microstructural characteristics developed during the build. These can be beneficial for future advance application in high value manufacturing.
- Running an E-PBF system can often be a challenge due the complexity of the machine itself, the pre and post work required for a build, and for the skills needed from each person involved in the manufacturing process. The system has limitations in terms of easy accessibility and can generate significant issues for new users. Training and experience is needed to run the system optimally.
- The high running cost of the system has a significant impact on project planning and preliminary investment needed for a build, in terms of buying powder, consumables,

workforce, and the running costs of the machine itself. This is a big limitation for small manufacturers (OGMs), which do not always have a high budget for investing in new technologies and research & development. Nowadays, the metal AM systems are expensive for a short-term investment and easy accessibility.

- The literature shows several different results in mechanical properties between articles. This is mainly due to the different E-PBF machines used for the build and the approaches used in post analysis. Lack of standards and testing can, at this level, generate confusion in reading and comparing results. Better support should be in place to help understand results and for cross-comparison.
- Limitations can be found in powder management. In fact, all the virgin powder received for an AM build needs to be analysed, processed (sieved, plus other requirements needed from the customer, standards, in house regulations etc.) before the build, classified and stored before and after the build. These steps, which are the minimum essentials to guarantee the conformity of the powder in use, require effort in terms of pre-testing analysis, workforce, instruments on site, and expertise. Solutions in the near future, on how to classify powder as received and on site classification and storage, are required to guarantee the right (potential) production environment within factories.
- The E-PBF system has some limitations in terms of changing settings and configuration. The current system is locked to several pre-set parameters or strategies that do not allow flexibility during the settings and build. This issue can be connected to a new way of manufacturing that can be achieved by modifying software and or hardware of the Arcam machine. Little flexibility is provided by the manufacturer, which is required to exploit more solutions and approaches in the E-PBF field.
- Little literature was found on post process components manufactured by E-PBF systems. Some of the post processing methods can be used to increase the properties of parts built in E-PBF. More information would be useful to develop the post process approaches and mechanical performance of the specimens.
- Literature shows that several innovative methods have been explored using the Arcam machine. A lack of articles and published studies are likely to be due to the ownership of the techniques adopted and its parameters used. Further investigation, as this thesis demonstrates, should be published for global sharing in order to facilitate and improve ways of manufacturing using powder bed electron beam fusion technologies (and AM solutions in general).

- It has been noticed that AM is currently challenging conventional machining in defined fields, as high value manufacturing and high performance materials. High buy to fly ratio components, and high complexity parts are also considered as being manufactured through AM methods. One of the limitations, as mentioned above, is the current lack of knowledge of manufacturers and their ability to invest and produce parts using AM solutions, and to define which parts are suitable to be manufactured using an AM approach. More case studies and shared knowledge is now available online. Despite this, manufacturers need more support to understand what AM is and when or where to use this technology. Government, universities, and other institutions are working together to ensure that this gap in knowledge will be covered in the future, but more work is needed over the coming years.
- Several materials have been tested so far with E-PBFs, but there are still issues in optimising parameters, generating the right environment inside the machine chamber, and the risk of potential cross contamination when changing from one material to another. Most of these issues are common in powder bed approaches. A better design configuration and shared knowledge could help to improve the current situation.
- There was a lack of detailed investigations into production for AM in the literature. Vendors are currently trying to sell combined production cell with smart solutions for increasing productivity. At the same time, international companies are ready to invest in production chains, but little information has been released to the public due to industrial competition and the approach used within this new manufacturing process.

## 2.12 Thesis Chapters Identified Through Literature Review

After investigating the literature, areas of study were identified. Table 2. 1 shows a summary of experiments delivered in this thesis, where aims and objectives, gaps, and novelties are described for each chapter in order to provide an overview of the impacts and targets for each experiment.

*Table 2. 1: Details of the experimental chapters explored in the thesis.*

	<b>Aims &amp; Objectives</b>	<b>Gaps</b>	<b>Novelties</b>
<b>Chapter 4</b> Experiment 1	- Fundamental understanding of heat distribution in the chamber	- Metallurgical properties depending on the location of the build	- Fundamental studies to understand the material properties vs build location
<b>Chapter 5</b> Experiment 2	- Manufacture and prove new hardware - Parameters optimisation	- Custom configuration - Reduction of material and time needed	- Reducing turn-around time and cost

	- Demonstrate the increase in productivity		- New configuration for flexible manufacturing
<b>Chapter 6</b> Experiment 3	- Demonstrate the technology and its benefits - Improve manufacturing time without compromising mechanical properties	- Advance building strategy to save melting time - Variation in microstructure along the build	- Different metallurgical structure along the build - New approach of solidifying loose powder in E-PBF
<b>Chapter 7</b> Experiment 4	- Prove the hybrid technique and its benefits - Understand mechanical properties and characteristics - Define E-PBF settings for most suitable dilution	- Increase flexibility during the build - Flexibility of adding real components or different material substrates - Use the starting plate as a part of the final component	- Add new field as remanufacturing, repairing, and combined materials in E-PBF

## Chapter 3: Experimental Methodology

### 3.1 Introduction

Having analysed the literature, several gaps and potential areas of investigation were highlighted. This thesis explores potential solutions to reduce the gaps currently identified. Machine hardware and advance techniques of manufacturing components were identified as the key topics for investigation. The highlighted subjects found during the review can be summarised as follows:

1. Understand the microstructural impact of parts located in different areas of the chamber;
2. Improve machine flexibility;
3. Investigate potential new solutions to increase productivity using alternative manufacturing approaches.

The literature review helped to understand the conventional methods used with E-PBF technologies and potential new approaches to be used. The following chapter describes the experimental methods used in the material characterisation chapter, pre- and post- analysis instruments, and parts treatments. Experimental methodology introduction and delivery is also explained.



### 3.2 Experimental Development

During the development of this thesis, 4 set of experiments were conducted to investigate the fundamentals of the E-PBF system, its hardware, and advance methods of manufacturing. In order to describe them, a summary of the chapters is given in Table 3. 1 where the main modifications between experiments are shown.

*Table 3. 1: Experimental stages and their characteristics (SF is related to speed function).*

Experiment	Chapter	Hardware	Pre-heat 1	Beam Focus	SF	Powder
1	4	Standard	Modified	Standard	Standard	PA
2	5	Reduce kit	Modified	Modified	Standard	GA
3	6	Standard	Standard	Modified	Modified	PA
4	7	Ti-6Al-4V Plate	Standard	Modified	Standard	PA

The experimental chapters presented in the thesis represent the work completed during the entire doctorate which is all delivered in 4 chapters. The current experimental chapters explain all the techniques and methods used. A brief introduction of the experiments are as follows:

1. Explains a fundamental study conducted with the standard A2XX configuration. Parts were built at different locations of the starting plate, where an investigation of machine behaviour, metallurgical and mechanical properties is discussed.
2. Shows a reduce kit installed inside the standard A2XX Arcam system. Development of the hardware and modification of the software control are analysed. Post microstructural and mechanical analysis of the parts manufactured is described. Build time and cost is compared to the standard chamber to understand potential benefits of having an “adaptronic chamber”.
3. Discusses an “in-situ shelling” approach to reduce time in production, where unmelted pre-sintered and partially melted regions were captured inside a solid shell in order to solidify them through a post HIP cycle. Different beam settings and manufacturing time are investigated to capture the benefits and limitations of the technique.
4. Describes an attempt at hybrid fabrication, where the starting plate becomes part of the component itself through the bonding of the first layers to the substrate. Metallurgical and mechanical tests were performed to understand the feasibility and advantages of this solution.

### 3.3 A2XX Electron Beam Melting Settings per Experiment

*Table 3. 2: Parameters and settings used during the experimental chapters.*

<b>A2XX Ti-6Al-4V</b>	
<b>Conditions</b>	<b>DEFAULT</b>
Layer thickness (μm)	70
Powder particle size (μm)	45 - 106
Powder processed	PA
Preheated T (°C)	720 - 740
Starting plate size (mm)	320 x 250 x 10
Starting plate material	316 SS
Beam current (kW)	60
<b>Preheat 1</b>	
Number of repetitions	4
Line order	15
Line offset	1.2 mm
<b>Number of contours</b>	
Inner	1
Outer	1
<b>Hatch</b>	
Focus offset (mA)	8
Speed Function	36
Line offset (μm)	200
Hatch path	Snake X-Y

The experimental tests were all conducted at the MTC using the same A2XX ARCAM system. Operators had full control of the system, the tests were completely by MTC experts, who followed the design of experiments defined for each stage of development. This section explores the key

parameters used during a build and a comparison of the settings modified during the experimental work.

Standard characteristics of the system are described in Table 3. 2, where layer thickness, powder particle size, preheat condition, line order, beam current, and line offset were kept the same for all builds. Chapter 4 used all the standard setting conventionally loaded due to the fundamental microstructural study on part location in X - Y and Z heights. Chapter 5 was performed using GA powder which has slightly lower morphological properties compared to PA particles; GA may contain more gas (argon or nitrogen [82]) trapped inside the particle itself compared to PA made powder. A different number of preheat 1 repeats were performed for each build manufactured with a reduced kit, with a reduced envelope size and hardware modifications. Four inner contours were used in Chapter 6, where an improvement in the contour thickness was required. SF variation was examined in Chapter 6. A focus offset variation were investigated in Chapters 6 and 7. A Ti - 6Al - 4V starting plate with reduced size was used in Chapter 7.

### **3.4 Melting Strategies**

Standard configuration was kept for some of the experiments performed during the doctorate. This paragraph describes the melting strategies adopted using the standard mode, how they work, and the changes made in case of modification.

A layer thickness of 70  $\mu\text{m}$ , a spherical particle size between 45 and 106  $\mu\text{m}$ , and a pre-heating T of 720 / 740  $^{\circ}\text{C}$  (tracked with the standard thermocouple at the bottom of the starting plate), were used in all the manufacturing experiments. The selection of the Ti - 6Al - 4V powder was as a result of its availability before the experiment. It was assumed that the powders used had similar properties and consequentially the settings were not changed.

Preheat stages are necessary after every new powder layer is spread. As explained in the literature section, the particles need to be charged before they are fused. Two stages called 'preheat 1' and 'preheat 2' which are charging and consequentially heat up the powder particles in the substrate region and in a more localised area. Increasing or decreasing preheat 1 has an impact on the heating T and consequently its pre-sintering level.

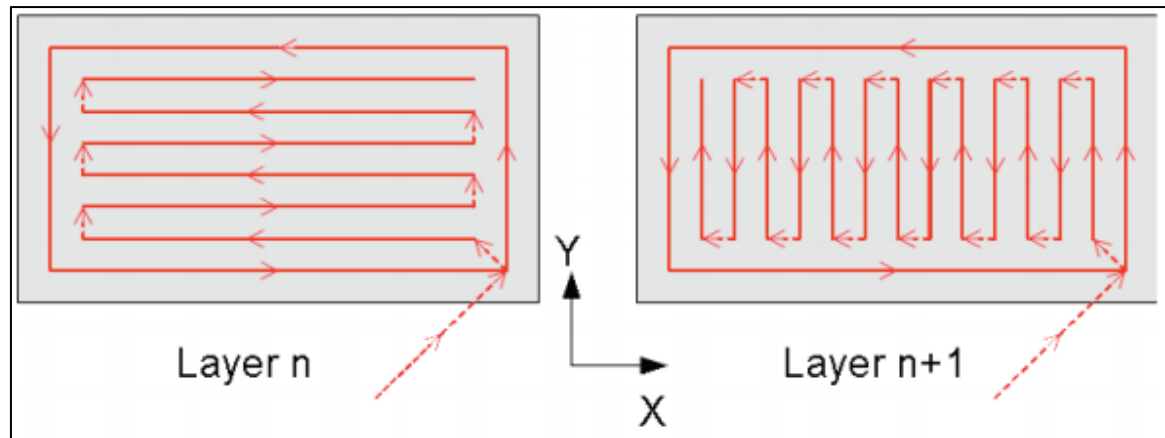


Figure 3. 1: Beam trajectories upon layers where contour and hatch melting are noticed [171].

A pre-set standard melting path was used during the melting of all manufactured parts throughout the experiments. As shown in Figure 3. 1, the melting theme is divided into two scanning approaches called hatching and contour, where hatching is used to melt the core of the geometry first, then the contour scan is used to melt the profile of the component. The hatching has a zig-zag scanning path, also known as ‘snake X-Y’, which turns its scan of 90° upon layer [171]. Two scanning lines were used for the contour melting, a single outer first and a single inner afterwards, were used to melt the line border of the specimen geometry with an overlap of 300 µm.

### 3.5 Materials

During the manufacturing stages used to explore how to improve productivity in AM, Ti - 6Al - 4V was used to investigate the process.

The Ti - 6Al - 4V powder used in this study was Plasma Atomized (PA) and Gas Atomized (GA) produced with a particle size distribution of 45 - 106 µm. The chemical composition requirements are described in Table 3. 3. Chemical composition and particle size have to respect the requirements necessary to meet the standard ASTM specifications for Ti - 6Al - 4V powder bed fusion [106].

Table 3. 3: Powder chemical composition required in Ti-6Al-4V (element % - ASTM F2924).

Powder	Al	V	C	Fe	O	N	H	Ti
Ti - 6Al - 4V	5.5-6.75	3.5-4.5	<0.08	<0.3	<0.2	<0.05	<0.015	Rem.

Chemical analysis has normally supplied by the powder manufacturer or supplier. In order to guarantee the quality and reliability of the atomic percentage, the end user sometimes carries out extra analysis on the powder in order to ensure the quality of it. Different analysis methods can be

used to post analyse the material composition; some of the tests were carried out at the MTC using different approaches.

Gasses, such as oxygen, nitrogen, and hydrogen were analysed using a Leco OHN836 system, where a plasma source burns a weighed specimen in a graphite crucible and an IR beam captures the amount of gasses released in the inert atmosphere. Carbon and Sulphur percentage were captured through a LECO CS744 IR system through the combustion of the specimen in oxygen; consequently, the IR analysis is able to capture the level of CO<sub>2</sub> and SO<sub>2</sub> in the released gas. Thermo Fisher Scientific iCAP7400 Spectrometer was used to detect all the remaining elements available in Ti - 6Al - 4V, where the radiation spectrometry captured after heating up the part using inductively coupled plasma allowed for the measurement of the composition (more details can be found elsewhere [172]).

The powder used during the build was pre-analysed through the abovementioned processes. All the analysis carried out ensured the conformity of the material for use. No builds were run with powder out of specification.

### **3.6 Powder Characterisation**

Several methods of characterisation are available to ensure the conformity of the powder. As such, it was assumed that all the PA and GA powder used during the chapters were very similar in term of powder properties. This paragraph briefly discusses the technology used for the inspection and the influence of the analysis on the characterisation of the powder.

Morphology tests, performed and compared using optical systems, showed that high magnification was required for observation and evaluation of the powder particles. More investigations of powder morphology can be conducted using other optical system such as powder morphology using a statistic image comparison or using laser diffraction or scattered light deflected methods (all available with dry or wet solution).

Due to the superficial characteristics, the morphology results can be compared with hall flow and apparent density. Two types of powder were used during the experiments, where hall flow, apparent density and particle size analysis were compared in order to understand the packing density and flowability of the powder. Characterisation of the powder flow was conducted on the powder batches used for all built samples, the minimum requirements are shown in Table 3. 4. Flow was measured utilising a Hall flow test performed according to the ASTM B213 - 17 standard, where 50 g of powder was required move through a standard orifice in <25 sec.

*Table 3. 4: Powder characterisation analysis requirements by ASTM standards.*

<b>Powder Characterisation</b>	<b>Hall Flow (sec / 50 g)</b>	<b>Apparent Density (g / cm<sup>3</sup>)</b>
<b>ASTM B213 - 17</b>	<25	
<b>ASTM B212 - 12</b>		>2.56

Statistical image analysis of the shape and size of the powder was performed using a Malvern G3 Morphology system to capture and compare pictures of single particles. The process allowed to classify the shapes analysed and their geometries, as described in ASTM B243 - 11 [173]. Other methods, such as sieve analysis and laser diffraction, are normally used in conjunction with one another to increase knowledge about the morphology and powder characteristics [174].

The dimensional trend of particles has a key role during the spreading and the melting of them in the powder bed process. Laser diffraction is the conventional method used to generate the dimensional curve characteristic of the powder analysed. The ISO13320 technique involves measuring the angle variation of a laser beam or a scattered light deflected by moving particles (in deionized water or non-liquid solutions such as gas or air, technical details are available elsewhere [175]). The Malver Mastersizer 3000 system used for the laser diffraction particle size analysis provided a curve for pre and continuous analysis of the particle morphology.

### **3.7 Samples Preparation**

The specimens were cut using either a fine cutter, or a precision cutter and wire EDM. Both cutters used a SiC cutting wheel and coolant; the parts were submerged in deionized water during the EDM cuts. Depending on the analysis required, the specimens where cut either in vertical X - Z or horizontal X - Y plane. Parts were all mounted in hot-mounted conductive Phenolic resin.

All samples were ground down from p400 SiC (grid paper) to p2400, followed by 9 µm supreme diamond suspension or 4000 SiC paper, followed by a final polish using 0.05 µm silica dioxide polishing suspension. For microstructure analysis, etching was carried out by swabbing the specimen in a Kroll etchant reagent (4 ml Hydro Fluoric Acid, 196 ml deionised water) for 5 - 10 seconds (sec) then submerging in water before spraying with ethanol and drying. The standards ASTM E 407 - 07 [176] metallographic etching reagent allow for the visualisation of  $\alpha$  and  $\beta$  structural details [177].

### **3.8 Micro-Hardness measurement**

Micro-Hardness measurements were carried out using a Buehler MicroMet 6030 on the X - Z / Y - Z plane of the samples. A 200 g and 500 g loaded diamond shape insert was used to generate indents during the automatic hardness process. The methodology used from the hardness system is connected to the shape of the indent generated during the process; the distance between the edges are related to the hardness of the specimens. A manual measurement was performed to provide the micro-hardness of the manufactured specimens which was automatically calculated from the software after obtaining indent length (more system details and standards can be found elsewhere [178]). The typical micro-hardness value for an A2XX system using Ti - 6Al - 4V is around 340 Vickers Hardness (HV) [179].

The indents pattern and its causes are explained in the experimental chapters.

### **3.9 Archimedes Test**

Due the post HIP treatment shrinkage, a volume analysis was performed using the Archimedes test. The principle was used to capture the density of the mass before and after heat treatment, as components tend to shrink during the HIP treatment due to the collapse of internal voids located inside the specimen [180].

The Sartorius YDK03 kit [181] (also known as Archimedes' system) was used with the 0.001 g Sartorius ENTRIS64 - 1S scale in order to capture volumetric changes. A comparison between the Archimedes' results captured before and after the HIP treatment, allowed for understanding of the voids trapped inside the manufactured components and the volume density of the parts.

### **3.10 Optical Microscopy**

Metallurgy investigation of part microstructure, and powder porosity were carried out using the Zeiss - Image.M2m [182] OM. Images were captured singularly at different magnifications or using the mosaic function which allowed for the visualisation of an enlarged surface area by combining multiple pictures together. Both black and white, and colour modes were used to improve the representation of defined areas of the specimens.

Some of the samples were inspected under a polarized microscope (PLM) filter in order to improve the ability to visualise the grain size and orientation, microstructure behaviour, and boundary geometries. Measurements were also captured to better define the microstructural characteristics and geometries of the specimens.

The top surface roughness was inspected and a comparison of specimens generated during the experiments was carried out. The measurements were captured using an Alicona IF series, with a filter of 2.5 mm. The flat region scanned was 2 x 2 mm in the middle region of the cuboids, which allowed to capture a Sa average of the specimens measured (more details of surface roughness and Sa can be found elsewhere [8, 183]).

### 3.11 Scanning Electron Microscope (SEM)

SEM solution and related techniques were adopted during the microstructural analysis of the particles; Energy Dispersive X-Ray Spectroscopy (EDX) were explored to gain a deeper understanding of the composition, the development of the structure, and other features (details of the techniques can be found elsewhere [184]). Two microscopes were used during the analysis of the specimens: a desktop Deben TM 3000 for preliminary studies (due the low specs of the system) and a state of the art Jeol 7000 system for high magnification inspection and detailed images.

*Table 3. 5: SEMs description and location.*

	Location	Electron Source	Voltage (keV)	Detectors
<b>Hitachi TM 3000</b>	MTC	FEG	20	SE, EDX
<b>Jeol 7000</b>	Met. & Mat. UoB	FEG	20	SE, BSE, EDX

Technical details of the analysis performed using the SEMs is described in Table 3. 5, where different microscopes, located in different places, were used for different experiment investigations. The Jeol 7000 system offered high magnification resolution and EBSD analysis, other simpler analysis were performed with the desktop Philips system which guaranteed the required quality for non-in-depth studies.

The use of high magnification SEM system also included backscattered imaging, measurement of features such as  $\alpha$  lath, surface fracture analysis, powder morphology inspection, and surface images of the specimens.

### 3.12 X-ray CT and $\mu$ -CT

In order to capture all the residual porosity and voids trapped inside the material, some post investigation was carried out using two different X-ray CT (X-CT) scans. Both use X-rays to generate a 2D cross-section of a physical object, where a 3D shape can be regenerated if successively



combined together [185], as shown in Figure 3. 2. The main difference between the X-CT and micro-CT ( $\mu$ -CT) is the pixel resolution; in fact, the  $\mu$ -CT system, depending on the shape and dimensions of part to be analysed, can reach a resolution of few microns or below.

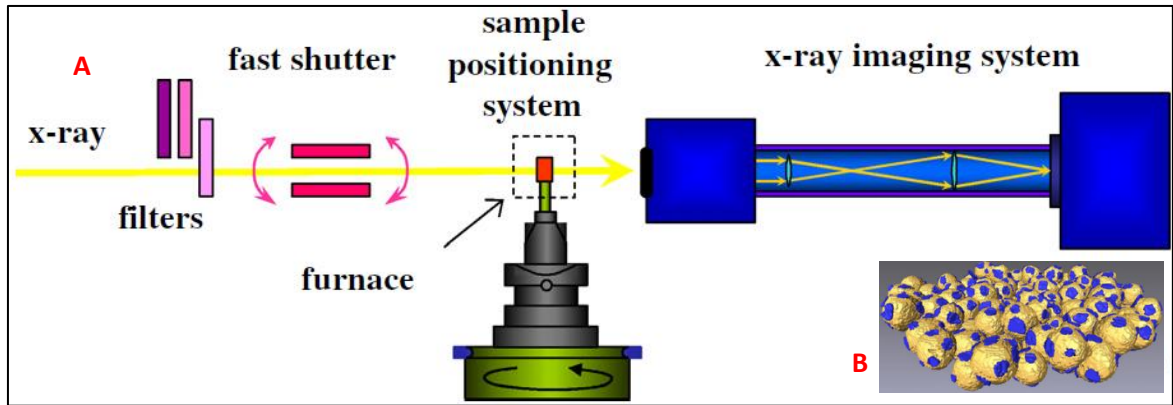


Figure 3. 2: Microtomography system set up at the European Synchrotron Radiation Facility (a), reconstructed image of powder particles at the beginning of sintering (b) [185].

In the performed studies, the post process analysis was conducted at the Harwell Centre. The samples were reconstructed using filtered back projections algorithms embedded in Nikon CT Pro3D. Afterwards, the correction of beam hardening and Hanning filters were performed before image segmentation and quantification (more details can be found elsewhere [186]). The post analysis has been performed using the Avizio software where different steps of normalisation were performed in order to analyse the parts scanned, depending on requirements.

All CT characteristics and settings are described in Table 3. 6.

Table 3. 6: CT systems and settings (set.) used to analyse the samples.

	Set.	Location	Acceleration Voltage (kV)	Current ( $\mu$ m)	Projections	Voxel size ( $\mu$ m <sup>3</sup> )
Nikon XT H 225 (X-CT)	1	MTC	115	82	1760	10.8
Nikon XT H 225 ( $\mu$ -CT)	2	Harwell Centre	80	81	3142	2.7
Nikon XT H 225 ( $\mu$ -CT)	3	Harwell Centre	80	81	3142	6.9

### 3.13 Mechanical and Fatigue Testing

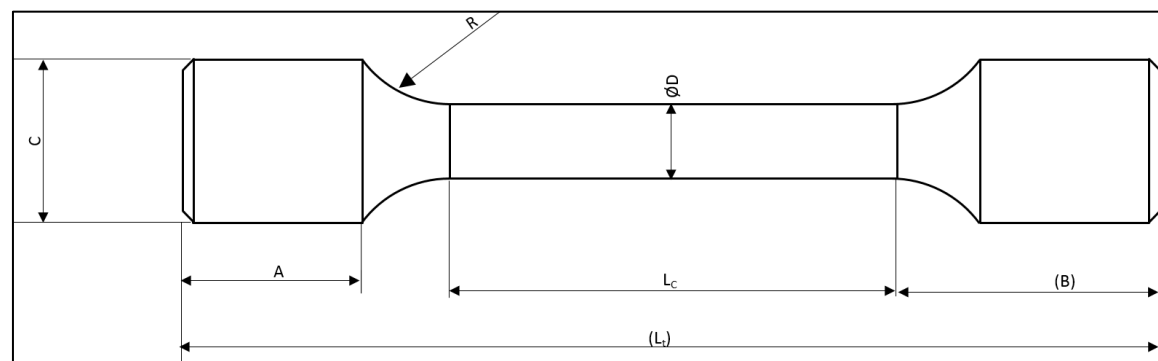
During the experiments, tensile and fatigue test bars were generated in order to better understand the mechanical characteristics of the parts manufactured using the E-PBF system. As described in Table 3. 7 tensile specimens were manufactured and described in Chapter 4 and 6. All the

machining preparation and the tensile experiments were performed at Westmoreland Mechanical Testing & Research Ltd. Only the high cycle fatigue (HCF) tests were performed at the University of Birmingham.

*Table 3. 7: Mechanical tests settings (set.) performed.*

Standard	Set.	Test	Load (MPa)	T (°C)	Layer Direction
ASTM E8	1	Tensile	Tension	RT	Horizontal and vertical
ASTM E466 - 15	2	HC Fatigue	400	RT	Horizontal (98 Hz)

Specimens in different orientation were manufactured for the tensile experiments; 0 °degree and 90 °degree were the build angles selected for the production of the specimens. Rounded bars with treaded sides was the geometry selected for the room T tests. As shown in Figure 3. 3, two gauge diameters of 4 mm and 6 mm were selected for the tension tests.



Diameter (D)	C		Grip length <sup>2</sup> (A)	Parallel Length ( $L_c$ )	Radius (R)	Reference Dimensions			
	Threaded	Unthreaded				$S_o$	$L_o$	B	$L_t$
	Diameter <sup>1</sup>								
4	8	8	12	29	4	12.57	20.03	15.46	55.00
6	10	10	15	43	6	28.27	30.04	19.47	80.00

*Figure 3. 3: Tensile bar characteristics represented in mm.*

Fatigue samples were manufactured with a 88.9 mm length and a 6.35 mm gauge diameter, 12.7 mm parallel length, 50.8 mm rods to a 12.7 mm (1/2") threaded ends. The analysis was performed with a frequency of 98 Hertz (Hz) at room T with a load in tension. Due to statistical purposes, 3 samples of each condition were performed, a set value of 400 MPa was utilised for the constant load during the experiment. The samples were prepared at Westmoreland Ltd. with the typical transverse machining approach and finished off with horizontal polish which helps to limit surface originated failures. An Alfred J. Amsler & Co. machine was used for the tests (Figure 3. 4).

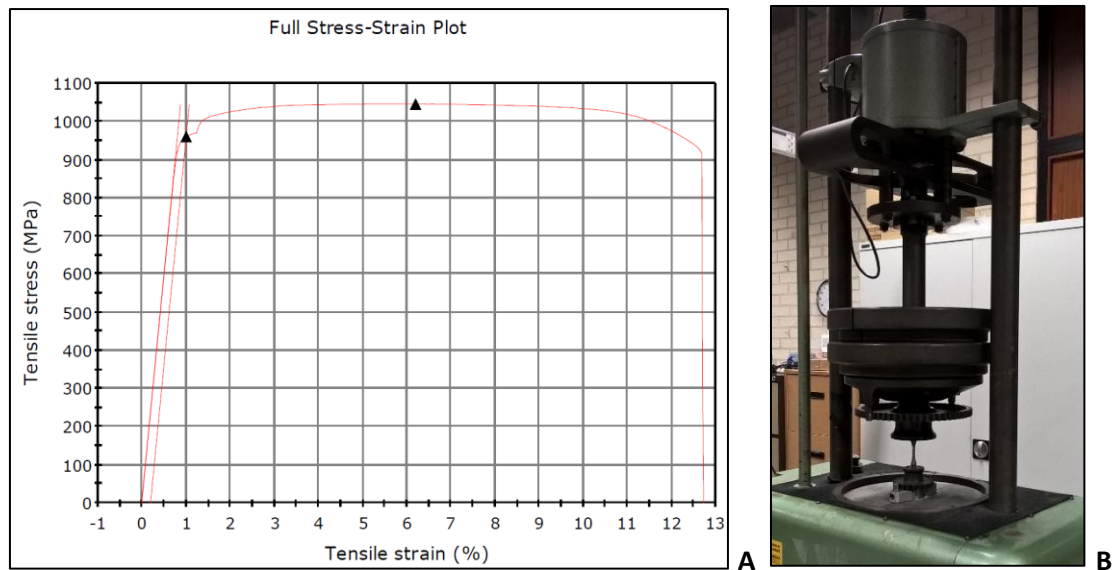


Figure 3. 4: Typical E-PBF Ti - 6Al - 4V tensile curve (a), fatigue machine used for the tests (b).

### 3.14 Hot Isostatic Pressing

Post processes such as a HIP treatment have been performed to close the potential porosity available in specimens. Different shells and cuboids were manufactured using different settings which generated some residual voids trapped inside the components. This resulted in shrinkage during the post heat treatment, which helped the bonding of the powder trapped inside the cylinders and cuboids, and the reduction in the voids trapped inside the parts. A minimal reduction in mechanical properties should be noted due to the increase in  $\alpha$  lath during the holding time at an elevated T.

The heat treatment was performed at Hauck Heat Treatment Ltd (TTI), where a constant pressure of 103 MPa, a T of 920 °C, and a holding time of 120 minutes were used during the HIPping process. Figure 3. 5 [187] shows an example of pressure and T applied during a HIPping cycle, where time at the established holding T and pressure were applied.

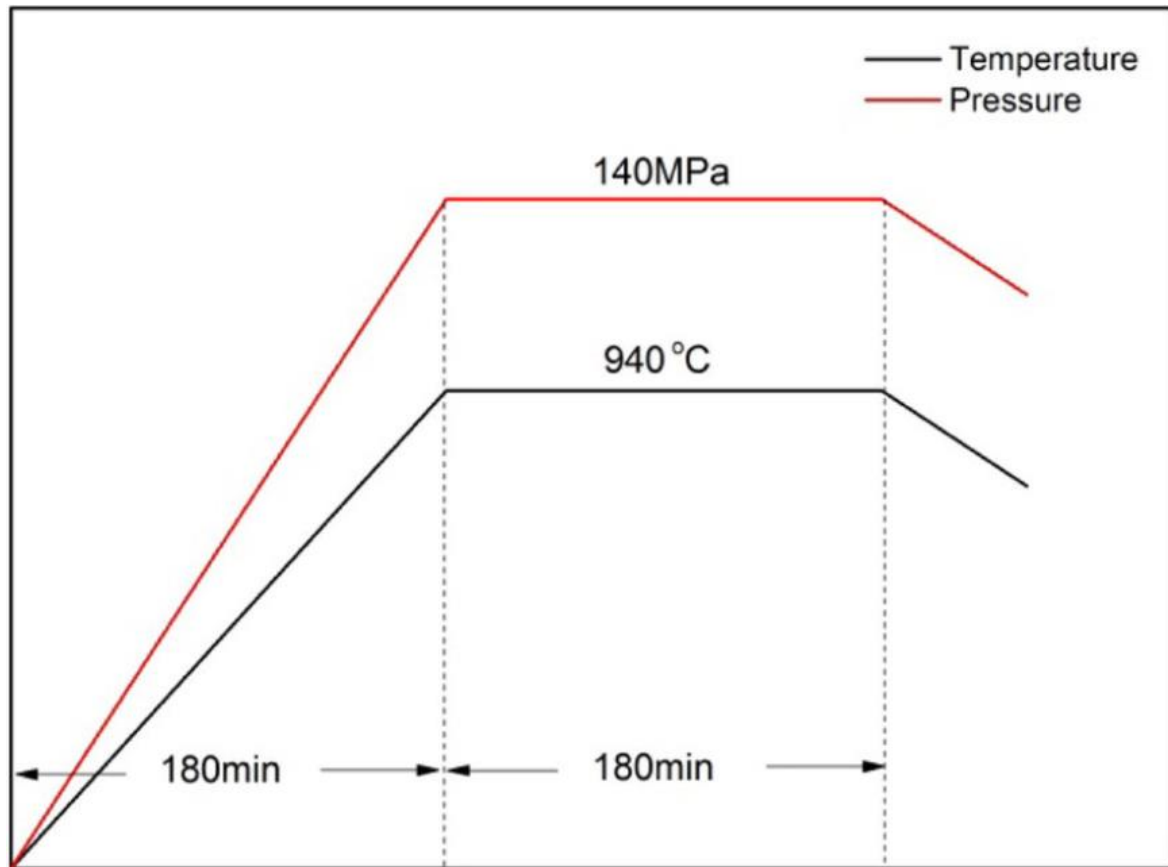


Figure 3. 5: Example of a Ti - 6Al - 4V cycle performed during a HIP cycle [187].

### 3.15 Starting Plate Preparation

Different substrates were used for the manufacturing of the builds achieved with the A2XX system. All the starting plate, before locate them inside the machine, were cleaned using a degreasing detergent sprayed on the surface and cleaned up with non-magnetic cloths. The cleaning process allowed to avoid potential contamination inside the chamber and the consequent risk of inclusion inside the components manufactured.

Different surface conditions were made onto the starting plate in order to generate a different starting condition and a consequent potential change in the bonding region between the 316 SS substrate and the first AMed layers. On top of the standard starting plate cleaning process, the substrate were treated with different etched, re-melted, and shoot peened conditions. The etched solution used was the same technique used during the preparation of the samples: Kroll's reagent swabbed for 10 sec around the interested region. An enclosed IPG YLR - 500 laser, located at the MTC, performed the top surface re-melted treatment (see Chapter 7.1 for more details).

A peening treatment were achieved using a shot peening system at Sandwell Ltd [188], were a coverage of 200 % of the surface with impacting iron spheres was performed. During the shooting, just the surface required was not covered of protective metal sheets. A post-cleaning method with glass beads were used to remove potential contaminations from the shoot spheres [189]. More details of the performance of the process and technical explanation can be found in Chapter 7.1.

## **Chapter 4: Heat Distribution Changes in a E-PBF Build Chamber**

### **4.1 Introduction**

Chapter 3 summarised all the requirements needed to set up the machine for the manufacturing of components. It also outlined the specification of the systems required for the post analysis of the components built in E-PBF.

As reported in chapter 2.6, changing the location of the parts inside the E-PBF bed can have an impact on the metallurgical and mechanical behaviour of the components varying in the X - Y plane or along the Z axis. The Geometry and the microstructure of the manufactured part can change depending upon the build location and the melting strategy adopted.

The following study was conducted to analyse the behaviour of parts located in different X - Y locations, a result of varying melting strategies at different Z heights. Different preheated areas were used in an attempt to understand the influence of solidification over the area and build location, where differences in beam energy and cooling rate can be noticed. Post metallurgical and mechanical properties were captured to compare the results across the manufactured parts. The study shows only a minimal change in the properties of the cubes manufactured as a result of the cooling rate achieved in the location of the specimens.

The main targets of the following chapter are described as:

1. Understand the influence of the heating envelope performed in E-PBF;
2. Microstructural impact of parts manufactured in a different chamber location;
3. Define a relation between microstructure, heat condition, and mechanical properties between specimens build with different conditions.

## 4.2 Experimental Procedure

### 4.2.1 Experimental Work and Build Preparation

An Arcam A2XX was used to conduct the trials at the Manufacturing Technology Centre (MTC) using the standard configuration chamber supplied by Arcam. The 3.5 kW E-PBF machine was vacuumed to secure the quality of the internal environment, the vacuum chamber is depressurised to  $\sim 1 \times 10^{-4}$  mBar and a controlled amount of inert Helium ( $\sim 1 \times 10^{-3}$  mBar) was introduced to avoid influences of beam scattering. By using a Helium vacuum controlled solution it was possible to avoid oxidation generated at high T which can compromise parts quality and machine integrity. A T of  $\sim 720 - 740$  °C was used to preheat the 320 x 250 x 10 mm thick 316 SS plate. All the machine preparation was done by Arcam trained E-PBF experts at the MTC who followed the standard internal procedure of setting up the powder bed system.

*Table 4. 1: Parameter setting used during the E-PBF build.*

	<b>Focus offset (mA)</b>	<b>Beam speed (mm/s)</b>	<b>Number of repetitions</b>	<b>Average Current (mA)</b>
<b>MTC-Preheat theme</b>	55	12000	4	5.6

Thirteen blocks with 10 mm squared bases and different heights were positioned along the diagonal of a standard A2XX starting plate. These were manufactured using three different preheating areas along the Z direction. Figure 4. 1 shows the complete build, where for the first 10 mm of building the blocks were processed with a preheating area of 250 x 200 mm, for building between 10 to 20 mm in Z direction a 176 x 176 mm square preheated surface was used. The last 10 mm (from 20 to 30 mm) a preheating area of 144 x 144 mm was used. This arrangement was developed using the maximum and minimum preheating areas supplied by Arcam for the A2XX system (250 x 200 mm and 144 x 144 mm). The preheating settings are shown in Table 4. 1, where a software equation directly calculates the energy density needed according to the surface area to preheat.

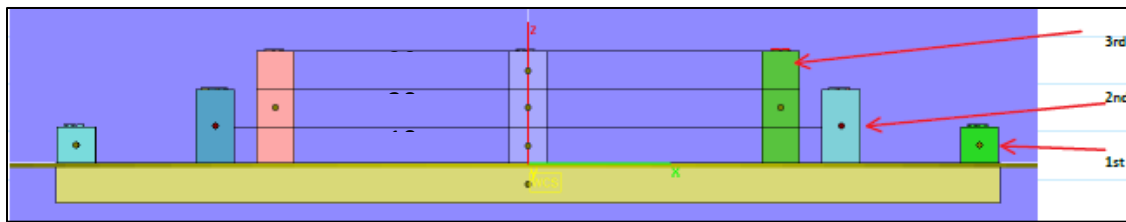
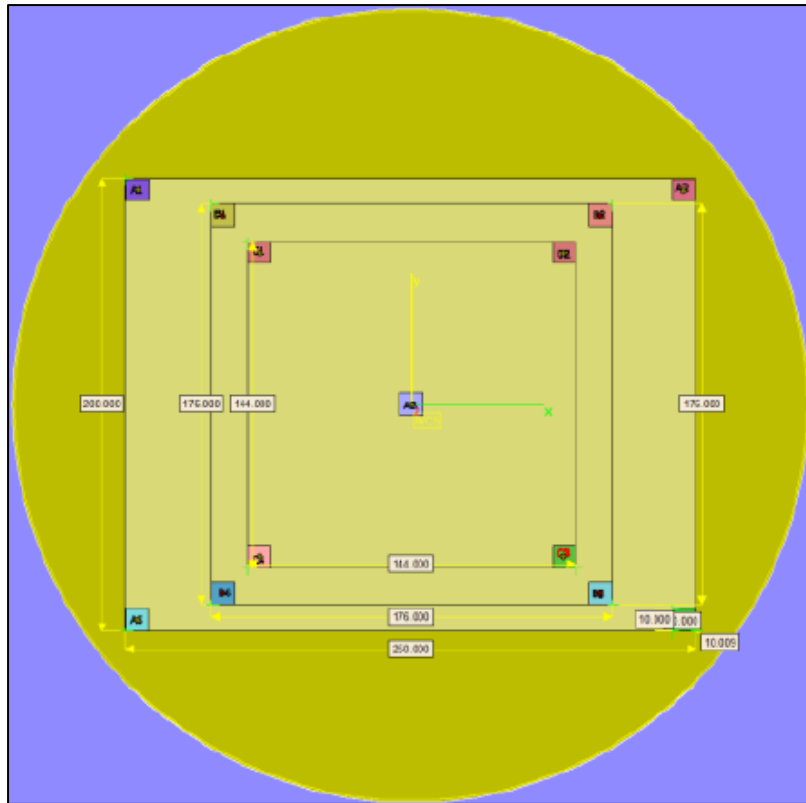
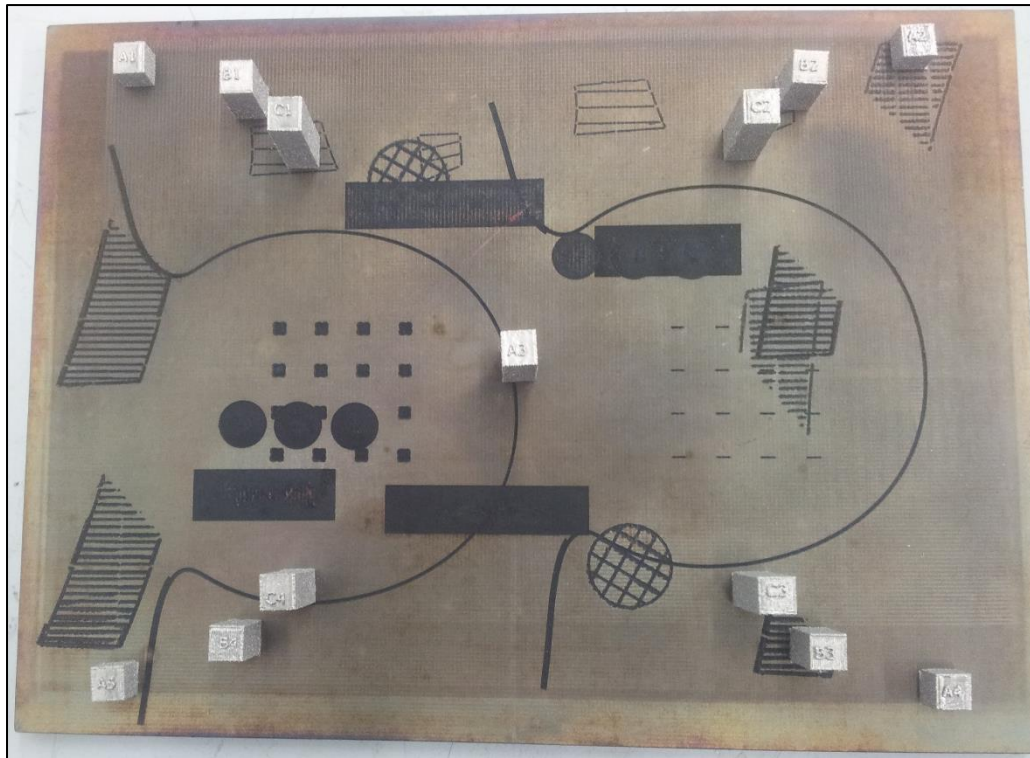


Figure 4. 1: 13 Samples generated by E-PBF using Ti - 6Al - 4V.

All the settings used were previously tested with success using the same machine at the MTC using the parameters showed in Table 3. 2. The cubes were built directly from the starting plate without the use of supports (Figure 4. 2).



*Figure 4. 2: 13 blocks after the manufacturing, they are attached on a 316 SS substrate. The reused plate shows drawings which have need cleaned before the current build.*

## 4.3 Results and Discussions

### 4.3.1 Powder Analysis

The low magnification x 100 SEM picture in Figure 4. 3 (a) shows the Ti - 6Al - 4V PA powder from Arcam. It can be observed that the particles morphology was generally spherical, with a small percentage of satellite particles. Increased magnification shows non-divided powder fused together (b), a low number of non-consolidated round particles with a splatter cup noticeable in (c), few deformed non-circular parts were captured during the analysis shown in (d).

Shape and size are critical for the success of the E-PBF process. A spherical shape with a low number of satellite particles, and a PSD of the particles inside the standard tolerances [106] increase the chances of having a successful build. Powder analysis showed a distribution inside the tolerances of quality required for the process; this observation was confirmed by the powder experts at the MTC through a series of powder analysis completed in the powder laboratory.



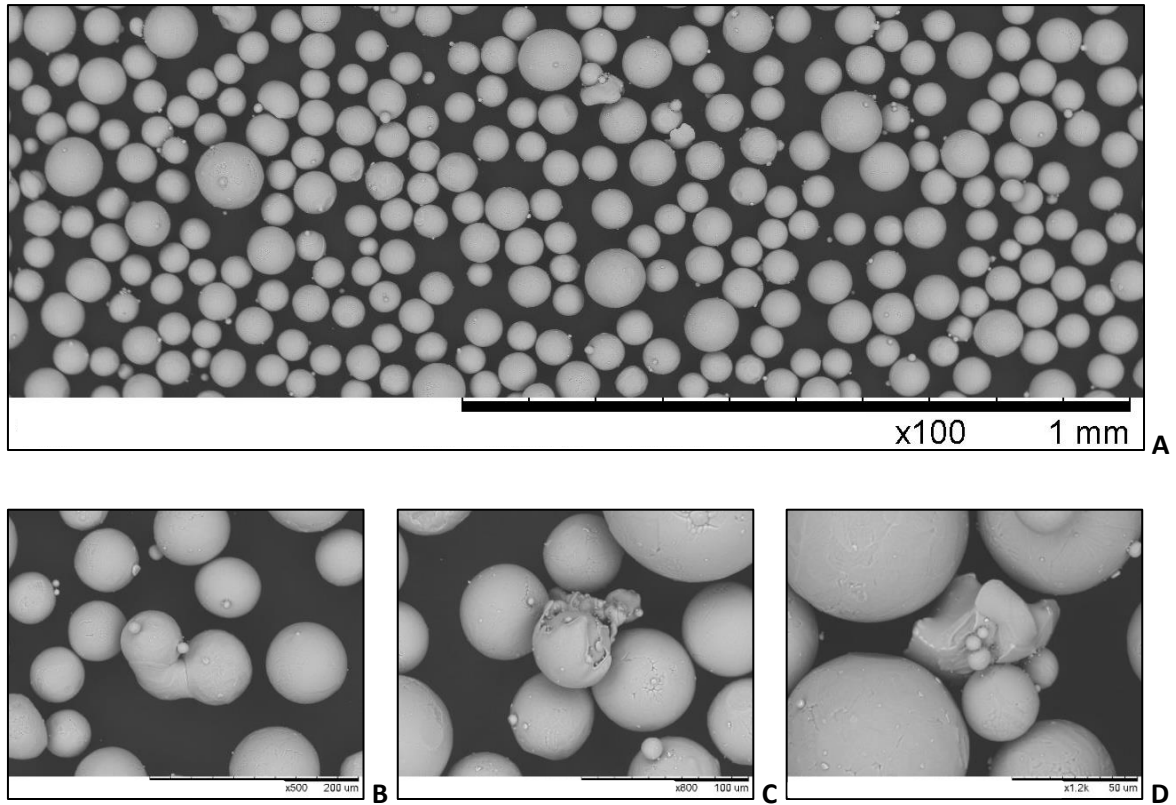


*Figure 4. 3: SEM pictures of PA 45 - 106  $\mu\text{m}$  powder batch used for the build.*

Cross-sectional optical microscopy of a Ti - 6Al - 4V PA powder sample (Figure 4. 4) shows evidence of entrapped porosity in a low number of powder particles. No significant level of porosity is noticed.

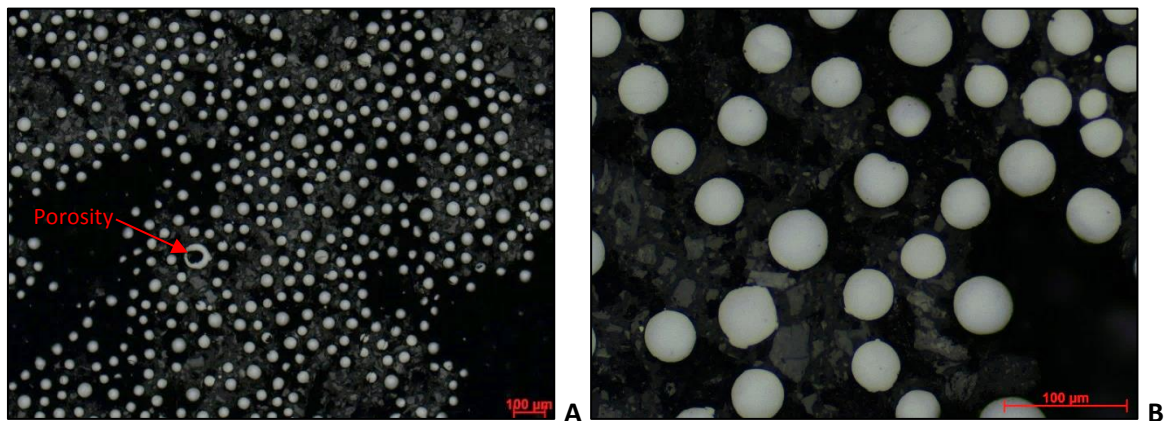


*Figure 4. 4: Polished powder analysis with low (a) and high magnification (b) captured by OM.*

The quality of the powder observed minimised the probability of finding gas pores inside the built part due the good characteristics of quality observed during the preliminary analysis.

An overview of the results for Arcam Ti - 6Al - 4V used powder based on the traditional Hall Flow ( $FR_H$ ) is provided in Table 4. 2. The  $FR_H$  results show that the 50 g used for the analysis meets the specification of <25 sec. Flow was achieved through the Hall flow orifice with a time of 21.56 sec average (Mean) with a standard deviation (STDEV) of 0.365 sec measured after 3 repeats. However, it was noted that the flow of used powder was slightly reduced compared with fresh powder, from 19.62 sec to 21.56 sec. This was almost 2 seconds slower than fresh powder condition. It may be due to the presence of irregular shapes and satellites generated during the re-use of the powder, but no major impact should be noticed during the process.

*Table 4. 2: Shown the flowability of the powder captured with Hall Flow technique.*

Conditions - RH 34%, Temp. 20°C		
Sample		$FR_H$ (sec/50g)
P864 Build Powder	Repeat 1	21.38
	Repeat 2	21.32
	Repeat 3	21.98
	<b>Mean</b>	<b>21.56</b>
	<b>STDEV</b>	<b>0.365</b>

### 4.3.2 Microstructure Analysis

Different formation of grains was noticed at the bottom side of the A3 specimen. In fact, for the first few hundred microns of the sample, as can be seen in Figure 4. 5, the grains dimension were smaller and more randomly distributed than the core of the specimen. The grains located in the bottom of the specimen have a geometry which helps the formation of the prior  $\beta$ -columnar grain boundaries that are running along the specimen in Z direction. Not many pores were observed.

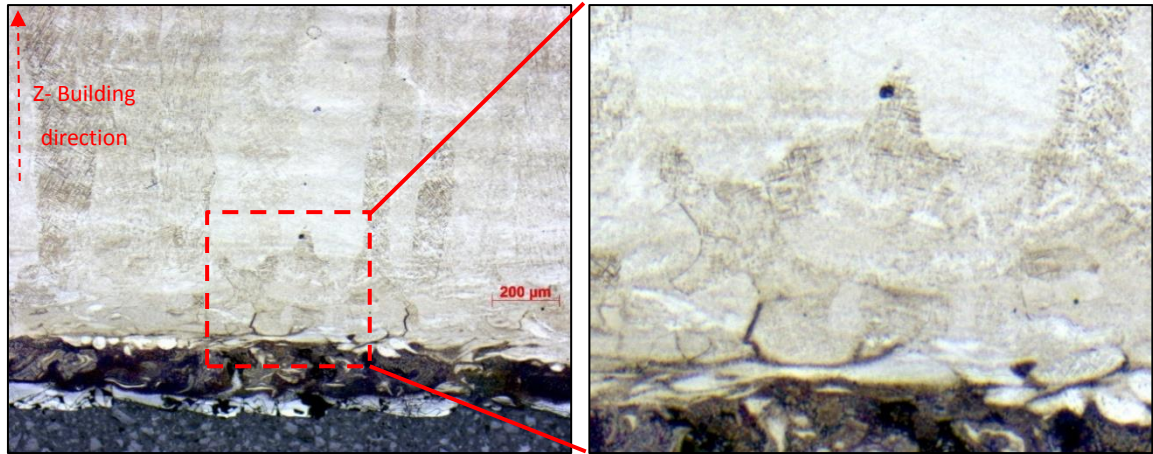


*Figure 4. 5: Equiaxed and columnar grains investigation on the bottom of the A3 specimen observed by OM.*

Figure 4. 6 (a) shows a micrograph from the middle section of specimen A3, showing a vertical boundary line that is the primary  $\beta$  grain boundary. The  $\alpha$  phase grains are precipitated inside the prior  $\beta$  grains. Figure 4. 6 (b) shows a surface region where the bonding took place between loose powder and previous solidified layer; the main large grain is growing inside the attached powder where perfect metallurgical bonding is created.

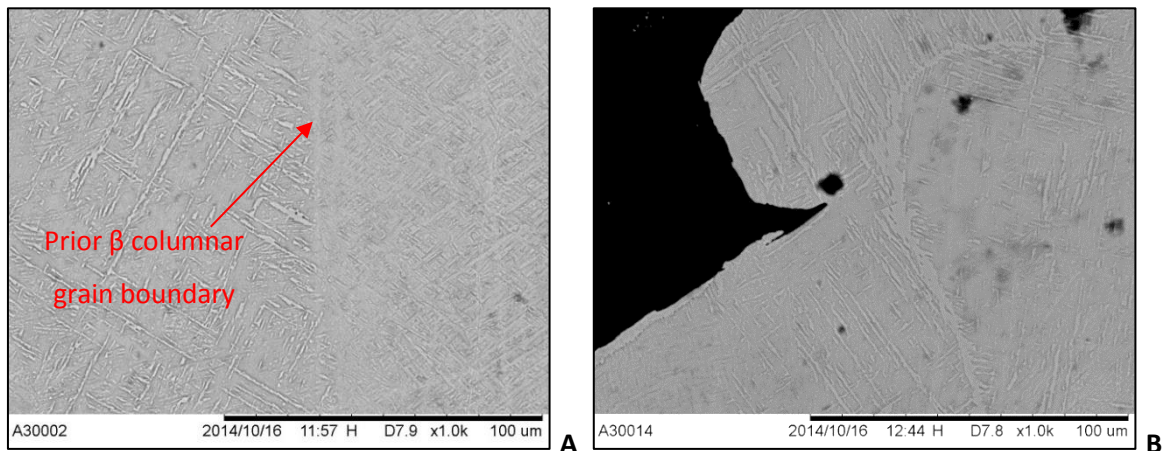


*Figure 4. 6: Mid (a) and edge (b) pictures of A3 specimen taken with SEM.*

After measuring the prior  $\beta$  grain average, an overview of the samples was considered in order to compare the microstructure in different locations. All the samples in Figure 4. 7 appear with an equiaxed prior  $\beta$  grain structure at the bottom of the specimen before developing into columnar prior  $\beta$  grains growing along the Z direction. The specimens have similar microstructural conditions all along the structure development; it is possible to observe the boundary of the melting of the final layer on the top of the B2 and A2 specimens.



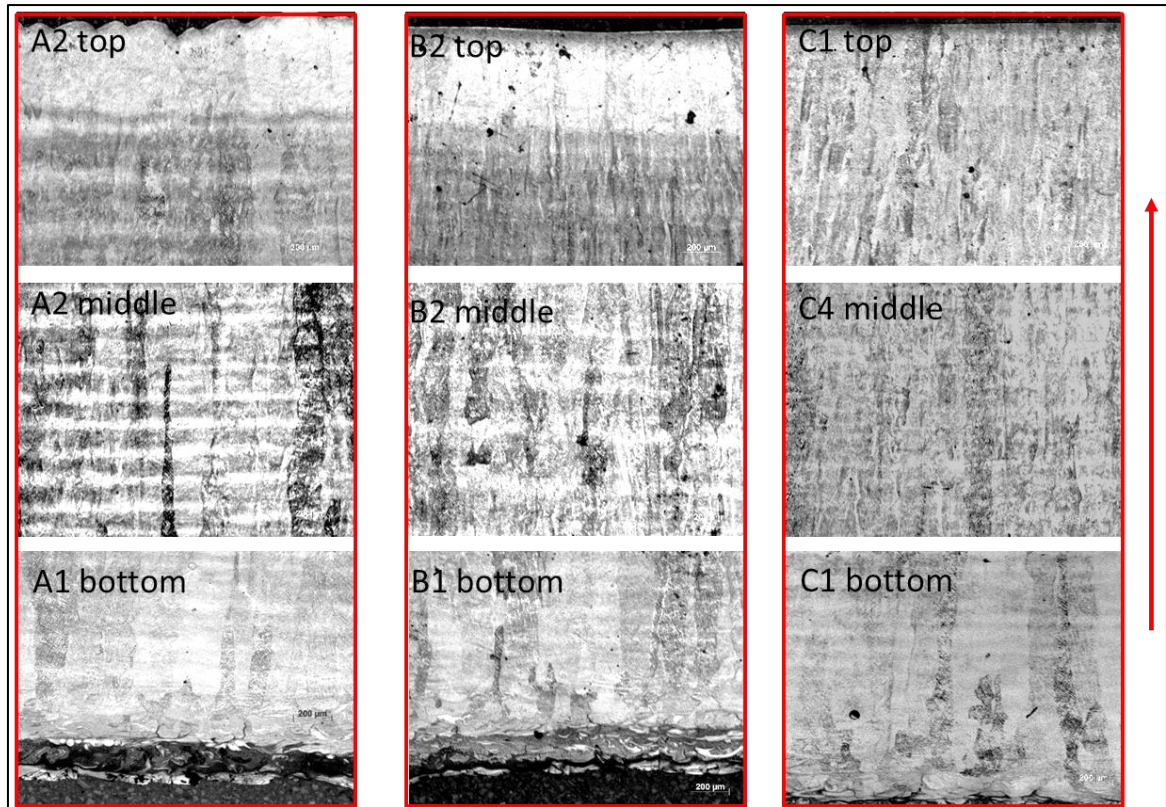


*Figure 4. 7: Comparison of specimens with different preheating strategy, along the building direction, analysed by OM.*

As shown in Figure 4. 8 the Z-direction cut shows columnar grain growth structure located in the A3 specimen. The prior  $\beta$  grain width was measured at an average of  $140\ \mu\text{m}$  which is similar or slightly bigger of what found in literature [190, 126, 191, 98], which is probably due to the different cooling rate available using an Arcam A2XX chamber and the machine settings used. The vertical formation of the grains is favoured due to the high T gradient occurring during the reheat layer band [120]. It was observed that the columnar grain size does not change during the building process, maintaining the same thickness average from the bottom to the top of the specimens, similar grain growth conditions were observed in literature [129], where Wrabe and co. observed similar prior  $\beta$  grain size were between samples along the Z direction. The investigation was undertaken from the formation of the columnar line (bottom region) to the close top of the specimen (top region).

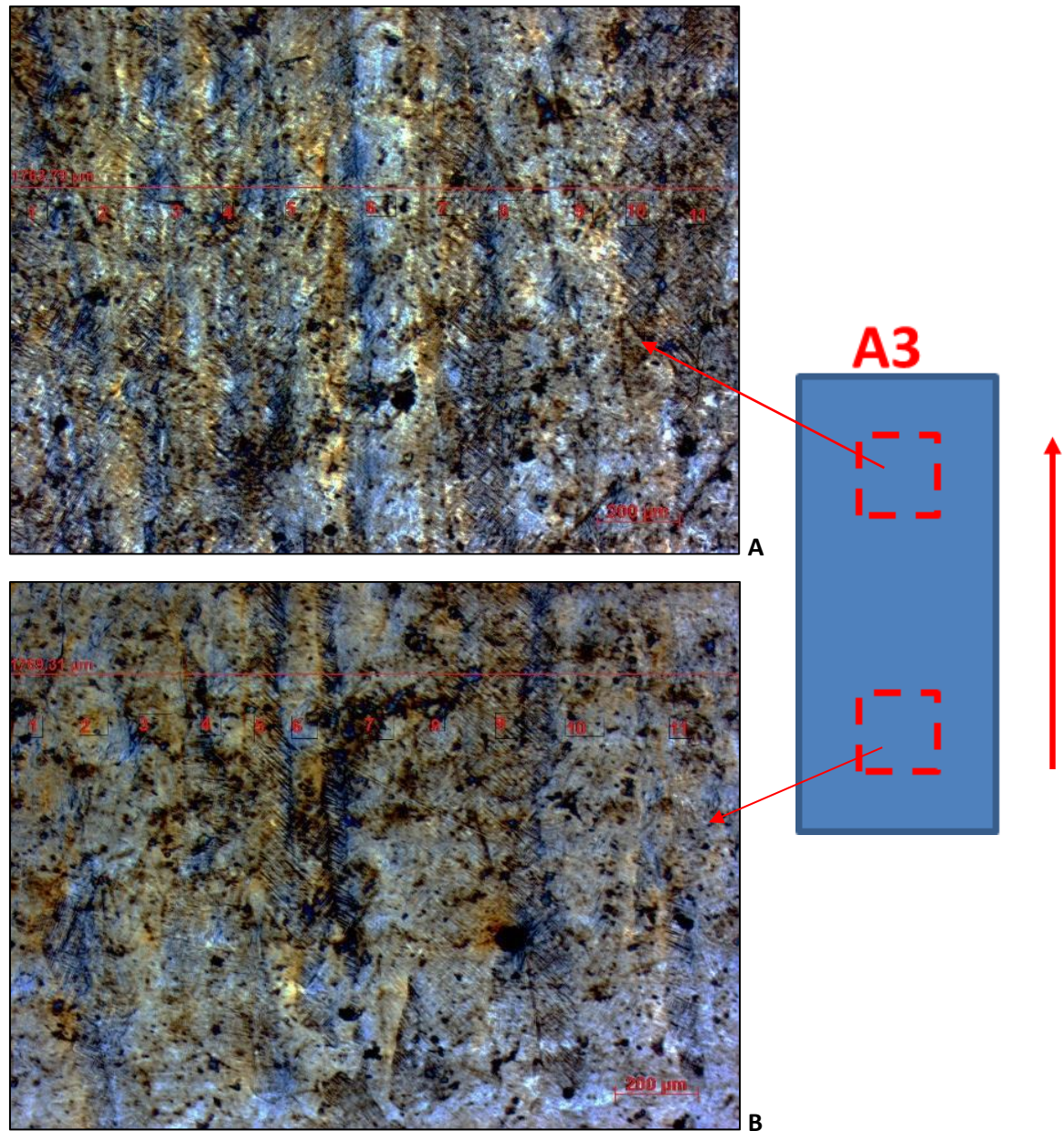


*Figure 4. 8: Polarised OM prior  $\beta$  grain boundaries analysis on the bottom (A) and on the top region (B) of the A3 specimen X - Z cross section.*

The core of the microstructure shows some changes in  $\alpha$  lath size. Figure 4. 9 shows a comparison between a specimen built at the edge of the preheating area and one built in the middle of the cake. It is possible to see that A1 has a more refined microstructure compared to A3, where an  $\alpha$  lamellae have a smaller dimension. This phenomena is potentially due to a quicker cooling rate in the external region of the powder cake, where heat dissipates to cooler powder particles in the edge region of the powder cake as showed in literature [192]. More analysis should be performed to better understand the phenomena as measuring  $\alpha$  lath thickness, or electron backscatter diffraction (EBSD) analysis.



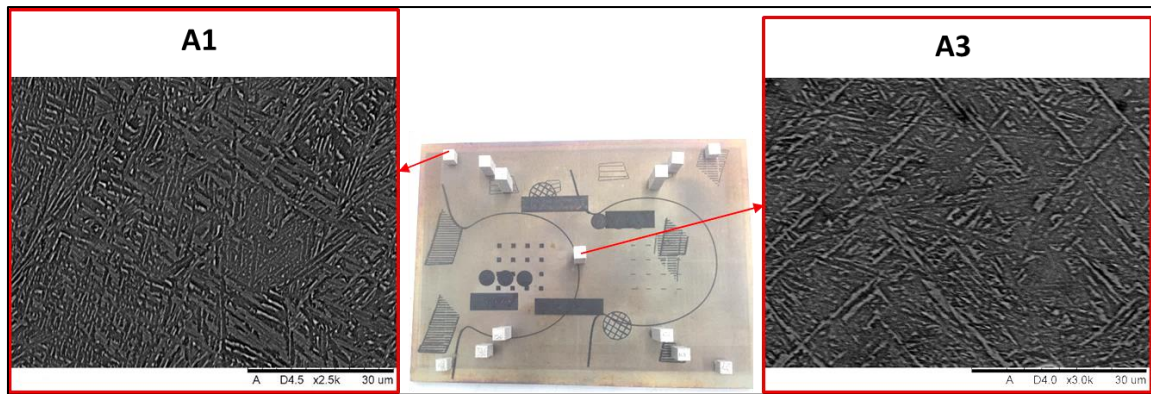


*Figure 4. 9:  $\alpha$  lath comparison between a sample built at the edge of the preheat region (A1) and a specimen built in the middle of the cake.*

#### 4.3.3 Contamination Issues

All cubes were built directly on the 316 SS starting plate without the addition of any support structures. Further analysis were conducted in the bottom area of the specimens; when contamination issues with the substrate were observed they were subjected to further investigation.

Figure 4. 10 (a) shows the bottom side of the A3 specimen. A tooth shape can be observed at the bottom of the image. It occurred when removing the cubes from the base material manually or with a plastic hammer support. Non-consolidated particles and porosity are visible in the first few hundred  $\mu\text{m}$  of the build, is probably due to the stabilisation of the microstructure. A very fine microstructure is noticeable in Figure 4. 10 (b), with cracks propagating from the bottom of the sample.

Concentration of other materials was noticed inside the specimen; Figure 4. 10 (c) displays low Iron concentration which is decreasing during the build layers. The pink/red colour mainly represented in the bottom side of the picture shows the amount of Iron contained inside the specimen.

Figure 4. 11 shows the contamination that has occurred from building on a 316L SS base plate, at the bottom of the specimen a high concentration of Iron (Fe 32.9 %) and Chromium (Cr 9.7 %) is observed. The concentration of these contaminating elements is observed to decrease from 0 to 80  $\mu\text{m}$  away from the base.

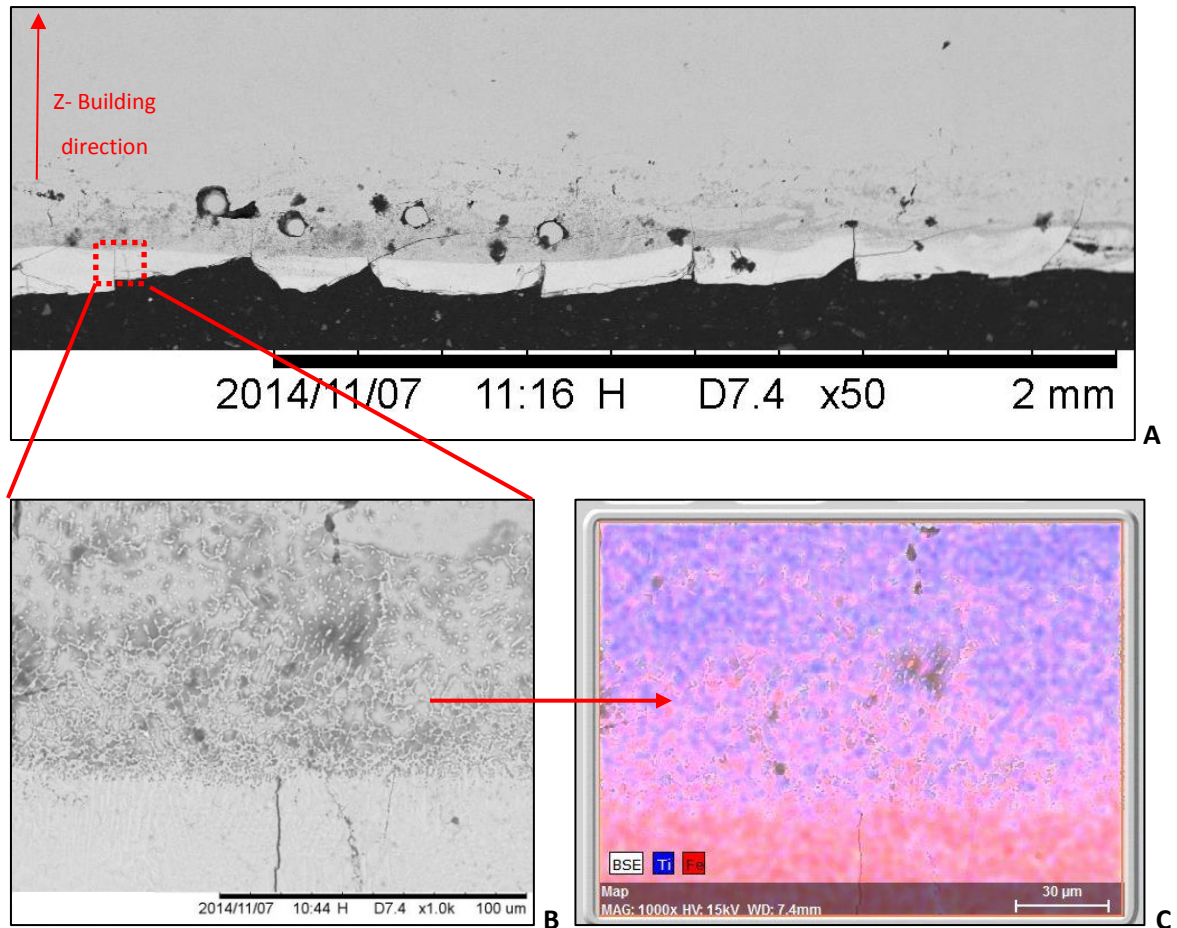


*Figure 4. 10: SEM and XRD analysis of contaminated area located at the bottom of specimen A3.*

The reason for the contamination could be the transferred material from the starting plate. In fact, the 316 SS used as a starting plate contains  $\alpha$  and  $\beta$  stabilisers (Chromium and Iron stabilise the  $\beta$  phase). For this reason, the contamination effects the precipitation in  $\alpha$  phases, thus changing the final microstructure composition and its properties into Fe - Ti intermetallics as showed in literature [63, 119]. The mentioned studies observed that the part interface returns to its original bulk properties after several layers (<500  $\mu\text{m}$ ) above the transition point, where the below layer with 316 SS element contamination is not reaching high T to transfer elements to the above layer.

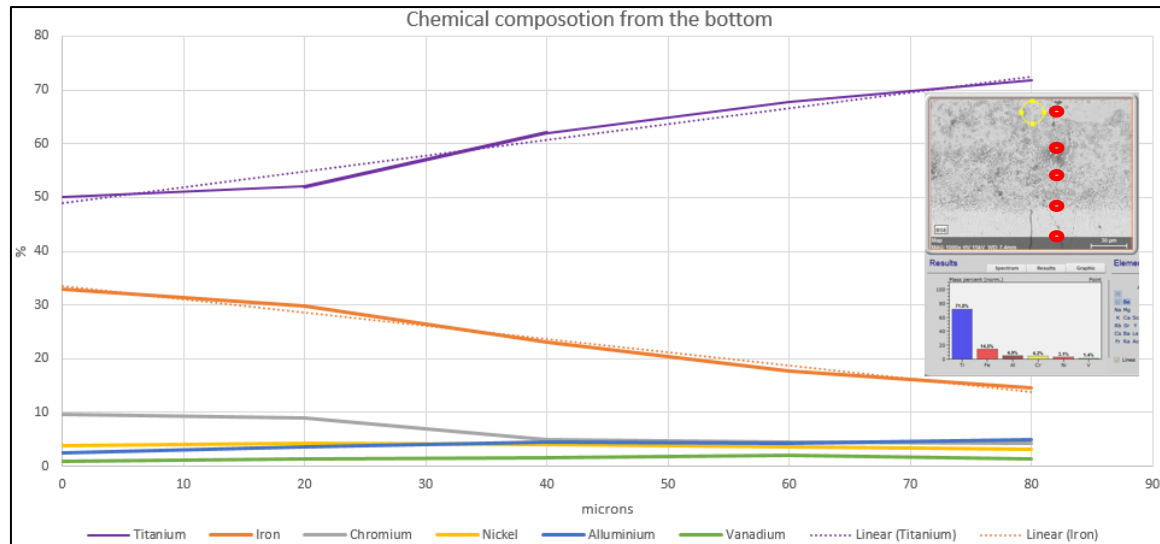


Figure 4. 11: Contamination amount from the bottom of the material up to 80  $\mu\text{m}$ .

Due to the above mentioned contamination and resulting formation of a brittle intermetallic structure at the bottom of the sample, the part can be removed from the substrate without considerable effort or the need for special removal tools. The transition microstructure between the starting plate and the AMed material can be easily broken if force is applied at the right position and angle.

#### 4.3.4 Micro-Hardness Properties

A study of the influence of preheating area on cube samples was carried out using a micro-hardness machine to detect the mechanical properties along the Z-axis. In addition, pre-analysis of grain size (see 4.3.2 paragraph) and different micro-hardness loads were investigated to ensure the validity of the data. Table 4. 3 compares different loads applied to the specimen, where HV results are similar for all conditions, with an average value around 332 HV. A reliable cross comparison of the samples was achieved; a load of 500 g was used to carry out all the mechanical tests in the study.

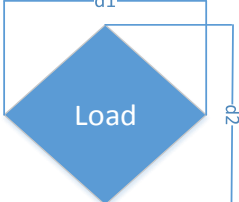
Results show different micro-hardness measurements for the 4 different samples (A1 - B1 - C1 - A3). Data were captured from 1 mm above the starting plate to 1 - 2 mm below the top of the specimen in Z direction (

Table 4. 4). During the first few hundred microns a higher hardness was observed for the materials; this is possibly due to the faster heat transfer to the starting plate and consequent refined  $\alpha$  laths or due to the more refined equiaxed prior  $\beta$  microstructure achieved in the bottom region, which end up improving the mechanical properties. The A1 specimen had a higher trend line (380 HV average) compared to the other samples which had a similar average hardness along the whole



build. All the hardness values tend to decrease with increased number of layers which is potentially connected to the increase in cake T, which is also referred to a reduced ability to conduct heat along the build with a consequence of slower cooling rates and larger alpha laths.

*Table 4. 3: Pre-setting of the micro-hardness system using different loads.*

Load	d1 (μm)	d2 (μm)	HV	
1Kg	76.13	73.8	330	
500g	54.76	51.76	327	
300g	42.41	39.07	335	
200g	34.06	32.39	336	
100g	23.37	23.37	339	

*Table 4. 4: Micro-hardness average calculated from the bottom to the top side of four different specimens.*

	A1	B1	C1	A3
<b>HV average</b>	380.6	345.7	351.5	345.3

As shown in Figure 4. 2, the A1 cube is located at the edge of the plate during the build and consequentially subjected to a faster cooling rate due to the smaller dimension of the Z height which helped to distribute a large part of the heat captured at the starting plate (250 x 200 mm of preheating area). It was also processed for shortest time compared to the other preheating areas; this allowed the A1 part to cool down quicker than the other samples. By increasing the amount of cooling it is possible to generate finer  $\alpha$  grains which can improve the hardness inside the melted material. Hrabe and Quinn [129] noticed the same phenomena of build location influence, showing a correlation between mechanical properties and part location; the cooling rate at different position inside the chamber can influence the characteristics of the specimens.

Figure 4. 12 presents all the values captured and compared during the micro-hardness tests. The other cubes analysed had very similar hardnesses, meaning that the preheating at 176 x 176 mm and 144 x 144 mm have a similar cooling rates, and therefore do not have significantly different microstructures. This is also due to the higher build in the core region which remains at a higher T with a consequent reduction in cooling time and consequent reduction in hardness properties.

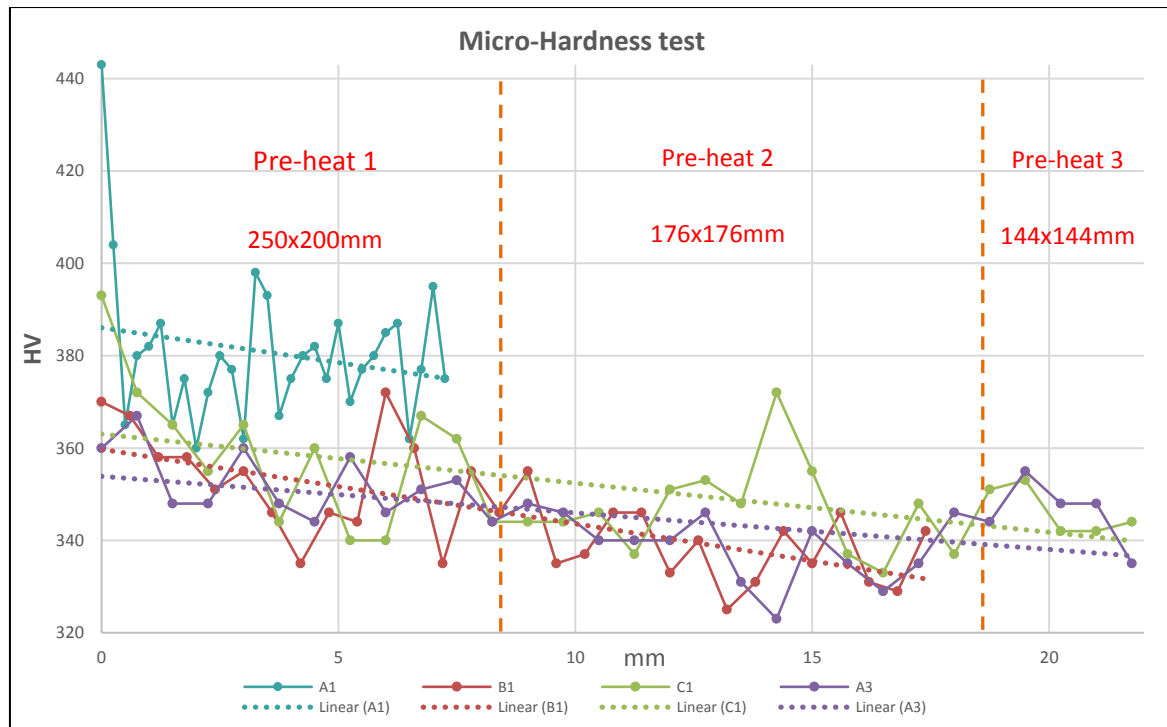


Figure 4. 12: Micro-hardness graph which captures the trend line of each specimen analysed.

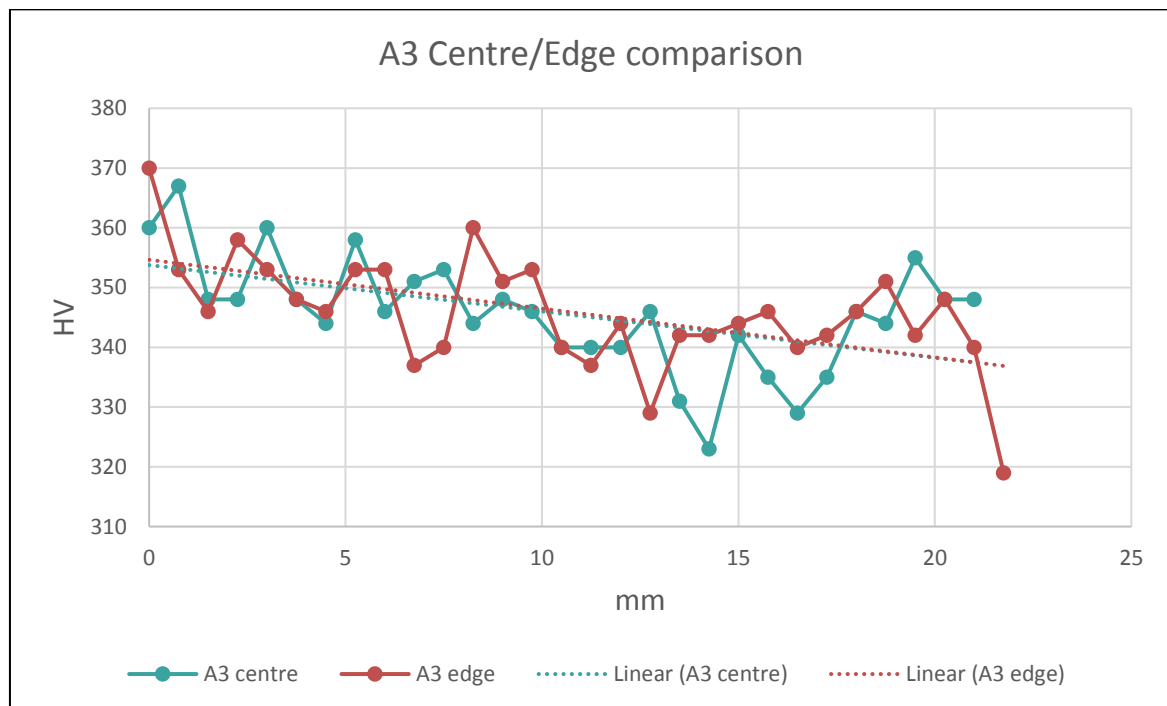


Figure 4. 13: A3 core and edge micro-hardness comparison graph.

Further hardness investigations were undertaken in order to analyse potential differences between the core and the edge of the specimen (1 mm inside the specimen). Figure 4. 13 illustrates a similar linear trend between the centre and the edge of the A3 sample; no relevant data were

detected during tests and post analysis. It can be assumed that core and edge of the specimen have similar micro-hardness behaviour as noticed from literature [129, 62].

#### 4.4 Conclusion

The present study represents the preliminary revision of a preheating inspection area related to Ti - 6Al - 4V alloy using an E-PBF system. The investigation includes metallurgical characterisation of the powder used and the cubes manufactured. Material composition and micro-hardness tests were also performed to capture differences between the samples.

- Linear columnar grains were growing regularly along the Z direction of the build. An average size of the grains in the middle of the specimens were estimated to be  $\sim 140\text{ }\mu\text{m}$ , as previously observed in literature [193, 194], with no significant differences between specimens being noticed. Smaller  $\alpha$  lath were noticed in the component located at the edge of the preheated area, which is probably due to the heat conduction to the substrate and to the non-preheated powder beside the cube, with consequent faster cooling of the component.
- The reduction in  $\alpha$  width can explain the high micro-hardness value achieved in the bottom region of the cubes manufactured in the corners of the 250 x 200 mm preheated area. Conversely the centrally located specimens have a lower hardness compared to the parts located to the side, which can be connected to the relationship between cooling time and T [100, 68]. A similar micro-hardness is noticed on the centre and side region of the specimens, which can be related to an even cooling time of the part. From the bottom to the top of the cubes a minimal decrease in hardness was noticed; the difference is potentially connected to the increase of the cake T during the manufacture layer upon layer [26].
- Contamination issues were observed at the bonding area between starting plate and the first few layers of building. It was mainly due to the  $\beta$  stabilisers materials contained inside the 316 SS plate which get transferred along the Z direction during the melting phase as also noticed by Mohammad et al. [119]. This brittle Fe and Cr intermetallic structure in the first few hundred microns allow the part to be snapped easily from the starting plate, but critically reducing the mechanical properties. The contaminated area can be critical for crack initiation and mechanical behaviour; as such it is suggested that it is machined away in order to improve the surface properties.

## **Chapter 5: Development and Analysis of the Pre-Sintering, Solidification, and Build Integrity of an Adaptronic Chamber**

### **5.1 Introduction**

Investigation on hardware and part properties manufactured with an A2XX E-PBF system were explored in the previous chapter. Mechanical properties, build behaviour, and hardware configuration analysed previously gave a full understanding of the whole machine behaviour achieved using both standard settings and hardware.

As introduced in chapter 2.6, modifying the original machinery hardware can have benefits during the manufacturing of parts. Customising the process can have the advantage of reducing manufacturing time, however it can also generate issues in configuring the new solution and set it up that has high efficiency and repeatability.

As referred to in the original AMAZE proposal: “An innovative adjustable 3D adaptronic build chamber design will be tested (this requires minimal hardware changes) which should not only increase the build speed but also reduce the quantity of support powder needed”. This build chamber has been manufactured with the intention of reducing the time of manufacturing and to generate benefits in a production environment.

In this chapter, a reduce kit, called adaptronic chamber, was tested in order to reduce the envelope size of the Arcam A2XX E-PBF system. Complete redesign of the hardware and manipulation of the software were necessary in order to develop the new reduced configuration. An investigation of heating effect was performed to understand the impact of the adaptronic chamber and the microstructure / mechanical behaviour of the parts. Post  $\mu$  - CT analysis and tensile specimens were investigated.

Direct comparison with the standard chamber was conducted in order to better understand the potential improvements having a reduced/customized kit. A cost calculation was generated to estimate the cost benefits achieved with the new hardware solution. The aim of this chapter was summarised in Figure 5.1 with the following main points:

1. Demonstrate the use of small build envelope in a bigger machine to save material usage during AM;
2. Gain an understanding of the key parameters necessary for optimising build rate without compromising material integrity;

3. Demonstrate the benefits of AM productivity through the use of small build chambers and hoppers.

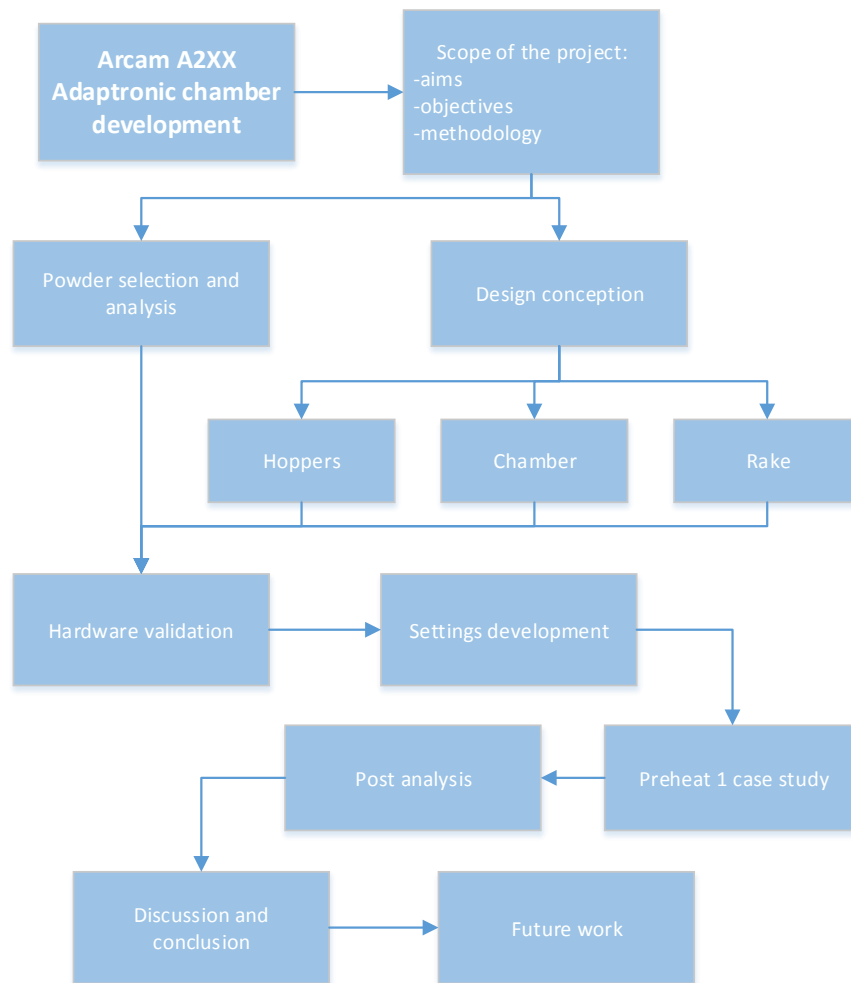


Figure 5. 1: Project development diagram.

## 5.2 Experimental Procedure

### 5.2.1 Machine

This experiment describes the development and demonstration of a reduce chamber, referred to as an ‘adaptronic build chamber’, manufactured at MTC for an E-PBF A2XX machine. The main objective of this work was preliminary focused on demonstrating AM process capability for decreasing/optimising the building envelope of the current systems and for reducing the minimum amount of powder necessary for a standard build which is currently 100 Kg. As a result, cost and time of manufacturing were monitored during the evaluation of the process.

The standard E-PBF A2XX system at the MTC has a physical build envelope size of 420 Ø X 380 mm, with two hoppers requiring 200 Kg's for a full build envelope, as shown in Figure 5. 2. However, the current A2XX machine electron gun design has a maximum beam envelope set to 350 Ø x 380 mm, and it requires a starting plate with a size of 300 mm x 220 mm for a conventional build.

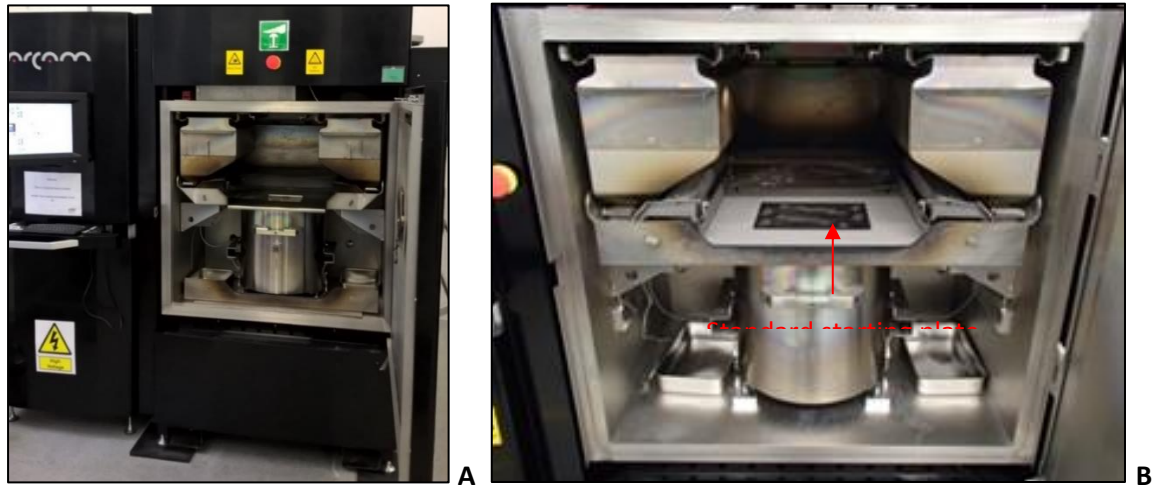


*Figure 5. 2: Arcam A2XX (a), and its standard starting plate (b).*

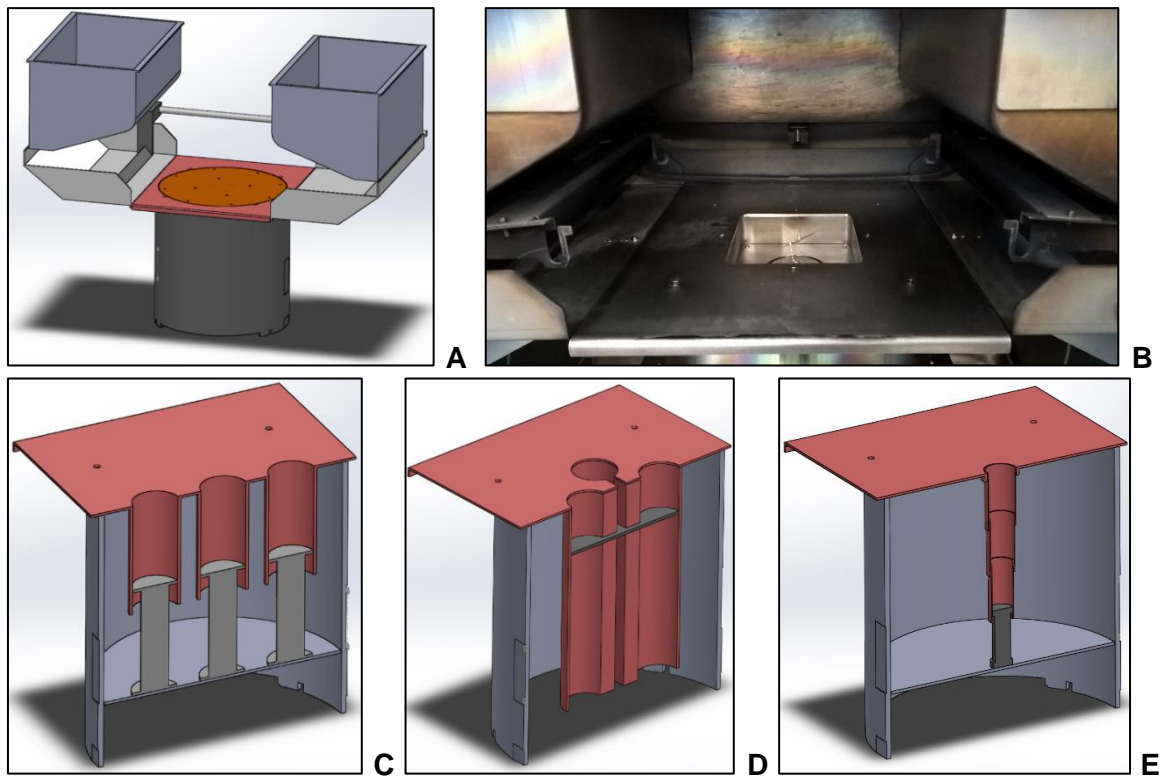
The Arcam A2XX platform does not have a reduced kit option from the manufacturer (neither a reduce chamber or a hopper). The study and the manufacture of the adaptronic chamber has been completely developed from scratch at the MTC through the support of engineers with different technical backgrounds.

Figure 5. 1 shows the approach used to develop the entire project through a flow diagram where sequential tasks were adopted to manufacture and process the new chamber. Scoping the project allowed a better understanding of the directions to take during the development of the system and a consequent case study to test it. Afterwards, the new hardware were mounted and tested before proceeding with a preheat case study. Post analysis was undertaken to capture the potential benefits of the process examined and future developments to be achieved.

### **5.2.2 Design Conceptions**

The first action was focused on manually measuring the current system and reproducing it in 3D shape using SolidWorks. Figure 5. 3 (a) shows the original chamber and hoppers. Afterwards an evaluation of the future design was considered to reduce the build envelope; the final square 190 x 190 mm design is showed in Figure 5. 3 (b). Before defining the final geometry, Figure 5. 3 (c - d and e) show different design strategies thought in first place where (reduced cylindrical shapes) that were analysed for the manufacture. Figure 5. 3 (c) and (e) show an alternative use of the piston

which moves the table up and down (Z axis), where (c) relies on the use of the original table to move the cylinders. Option (d) is focused on using the Z axis piston to move the custom made plate. Considering this, the mentioned (c - d) options had a limitation in Z length due to the depth of the chamber, option (e) represented a telescopic chamber which had the advantage of allowing the table to come closer to the starting sheet which allowed for an increase in the manufacturing height.



*Figure 5. 3: Original A2XX 3D hardware (a), manufactured chamber (b) new chamber design options (c - d - e).*

### 5.2.3 Hardware

A first generation 120 x 120 mm square chamber was manufactured and tested. Due to E-PBF software algorithm constraint, that was limiting the preheating area to 140 X 140 mm of E-PBF envelope, modification of the settings and difficulties of controlling the heat balance generated in the reduce chamber, MTC decided to manufacture a bigger chamber which had the same dimensions as the standard A1 Arcam system with an area of 190 x 190 mm (Figure 5. 4 (b)). The new build envelope was designed with consideration of easy manufacturing, assembly and cost savings. By manufacturing this envelope, it was possible to use the standard settings of the Arcam A1 system as a reference for starting the development of the new adaptronic chamber set of parameters.

In addition to the reduced chamber redesign, other hardware parts were considered for modification, such as the hoppers, the rake and the hopper sheet aperture. Figure 5. 4 is shows all the changes done to the hardware - where the hoppers (Figure 5. 4 (b)) were modified to reduce the volume of powder in order to deliver it to the central region of the rake. To achieve this, two metal sheets were displaced and fixed inside the hopper which allowed the powder to be seated in the centre. The modification allowed a decrease in maximum powder volume from 100 Kg to 40 Kg up to the top of the hopper. The powder was then forced into the central region of the building envelope through a reduced powder outlet (Figure 5. 4 (c)) seated at the bottom of the hopper, preventing the excessive spreading—observed with the standard hopper aperture. After constraining the powder to the mid region of the system, the standard rake (Figure 5. 4 (d)) was modified by removing the blades on the sides, maintaining just the 220 mm in the centre in order to spread the powder over the chamber.

The parts were successfully manufactured and no issues were noticed during the assembly into the A2XX system. After mounting the new hardware, all the components where successfully tested in an open system mode where was possible to verify the efficiency of the new components.

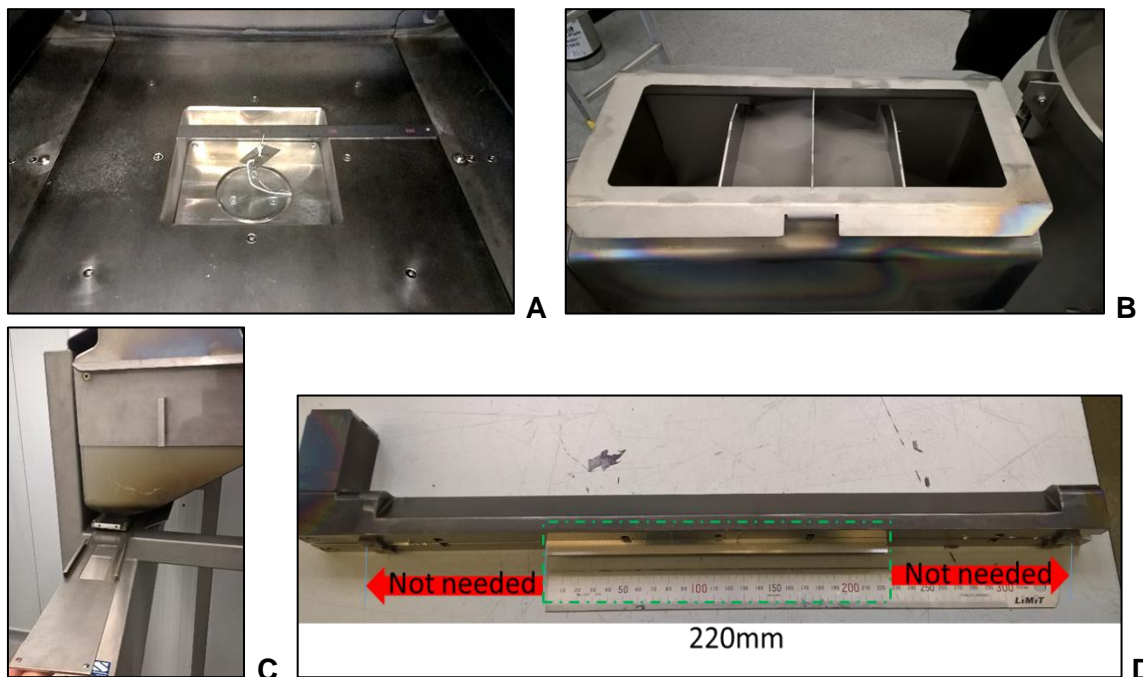


*Figure 5. 4: New adaptonic chamber 190 x 190 mm (a), reduced powder hopper sheets (b), reduced powder outlet opening (c), rack teeth reduction to 220 mm (d).*



### 5.2.4 Parameters Development

After completing the manufacture of the hardware, a software investigation was conducted to better understand the influence of the new chamber geometry and the consequent impact on time, cost, and microstructural development. Having a smaller chamber can change the heat dissipation and / or irradiation of the powder when it is heated up and during the cooling phase which can have an impact on the microstructural behaviour of the material used, cooling time, and preheating time.

The preheating stage in E-PBF is used to sinter the powder spread upon each layer reaching a defined T before the final stage of melting; for this reason new volumetric and heat transferred studies were necessary to validate the reduced kit.

### 5.2.5 Powder Analysis

Briefly described in chapter 3.5, GA powder (Figure 5. 5) shows mostly spherical powder populated with broken, agglomerated, elongated, and satellite particles. At higher magnification it can be seen that the surface of the spherical particles were uneven. Heavy satellite and hollow particles were also observed, as were internal gas pore.

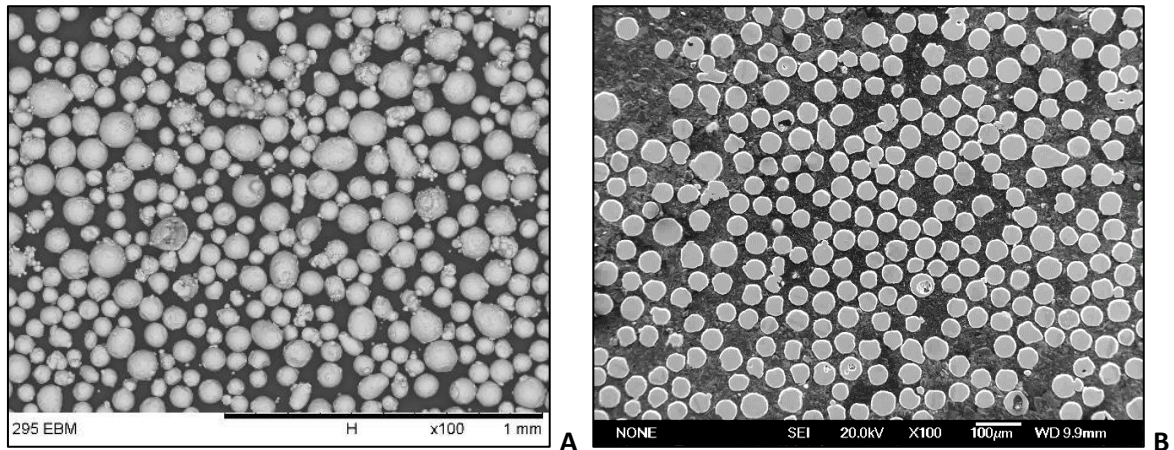


*Figure 5. 5: Gas atomised powder from TLS, surface (a) and section (b) characteristics.*

Full analysis of the powder was completed during the AMAZE project. Main characterisations were conducted in order to accept/reject the material based on standard specifications. Hall flow and apparent density results were compared to the ASTM B212 - 12 [195] with the value of <25 sec and >2.56 g / cm<sup>3</sup> respectively. As observed in Figure 5. 6, GA powder satisfied the hall flow minimum requirement, noticing that the analysed powder has low flow-ability probably due to the non-perfectly spherical particles and its satellites. GA powder showed a poor apparent density score of

2.43 g / cm<sup>3</sup> which is probably due to the irregular morphology of the powder (Figure 5. 5 (a)). The particle size analysed, as showed in Figure 5. 6, represent the powder distribution curve and particle percentage of the GA powder used in the experiments. The complete analysis of the powder can be found elsewhere [196].

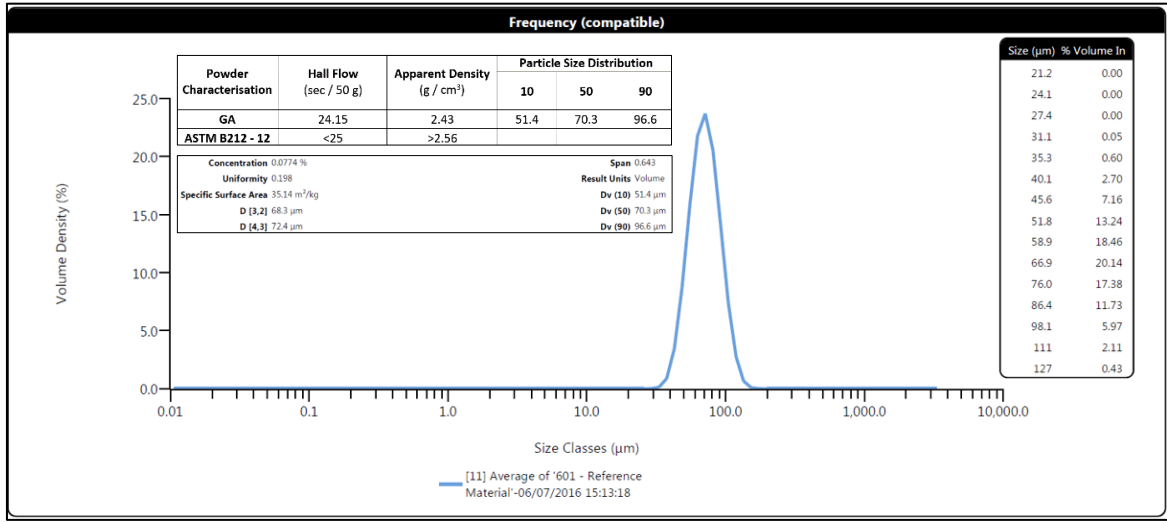


Figure 5. 6: Hall flow, apparent density, and PSD curve analysis of GA powder supplied by TLS.

Figure 5. 7 presents an estimated analysis of 5 g of randomly selected recycled GA powder particles. A high percentage of agglomerated spherical particles were noticed, probably due the pre-sintering phase occurring in E-PBF. Due its vibration and particle size filters, sieving can help to reduce the amount of elongated particles and to detach the agglomerated particles during the process.

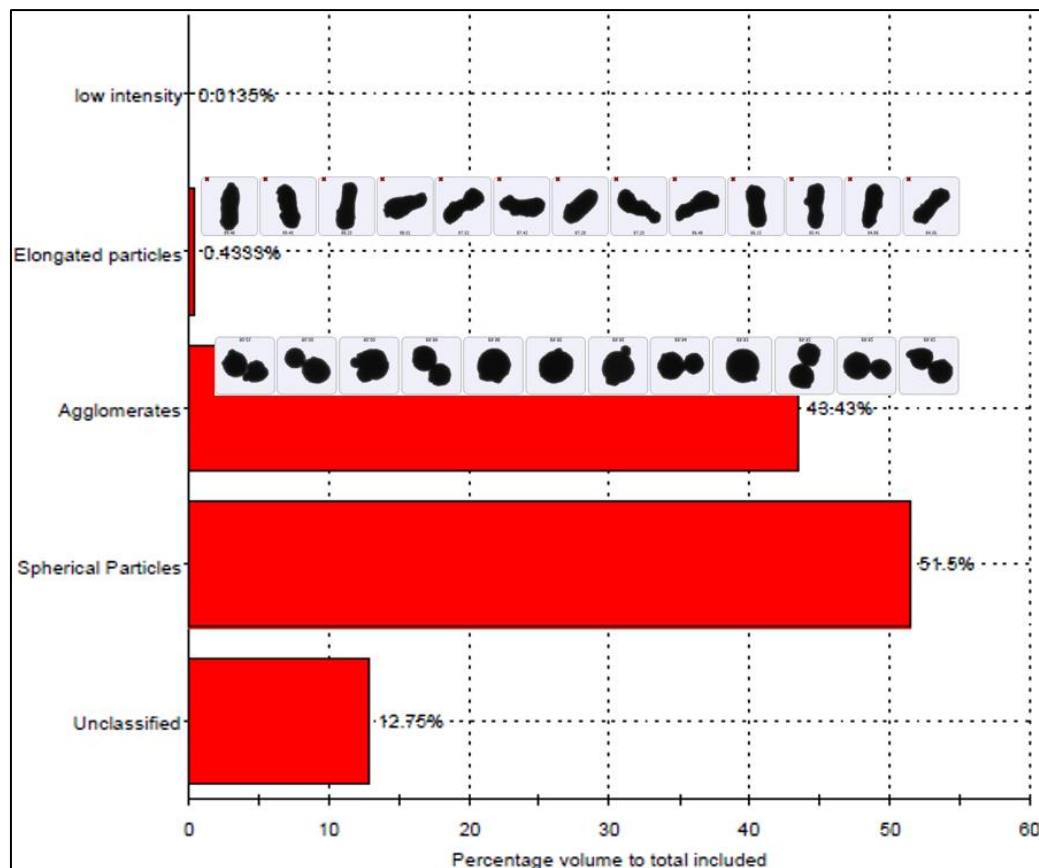
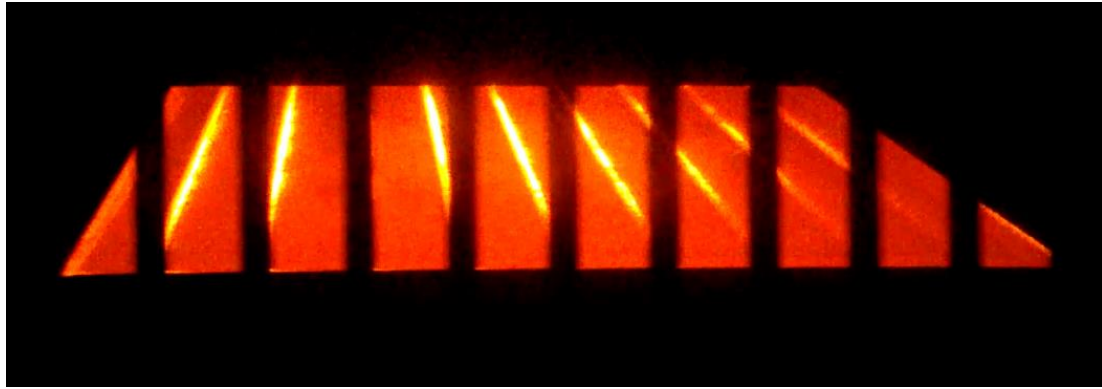


Figure 5. 7: GA powder morphology analysis captured using a Malvern G3 Morphology system.

### 5.2.6 Preheat 1 influence - Case Study

An investigation was performed to understand the impact of preheat 1 on the parts manufactured and the behaviour of the adaptronic chamber. Unlike, other PBF such as laser processes do not require powder sintering prior to the selective melting phase. The sintering process in E-PBF systems is controlled by preheating, or by slightly heating up/charging the powder particles that are spread on the top of each layer using electron waves with lower energy density compared to the melting phase. The waves are randomly distributed along the surface as shown in Figure 5. 8, that cover the same building area numerous times before reaching a defined sintering T of  $\sim 720^{\circ}\text{C}$  for Ti - 6Al - 4V. As shown in Figure 2. 2, several sec are taken to preheat each layer which has a significant impact on build time.

A case study was developed to better understand the effect of preheat 1, and its pre-sintering influence, during a build. The preheat 1 consists of repeated waves of defocused electrons used to sinter the new layer of powder that is spread on the surface before melting; it avoids the powder from being repelled and causing a powder charge, usually referred to as 'smoke', during the melting stage.



*Figure 5. 8: preheat 1 lines observed during the process.*

The current A2XX preheat settings are shown in Table 5. 1. The simple modification of the number of preheat 1 repeats occurring during the sintering of the powder particles was considered. The standard preheat 1 value of four repeats was taken as a reference and two values above and below of this standard setting was used to perform the tests (2 and 8 repeats).

*Table 5. 1: Preheat 1 main settings.*

	Line order	Line Offset (mm)	Number of repeats	Beam current (mA)
<b>Preheat 1</b>	15	1.2	4	30

In addition to preheat 1 investigation, an overall reduction in manufacturing time was targeted. In order to achieve this, a number of raking tests were performed to understand if it was possible to rake just 2 times instead of the standard 3 moves. Following off-line tests, it was possible to observe that it was achievable, although there were uncertainties about it being a complete success. The powder fetching sensors were then modified in order to capture the powder just from one side due to the rake returning to the same position. Just one hopper was fed with powder.

### 5.2.7 Experiment Set-Up

A set of 3 builds were made, where all the settings (preheat 2, contour, hatching) were kept the same, excluding the preheating 1 repeats that were modified as showed in Table 5. 2.

Every build was designed with 4 tensile bars, 4 rectangular bars, and 6 cylinders in order to conduct mechanical, metallurgical, and inspection post analysis. Figure 5. 9 shows powder spread along the starting plate and a completed build that has come out from the adaptronic chamber. All the hardware parts designed for the adaptronic chamber (new chamber, reduced hopper, and

modified rake) were used for the experiments. GA powder mentioned above and standard pre and post turn around process were used to manufacture all builds.

*Table 5. 2: Preheat conditions used for the trials.*

	Number of Repeats
Low preheat	2
Standard preheat	4
High preheat	8

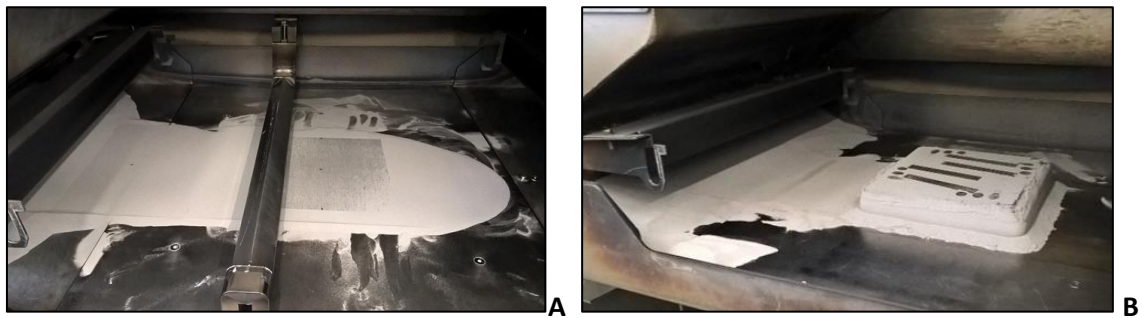


*Figure 5. 9: Reduced length powder spreading (A), new 190 x 190 mm adaptronic chamber cake (B).*

## 5.3 Results and Discussions

### 5.3.1 Microstructural Investigation

After completing 3 builds using different preheat 1 conditions, the parts were conventionally cleaned from remaining powder through a PRS and supports in order to be ready for post analysis investigation.



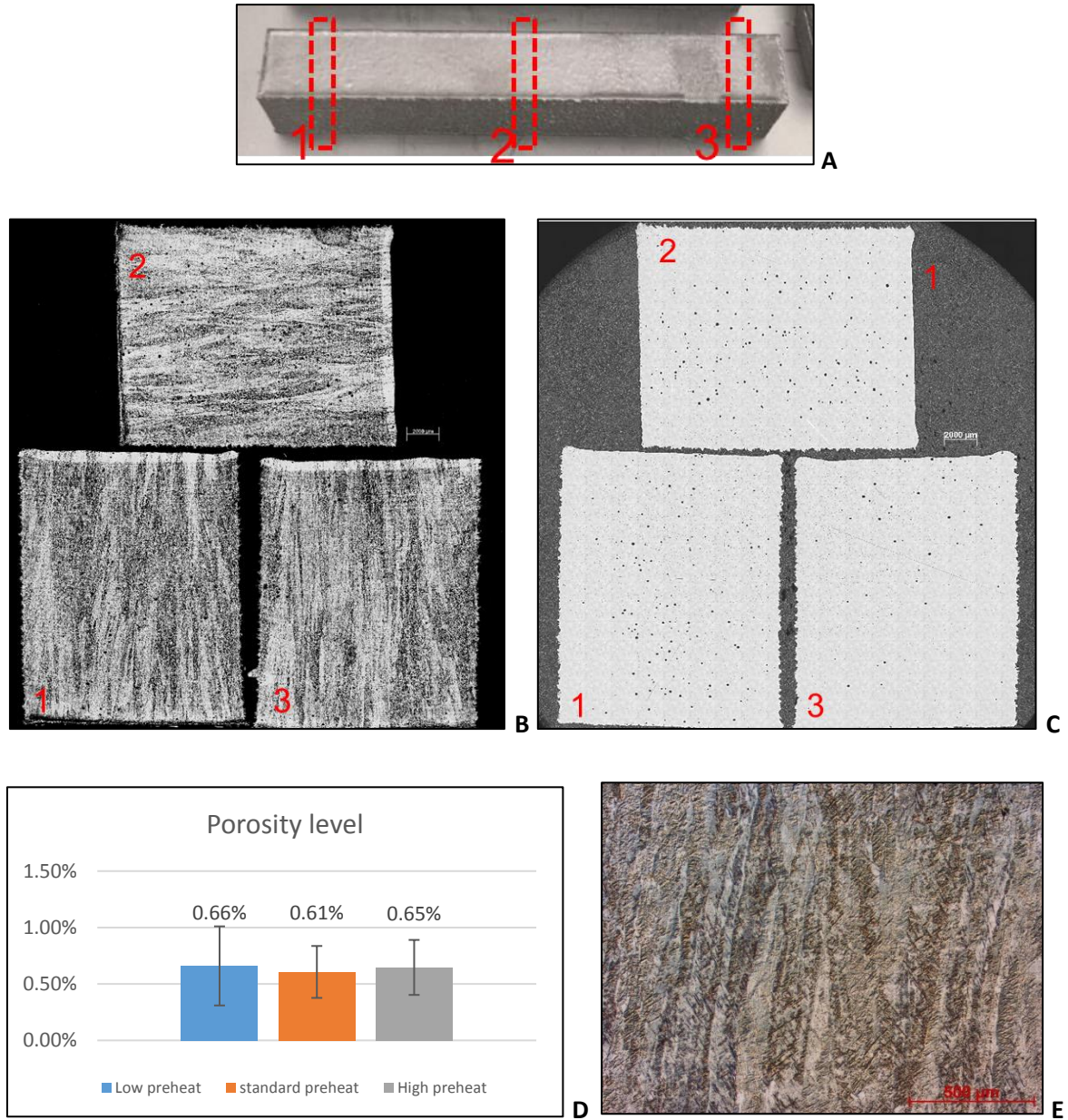
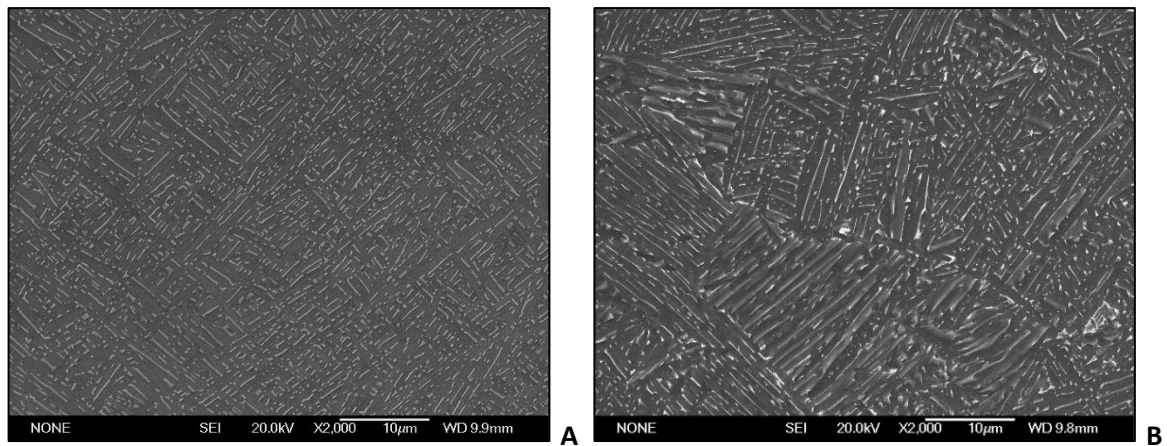


Figure 5. 10: Cylinders manufactured during the adaptronic chamber build (a), "low preheat" samples cut and Kroll's etched (b), "standard preheat" porosity sections (c), porosity comparison average between preheat conditions d), columnar main  $\beta$ -grains observed along the build direction in the standard preheat sample under polarised OM (e).

As shown in Figure 5. 10 (a), one rectangular bar for each condition were sectioned and polished in 3 different locations and then analysed in order to perform post metallurgical analysis. Standard preheat shows the lowest level of porosity of 0.61 % compared to the other preheat conditions which are very similar with a percentage  $<0.66$  % as shown in Figure 5. 5 (d). Entrapped spherical pores (c) were found as a result of the gas atomisation process, which are mainly located in the

central region of the polished parts. A post HIPping treatment should help to reduce the amount of gas pores due the combined heat and high pressure released during the process.

Columnar prior  $\beta$ -grains were noticed in the building direction. Generally, it is possible to observe that all items manufactured in each preheat condition showed the usual E-PBF microstructural formation noticed under the OM, no cracks or lack of fusion were seen.



*Figure 5. 11: Z - X SEM low preheated section (a), X - Y section of a high preheat part (b).*

SEM analysis presented in Figure 5. 11 shows the typical colony and basket wave-Widmanstätten microstructure achieved during the E-PBF process where a coarse columnar prior  $\beta$ -grain structure developed layer by layer following the Z direction of growth. The phenomena occurred during the partial re-melting of the previous layer which helps the solidification and consequent formation of the prior- $\beta$  grains following the Z direction of growth during the cooling. The fine  $\alpha$  grains developed in  $\beta$  occurred during the cooling transition, which classified the material as  $\alpha + \beta$  alloy. The constant preheating T of  $\sim 720$  °C maintained during each layer significantly reduced the residual stresses normally generated during cooling, thus avoiding important traces of martensite.

### **5.3.2 Material Analysis**

Additional investigation was performed to understand the material composition after being processed with the A2XX system in order to capture potential weakness occurred as material evaporation (mainly for Al), inclusion or impurities.

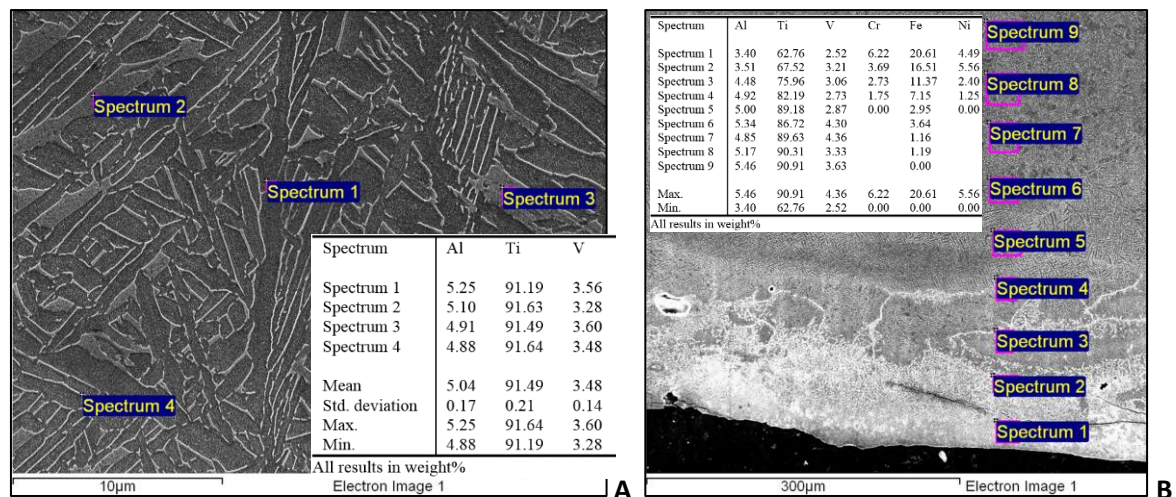


Figure 5. 12: EDX analysis of a standard manufactured samples with related spectrum elements.

Several random areas were analysed using all the conditions performed during the experiment. All the data captured should meet the ASTM 2924 - 14 Ti - 6Al - 4V standard [106] which describe a minimum Al and V content of >5.5 and >3.5 % respectively. As showed in Figure 5. 12 (a), different areas were casually selected for material properties investigation, where selected areas and point were distributed between prior  $\beta$ -grain,  $\alpha$  and  $\beta$  phases. The table integrated in the picture resume a tendency noted during the investigation, where a well below the Al limit weight percentage was noticed in the samples analysed. Further investigation using more accurate material analysis system with a direct comparison with the supplier properties should be done in order to understand the exact Al content value and its potential impact in mechanical properties. The vanadium weight noticed during the EDX analysis were oscillating to the minimum percentage of V requested from the standards. Further investigation should be done to the powder used for the builds, especially if considered for the manufacturing of a part to be used.

As showed and explained in the previous chapter and from literature [119] [63], bottom region contamination from the starting plate were noticed in all specimens analysed using an EDX technique. Figure 5. 12 (b) shows an X - Z section of a low preheat specimens, where material composition analysis were captured from the bottom region up to <400  $\mu$ m. It was possible to notice a decreasing contamination from the bottom to the top of Cr, Fe, and Ni elements which were transferred from the re-melting of the previous layers starting from the substrate. Standard Ti - 6Al - 4V elements return stable after few hundred microns above the interstitial region between starting plate and parts.



### 5.3.3 Micro-Hardness Properties

Mechanical properties were measured using a micro-hardness system, where an average of 5 indents, performed at 500 g, were measured from 1 mm above the bottom surface with a distance of 3.25mm each vertical indent and a 2.5 mm equally distributed linear indent.

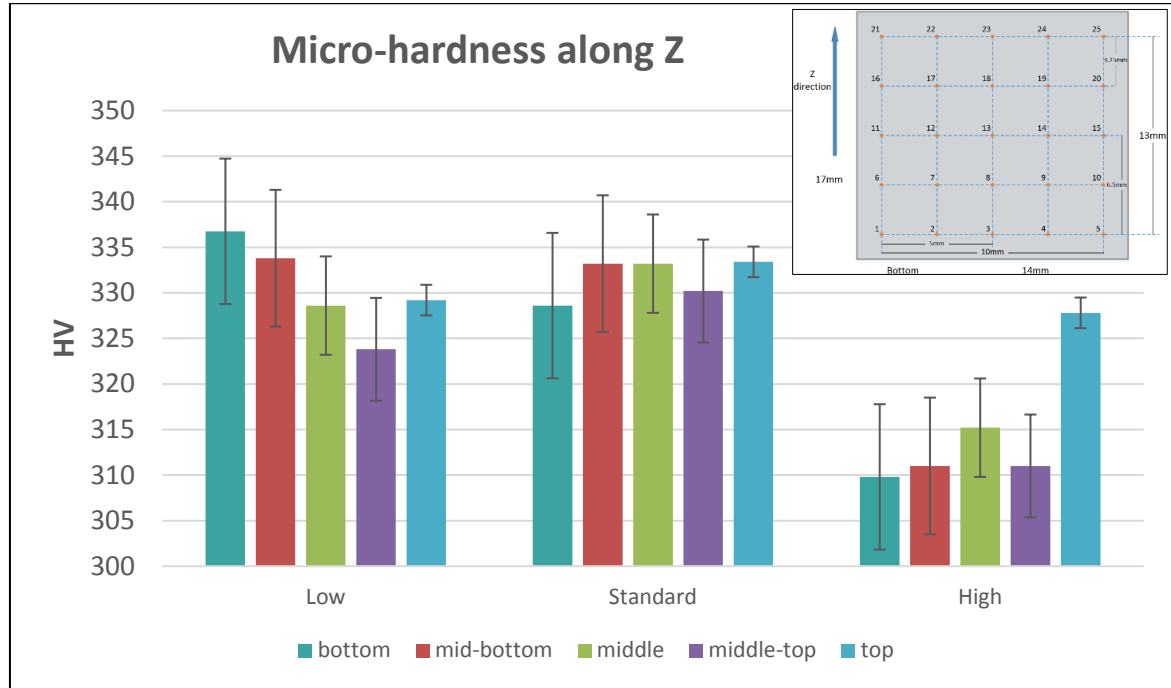


Figure 5. 13: Micro-hardness performed along X - Z direction.

Figure 5. 13 shows the average of 5 measurements taken from bottom to the top of the specimens, where all top measurements have a similar value of around 330 HV. The low preheated specimen has the highest hardness in the bottom region, probably due to the rapid cooling achieved after scanning the powder just two times and the consequent heat dissipation to the substrate; it decreases after the overall T of the cake rose up during the build, and consequently the cooling time increased, reducing the hardness. The standard preheat condition with 4 preheats has a stable hardness from the bottom to the top region. This is potentially due to the preheat balance achieved along the entire build. Having 8 preheats resulted in the lowest hardness level, which could be caused by the high T achieved during the preheating stage and the consequent low cooling rate, which helped to increase the  $\alpha$  lath length with a consequent drop in hardness.

The mechanical properties captured with low and standard settings shows similar values observed in literature [197, 198, 199] where different Arcam system were used. Literature shows that the mechanical properties can also be related to the Arcam model itself and its characteristics [200]. Higher micro-hardness properties were observed in Chapter 4, where the measurements captured

was around 350 HV. The slightly higher micro-hardness measured could be connected to the location of the indentations which were much closer to the substrate. In that region the cooling rate is faster due the heat propagation to the starting plate. The consequence of this was a higher cooling rate, reduction in  $\alpha$  growth, and increase in hardness.

#### 5.3.4 $\mu$ -CT Analysis of Pre-Sintered Powder

After scanning the necking region of the tensile bars, other  $\mu$ -CT scans were performed to analyse the powder density of the loose powder captured inside the 3 mm cylindrical can with a shell of 1 mm thick and height of 3 mm.  $\mu$ -CT setting are showed in Figure 3. 2. Low, standard, and high preheat conditions showed in Figure 5. 14 were scanned and reconstructed with a voxel size resolution of  $2.72 \times 2.72 \times 2.72 \mu\text{m}^3$  (more system details can be found in Table 3. 6 set 2). Low preheat (c) shows a vast empty space and few pores on the top of the specimen which is probably due to the lack of pre-sintering and supports on the top of un-melted powder; the particles that are hit by high velocity electrons tend to fly or move away before being melted. Having a high preheat (a) helps by increasing the pre-sintering level of the cake and consequentially improves the melting phase with reduction in pores and voids. The cans with high and standard preheat have a more homogenous shell. More consistent surface roughness is noticed with the low preheat sintering strategy.

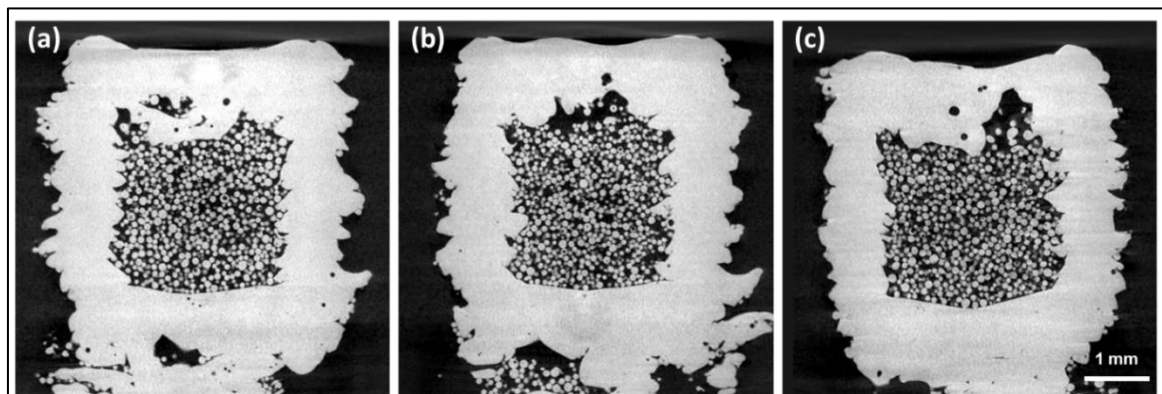


*Figure 5. 14: 2D slice of the reconstructed volume in Y - Z direction of cans made with high (a), standard (b), and low (c) preheating strategy.*

A 3 dimensional reconstruction was used to gain a general overview of the specimens. As shown in Figure 5. 15, several post processes analyses were performed to better understand the characteristics of the parts. Comparing the porosity located in the shells manufactured with different preheat repeats, a low percentage ( $\sim 0.13\%$ ) of gas / voids trapped inside the melted region were observed, which is considered minimal. The condition with lowest preheat repeats (2

scans) had the highest mean diameter which is potentially connected with the low preheat condition and a consequent lack of fusion during melting.

More analysis was conducted to investigate the packing density achieved with loose trapped powder inside the shells. A square 1.7 mm x 1.7 mm x 1.7 mm block was captured in the core region of the specimens where the pre-sintered powder sits. After refining the data shown in Figure 5. 16, a quantification showed that 46.1 % of packing density was achieved from the standard preheat condition, which was the highest of all conditions. High preheat settings have a similar packing density of 45.1 % and the low condition had the lowest percentage of 42 %. Similar data between high and standard condition were also observed in the average co-ordination number and average neck ratio. Slightly higher packing density was observed by Chen et al. [201] where a consistent porosity of around 50 % was noticed.

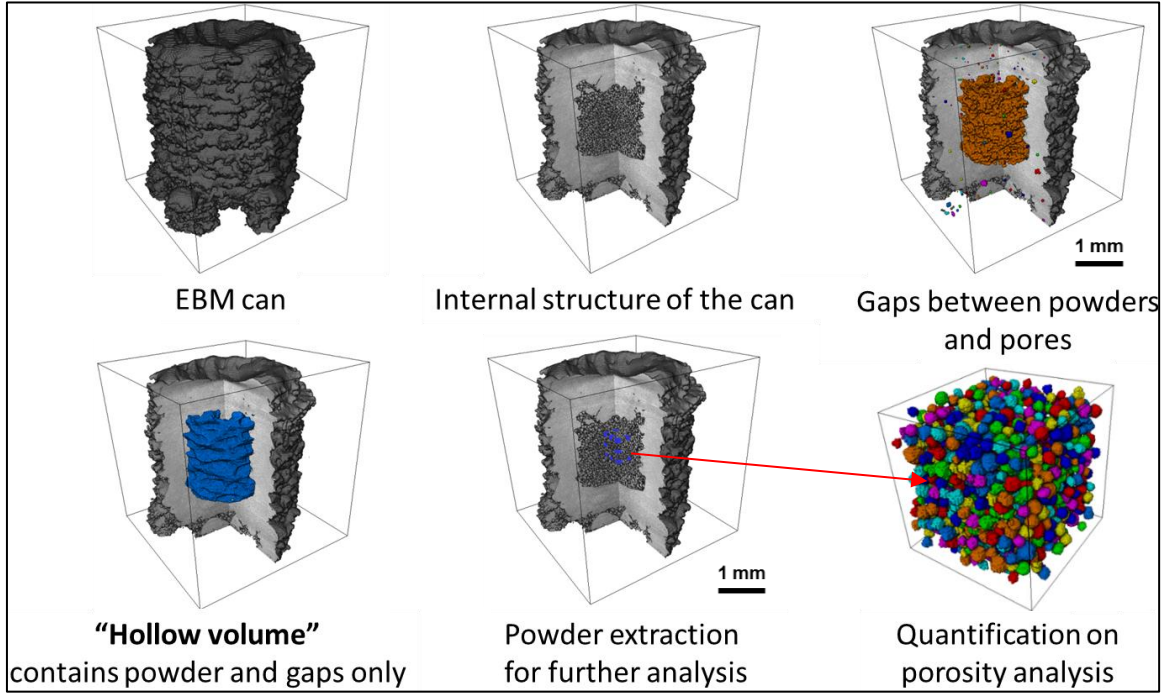


Figure 5. 15: Pore and pack density quantification

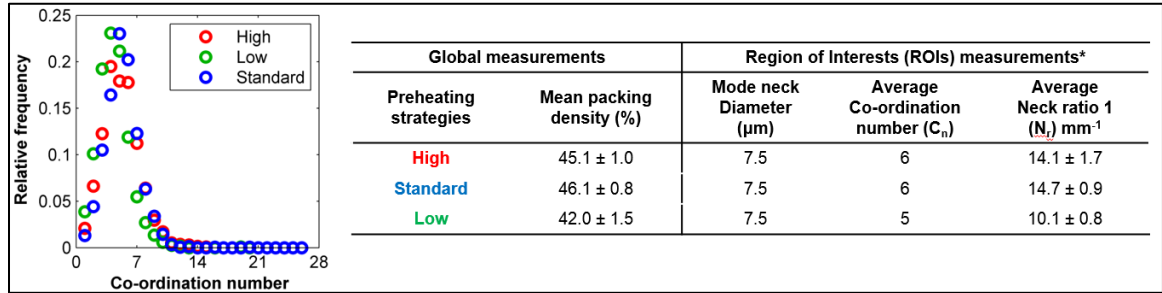


Figure 5. 16: Quantitative analysis of packing density and its variables captured in each condition.

A comparison to the original CAD file was performed using the average of 4 cylinders for each condition in order to capture the superficial tolerances achieved during the build, as shown in Figure 5. 17. Pre-sintered powder was surrounding the high preheat cylinder which helped to generate an oversize dimension. Due to the exceeded heat distribution, similar behaviour was noticed for the standard preheated parts, with slightly improved surface roughness and parts close to the nominal geometry. The low preheat condition had the smoother surface with low deviation errors. However, the lack of preheating resulted in having a smaller dimension than the expected geometry.

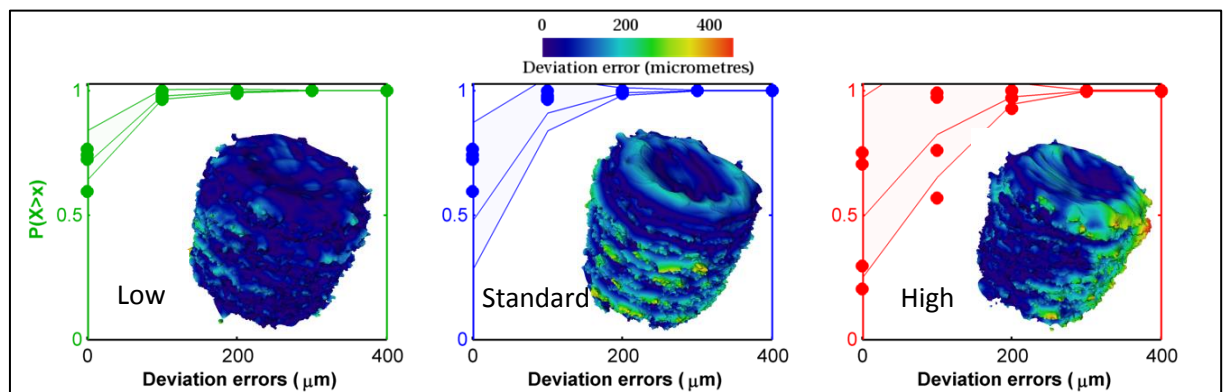
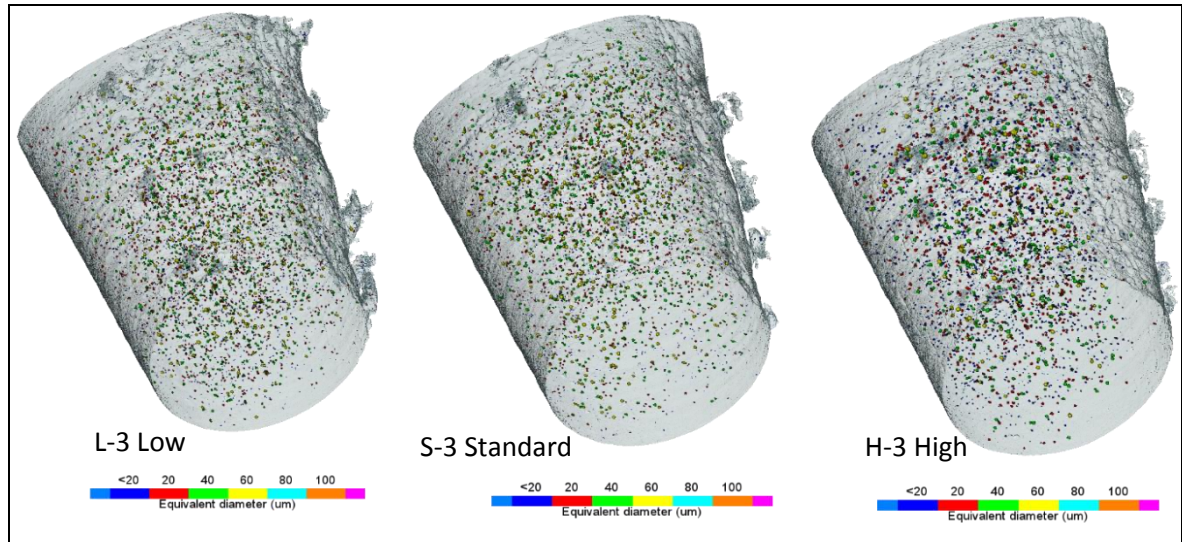


Figure 5. 17: Comparison between the physical parts and CAD file.

### 5.3.5 $\mu$ -CT Investigation of Tensile Bars

An extra  $\mu$ -CT investigation was carried out in the gauge region of the specimens. Scans were performed on each of the four tensile bars generated per condition, and reconstructed with a voxel size resolution of  $6.9 \times 6.9 \times 6.9 \mu\text{m}^3$  (more system details can be found in Table 3. 6 set 3). Figure 5. 18 shows the gauge region scan of samples L - 3, S - 3, and H - 3 which was captured as build; before the parts were machined for tensile performance. It is possible to notice that near the surface region there is a limited numbers of pores compared to the core of the specimens. The  $6.9 \mu\text{m}^3$  voxel size resolution does not allow to capture visual details of the parts.



*Figure 5. 18: Prospective images of randomly selected tensile bars analysed by  $\mu$ -CT for porosity investigation.*

All the numbers captured were post-processed as showed Figure 5. 19, where they were considered from above the value of  $\sim 21 \mu\text{m}$  due the resolution of the scan. It is necessary to remember that the porosity capture is in diameters and not in volume which means that it does not allow to capture elongated shapes and consequent volume of them. The frequency plot (a) shows the total number of pores identified from samples produced by different preheat conditions. The low preheat samples exhibited the largest number of pores compared to other samples. The pore fraction plot (b) show that all samples (under low, standard and high preheat conditions) exhibited a similar pore volume distribution having a mode pore equivalent diameter of  $100 \mu\text{m}$ . However, the standard and high preheat samples exhibit a few large pores ( $> 150 \mu\text{m}$ ), *e.g.* the high preheat samples show a maximum pore diameter of  $270 \mu\text{m}$ . This observation suggests that an increase in the number of scan repetitions allow pores to grow via Ostwald ripening, *i.e.* there is a reduction in the pore frequency. This hypothesis is supported by Figure 5. 19 (c) where the position of the curve indicates that low preheat samples have the highest cumulative pore fraction at small pore equivalent diameter compared to other samples.



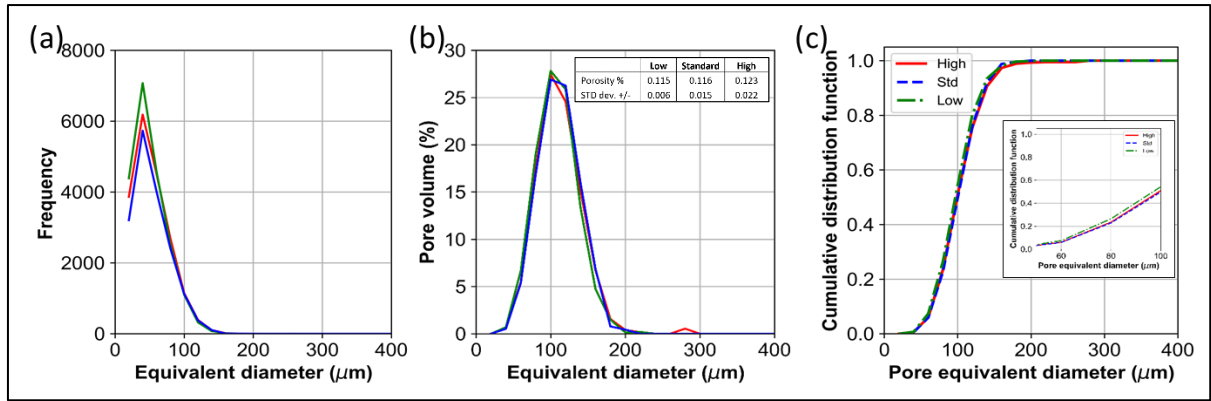


Figure 5. 19: Pores analysis performed by  $\mu$ -CT of the 3 pre-heat conditions investigated.

### 5.3.6 Mechanical Properties

Tensile bars were performed to understand the preheat differences for each condition. As shown in Figure 5. 20 (a), four mechanical tests for each condition, using ASTM E8 standards (see Figure 3. 4 Set 1 for further details), were manufactured during the build. As observed in Figure 5. 20 (b), all the fracture surface occurred around the middle region of the necking area with visible plastic elongation and a ductile fracture. Before describing the mechanical results, it is important to acknowledge that the mechanical conditions vary depending on the machine type used as described in literature [200].

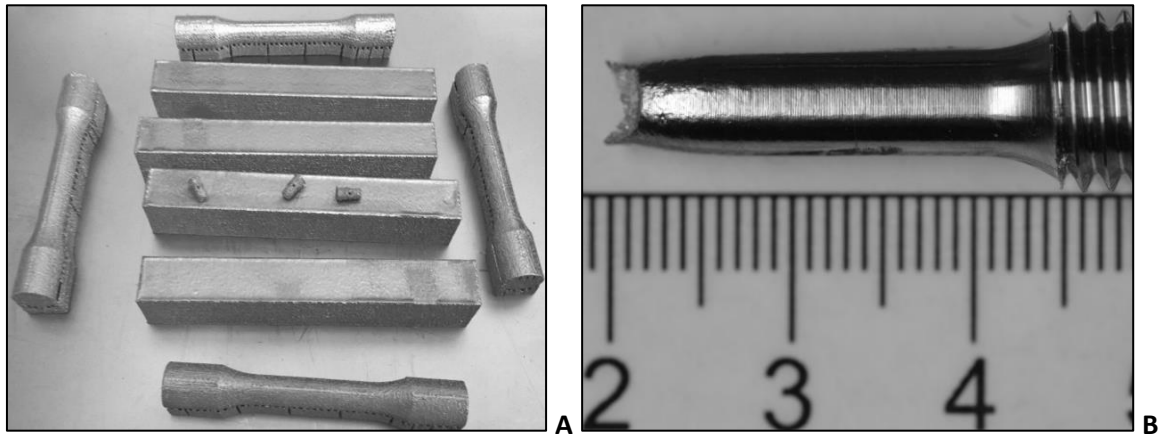


Figure 5. 20: Tensile bars, cuboids for fatigue and microstructural analysis, and 3 mm  $\phi$  x 3mm shells manufactured on each experiment condition (a), necking region of S - 1 tensile sample (b).

A cross comparison measurement shown in Table 5. 3 reveals similar mechanical behaviour between the conditions. All the values measured have a similar performance on average, which have similar mechanical properties as found in literature [202, 128, 68]. Looking in more detail at the single performance of the bars (Figure 5. 21), especially in low preheat condition, L - 2 shows

an elongation of 10.3 % which is below the average of 14 % achieved for the other tensile bars. In comparison, L - 1 shows an elongation of 16.1 % which exceeds the average of the other bars. In addition to the elongation, low preheat bars show the highest Yield strength of the specimens performed. Even if minimal, it can be connected to the slightly faster cooling rate achieved using just two preheating scans, which may refine  $\alpha$  lath with a consequent increase in mechanical properties. Standard and high preheat have almost the same values; standard has a minimal standard deviation between the specimens performed, which is possibly due to a better process stability in X - Y direction along the build.

*Table 5. 3: Mechanical properties results.*

	Sample	Modulus (GPa)	0.2% PS (GPa)	UTS (MPa)	Plastic El. (%)
<b>Standard preheat</b>	S - 1	115	874	981	14.4
	S - 2	116	872	982	14
	S - 3	115	867	979	14
	S - 4	114	864	976	13.3
	Average	115	869.2	979.5	13.9
	STD dev	0.82	4.57	2.65	0.46
<b>Low preheat</b>	L - 1	115	878	985	16.1
	L - 2	113	873	983	10.3
	L - 3	115	877	984	13.2
	L - 4	115	874	985	14.3
	Average	114.5	875.5	984.2	13.5
	STD dev	1	2.38	0.96	2.43
<b>High preheat</b>	H - 1	115	862	974	13
	H - 2	114	870	978	15.4
	H - 3	118	860	973	13.8
	H - 4	116	860	972	14.7
	Average	115.7	863	974.2	14.2
	STD dev	1.71	4.76	2.63	1.05

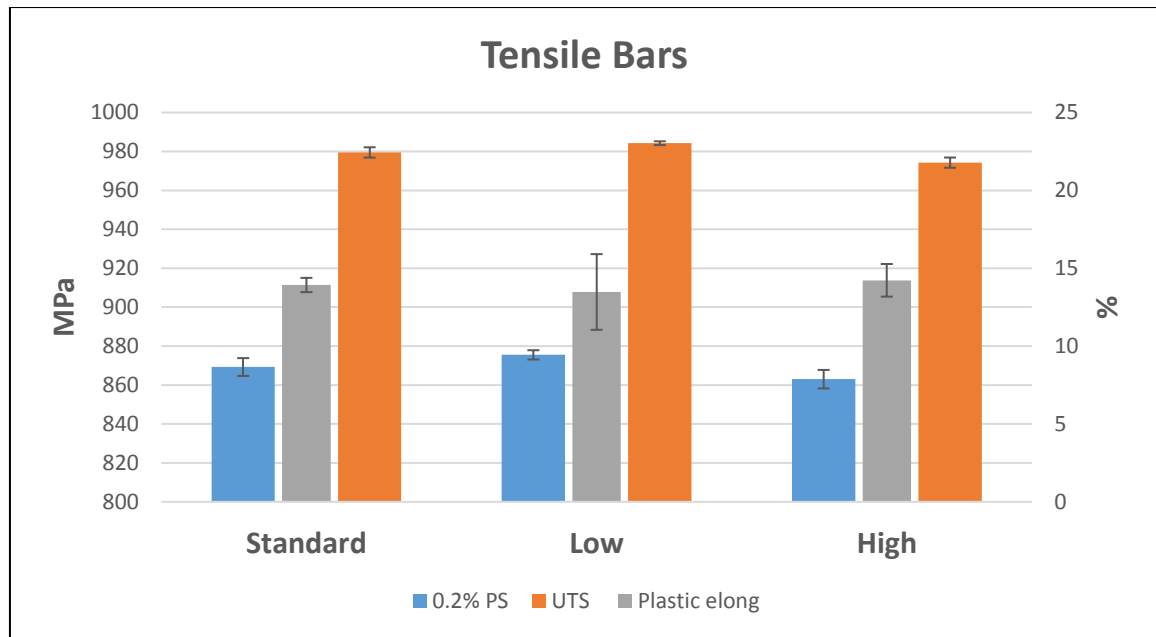


Figure 5. 21: Chart of the three different preheat conditions.

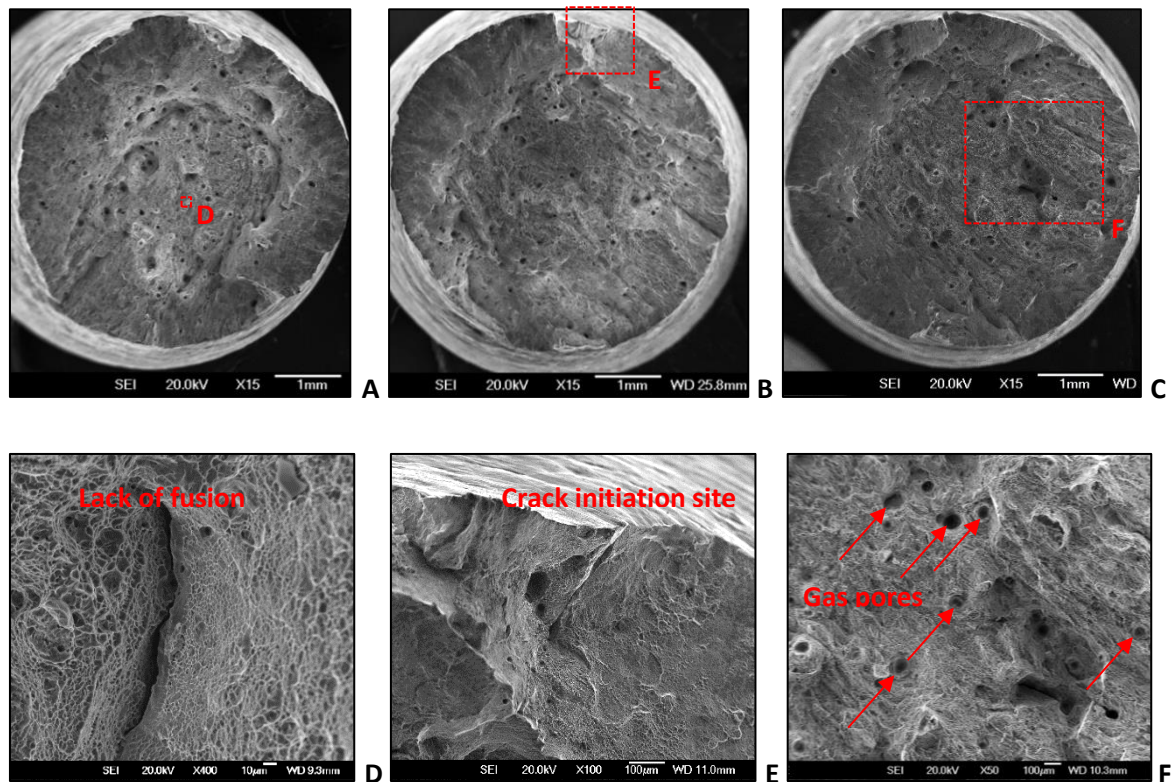


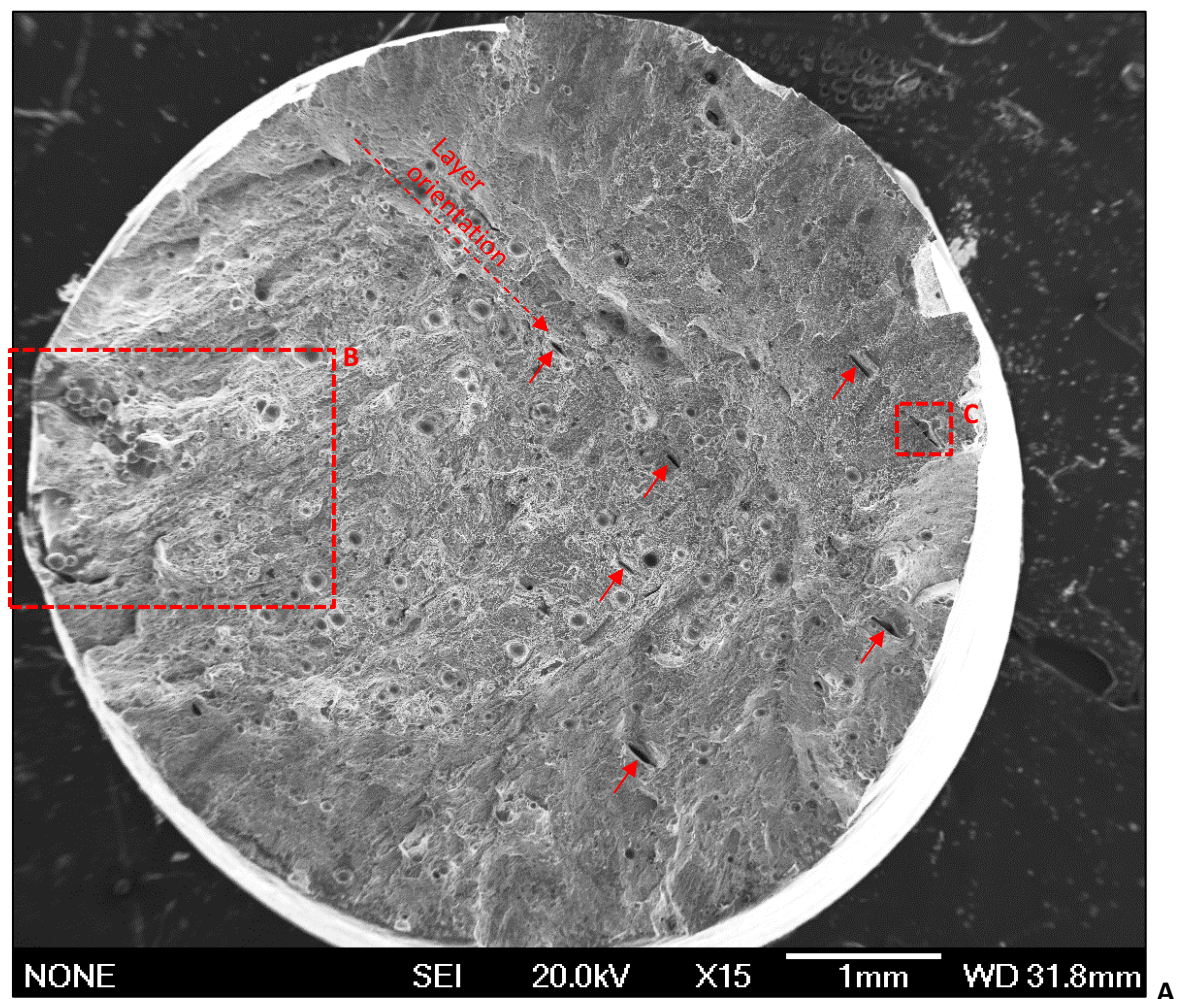
Figure 5. 22: SEM surface fracture analysis of L - 1 (a - d), S - 1 (b - e), H - 1 (c - f).

As Figure 5. 22 shows, SEM analysis was performed and cross compared between the necking regions of the tensile specimens. They were represented by spherical pores and ductile fracture along the surface captured (d - f). Crack initiation site (e) and small cracks generated during the



tensile performance (d) were observed between specimens, and similar characteristics were observed between the performed bars.

However, L - 2 reported in Figure 5. 23 (a) shows lack of fusion (indicated with red arrows) aligned in the same direction as the manufactured layers. This phenomenon was due to the low preheating condition, which was not sufficient during the consolidation phase, thus resulting in a lack of fusion. Figure 5. 23 (b) represents the magnification of a weak area near to the surface of the tensile bar, where loose powder was not properly consolidated, and consequently a crack started to propagate through the entire sample. Lack of fusion with a trapped powder particle is magnified in Figure 5. 23 (c). The abovementioned description of L - 2 summarises the reasons for the reduced elongation observed during the tensile performance. Similar issues were reported by Krabe at al. where uncompleted melting near to the surface generated early failure of the specimen. A HIP cycle was suggested to ensure closure of the voids and pores un-melted during the manufacturing process [129]. The other low preheated specimens do not show a lack of fusion in the surface fractured area which can be related to a localised case, which needs to be investigated in more detail.



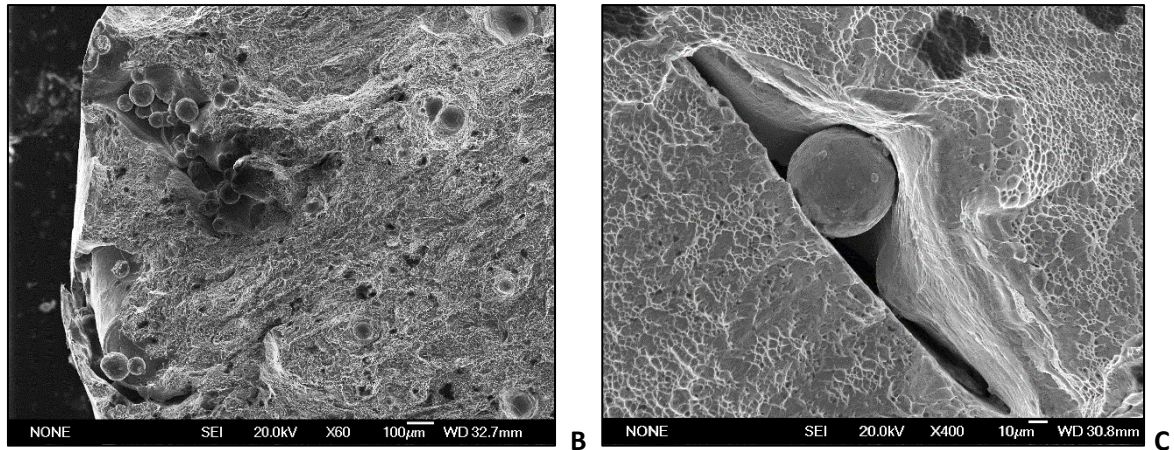


*Figure 5. 23: L - 2 surface fracture captured by SEM with lack of fusion and porosity highlighted (a), crack propagation point with un-melted powder (b), lack of fusion with non-fused powder particle (c).*

Ductile dimpled surface and round shaped pores located on the surface of the sample presented in Figure 5. 23 show a similar fracture that occurred in all specimens tested. The level of porosity achieved in the samples was due to the high porosity level trapped inside the GA powder particles. Excluding L - 2, very few surface fracture differences were observed between low, standard, and high preheated samples.

One of the main reason connected to the good mechanical properties achieved with porosity and lack of fusion can be attributed to the shape of the pores and the lack of fusion orientation. Boccaccini discussed the influence of stress concentrations in pores [203], where pore geometry and orientation have different stress concentration factors depending on the direction of the stress applied. The gas pores trapped inside the specimens have a spherical shape, with a consequently low crack initiation rate. This is due to local plastic deformation that occurred in the edges before the stress reached the Yield strength of the material [204] (see Figure 5. 24 (a)). However, the lack of fusion has an elliptical shape, and the longer length of the pore orientation is parallel oriented to the pulling direction. Figure 5. 24 (b) shows a potential lack of fusion at 90 degrees shifted compared to the one achieved in the tensile specimens, where the long length of the porosity was aligned with the stress direction. In this case, during the mechanical tests, the lack of fusion tend to stretch and consequently close, which reflects minimum impact on the mechanical performances. More investigation, like fatigue analysis, should be done in order to better understand the impact of pores and lack of fusion found in the specimens.

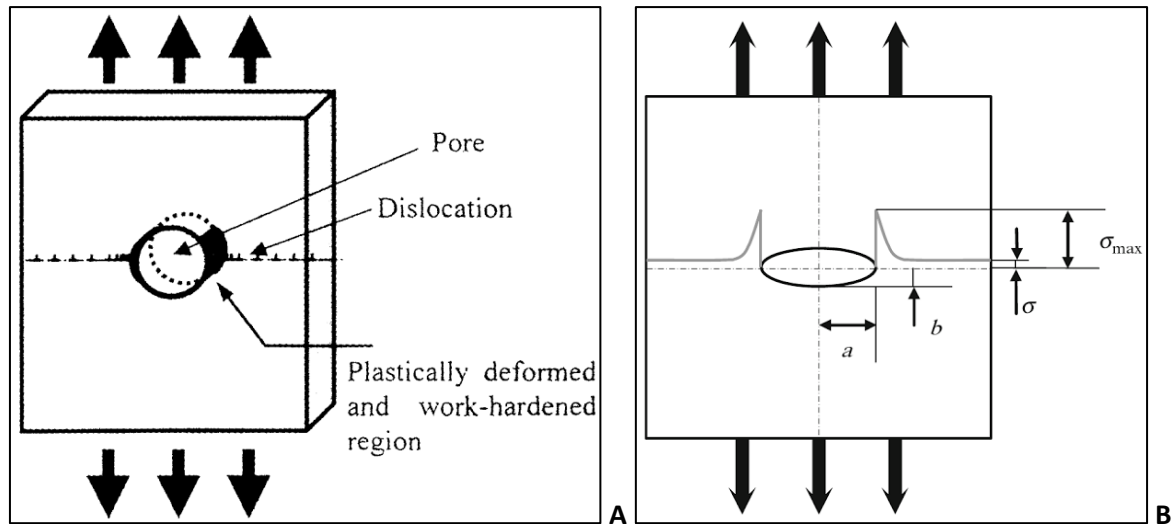


Figure 5. 24: Stress concentration edges in a cylindrical pore (a), high stresses edges in an elliptical pore (b) [204].

### 5.3.7 Fatigue Tests

After performing mechanical tensile tests, further investigation was carried out to better understand the impact of pores and lack of fusion found in the specimens. HCF analysis of three specimens of each condition were performed to capture potential early failures and their reasons. The details of the experimental settings can be found in Figure 3. 4 Set 2.

Table 5. 4: Roughness surface captured on the top region of the E-PBFed specimens. (\*) no failure happened before  $10^7$  cycles. (+) failure outside the gauge region.

	Sample	Gauge size (mm)	Frequency (Hz)	Load (KN)	n. of Cycles	
Low preheat	#1	6.42	98	12.95	1332700	+
	#2	6.4	98	12.87	10000000	*
	#3	6.41	98	12.91	2137500	+
Standard preheat	#1	6.39	98	12.83	2672800	
	#2	6.39	98	12.83	10000000	*
	#3	6.38	98	12.79	10000000	*
High preheat	#1	6.38	98	12.79	10000000	*
	#2	6.39	98	12.83	4866200	
	#3	6.39	98	12.83	10000000	*



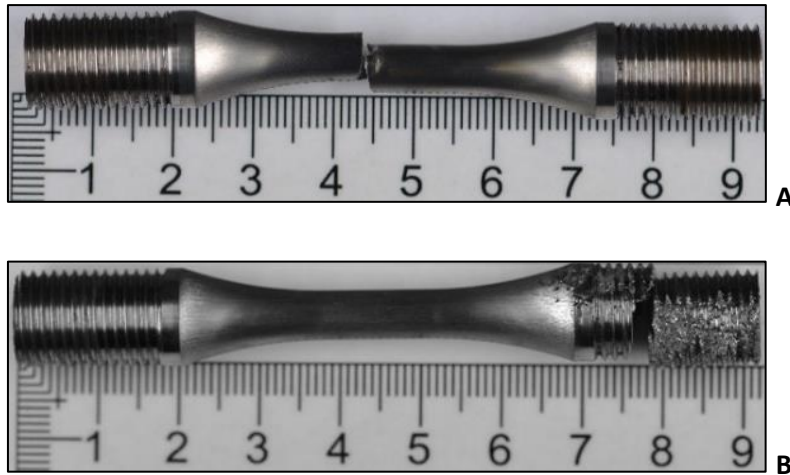


*Figure 5. 25: Post HCF image of high preheat #2 (a), and low preheat #3 specimens (b).*

Table 5. 4 describes the load used per specimen condition and the number of cycles achieved for each as-built fatigue specimen. Using a standard pre-set load of 400 MPa, standard and high preheat have one specimen failing before  $10^7$  cycles in the gauge length region as Figure 5. 25 (a) shows. Low preheat specimens had two failures on the three specimens tested, both of them failed in the threaded region as represented in Figure 5. 25 (b).

Standard and high preheat as-built specimens had a failure of 2672800 and 4866200 cycles respectively, with a similar surface initiation site on the surface region in the gauge length area. As Figure 5. 26 shows, the crack initiation site originated in pores localised on the surface of the specimens. The pore (Figure 5. 26 (b)) acted as an initiation point, where the crack propagated into the specimens showing early failure generated from porosity trapped in the part during the manufacturing of the specimens. It is possible to assume that the pores trapped inside the GA powder during the atomisation process had a high impact on surface crack initiation. Figure 5. 26 (d) shows the high number of argon spherical pores trapped during the melting phase. Similar results were found in literature [202, 33, 205] where superficial porosity acted as a crack initiation site originating an earlier failure compared to samples being HIPped. They demonstrated that post HIP the specimens can reduce the trapped porosity and consequently decrease the risk of early surface failures from trapped argon gas.

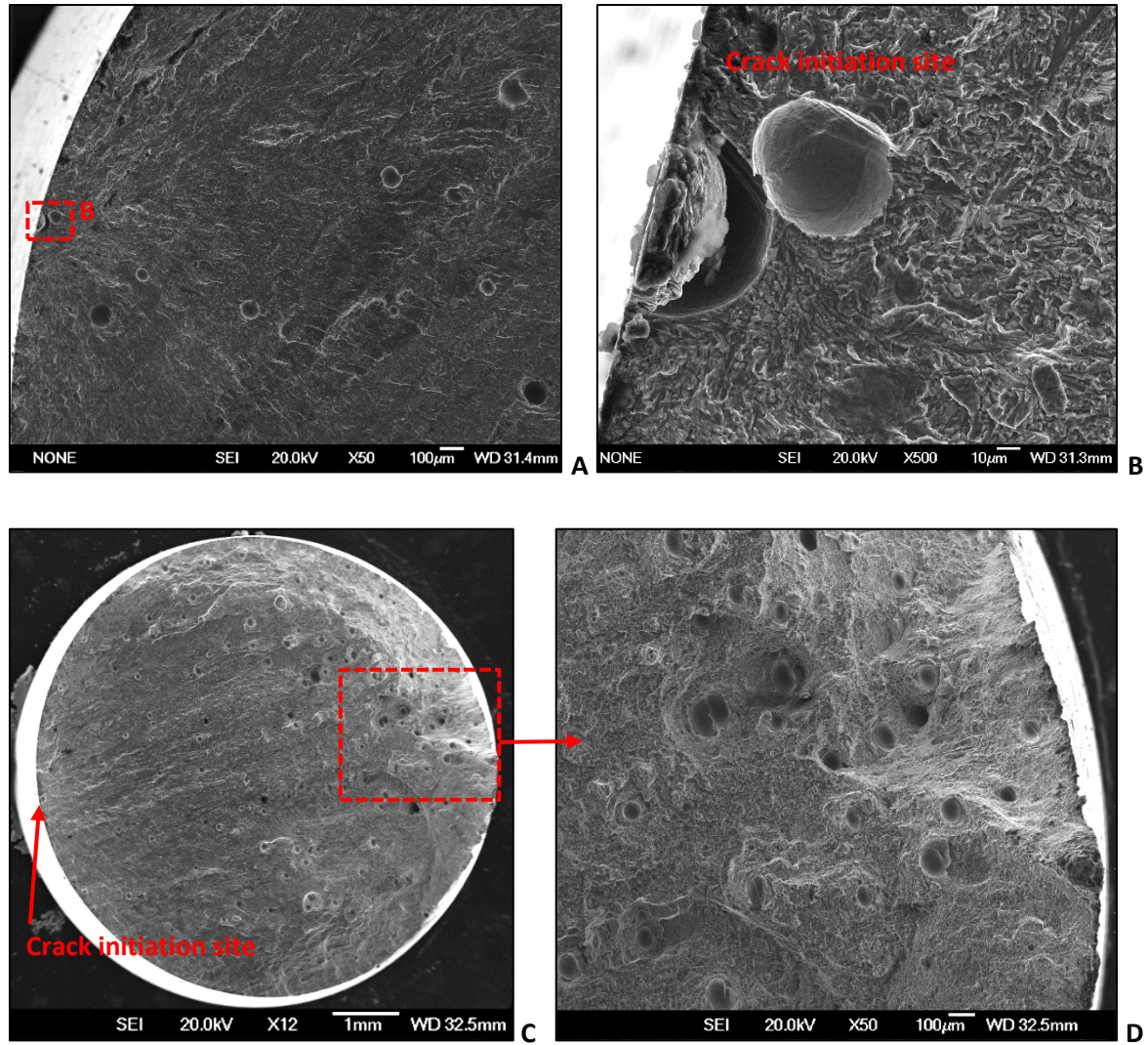


*Figure 5. 26: SEM fatigue surface fracture of standard preheat #1 (a) and its crack initiation site (b). High preheat #2 (c) and a localised pores region (d).*

Before mounting the low preheat specimens for the tests, lack of fusion was visually observed in the threaded region of the three fatigue parts to be performed. Low preheat sample #1 and #3 failed at 1332700 and 2137500 respectively, where localised lack of fusion was the main issue in the crack initiation. In sample #2, even if superficial defects in the threaded region were noticed, it ran out at  $10^7$  cycles. Both of the early failed samples had the surface fracture localised in the threaded area, where the stress concentration during the fatigue test was  $\sim 100$  MPa (its diameter was twice as big as the gauge size). It is possible that the reason for early failure in that site was due to the enlarged lack of fusion localised in that region, as showed in Figure 5. 27 (a), where a crack propagated along the centre of the specimens. A more detailed image (b) of non-melted powder shows the crack initiation point starting from a region of voids and partially melted structure. Components with larger defects, as shown in sample #1 and #3, have high impact on

parts which should be considered not suitable for aircrafts or for assemblies where high stress performance is required. Currently, there are no methods to re-solidify a superficial non-fused region. A solution can be found in removing the issue through subtractive methods or improving the sintering parameters as suggested in literature [28].

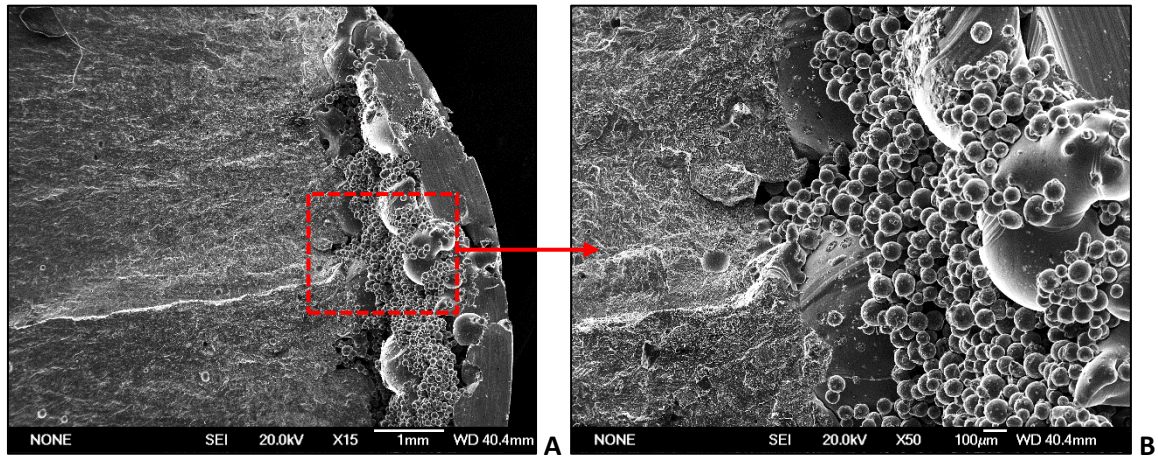


*Figure 5. 27: SEM image of low preheat #3 sample. Crack propagation site (a) with non-consolidated powder particles (b).*

In all samples that failed before  $10^7$  at 400 MPa, microstructural issues were noticed. The other samples had a long-life cycle due to low level imperfections in the specimens, especially on the surface region. The study performed can be connected with other investigations in literature [206, 207, 35, 198, 208, 209]. Unfortunately, there were difficulties in cross comparing the results due to an alternative methodology followed for performing the specimens and the settings used for manufacturing the fatigue parts.

### 5.3.8 Chambers Comparison

Experimental data captured, analysed and compared during the adaptronic chamber builds were then compared with the standard Arcam chamber samples. Table 5. 5 presents all the data compared between the chambers in a hypothetical build of 150 mm in height. The reduction of starting plate size (300 mm x 150 mm Vs 170 mm x 170 mm) and adaptronic chamber dimensions (420 Ø mm Vs 190 mm x 190 mm) showed a substantial reduction in the amount of powder required at the bottom of the starting plate (64 % less) where it sits before running the build, as also shown in previous studies [210, 131, 132]. Reducing the chamber size halved the initial starting plate preheating time and the cooling time phase due to the reduced amount of powder in the chamber and the consequent increase of dissipation/irradiation of the heat generated during the process. Changing the raking/recoater strategy from three to two passes resulted in 5 sec saving



per layer. Micro-hardness demonstrated a good stability using the standard preheat setting in each location of the cubes. The low preheat condition resulted in a good hardness, but not complete stability due to the thermal changes occurring during the build. The high preheat condition, as suggested before, has a hotter bed compared to the other conditions which resulted in having bigger  $\alpha$  platelets and lower hardness properties. Standard preheat shows the best micro-hardness stability during the entire build.

*Table 5. 5: Conventional Vs adaptronic chamber comparison.*

	<b>Chambers</b>		
	<b>Conventional</b> 420 Ø mm	<b>Adaptronic</b> 190 x 190 mm	<b>Savings</b>
<b>Powder required to fill the chamber before starting the first layer</b>	15 Kg	4 Kg	<u>11 Kg</u>
<b>Start plate pre-heating time (~720° C)</b>	60 min	28 min	<u>32 min</u>
<b>Amount of powder required for 150 mm tall build</b>	80 Kg	14 Kg	<u>66 Kg</u>
<b>Powder cost for 150 mm build</b>	12 K £	2.1 K £	<u>9.9 K £</u>
<b>Cooling time</b>	~7 h	~3 h	<u>4 h</u>
<b>Raking time (recoating)</b>	19 sec	14 sec	<u>5 sec</u>

## 5.5 Conclusion

In this case study it has been demonstrated that E-PBF machines with larger build chamber and hoppers are capable of being integrated with smaller build envelope chamber.

- After considering different design approaches, the development of the new hardware was achieved with success, with the installations of the items being perfectly suited to the A2XX E-PBF system without particular problems. A few issues were faced during the development of the new adaptronic chamber parameters; the new chamber configuration of 190 x 190 mm was a strategic move in order to use the Arcam A1 E-PBF system settings. No customised settings, neither preheat nor melting theme, were explored.
- The parts manufactured during the case study with different preheat 1 repeats (2 - 4 - 8) were successfully manufactured and post processed. All the builds were produced without particular issues. A very similar level of porosity between the builds was observed, which was mainly related to the quality of the GA powder used for the manufacture of the samples. Metallurgical analysis shown that the typical  $\alpha$ - $\beta$  microstructure was achieved using an E-PBF system. A decrease in micro-hardness was noticed in high preheated samples, where the reduction was mainly due to high T achieved after 8 preheat repeats, with the consequence of a higher holding T and slightly bigger  $\alpha$  platelets. Similar results were observed by Al-Bermani et al. [63], where decreasing T resulted in higher mechanical properties due to a refined  $\alpha$  lath. Standard and low preheat specimens had a similar micro-hardness values of around 330 HV, where the standard samples were more constant in hardness along the 15 mm build height. The micro-hardness captured during this experiment are similar or slightly lower than presented in the literature [8, 129]. Micro-hardness values demonstrated a good stability using the standard preheat setting in each location of the cubes. Low preheat resulted in a build with a good hardness, but the sample was not completely stable due the thermal changes occurring during the build.
- By using a reduced kit was possible to optimise the total powder required for the build which can be quantified as 14 Kg on a build of 150 mm; this means a substantial reduction in the amount of powder required (79 % less), which has a consequence on cost, and pre/post process time. The amount of powder saved is remarkable, and because it is therefore less powder to be recycled as would be the case in a standard build, the amount of scrapped powder decreases.
- A reduction in time and the amount of powder required to run (turn around and parts manufacture) in the A2XX system was achieved. Preheating time (heating up the starting plate and preheat 1 phase) and cooling time after the completion of the build was considerably reduced due to the compacted size of the chamber/starting plate/building envelope.



- The GA powder used for the build resulted in pores trapped inside the particles, and consequently inside the specimens. The pores did not generate issues in terms of mechanical properties or behaviour of the manufactured parts. However, the amount and size of pores should be monitored in order to achieving pores below a critical acceptable diameter (dependent on the application of the part), which is not yet well defined.
- Scanning  $\mu$ -CT data shows an empty area located just below the specimens. Low heated cylinders have the biggest empty region compared to the other samples. This occurs when the powder is not completely pre-sintered and so during the melting phase it tends to shift or fly away due to the high velocity impact of the electrons to the low pre-sintered powder. This also occurs due to the lack of supports in a flat surface which may result in an irregular surface or the collapse of the shape as documented in literature [211]. Few porosity differences were observed between the shells either with metallurgical or the 3D investigation. The packing density achieved during the preheating phase is >46.1 % with the standard settings which is lower than the apparent density normally achieved in Ti - 6Al - 4V GA powder of 53 %. However, it has a similar value observed with the in-situ shelling Archimede's tests (Chapter 6).
- Metallurgical and mechanical properties showed promising results for more customised analysis. This development can be taken further in the production of AM parts where the chamber can be customised around the part/s required, or for the study of new alloys where a small build envelope and low quantity of powder is required to optimise the study. In addition, it is important to highlight that changes in T during heating and cooling can influence the microstructure and consequently the mechanical properties, which can influence the performance of the parts manufactured.
- The mechanical properties achieved with tensile tests reflect the values presented in literature [127, 147] which are well above the standards required for Ti - 6Al - 4V in E-PBF [106]. However, the low repeats condition shows lower stability in elongation compared to the standard and high preheated strategies. More investigation should be conducted in order to understand the reason for the lack of fusion, which could be due to a lower pre-heated area of the bed location or a low T achieved before the melting phase.
- Fatigue results showed the issues of using GA powder, with the consequent high amount of pores trapped inside the specimens. Without post treatment as HIPping, surface localised pores can be fatal during fatigue performances as occurred with the tested samples.

## **Chapter 6: In-Situ Shelling in E-PBF**

### **6.1 Introduction**

The previous experimental chapters were focussed on a better understanding of the machine characteristics and build behaviour, where manufacturing and modified hardware parts were explored. In light of that, advance manufacturing strategies need to be explored in order to increase productivity using an E-PBF system.

Shooting electrons in a vacuum environment is one of the characteristics of the E-PBF system. An advantage of an almost oxygen-free environment is that it allows the potential voids generated during the process to be closed using post treatments such as HIPping.

The following chapter describes the advantages of fully solidifying unconsolidated regions of the specimens during a post HIP cycle. Potential benefits such as saving manufacturing time and achieving a non-conventional microstructure were identified during the literature review (see chapter 2.7 for more details). Shells with different melted core levels were manufactured to investigate the feasibility of the technique and its benefits. Post analysis was undertaken to establish mechanical behaviour and ideal conditions for manufacturing [139, 140].

This chapter's purpose is to:

1. Prove the feasibility of the technique;
2. Improve build time using advanced manufacturing themes;
3. Understand the impact of microstructure and mechanical properties of the settings used;
4. Define future ways of advanced manufacturing such as changing microstructure and shrinkage prediction.

### **6.2 Experimental Procedure**

#### **6.2.1. Parts and Build File Preparation**

A build of 16 cylindrical shells with different hatching parameters was manufactured to test the metallurgical structure before and after a HIP treatment. Machine settings and parameters were modified for post analysis investigation purposes, where different SF and BF were used to change the consolidation level of the parts. Manufacturing time with potential benefits in build cost was

tracked in the experiment. Final mechanical tests were performed to establish the boundaries of the technique.

During this study, a fabrication of symmetrical cylinders with an external height and diameter of 15 mm each were manufactured keeping a uniform shell thickness of 1.5mm. Due to post HIPping treatment requirements, internal and external rounded corners were designed in order to facilitate potential shrinkage occurred during the post treatment.

Figure 6. 1 (a) shows the 3D CAD image of the cylinder shape and its shell thickness of 1.5 mm (b). A main body cylinder (1) and bottom and top closing caps (2 and 3) shown in Figure 6. 1 (b) were designed to encapsulate the central core region (1 - core) from the side ends. The reason for generating a closed shell was connected to the need to seal the core area where different hatch settings were investigated. Using this strategy allowed capture of the hatching time needed to melt the core region and the metallurgical properties of the cylinders depending on the variable used. The 1.5mm thickness shell was taken from literature, where Leitch et al. [139] defined that >1.2mm was a safe thickness to prevent leaks during a post HIP treatment in E-PBF.

In order to change the hatching parameters in the core region, whilst keeping the shell  $\sim 1.5$ mm, an increase from 2 to 5 contour lines were used. This strategy allowed a thicker shell and the benefit of changing the hatching strategy without compromising the thickness of the shell required for the HIPping process. Top and bottom caps were manufactured using the original settings.

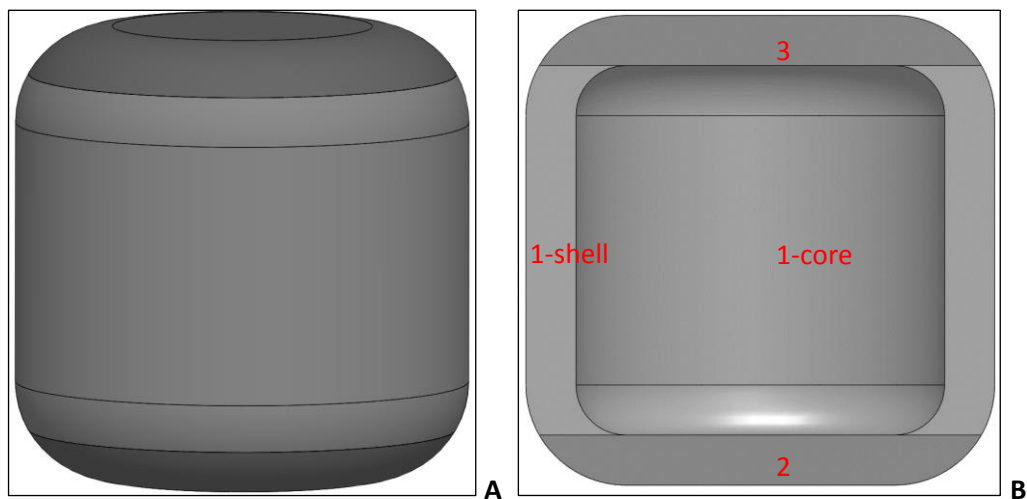


*Figure 6. 1: CAD model of the shell (a) and its internal X - Z section (b).*

## 6.2.2. Hatching Parameters and Machine Settings

An Arcam A2XX electron beam system was used to melt Ti - 6Al - 4V PA 45 - 106  $\mu\text{m}$  powder. Fully melted shells were manufactured using the standard MTC contour and different hatching parameters were investigated to achieve a fully melted, partially consolidated, and loose powder cores inside the cylinders. BF and SF varied around the standard settings as shown in Table 6. 1. Four cylinders for each of the 16 different conditions were manufactured. The variation of settings was focused on achieving different part density with a potential impact on manufacturing time. More details of the hatching settings are found in chapter 2.1.4.

*Table 6. 1: Themes used during the experiment. (\*) Standard MTC settings.*

Theme	#1	#2	#3	#4	#5	#6	#7	#8	#9	#10	#11	#12	#13	#14	#15	#16
Speed function	26	26	26	26	26	36*	36*	36*	36*	36*	46	46	46	46	46	-
Beam focus offset	0	9*	19	29	39	0	9*	19	29	39	0	9*	19	29	39	-

Variable #16 was manufactured without the hatching phase in order to trap semi-sintered powder inside the shell. The BF variation was changed to understand the influence of focusing and defocusing the beam and its impact on the microstructure. Modified settings in SF were also investigated; the scope was modifying the energy density delivered during the melting phase.

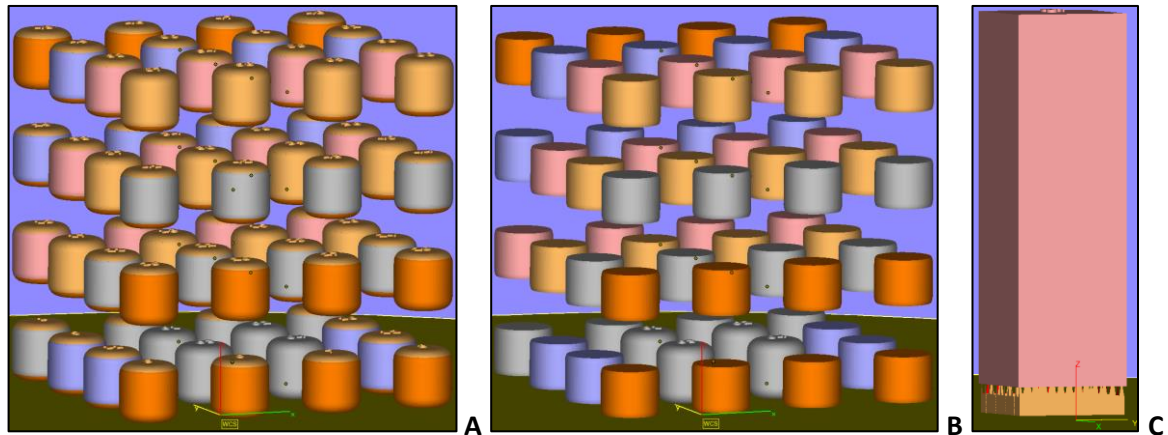


*Figure 6. 2: Materialise Magics file made for the build (a), with a representation of the cylinders main body (b). Tensile bar with encapsulated powder from the middle to the top region; supports are shown at the bottom of the cuboid (c).*

An even distribution of the specimens was used during the design of the parts in the build chamber using Materialise Magics software which enabled the manufacturing time of the cylinders to be

tracked (through the log file data sheet) and to guarantee an even melting method along the X - Y and Z directions. Figure 6. 2 (a) shows the distribution of the cylinders inside the powder bed, where differentiation of colours show the different settings used for each condition (four specimens for each of the 16 hatching variables combinations manufactured). A representation of the cylinders main body are shown in Figure 6. 2 (b), where the cylinder caps were loaded as a different part. The four mid-bottom cylinders (b) represent variable #16, where the cores contain un-melted pre-sintered powder. Four tensile blocks were fabricated (c) in the same build, half of the total height of the cuboids contained loose pre-sintered powder trapped in a shell which was kept for post HIP consolidation purposes. All the samples manufactured had the same customised supports located on the bottom surface of the component.

A calculation of energy distribution in the hatch phase was generated in order to define the amount of energy dissipated by the values used for the aforementioned variables. It is expressed by:

$$Q = \frac{A * V}{v}$$

$$E = \frac{Q}{d * t}$$

Where  $E$  refers to energy density ( $J / mm^3$ ),  $A$  beam current (mA),  $V$  acceleration voltage (kV),  $Q$  line energy ( $J / mm$ ),  $v$  scan speed ( $mm / s$ ),  $d$  hatching space (mm), and  $t$  as layer thickness (mm). The fixed variables were 18 mA of beam current, 60 kV of acceleration voltage, 0.2mm hatching space and 0.07  $\mu m$  layer thickness. Similar studies can be found in literature [111, 171, 212, 213].

*Table 6. 2: SF table with related speed and energy density.*

SF	Speed (mm / s)	Line Energy (J / mm)	Energy density (J / mm <sup>3</sup> )
26	1529	0.706	50.453
36	2094	0.516	36.840
46	2659	0.406	29.012

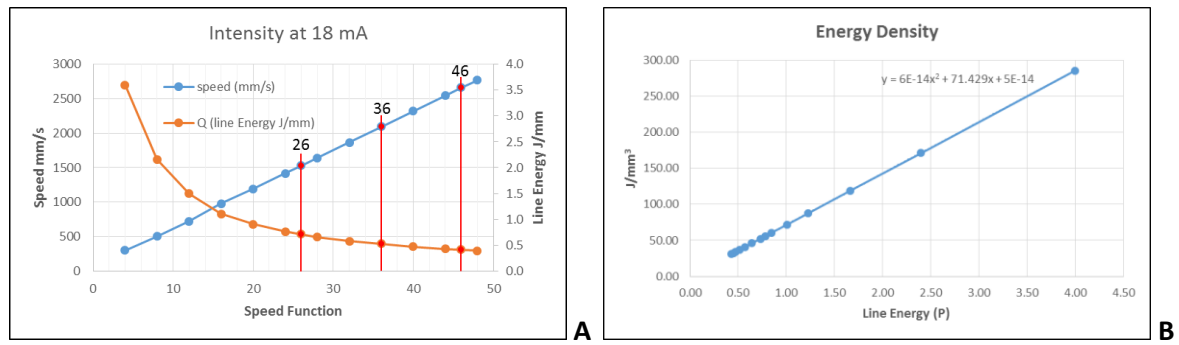


Figure 6. 3: Energy density distribution in relation to the line energy (a). SF values used during the experiments (b).

The BF used during the experiments was connected to beam speed and line energy used during the trials. Table 6. 2 (a) shows a linear increment in speed directly related to the increase of SF. Conversely, the line energy decreases with the increase of the SF releasing less line energy as SF increases. The line energy values are connected to the energy density delivered onto the layer as shown in Figure 6. 3 (a). The values calculated and used during the tests are reported in Figure 6. 3 (b), where the lowest SF of 26 delivers a high energy density of  $\sim 50 \text{ J / mm}^3$  that drops to almost half when the SF is increased to 46. In addition to the aforementioned equations, the BF variable should be also considered with regard to the energy distributed in the spot size area of the beam. The following chapter analyses the variables selected for the investigation.

## 6.3. Results and Discussions

### 6.3.1 Post Analysis Procedure

After the manufacturing of the specimens, all the bottom supports shown in Figure 6. 4 (a) were removed from each part. One cylinder per condition was vertically (X - Z plane) sectioned in order to capture the porosity achieved with each of the different settings used. Two of the three remaining cylinders per condition (16 conditions in total) - before sending them for a post HIPping treatment - were subjected to Archimedes measurements (more details of the process are found in chapter 3.8) as represented in Figure 6. 4 (b). The test was performed in order to capture the density variation achieved before and after the HIP treatment. X-CT analysis (see chapter 3.12 for technique explanation and Table 3. 6 set 1 for system details) with a resolution of  $10.8 \times 10.8 \times 10.8 \text{ } \mu\text{m}^3$  was performed on the remaining samples of each condition. Micro-hardness measurements and microstructural analysis were also completed on both unHIPped and HIPped

specimens to better understand the potential changes that occurred during the post heat treatment.

All the values recorded in the above tests were cross compared with each other, before and after HIPping. The results are explained in the following paragraphs.

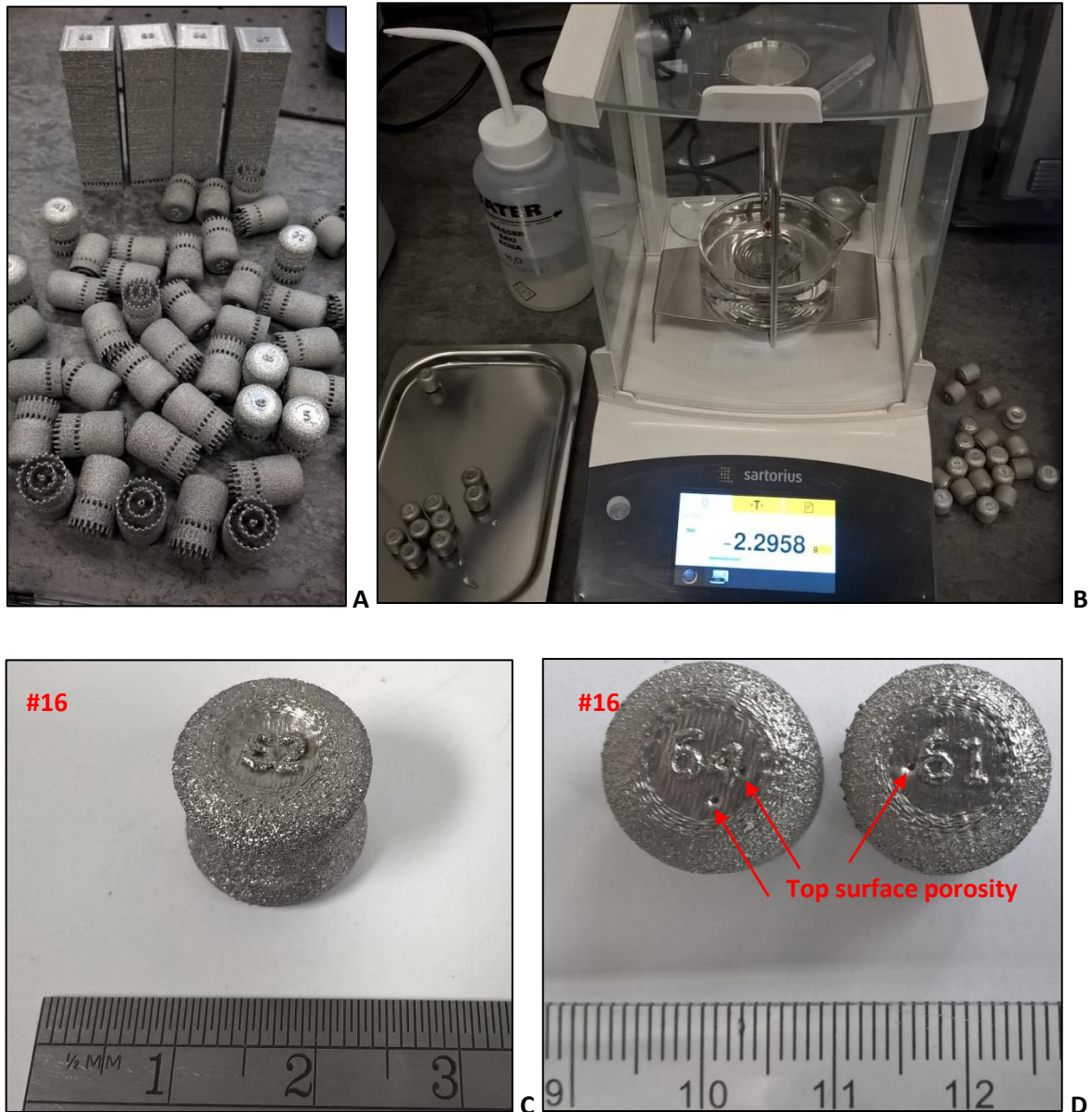


*Figure 6. 4: Cylinders and tensile specimens with supports after the build (a). Archimedes' test equipment used to test the samples before and after the HIP cycle (b). Samples #16 shrank after being HIPped (c) and porosity localised on the top surface of loose powder samples (d).*

After the HIPping cycle was performed (Figure 6. 4 (c) shows post HIP treatment of #16 and its shrinkage), the specimens were again tested for density and then sectioned for further inspection. Figure 6. 4 (d) reports the reason for failure of three of the four samples in condition #16, where

pre-sintered powder was trapped inside the shell. Pores on the top melted region of the shell were observed, which potentially caused the incomplete consolidation during HIPping. The leak prevented the shell sealing, causing failure during the process. Similar results can be observed in Figure 5. 14 where a large empty region was observed under the top melted surface of the  $\mu$ -CT reconstructed cylinders. The cause of the failure can be linked to the component design, where an overhanging feature, without supporting structure, can result in poor melt quality, curling effects, turbulence, instability during the solidification [164, 33], and consequent imperfections of the layers' structure. All the other shells, with different hatch settings, did not fail during the HIP treatment. The shells were completely sealed, generating the desired shrinkage during the HIPping process.

### 6.3.2 Optical Microscope Porosity Measurements

The parts that were OM analysed before a HIP treatment exhibited a range of different porosities. All the samples with a BF of 0 – 9 – 19 displayed a porosity of <0.29 %, which is considered relatively low for E-PBFed parts. Increasing the SF and consequently the BF, and obtaining a drop in energy density, resulted in a noticeably high level of porosity. Table 6. 3 gradually shows the level of porosity obtained with different settings. The red line shows a hypothetical porosity line related to BF in Figure 6. 5 (b), where the components started to have a significant levels of voids trapped in the shell.

The amount of consolidated regions revealed from the OM was confirmed by weighing the components through Archimedes tests. Figure 6. 5 (c) shows the relationship between the amount of voids and the specific weight of the components, where an incremental trend of voids was observed. Pores were generated when there was not enough energy density distributed on the surface, i.e. where increasing the beam focus or SF had an impact on voids and lack of fusion percentage [33, 68, 119, 213].

*Table 6. 3: OM 2D % porosity observed in the specimens with related BF and SF.*

	#1 0-26	#6 0-36	#11 0-46	#2 9-26	#7 9-36	#12 9-46	#3 19- 26	#8 19- 36	#13 19- 46	#4 29- 26	#9 29-36	#14 29-46	#5 39-26	#10 39-36	#15 39-46	#16 -
OM	0.06	0.14	0.08	0.04	0.15	0.09	0.20	0.29	0.28	0.23	10.09	21.01	14.97	17.70	30.81	



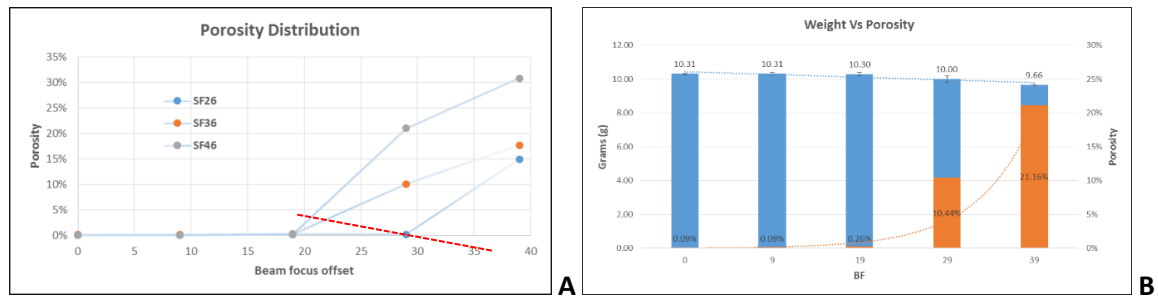


Figure 6. 5: OM porosity associated to BF (a), and its relation between weight and porosity (b).

On top of the data collected, OM pictures of each etched section were captured in order to investigate the melting behaviour and its porosity location. The conventional / standard #7 settings exhibited a percentage of 0.15% porosity, observed with the OM. The parts with less porosity were found in samples #1, #2, and #6 where the BF was finer with a high energy density, as shown in Figure 6. 6 (a). Sample #8 and #13 (d) had the maximum porosity of 0.29 % and 0.28 % respectively using a BF <20, which can be considered acceptable for AMed parts. Samples #5 (b), #9 (c), #10, #14, and #15, with lower energy density, had a porosity between ~10 % to ~30 %, which is not suitable for high performance applications, for example aerospace standards [106]. Sample #5 (b) shows porosity with localised voids connected together, with a high number located close to the shell. Similar pores were found in sample #9 (c), where the emission of low energy density presented a higher number of small localised pores. They incrementally decreased the energy density with a consequent higher trend of pores distributed around the core region. The high porosity observed close to the shell in the hatching region can be attributed to the turning function and its increment of beam traverse speed which further reduced the energy density in the edge area. Similar results were observed by Tamas-Williams et al. [57], where tunnel defects were noticed in the turning function region and below overhanging features, caused by lack of energy needed to completely solidify the layer. During their study, a post HIP cycle was used to close up the voids generated during the manufacturing process. A clear explanation of turning function and its impact was analysed.

X - CT scans in #16 (e - f) revealed an even distribution of the powder inside the core region of the cylinder but more voids were observed around the shell. This was potentially due to the contour scan moving away the particles close to the melted region. When the electrons impacted and consequently melted the substrate, they generated localised turbulences which tended to push the near-by powder away creating localized pore areas around that region, as reported in literature [114, 117].

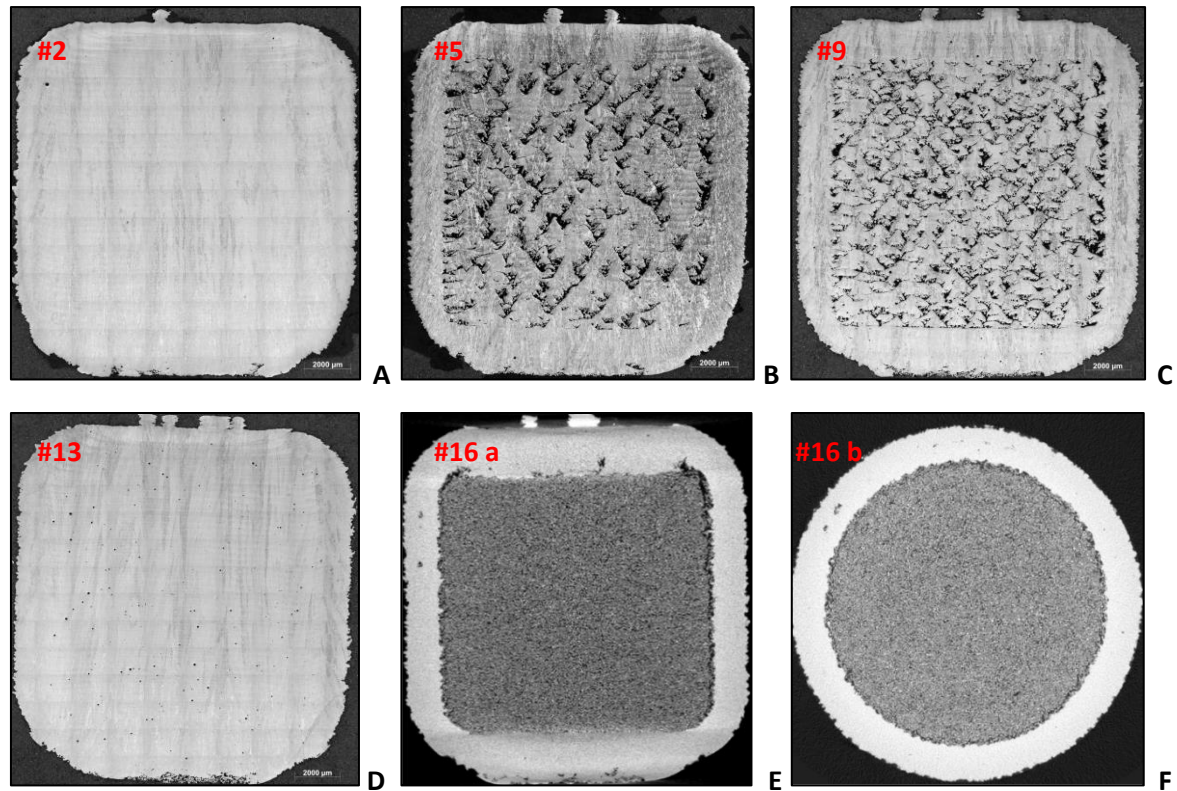


Figure 6. 6: OM etched X - Z section of sample #2 (a), #5 (b), #9 (c), #13 (d). X-CT scan of loose powder shell in sample #16; X - Z (e), and X - Y (f) orientation.

High porosity, evenly distributed, can be connected to Table 6. 2 (a) where the beam energy is reduced when the SF is increased. Defocusing the beam, as Figure 6. 7 shows, generates a lack of fusion as reported by Gong et al. [33, 213], where un-melted regions with consequent voids were observed. Due to the increase in beam focus size, and the consequent decrease in beam energy, voids were observed with different distribution and location. More investigation needs be done to understand the behaviour of the voids and their consequent impact on the structural integrity.

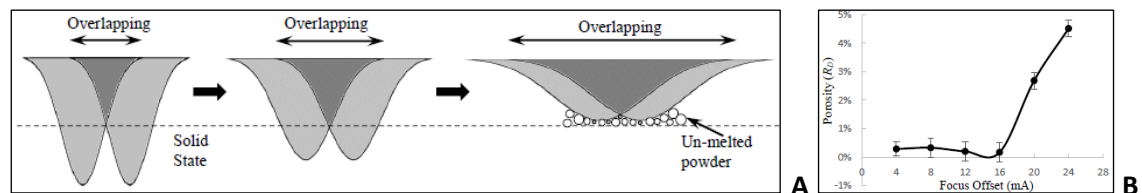


Figure 6. 7: Influence of BF and energy density distribution on porosity [33, 213].

### 6.3.3 Microstructural Behaviour after HIP Treatment

After performing preliminary analysis of unHIPped parts, the specimens were sent for a standard Ti - 6Al - 4V HIP cycle (see chapter 3.13 for further details). Archimedes tests, OM inspection in X -

Z 2D section, and micro-hardness measurements in the core region were performed to cross compare the results achieved with the samples without post HIP treatment.

Calculations were carried out to capture the shrinkage of the specimens based on Archimedes test, where Figure 6. 8 shows the values considered (a), the equations used (b), and the core mass (c) identified for generating the outcome data. The weight of the shell ( $V_{c1}$ ) was assumed from the volume measured in the CAD data. The other values required were taken using the Archimedes' system before and after the HIP treatment.

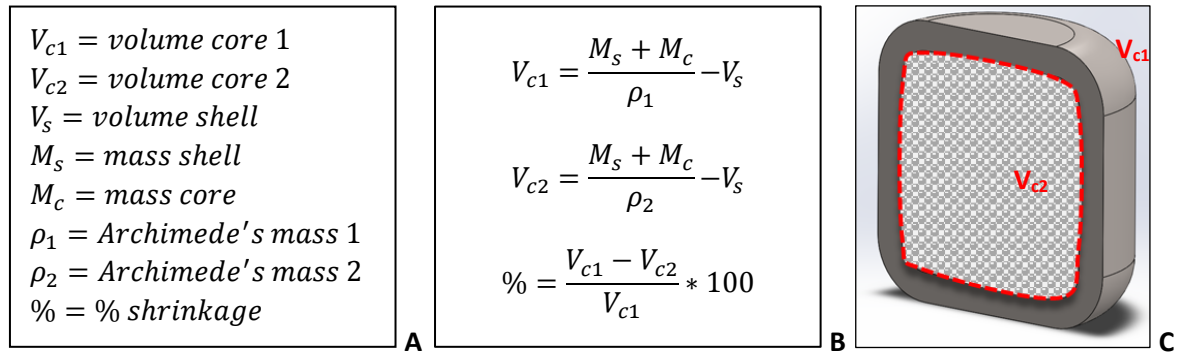


Figure 6. 8: Values (a) and equations (b) used for calculating the shell core (c) using an Archimedes test rig.

Figure 6. 9 compares porosity values captured from 2D OM before HIPping and Archimedes' densities estimated before and after the HIP treatment. A similar trend of porosity was noticed with both techniques; the highest level of shrinkage was observed using the Archimedes test in parts with lower percentage of voids compared to the OM analysis. An increment of porosity above 1% was noticed in sample #9, #14, #5, #10, and #15 respectively, where a combination of settings between 29 - 39 BF, and 36 - 46 SF were used. All the samples with 0, 9, or 19 BF and 26 SF all presented with porosity below 1%. The main explanation for this can be connected to the higher energy density delivered with a thinner BF and a reduced SF. The relationship between energy density delivered (see Figure 6. 3 (a) for details) and porosity can explain the generation of voids inside the structure, due to loss of energy as explained in literature [214]. However, it is possible that during the cutting and polishing of the 2D sections a non-precise measurement could be given by the porosity software due to extra material being removed or added during the polishing phase (as abrasive disk, or silica bits). Therefore, a minimum error should be considered for the shells with high porosity. The same principle should be applied for the Archimedes' test, where the light weight of the specimens can generate a minimum error during measurement. However, an average of 2 specimens per condition tested was used to improve the final values captured.

Sample #16, which was only evaluated with the Archimedes' test due to its loose pre-sintered powder core characteristic, displayed a void level of ~54 %, which is consistent with the pre-sintered packing density achieved in E-PBF during its spreading along the bed surface. A similar value was also observed from the  $\mu$ -CT scans captured in chapter 5, where a ~53% void was observed.

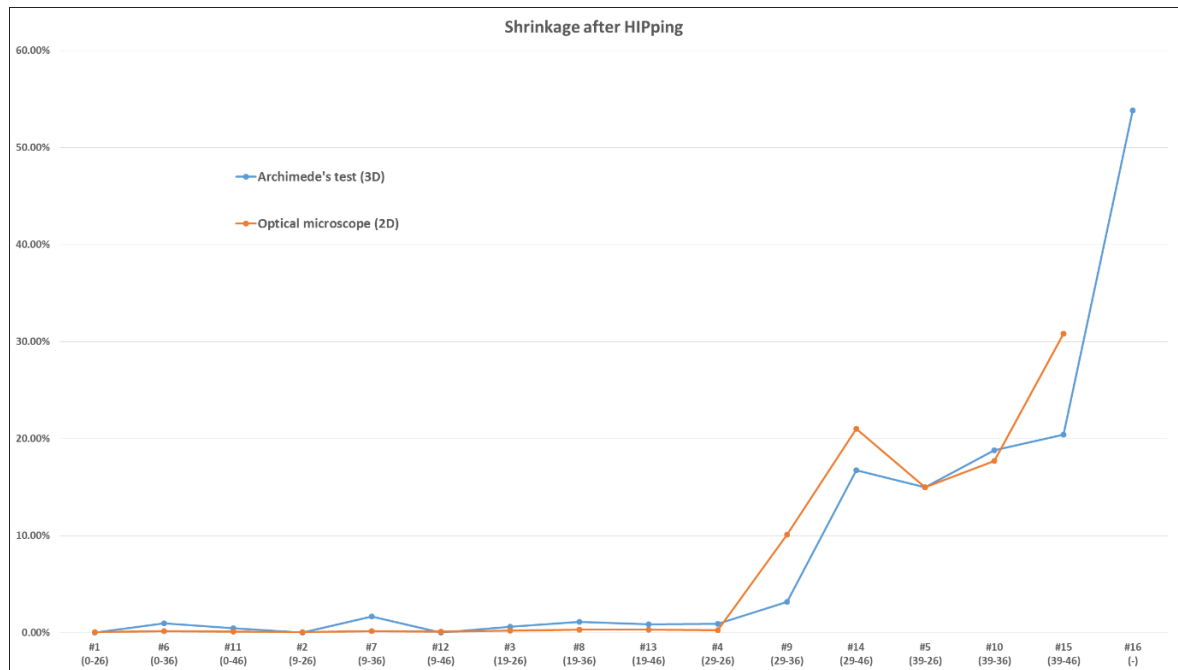


Figure 6. 9: Shrinkage comparison between optical 2D and Archimedes' 3D analysis after a thermal HIP cycle (BF - SF).

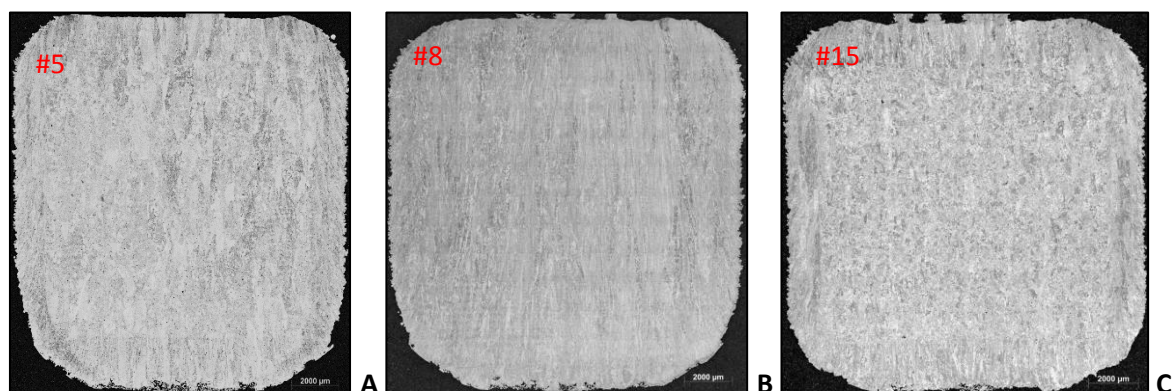


Figure 6. 10: OM 2D mosaic X - Z section of sample #5 (a), #8 (b), and #15 (c) after being HIPped.

The HIPped component mosaics in Figure 6. 10 show a minimal porosity in the core region which was quantified as <0.1%. The pictures show the columnar main  $\beta$ -grains generated in the shell

region, which can be considered as standard microstructural characteristic of E-PBFed parts. The components with a low percentage of voids before the HIP treatment show the conventional microstructure observed in E-PBF, where dual-mode/Widdermatten and columnar grains were observed [118, 119, 120, 121, 122, 98]. Samples with high porosity, and high level of shrinkage, show a slightly different structure inside the core region compared with the conventional structure observed in PBF. Mixed columnar and equiaxed grains were noted in the core region of specimens with highly non-consolidated areas before the HIP cycle, which remained after the compaction of the voids during the post HIP treatment. The mixed type of microstructure can be mainly observed in samples #9, #14, #5, #10, and #15, where the energy density was not enough to completely solidify the layers generating residual voids in the core region. Using this technique, columnar main  $\beta$ -grains were broken at different Z heights, preventing the vertical grain growth normally noticed in powder bed technologies.

Further microstructural details were observed by OM, shown in Figure 6. 11, where a mixed microstructure was observed in the core region of specimen #15 (a). Defined main  $\beta$ -grains were noticed in the shell section. A well-defined line was noticeable between the change of the standard shell and modified core settings (c – d). The cylinder with loose powder, as shown in Figure 6. 11 (b - d), had noticeable shell shrinkage that left a uniform thickness all around the shell. Relevant shrinkage was observed with specimens with a high percentage of porosity. The shrinkage and consequent deformation is directly related to the voids captured inside the shell as observed in Figure 6. 11 samples #15 and #16. In the core region the consolidated powder had an equiaxed structure, achieved after post HIPping treatment, with no pores visible at the interface between the shell and the post consolidated powder. Columnar main  $\beta$ -grains were observed in the core region of specimen #4 (b - d), which was classifiable as a common grain observed in PBF. A region with an after-HIP pore compaction was observed (d) within the columnar grains.



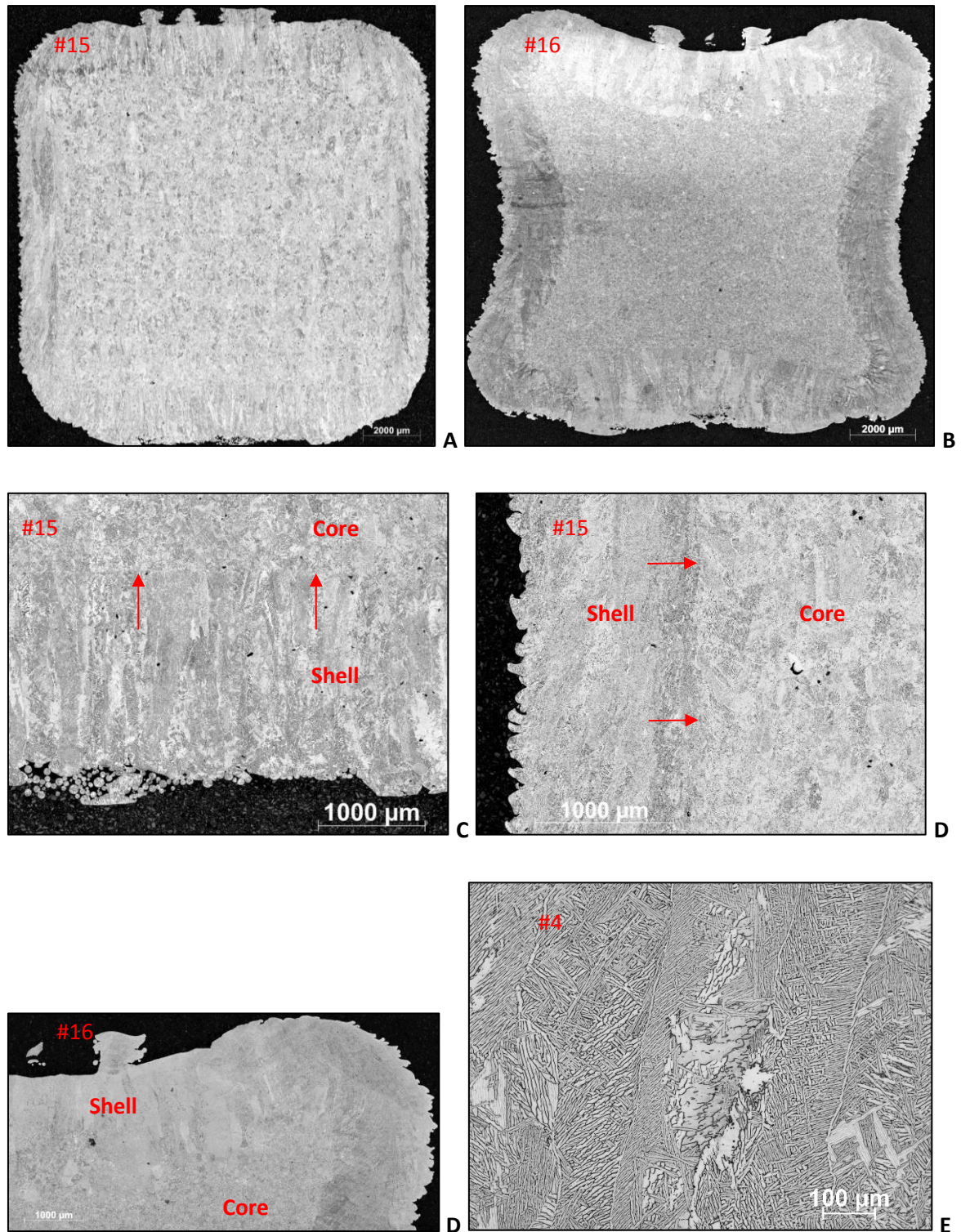
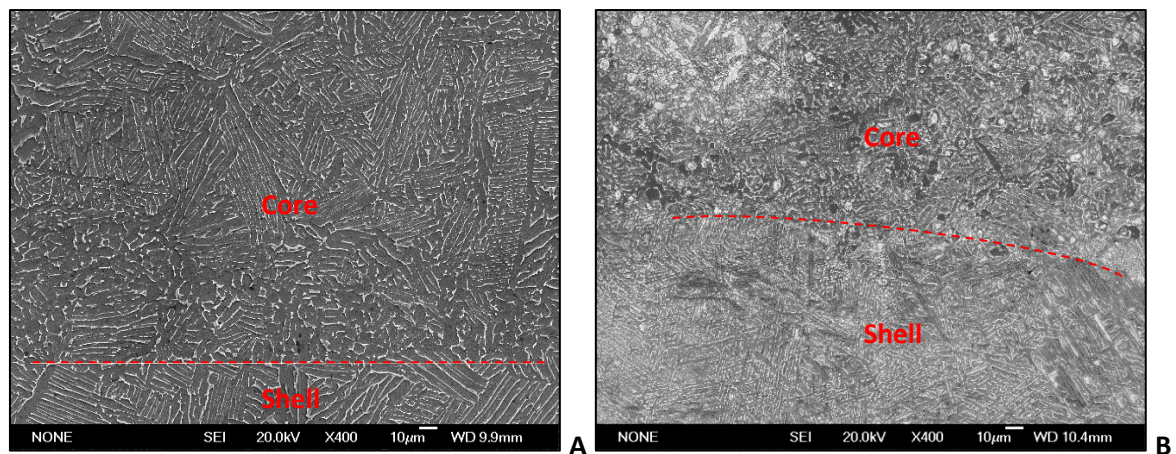


Figure 6. 11: OM X - Z microstructural sections of #15 shell and core (a), and a close OM image of a void compaction happened after HIPping in sample #4 (b).

A mixed structure, as achieved in the post HIPped porous samples, could change the behaviour of crack propagations generated from the surface. Due to a nearly equiaxed structure, it tends to change direction on cracks that would normally propagate through the  $\beta$ -main grains. This

phenomenon can impact the crack growth ratio in the specimen, depending on the force direction. More investigation of crack propagation effectiveness should be performed to better understand the efficiency of the method. The closure of the voids during the HIP cycle also tends to break the  $\alpha$  lath boundary seen in columnar  $\beta$  main grain, as is visible in Figure 6. 11 (e). The structure observed could change the mechanical fatigue and microstructural behaviour of the components under stress. An investigation into microstructural heterogeneity behaviour using similar E-PBF microstructures was observed by Seifi et al. [37], where no preferential paths during a crack propagation were observed through lath, colonies, and main  $\beta$ -grains in different locations of the build height.

In the polished samples by SEM, no significant macrostructural variations or gaps were observed in post-HIP treated samples. Similarly, in Figure 6. 11, longitudinal and transverse sections show no obvious boundary between shell and core. Figure 6. 12 (a) and Figure 6. 13 show a conventional E-PBF basket weave lamellar  $\alpha + \beta$  microstructure without observing major differences in the interface region between the shell and the core, where good bonding was generated. Variable #16 (b) shows differences between the fully melted region (shell) and the core, which was represented by a much finer randomly distributed lamellar structure and equiaxed grains with a spherical geometry between 5 and 15  $\mu\text{m}$ . No significant bonding anomalies were observed in the E-PBFed and the HIPped interface region, which potentially indicates a strong bond as was previously observed [215, 216]. However, more investigation is needed to fully understand the mechanical properties of the specimens.



*Figure 6. 12: SEM bottom shell / core interface of #15 (a) and #16 (b).*

A detailed analysis of  $\alpha$  lath widths was performed in the middle of the specimens, where an average of >20 measurements of each of the four pictures of each specimen were equally captured



between conditions. Due to the complexity and the high number of measurements taken, a similar methodology to capture  $\alpha$  lath widths in the middle of the specimens was used for each picture. This approach allowed a cross comparison of the samples analysed. Figure 6. 13 shows an example of three investigated regions captured from settings #5, #8, and #15 before and after the HIP cycle. A finer  $\alpha$  lath was measured before running a HIP cycle. The variation was attributed to the post heat treatment which tends to increase  $\alpha$  lath width and impacts the  $\alpha$  colony scale factor [217, 67]. Consequentially, mechanical properties have a reduction in TS, and UTS, together with an increase in elongation properties [218, 64].

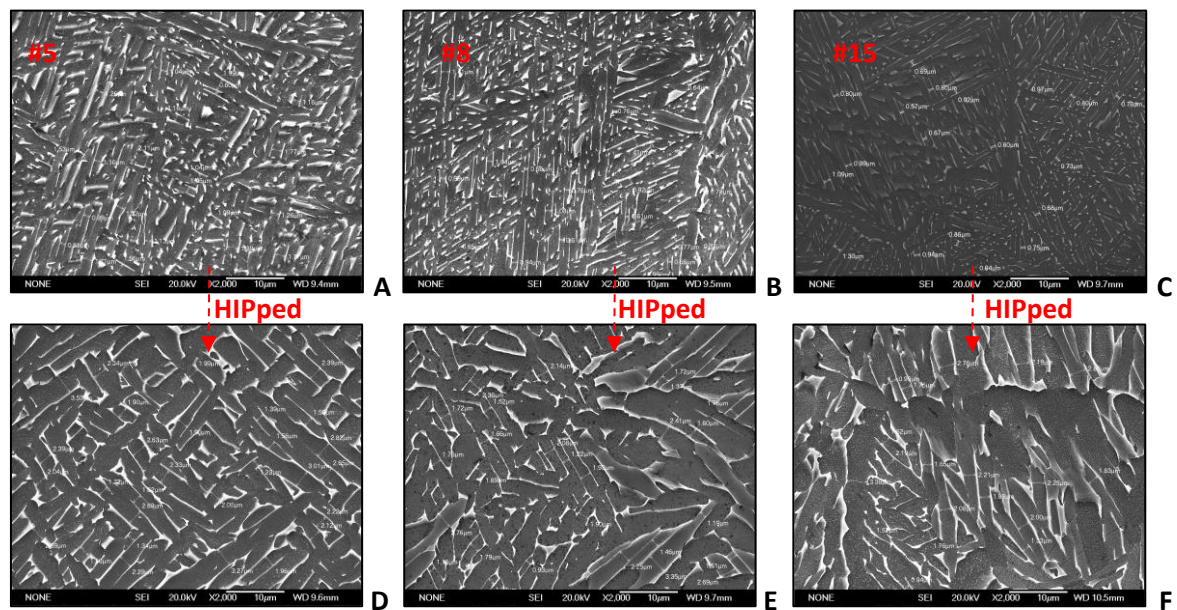


*Figure 6. 13:  $\alpha$  lath average measurement of sample #5 (a - d), #8 (b - e), and #15 (c - f) before and after HIP treatment.*

More detailed analysis of the measurements were captured in Figure 6. 14, where most of the non-HIPped samples show  $\alpha$  lath width between  $\sim 0.9 \mu\text{m}$  and  $1 \mu\text{m}$ . Samples #4, #5, #9, #12 and #13 had a value above  $1.1 \mu\text{m}$  and  $1.3 \mu\text{m}$ . More research is required to better understand this minimal increase in lath width. However, the interrelation between energy density delivered from the settings, the amount of porosity noticed, and the cooling rate are critical factors for  $\alpha$  lath width refinement. The HIPped cylinders had an increase in  $\alpha$  lath width of around 200% and more, which reflects previous studies performed in the past [199, 63]. Higher standard deviation was observed in the post HIPped samples, which is a result of the range of transformations happening during post treatment. Although variation between the samples is minimal, more investigations should be done to better understand the differences in  $\alpha$  lath width. More observations are shown in the mechanical properties section (chapter 6.2.4).



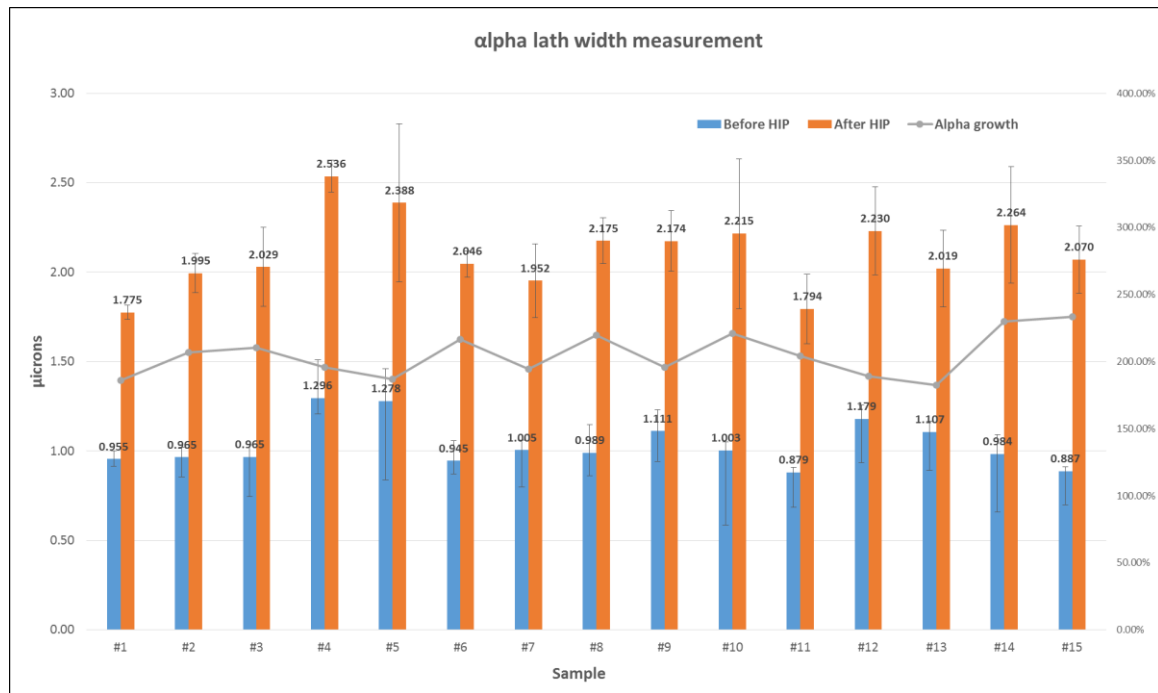


Figure 6. 14: Average measurement if  $\alpha$  lath width between different manufacturing conditions.

### 6.3.4 Mechanical Properties

Micro-hardness measurements were made before and after the HIP treatment in the core region of the specimens, where an average of nine equidistant 1mm indents in the central core region were cross compared between samples (see Chapter 3.7 for micro-hardness details). It was observed, as shown in Figure 6. 15, that the micro-hardness of as-built components was between 360 and 375 HV in all parts measured. This was slightly higher than the 340 HV measured by Kahlin et al. [179], but aligned with the study conducted in Chapter 4.2.4 and other literature [129]. There is a slightly higher hardness value on the parts that were not fully solidified (>99.5 %) after manufacturing; this is potentially due to the rapid cooling achieved using less energy density and to the voids situated inside the parts. During the heating and cooling process some differences in  $\alpha$  and  $\beta$  formation were expected, with a consequent impact on prior  $\beta$ -grain width, as reported by Narra et al. [212], where the energy density distribution and consequent beam melt pool has a direct impact on microstructural growth and properties. The influence on scanning speed and consequent energy distribution influence can also be observed in literature [33, 68, 112, 191]. However, considering such a small fluctuation between the micro-hardness results, more investigation should be done to assess the variation in properties between the as-built specimens. Hrabe and Quinn [129] conducted an investigation into tensile properties, micro-hardness, and  $\alpha$  lath thickness along the build direction of E-PBF parts, where all the results captured were very similar to the entire mechanical study of this chapter. Nevertheless, it was highlighted that the

results can vary slightly, depending on E-PBF machine and pre-heat used and intra-build variation during the process.

After post-HIP treatment an expected decrease in micro-hardness was observed, where the values oscillate between 339 HV to 355 HV, as reported in other studies [219]. The change in micro-hardness between the samples, pre and post treated, was between 2% and 8%; this variation can be significant in case of a specimen close to the minimum hardness level required from standards [106]. However, further analysis is required to fully understand the influence of hardness changes that occur during the HIP treatment and their impact on the manufactured parts.

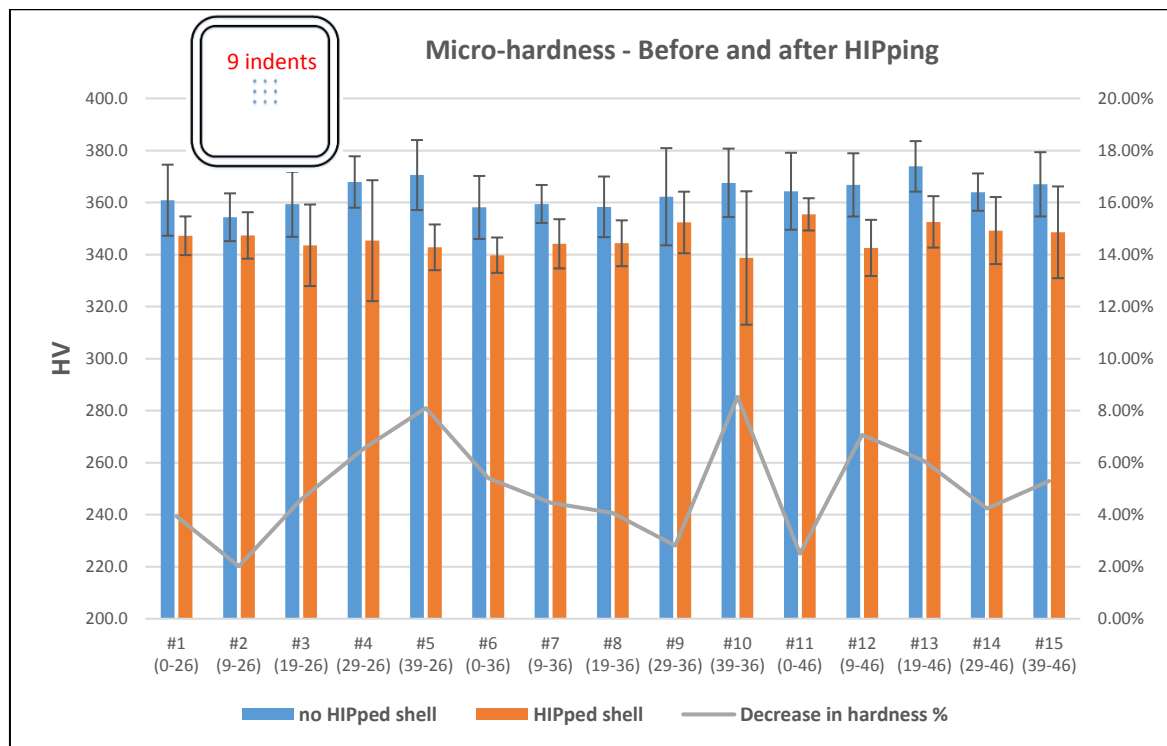


Figure 6. 15: Micro-hardness measurement before and after HIPping and indents location.

Four samples were manufactured to perform mechanical tests. Figure 6. 16 (b) shows the manufacturing approach used to make the tensile bars, where half of the specimen was fully melted (using settings #8) during the build and the other half was solidified after trapping loose powder in a shell for post HIP treatment. One of the specimens was sectioned and OM analysed (a) to capture the percentage of pores - which were almost absent - and the shrinkage obtained during the HIPping process as previously described. A high magnification OM picture (c) shows a strong bonding interface between the shell and the core; columnar main  $\beta$ -grains were observed in the E-PBFed region and rounded equiaxed grains in the HIPed section.

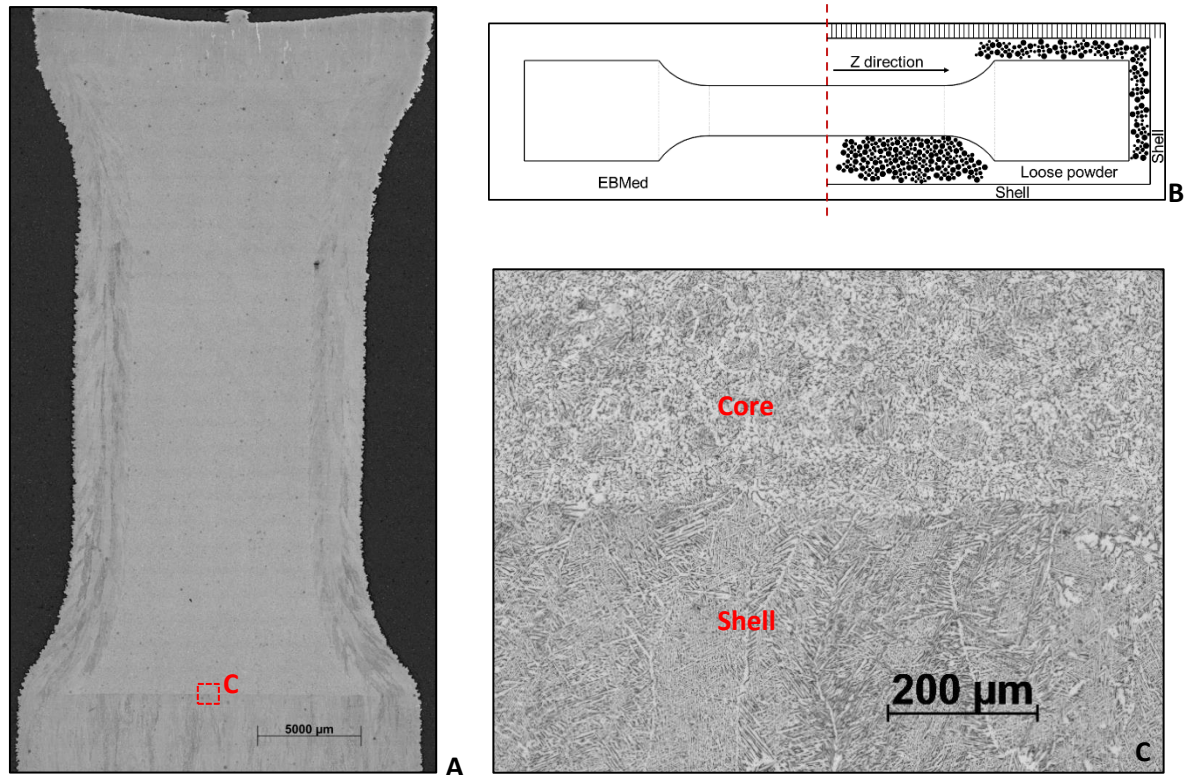


Figure 6. 16: HIPped region of a tensile specimen before being machined (a). 2D drawing of an in-situ shelling tensile bar (b), and the interface between HIPped powder and E-PBFed region (c).

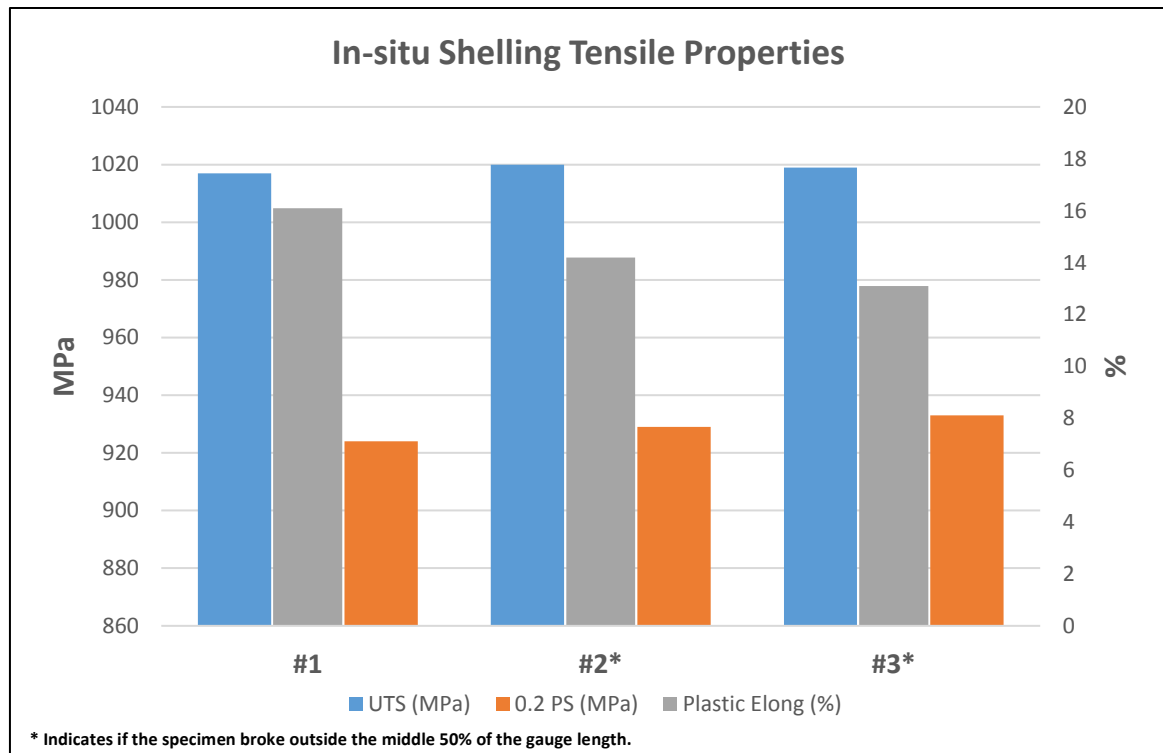


Figure 6. 17: In-situ shelling mechanical properties.

Figure 6. 17 shows the comparison of three tensile specimens tested after a post consolidation treatment. A UTS of around 1 GPa and YS above 900 MPa were measured in all the samples; the values were slightly higher in comparison to the polished HIPped samples found in literature [197, 198, 199]. A reason for this can be attributed to factors such as a potential high oxygen content into the powder used for the manufacturing of the specimens, since high oxygen content can improve mechanical properties of the material [105]. However, elongation almost above 14% was recorded for all specimens, which can be attributed to the post HIP cycle treatment which normally increases ductility and fatigue properties of a specimen [220]. Sample #1 shows an increase of 22.9% in elongation compared to sample #3, and slightly lower mechanical properties than the other samples, with the fracture outside the gauge length (#2 - #3). More investigation into oxygen content analysis, more tensile specimens, and fatigue tests need to be performed to better understand the mechanical properties and performance of the material.

Surface fracture analysis was carried out on samples #1 and #2 as shown in Figure 6. 18. The morphology of the tensile specimens was represented with half the structure solidified via the E-PBF process and half with consolidated particles HIPped below the transus zone, as shown in Figure 6. 16. Both samples show ductile behaviour (c – f), indicated by the small dimples over the whole fracture surface. No significant lack of fusion or porosity was observed in the specimens. Sample #1 (a) shows few initiation points, mainly generated close to the surface (b). From the microstructural investigation, no spherical powder shapes were noticed which could indicate a failure in the E-PBFed region. Sample #2 shows similar initiation sites in the surface region (d) with traces of spherical shapes on all the surface inspected. The ovalised shapes (e) can be a result of powder debonding during the tensile action, which can be related to the fracture that happened in the HIPped area. The difference in elongation noticed in Figure 6. 17 between samples #1 and #2 can be connected to the microstructural behaviour of the parts, where tensile oriented columnar grains have a better elongation. This is compared to the equiaxed grains generated by HIP consolidation, which can be defined as ~14%, as reported by Zhang et al. [221]. However, more trials should be performed for a statistical analysis of the mixed structure of the samples. As mentioned in literature (Chapter 2.7), no relevant investigation into this topic have been found so far.



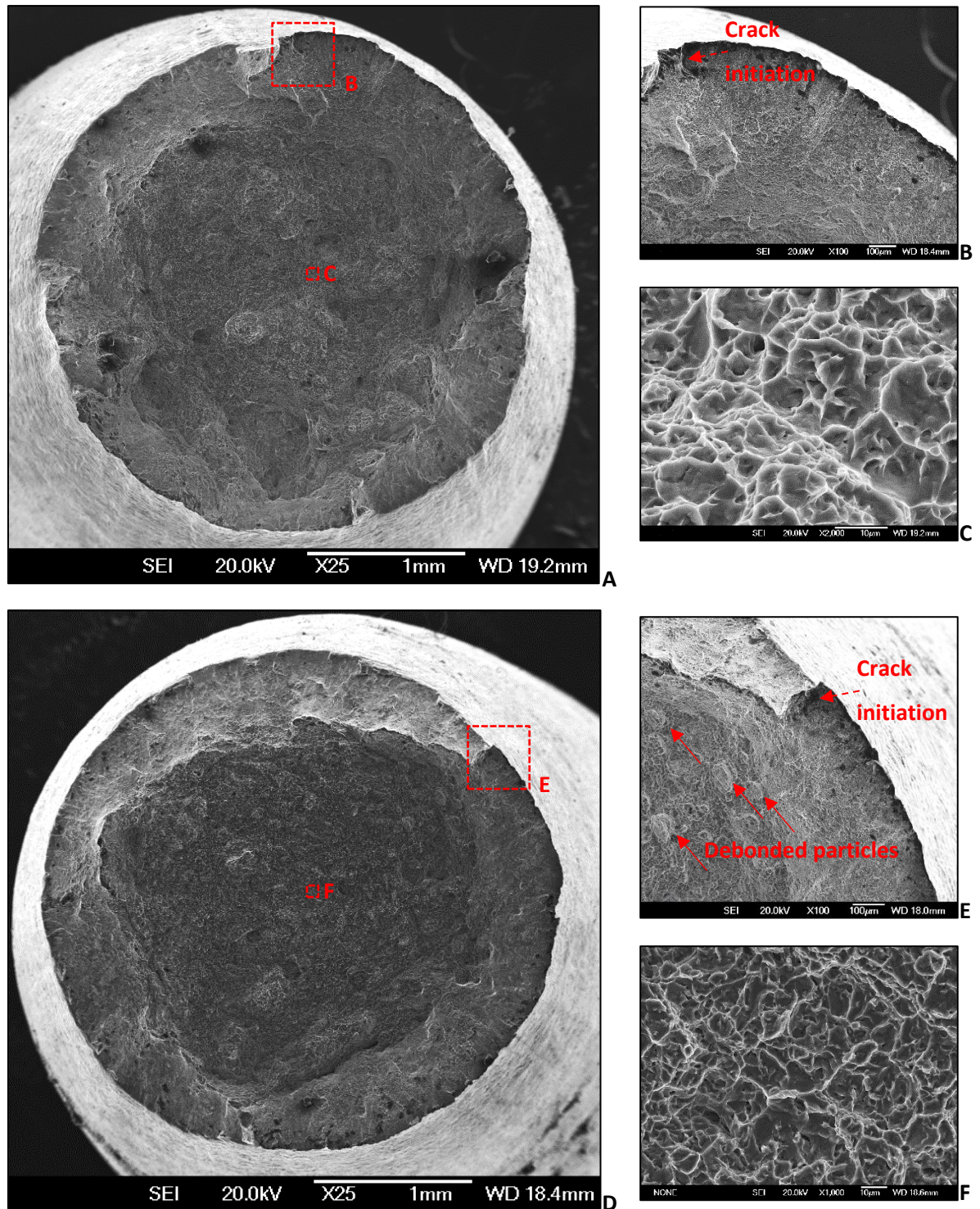


Figure 6. 18: SEM surface fracture of tensile sample #1 (a), with a crack initiation region (b), and its ductile fracture (c). Tensile sample #2 surface fracture (d), with a crack initiation region and particles debonded (e), and its ductile fracture (f).

### 6.3.5 Manufacturing Time Calculation

The running time of each melt theme was captured from the A2XX log file; the contour and hatching phase was considered for the comparison of the four cylinders manufactured, per condition. Figure 6. 19 shows the time captured in each melting condition and porosity previously measured using OM and Archimedes tests. The shells were manufactured in 10:31 sec. This number needs to be subtracted from the total manufacturing time for hatching calculations. Samples #12 - #13 - #14, which were made with a SF of 46, have the lowest manufacturing time - this can be attributed to the high scan speed delivered - but only specimen #12 showed a porosity of <0.5 %. When the BF was set to a value between 0 and 39, the manufacturing time of the specimens increased above 36 minutes. A BF between nine and 19, and a SF between 36 and 46 generated the best time vs porosity results in the table, excluding sample #7. The BF and SF in sample #7 were considered as standard settings. Its hatching time was almost 45% slower than the faster, almost fully dense, specimen (#12). More investigation needs to be done with setting #7. An adjustment of the parameters should be considered to improve the manufacturing time of the components. A BF of 39 shows poor manufacturing speed and porosity percentage so the value of 39 can be considered outside the manufacturing range.

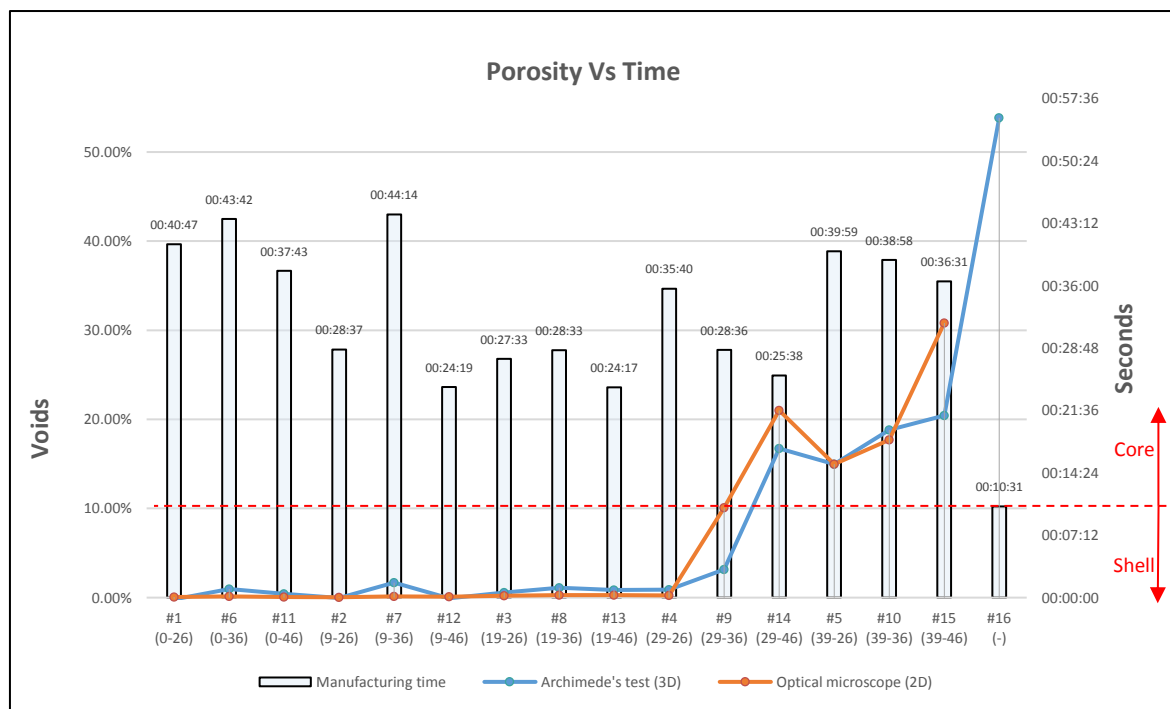


Figure 6. 19: Time Vs OM porosity Vs shrinkage of each condition manufactured.

A remarkable time was observed in sample #16, where loose powder was trapped inside the shell and no etching time was required to melt the core of the specimen. Free core melting could

drastically reduce the time in manufacturing due to the post solidification that occurs during post HIP treatment. However, the significant shrinkage that occurs during the HIPping cycle needs to be compensated for. An equiaxed microstructure is generated, in contrast to the columnar  $\beta$  grains normally observed in PBF technologies, which may change mechanical properties and fatigue behaviour. Simulation can be used beforehand to predict the shrinkage and metallurgical composition of specimens [215].

## 6.4 Conclusion

An in-situ shelling investigation is described in this chapter where different hatching strategies were used to melt the powder in a shell. The literature review revealed a gap in this area, with just a few articles touching on the topic superficially; deep investigation into mechanical properties and manufacturing of components were not found. Varying energy density by changing spot size and beam focus was used to better understand microstructural development, their properties, and advantages in manufacturing.

- Tweaking the classic skin and core procedure was the approach defined during the design of the cylinders. The benefit of using a thicker skin by increasing the number of contours (1 + 4 in total) was to allow the modification of the core settings with complete freedom. Similar studies were investigated, where laser powder bed technologies using embedded powder in a shell (SLS) [135] and canisters were to be filled afterwards (L-PBF) [215]. E-PBF articles were presented in Hamburg [139, 140] where powder was encapsulated inside a shell with different thicknesses. The preliminary investigation completed in this chapter aimed to validate the theory of changing the core settings using a fully solid shell able to resist a HIPping cycle for the solidification of the internal voids.
- A set of 16 different parameters were successfully manufactured. A range of porosities were observed through OM and Archimedes in the cylinders before post HIP treatment. A density of >99.5% was observed in all post heat treated samples. The In-situ shelling approach can be used for the manufacture of parts in E-PBF.
- Two out of three samples #16, with loose powder, did not shrink during the HIP cycle. The cause was mainly attributed to the holes located at the top of the shell, due to the overhanging design and consequent imperfection during solidification [164, 33]. A design improvement needs to be considered for future manufacturing.
- Good bonding was noticed between the skin and the core after the HIP treatment in the bottom, side, and top region of the shell.



- In components with high percentage of pores, columnar grains generated from the skin region were broken up in the interface area between skin and core. The core showed broken columnar grains along the Z axis due the random distribution of pores which stopped the growth of the grains.
- The hatched region demonstrated combined randomly columnar and spherical grain structures, noted after a HIP treatment. The mixture of structures was a result of the heat and pressure applied in post treatment. It differs to the conventional microstructure noticed in PBF components.
- The range of parts generated with different variables all displayed similar micro-hardness and  $\alpha$  lath thicknesses, with no notable differences before and after a HIP treatment. Microstructural changes were observed between the specimens after post HIP treatment; no major differences were found between them and the available literature.
- Tensile tests showed good bonding interface between the E-PBFed part and the fully solidified powder particles. Similar properties were observed with the cylinders. Slightly improved mechanical properties were noticed, the high level of oxygen contained in the powder can be considered the potential reason of the values recorded. However, all the results were above F2924 standards [106].
- Given the manufacturing time and mechanical properties of the parts built, it might be possible to optimise the parameters in order to reduce production time. Better productivity could increase machine turnaround with a corresponding reduction in manufacturing cost.

## **Chapter 7: Hybrid Manufacturing in E-PBF**

### **7.1 Introduction**

In previous chapters, hardware investigation and part analysis were explored. Topics such as machine fundamentals and advance part solidification were discussed. These experiments allowed for the full investigation of part production and advance methods needed to achieve them.

Due to the maturity of the E-PBF technology, interest in its application in hybrid manufacturing is rising (see chapter 2.8 for further details). More options in terms of material and process development are being developed to provide more flexibility and solutions whilst manufacturing parts with an E-PBF system.

This chapter investigates hybrid manufacturing using the starting plate as an integrated part of the substrate. Literature has been considered to gain insight into its demand in the market and the advantages of being in a vacuum environment which can facilitate the bonding between the materials and consequently the mechanical properties.

Two experiments were performed using different Ti - 6Al - 4V grade 5 hot rolled and annealed substrate starting plates of 10 mm and 40 mm thick respectively. Both have a surface area dimension of 170 x 170 mm which is the standard Arcam A2 size; the area of preheating and melting were set according to the Arcam A2 platform. The first 10 mm thick substrate was used to better understand the characteristics of the first few layers whilst modifying some machine settings, the starting plate condition and the beam focus in order to analyse the bonding characteristics achieved with the substrate. The 40 mm substrate was then used to manufacture tensile specimens with the optimised settings analysed during the first build. Microstructural and mechanical property evaluations were performed to capture the main values between different conditions.

The following chapter intends to:

1. Define E-PBF settings required to achieve strong bonding between the starting plate and the first few manufactured layers;
2. Understand what is achievable with this new approach and its pros and cons;
3. Investigate the microstructural and mechanical properties of the manufactured components.

## **7.2 Experimental Procedure**

### **7.2.1. Substrate Preparation**

In order to vary the bonding interface between the substrate and the powder solidified by E-PBF, the substrate was equally divided with four surface conditions: as manufactured, Kroll etched, shot peened, and laser re-melted. The different surface treatments generated four different microstructural conditions on the surface with different characteristics described as follows:

- As manufactured represents the normal bonding condition without any advance surface treatments; the substrate was cleaned using the standard procedure used with conventional starting plates and builds.
- Etched condition was made by swabbing wetted cotton (>10 sec) in a Kroll's reagent in a quarter of the starting plate. The etchant attacks the microstructure which helps to relief the

surface strains caused by cutting. Potential benefits from a solid state diffusion prospective can be generated.

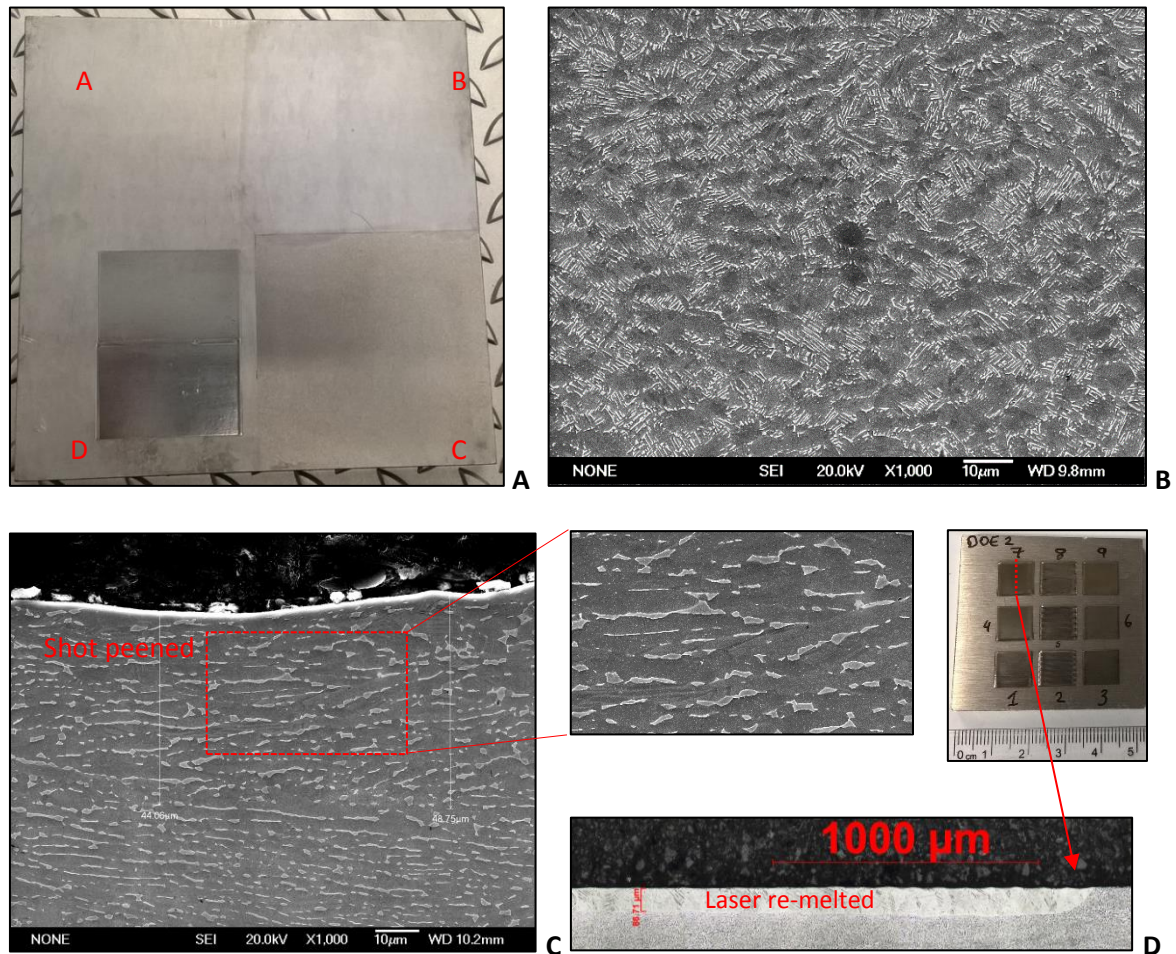


Figure 7. 1: E-PBF starting plate with 4 different substrate conditions (a). SEM region of the starting plate microstructure (b). Y - Z SEM section of peened surface and its plastic deformation length (c). Preliminary DOE studies to capture the laser re-melted region of DOE 2, and a Y - Z OM section of variable 7 and its  $\sim 86 \mu\text{m}$  re-melted region (d).

- Compressive stresses were introduced using a shot peening system. The compressive stresses usually achieve a plastic deformation impact normally less than  $100 \mu\text{m}$  deep, shown for Ti - 6Al - 4V, as reported in literature [222]. Figure 7. 1 (c) shows the elastic bands generated after the shot peening treatment which could benefit at recrystallization level. This would balance the stresses in the interpass region, reducing potential distortion.
- Several designs of experiment (DOE) were performed with a direct energy deposition system using focused laser beam in order to achieve a re-melt surface thickness equal or superior to the re-melted region achieved in E-PBF, which is  $\sim 100 \mu\text{m}$  (using a A2XX system) depending on settings [121]. Due the limitations in the re-melted region, achievable with the laser system

and its shielding device, two overlapped areas of 50 x 35 mm were made to create a total laser re-melted region of 65 x 50 mm. Figure 7. 1 (d) shows the re-melted region achieved during preliminary re-melting tests on a Ti - 6Al - 4V cold rolled 10 mm thick plate. A value of 30  $\mu\text{m}$  hatch space, 66 % overlap, 300 mm / sec speed, 425 W laser power, and a bi-directional/zig-zag path with blown pure argon on the surface was enough to achieve a re-melted zone twice as deep as the EB layer thickness. The aim of the laser re-melted structure was to vary the bonding interface between substrate and E-PBFed part.

Flatness of the substrate is considered an important variable during normal builds. Given the scope of the hybrid build of re-melting a starting plate surface region, it is reasonable to suggest that the flatness of it should be less than the thickness of the layers (70  $\mu\text{m}$ ). If it is outside the mentioned tolerance, the powder will not be evenly spread on the starting plate surface due to consequent risk of issues during the melting of the first few layers or potential faults taking place during the raking stage.

*Table 7. 1: Surface roughness (Sa) captured in different surface condition and starting plate thickness.*

	<b>10 mm (<math>\mu\text{m}</math>)</b>	<b>40 mm (<math>\mu\text{m}</math>)</b>
As manufactured	0.99	1.99
Etched	0.99	1.99
Shot peened	1.86	2.31
Laser re-melted	0.75	0.75

Surface roughness does not have a big impact on spreading the powder on the starting plate surface. Given that, having different surface treatment conditions, the starting plate resulted of having different surface roughness that were captured and quantified in Table 7. 1. It is notable that the thicker 40 mm plate has a rougher initial surface compared to the 10 mm thick plate which does not change, in both cases, after the Kroll's etch treatment. The peening treatment decreases the surface roughness due to superficial compressive deformation taking place during the ball's impact on the substrate creating a rougher surface. After performing the laser re-melting treatments, the surface conditions showed improved and similar roughness compared to the raw material. With reference to the conditions achieved before the build, it is possible to assert that the powder may change its rolling properties depending on the surface behaviour of the treated conditions.

### 7.2.2 Software and Parameters

During the generation of the build file, the Arcam A2 starting plate settings were used. This allowed the system to calculate the energy density needed in a 170 x 170 mm plate compared to the standard 350 x 200 mm version conventionally used with the A2XX system. The selection of the envelope was achieved through the Magics software which automatically calculates the energy density and the consequent heat balance needed for the manufacture of the reduced build size.

After the modification of the substrate with four different superficial conditions, three different beam focus conditions during melting were considered to better understand the impact of them in terms of energy density and bonding interface characteristics. The standard beam focus condition of 9 mA has been used as a reference value. In order to vary the standard value, two sets of variables below and above the standard value were identified. On top of the standard value of 9 mA, a beam focus of 0 and 19 mA were selected to be performed on each substrate condition with the manufacturing of four cubes per variable.

Preheat 1, preheat 2 and contour themes were kept the same for all the cubes. Table 7. 2 shows the standard hatch settings used for the manufacturing of the cubes. Parallel “snake X - Y” hatching scans were adopted during the melting of the layers with a 90° rotation between each layer.

A constant current of 60 kV and a layer thickness of 70 µm was used during the build. On top of the three different E-PBF beam focus conditions (0 - 9 - 19 mA respectively), a constant SF of 36 and a fixed line offset value of 0.2 mm during melting was used.

*Table 7. 2: E-PBF hatch settings used during the hybrid builds.*

System	Preheating T (°C)	Line order	Line offset (mm)	Constant current (kV)	Beam current (mA)
A2XX	720	15	0.2	60	30

### 7.2.3 DOE Preparation of the Substrates

As introduced earlier, two different builds were made to better understand the bonding characteristics between the substrate and the AMed parts and to capture the mechanical properties. PA powder 45 - 106 µm from TLS was used to manufacture the parts with an A2XX Arcam E-PBF system. The first build, also known as DOE 1, had a 10 mm thick starting plate and

was used to analyse the mechanical bonding between different beam offset and starting plate preparation. Four 10 x 10 x 8 mm cuboids were manufactured for each beam focus variation (0 - 9 - 19 mA) and surface condition. A grand total of 48 cuboids were made. Figure 7. 2 shows the Ti - 6Al - 4V starting plate with four different A - B - C - D surface regions, where 12 cuboids on each condition where manufactured. Numbers 1, 2, and 3 represent the different beam offset 0 - 9 - 19 mA respectively used during the build.

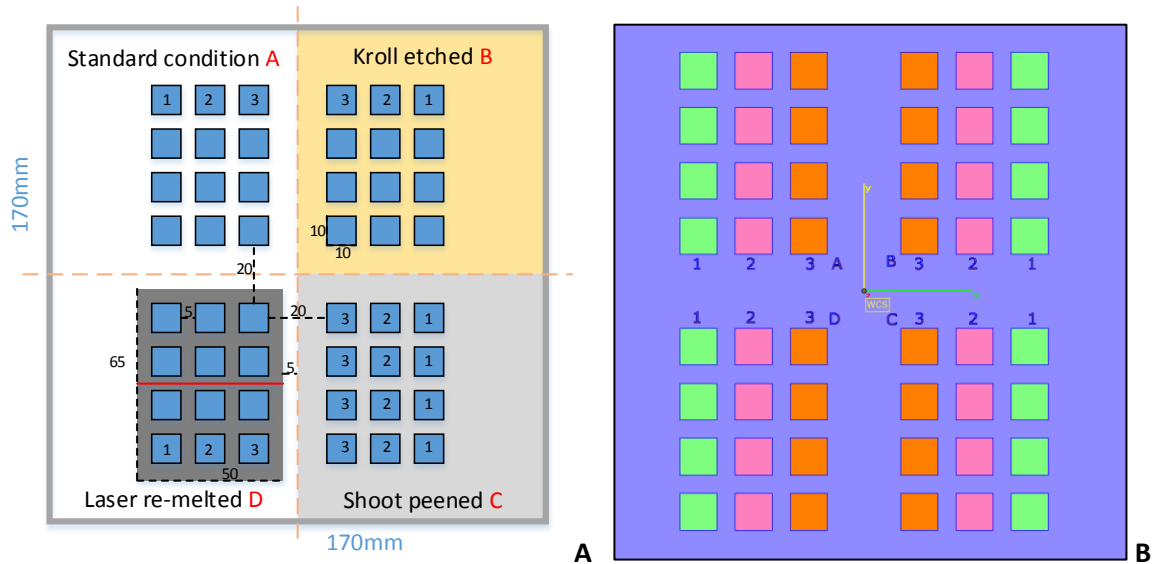


Figure 7. 2: DOE 1 substrate design with cube designation numbers (a), Magics snap shot of the starting plate with substrate treatments and cuboids location before the E-PBF build (b).

After the first build of 48 cuboids and its post analysis, a second build with a starting plate of 40 mm thickness was designed with tensile specimens. Figure 7. 3 (a) shows the location of horizontal and vertical tensile bars built in different locations of the substrate during DOE 2. The aim of the design was focused on leaving the interface region close to the centre of the gauge length for the vertical tensile ones, and asymmetrical (along the specimen axial) for the horizontal specimens. Vertically oriented 3 mm thickness in-situ shells with enclosed powder were manufactured to encapsulate loose pre-sintered powder to be HIP treated afterwards. The thermal post process allows for consolidation of the loose powder and the consequent ability to generate the tensile specimens. A pre-selected melting theme, from DOE 1, was used to perform all the tensile bars during DOE 2, the reasons for which are explained in the following chapter.



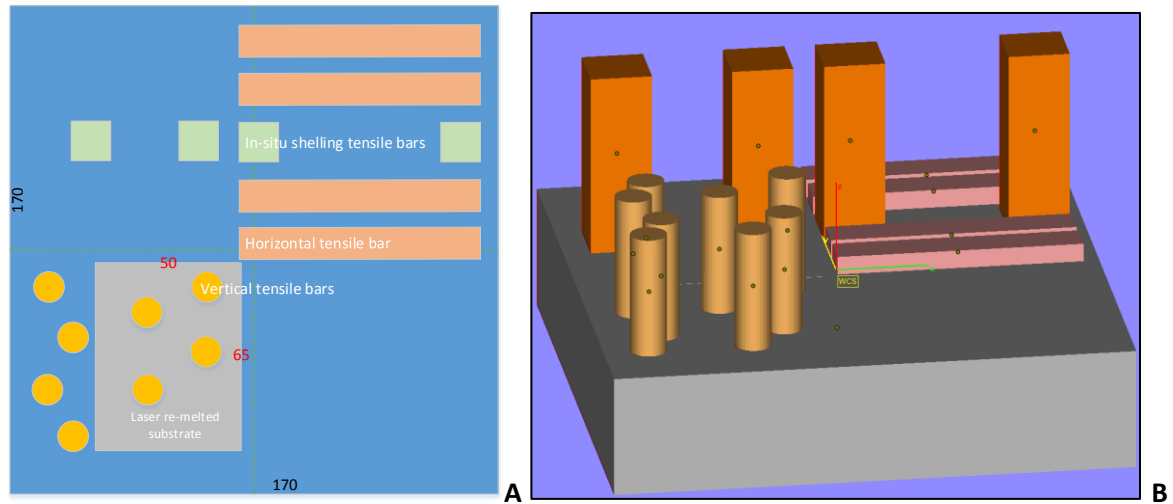


Figure 7. 3: DOE 2 substrate design with tensile bar descriptions (a), Magics 3D snap shot of 40 mm starting plate and tensile bars location before the E-PBF build (b).

## 7.3 Results and Discussions

### 7.3.1 Parts Manufacture

After preheating the starting plate, layers were spread upon each other using a standard melting contour strategy. As Figure 7. 4 shows, 48 equally spaced 10 x 10 x 8 mm cuboids were completely manufactured on a Ti - 6Al - 4V substrate with dimensions of 170 x 170 x 10 mm. The build showed a lack of fusion at ~0.7 mm from the starting plate, which was observed in the central region of the build. Visual inspection does not show other issues.

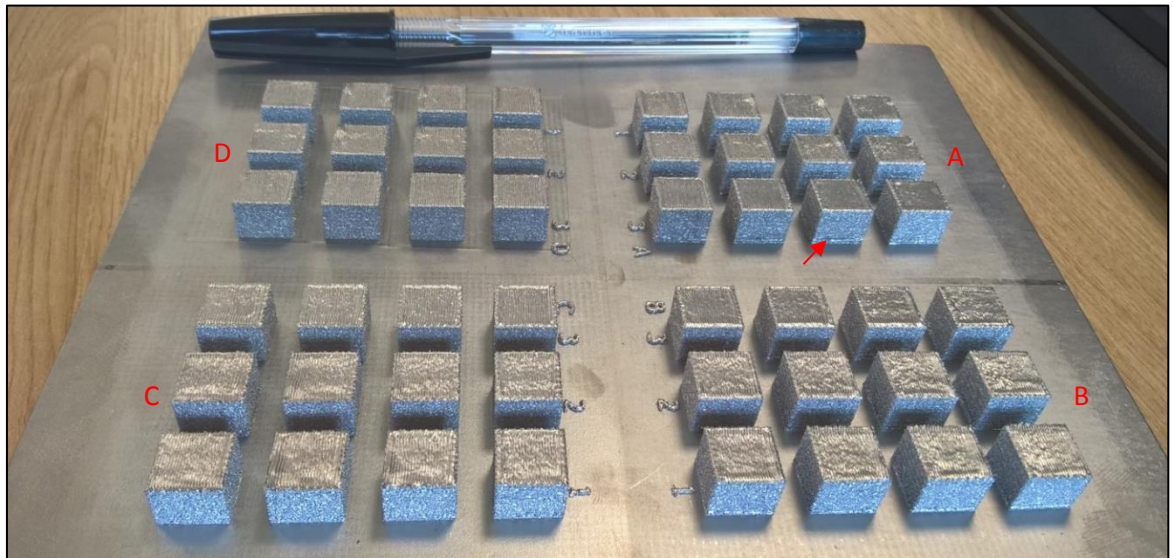


Figure 7. 4: 48 cuboids manufactured on a Ti - 6Al - 4V substrate, lack of fusion observed.



The manufacturing of the second build (DOE 2 - Figure 7. 13), with a substrate of 170 x 170 x 40 mm, was successfully accomplished. No defects were noticed after a visual inspection analysis. Both of the substrates were cleaned from the semi-sintered powder using the PRS, and a consequent visual inspection was undertaken to capture potential imperfections occurring during the manufacturing of the parts.

### **7.3.2 Starting Plate Post Analysis**

The analysis of the DOE 1 starting plate revealed that by preheating the substrate at 720 °C, a complete stress relief took place which had an impact on the different substrate conditions. As shown in Figure 7. 5 (a), no traces of deformation bands were observed below the shot peened surface. By raising the substrate above 720 °C for more than 2 hours, all the compressive stresses were released. That said, it is possible that the normal, etched and shot peened surface conditions had the same metallurgical behaviour before melting the first AMed layer. The laser re-melted region shown in Figure 7. 5 (b) was around 30 to 40 µm, which was three times less than the length planned. The reason for the low penetration achieved was mainly due to a poor laser offset calibration, which resulted in less energy density per area with a consequent reduction in the re-melted region.

After heating the 10 mm thick substrate to 720 °C, it was clear from the powder spread on it through the rake that the substrate was not completely flat, as it was sitting mainly in the central region of the starting plate. The convex shape observed was probably generated after the mechanical shot peening and the laser re-melting treatments, previously carried out on the substrate, generating residual compressive stresses on the top substrate and a consequent convex deformation of the plate. Despite that, the build started and ended without major issues. After the cooling down of the system, the substrate (Figure 7. 5 (c)) had a final bending curve of 2 mm deep from the side to the middle of the substrate. The complete distortion may have occurred because of the low cooling rate of the material in the chamber, which relieved the residual compressive stresses generated during the mechanical treatment.

The second build, using a substrate 40 mm thick, did not show any superficial curves or bends. The thickness of the substrate probably managed to localise the residual stress generated during the surface treatment processes just in the top region of the starting plate, avoiding important deformation of the entire substrate. However, having a thick substrate led to other issues such as the pre-heating T reading. In fact, the thermo-couple located at the bottom region of the starting plate had a slow response from the heating up of the starting plate during the pre-heating phase

of the machine. The delay time allowed, to transfer the heat from the top heated region to the low area of the starting plate, was very slow and difficult to capture. After following the G. Mandil et al. technique [150] of capturing the transition T from the heated area to the bottom region, and waiting for the heat to transfer to the bottom, we decided to change the technique due a lack of efficiency. From the experience of the operator, the pre-heating phase was manually stopped above 700° C, to allow the build to commence. Otherwise, no other problems were found during the entire build cycle. A summary of the substrate findings are shown in

Table 7. 3

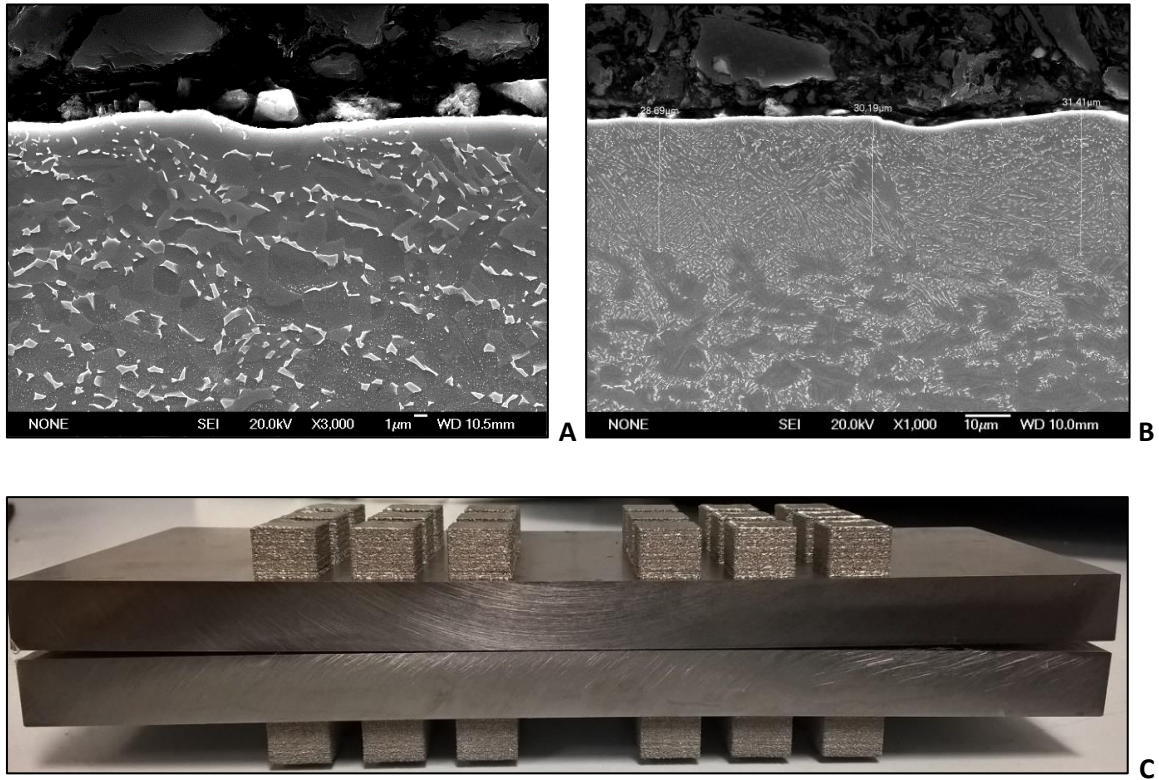


Figure 7. 5: SEM pictures of shot peened C1 substrate (a), laser re-melted region on sample D1 (b), bended substrate after being stress relieved during the build cycle where substrate was cut and overlaid (c).

*Table 7. 3: Summary of findings observed in the substrates and their conditions.*

	<b>Main findings</b>
<b>10 mm substrate</b>	<ul style="list-style-type: none"> <li>-residual stresses were generated during shot peening and laser re-melting treatments</li> <li>-substrate distortions were achieved after being stress relieved in a E-PBF cycle</li> </ul>
<b>40 mm substrate</b>	<ul style="list-style-type: none"> <li>-issues on capturing pre-heating T due to substrate thickness</li> <li>-no distortion observed after the completion of the build</li> </ul>
<b>Standard condition</b>	-no relevant findings were noticed
<b>Etched condition</b>	-no relevant findings were noticed
<b>Shot peened condition</b>	<ul style="list-style-type: none"> <li>-deformation bands disappeared after being heated up &gt;700° C during the build cycle</li> <li>-the compressive stresses disappeared during the build</li> </ul>
<b>Laser re-melted condition</b>	<ul style="list-style-type: none"> <li>-poor re-melted region generated during the laser treatment due to issues with machine settings</li> <li>-refined lamellas compared to substrate were observed in the re-melted area</li> </ul>

### 7.3.3 Microstructural Characteristics

Metallurgical analysis was performed in the bonding region of the substrates where the melting penetration achieved in the “contour theme” zone reached more than 200 microns on all specimens in a region around 0.7 - 0.8 mm from the side wall. As observed in Figure 7. 6, two beam lines are fusing the contour region using two different beam energy and speeds, which resulted in the internal contour line having higher dilution compared to the external one. The contour theme zone reached a maximum dilution of more than 200 microns on all specimens in a region of around 0.7 - 0.8 mm from the side wall.

Figure 7. 6 shows a constant linear penetration of the AMed material into the substrate around 130 microns (specimen B2) that linearly happens along all the fusion region fused by the “melting theme”, which is almost double the E-PBF layer thickness. The fused material into the substrate is a combination of the powder spread on the first layer and the re-melting of the substrate. Similar microstructure was noticed in all three beam conditions applied and the substrate pre-treatments. The change in BF and substrate pre-treatment did not influence the re-melted region observed.

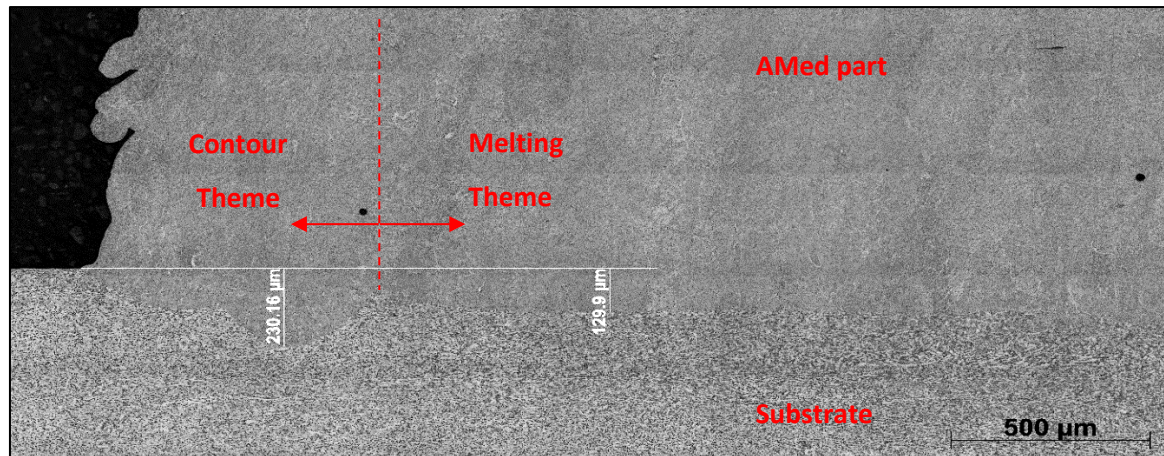


Figure 7. 6: OM region between substrate and deposited region of the etched B2 cube.

As previously observed, Figure 7. 7 (a) shows a lack of fusion around 0.7 mm above the starting plate along the mid region of the layer. The SEM picture (b), extracted from sample C1 lack of fusion (a), illustrates the missing fusion of few powder particles generating a reasonably big horizontal void, which can potentially generate critical issues in cases of mechanical stresses. The lack of fusion was due to a process instability (potential powder spreading inconsistency issues [38]). In order to solve this issue it is possible to run a HIP cycle to reduce the pores and homogenise the structure [67].

Figure 7. 7 (c) shows columnar grains starting from the fusion area which represent the typical prior  $\beta$ -grain observed in powder bed technologies [121].  $\alpha + \beta$  structure was noticed all along the structure where prior  $\beta$ -grains grows following the vertical direction of cooling [120]. HAZ was noticed below the fusion zone with minimal impact on the starting plate quantified as less than half millimetre (Figure 7. 7 (d)).

The bonding region does not show neither porosity nor micro-cracks. Smooth curves were observed along the solidified boundary area as shown in Figure 7. 8 (a). The boundary line is well defined between the coarse substrate microstructure and the refined basket-weave microstructure, where a rounded dilution from the electron beam impact is observed. Figure 7. 8 (b) shows the interface between the AMed part and the laser re-melted substrate; it was noticeable that both surface regions have refined grains and a strong microstructural bonding which may increase the welding toe strength and reduce potential cracks in the additive/substrate intersection. The interface below the re-melted region does not show bonding imperfections. Prior  $\beta$ -grains were observed just below the bonding line where the heated affected zone is; Figure 7. 8 (c - d) shows the growth of  $\alpha$  grain boundaries from the HAZ, growing into the re-melted region of



the component. They were generated during an increase in T of the substrate which reached more than 1000° C, above the beta transus, where main  $\beta$ -grain recrystallize. In some areas it seems that the  $\beta$ -grains generated in the HAZ region are going through the re-melted zone and continue their growth in the first AMed layer, which means that a strong bonding interface was generated. Successful fusion was observed in all the specimens which showed very similar bonding interface. Deeper investigation should be performed to capture the bonding differences between substrate preparations.

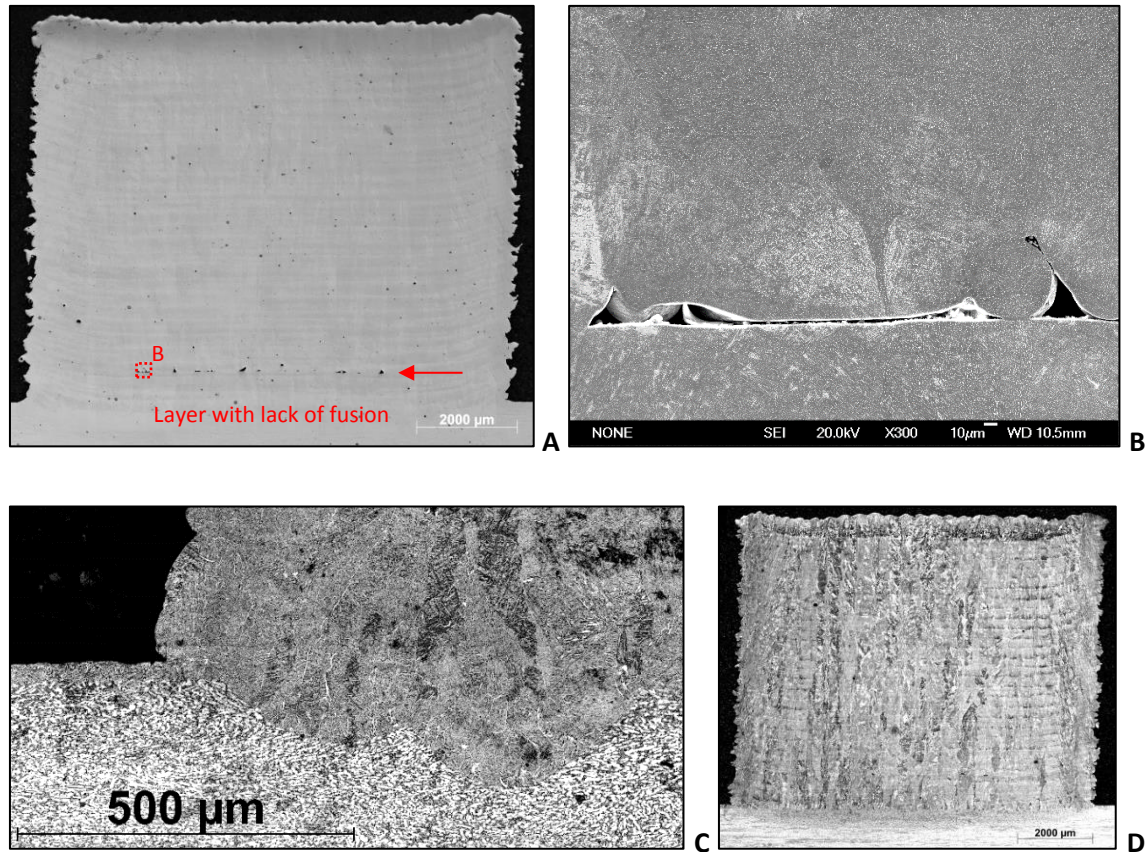
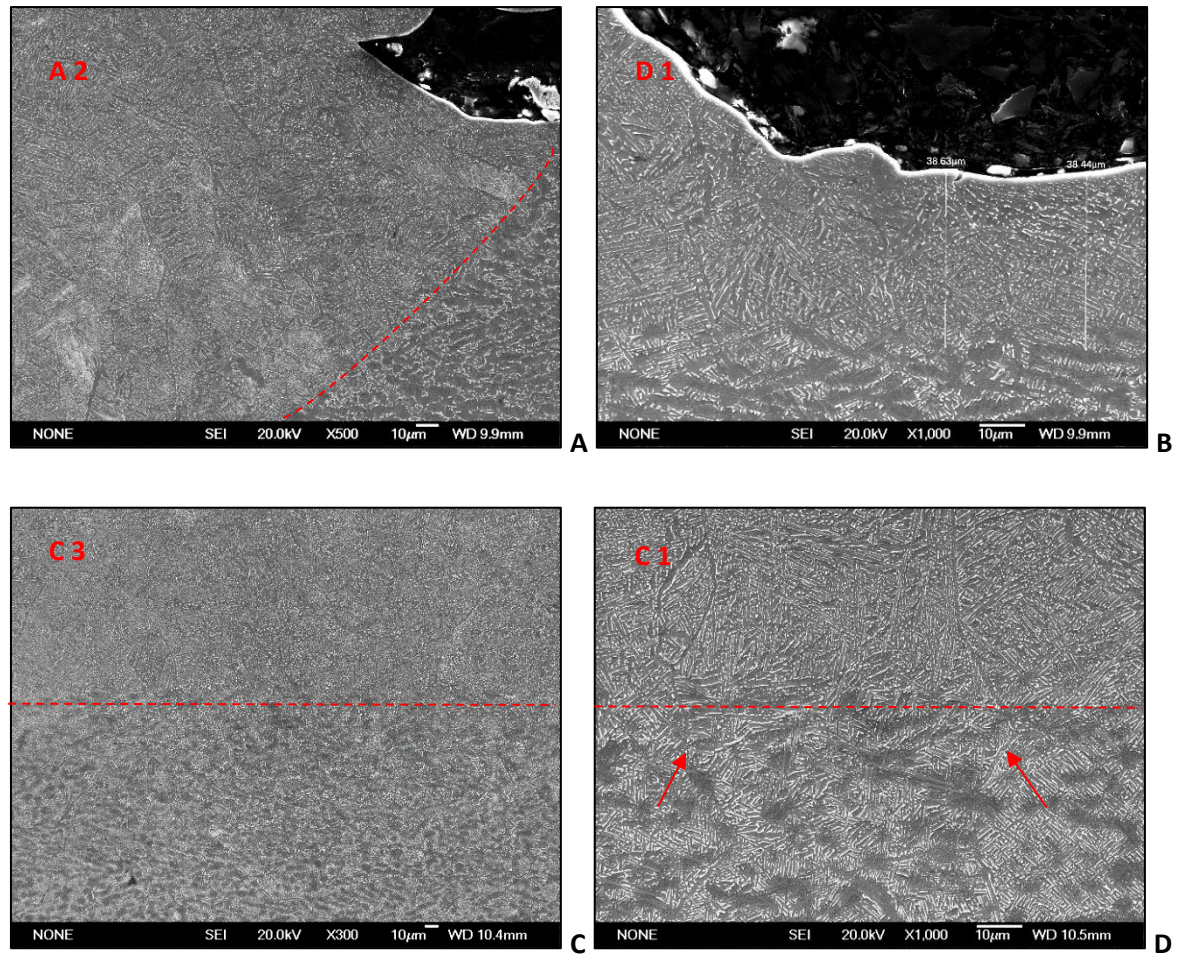


Figure 7. 7: OM sample C1 X - Z plane section (A), SEM lack of fusion from sample C1 section (B), OM EB penetration and microstructure from the laser remelted D3 substrate (C), OM mosaic of etched D2 part (D).



*Figure 7. 8: Fusion zone of bottom left X - Z A2 sample section (a), laser re-melted bottom left X - Z D1 sample section (b), central fusion interface of sample C3 (c) and C1 (d) with main  $\beta$ -grains growing through the fusion zone.*

### 7.3.4 Beam Focus Influence

Beam focus (BF) measurements were captured to better understand the changes and properties of the beam between the three different conditions used during DOE 1 (0 – 9 – 19 mA). Four specimens per condition, as Figure 7. 9 (a) partially shows, were manufactured. Beam size, line overlap, electron beam penetration into the starting plate and X – Y axis surface roughness were cross compared between the BF conditions. A study of the variables was carried out taking the average of at least three samples of each condition. All analysis was performed using OM and SEM.



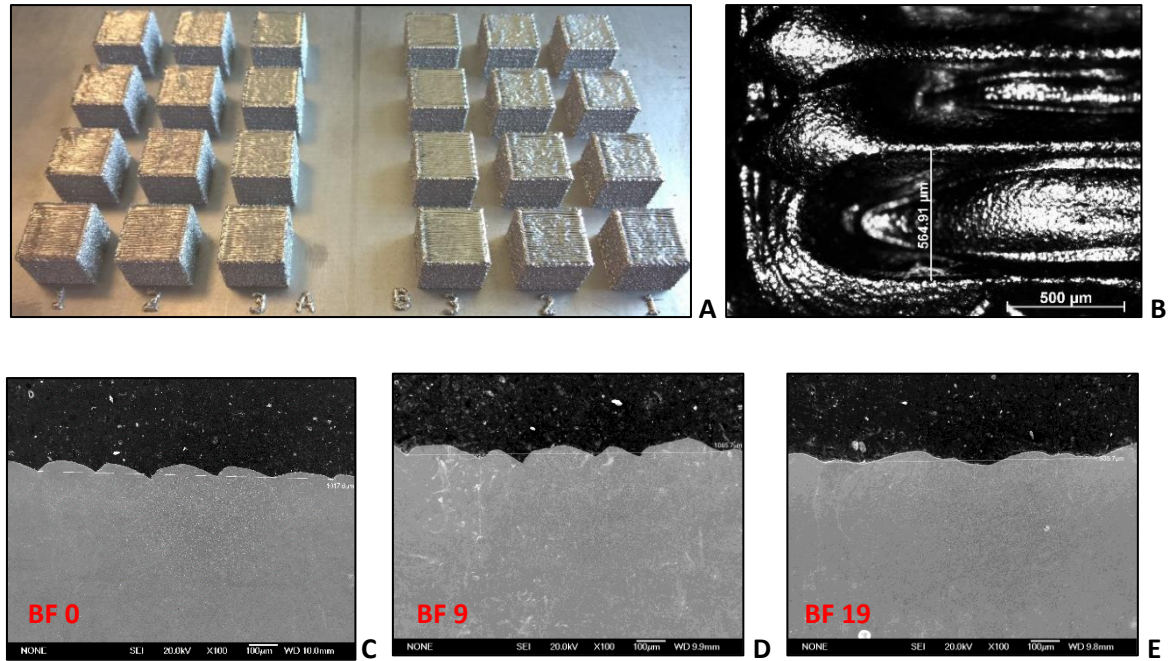


*Figure 7. 9: Close image of half of the cuboids analysed during the BF investigation (a), A2 top line scan measurement captured with OM (b). SEM cross section pictures of A1 (c), A2 (d), and A3 (e) top surface with relative overlap measurements.*

Top OM surface pictures of the specimens (Figure 7. 9 (b)) were taken to compare the beam size achieved on the top layer. Figure 7. 9 (c - d - e) shows the comparison of the taken measurements, where a similar overlap between specimens of around 200 μm was observed. Slightly bigger beam size dimension in condition BF 19, where a re-melted region of ~ 650 μm was observed, around 40 μm bigger than the melting achieved from BF 0 and 9. The last melted line of the cuboid's top surface was bigger in BF 19 condition due to an increased size of the defocused beam, which has a larger energy distribution that allowed a wider melted surface [223]. BF 0 and 9 show a similar beam width condition, which can be connected to a sharper beam spot size achievable with the A2XX coils and a consequent reduction in width if compared to the defocused BF 19 condition (similar studies and results can be found in literature [111, 126]).

It is possible that the beam overlap of 0.2 mm, fixed from the machine settings, shown in Figure 7. 9 (c - d - e), was confirmed between the BF parameters. The pictures display a different surface distribution between the different BF conditions, where their waviness decreased from BF 0 to BF 19. To better understand the results, a top middle surface area of 2 mm<sup>2</sup> investigation was performed to capture the surface roughness (Sa) comparison between samples. An average measurement of three samples of each condition was calculated. As Figure 7. 10 shows, a surface roughness of 15.35 μm, 17 μm, and 10.52 μm was captured from 0 - 9 - 19 BF respectively. BF 0

and 9 show a very close connection as demonstrated in the previous BF observations. The reduced roughness measured from BF 19 can be explained by a factor of energy density distributed on the surface. In fact, having a larger beam size with less energy density may result in less turbulence during the melting of the material with a smoother solidification phase, which decreases the surface roughness of the solidified powder. The results captured can be referred to top surface Sa measurement found in literature [224, 8].

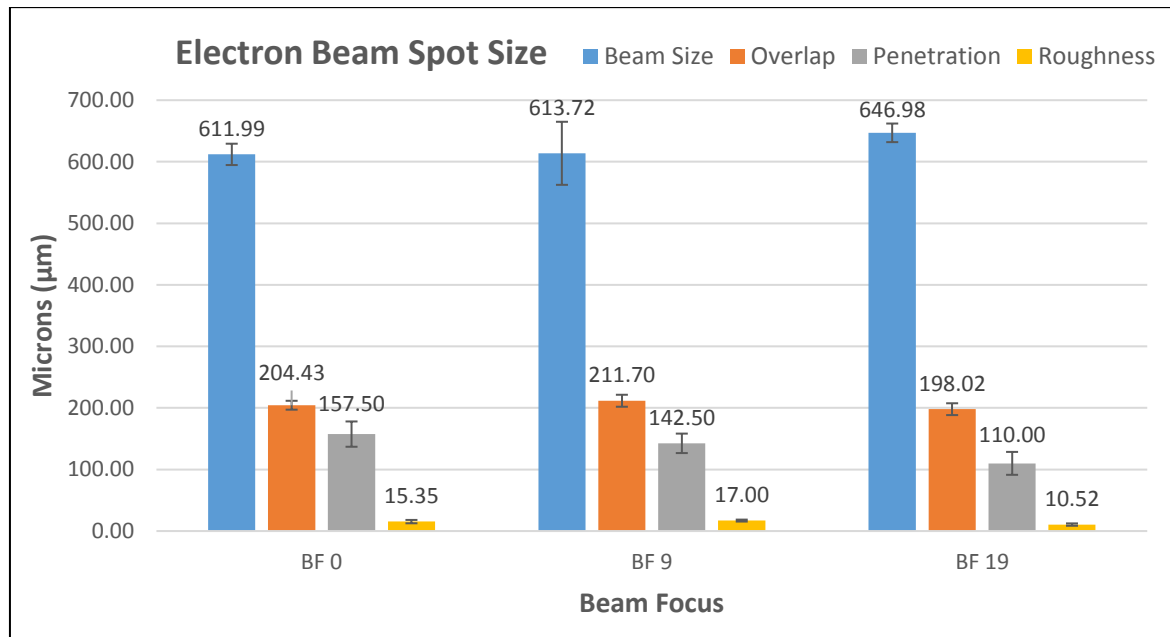


*Figure 7. 10: BF influences measured in the build.*

Beam penetration was captured measuring the length of the dilution into the starting plate after polishing the samples along the building direction, which can also be called melted region or fused area. The interested zone has a continuous linear dilution along the substrate in the hatch region as shown in Figure 7. 6. The measurements shown in Figure 7. 10 show an average of around 150 μm for the 0 and 9 BF condition and a penetration of 110 μm for the defocused 19 mA condition. The lower dilution of BF 19 can be connected to the reduced energy density achieved with a defocused beam, with a consequent reduction in energy density and dilution as reported above. Despite this, the interface between the starting plate and the first layer has the same microstructural bonding independent of the 3 BF conditions used. Similar hybrid studies [142, 150] show a good bonding interface between Ti - 6Al - 4V to Ti - 6Al - 4V and In 718 to 316 SS, and vice versa.

### 7.3.5 Micro-Hardness

Figure 7. 11 shows the location of indents captured from a sectioned X - Z plane in the middle of Y thickness, using a load of 200 g. They run from 0.4 mm above to -0.7 mm below the fusion area in order to cover the hardness changes between the AMed part and the starting plate/substrate after the addition of the materials on top.

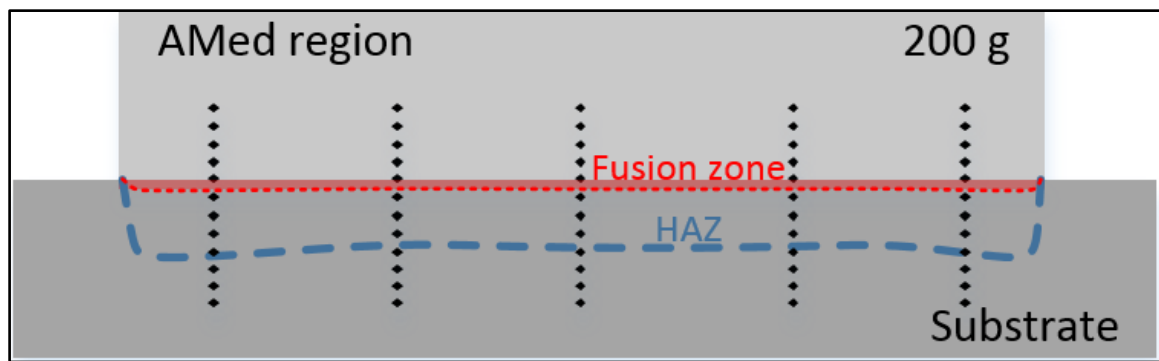


*Figure 7. 11: Equispaced 200 g micro-hardness indents.*

Figure 7. 12 shows the average hardness value and its trend line running from the AMed surface to the starting plate. It is possible to observe that the AMed region has a value around 390 HV which then increases to 400 HV close to the fusion region (which is similar [8] or slightly above literature values [62]), identified around the 0 mm bonding region. The increase in hardness is probably due to the rapid cooling rate achieved by dissipating the heat to the starting plate. This helps to rapidly cool the first layers with a consequent reduction in  $\alpha$  lath width and an increase in micro-hardness. However, the contamination of material explained in literature [119] and in chapter 4 may also contribute to the change in hardness located in the first few layers. The HAZ, quantified after the fusion region, runs around half a millimetre below the bonding region. It is represented by a high level of hardness close to the fusion region, where the material had a refinement of grains whilst heating up and cooling down the material, which decreased proportionally to the HAZ area and its heating influence. The Ti - 6Al - 4V starting plate, without thermal influence from the AMing process, has a hardness value of just around 350 HV (as referenced in literature [219]). The micro-hardness of the starting plate captured during DOE 1 was assumed as a constant for the DOE 2.

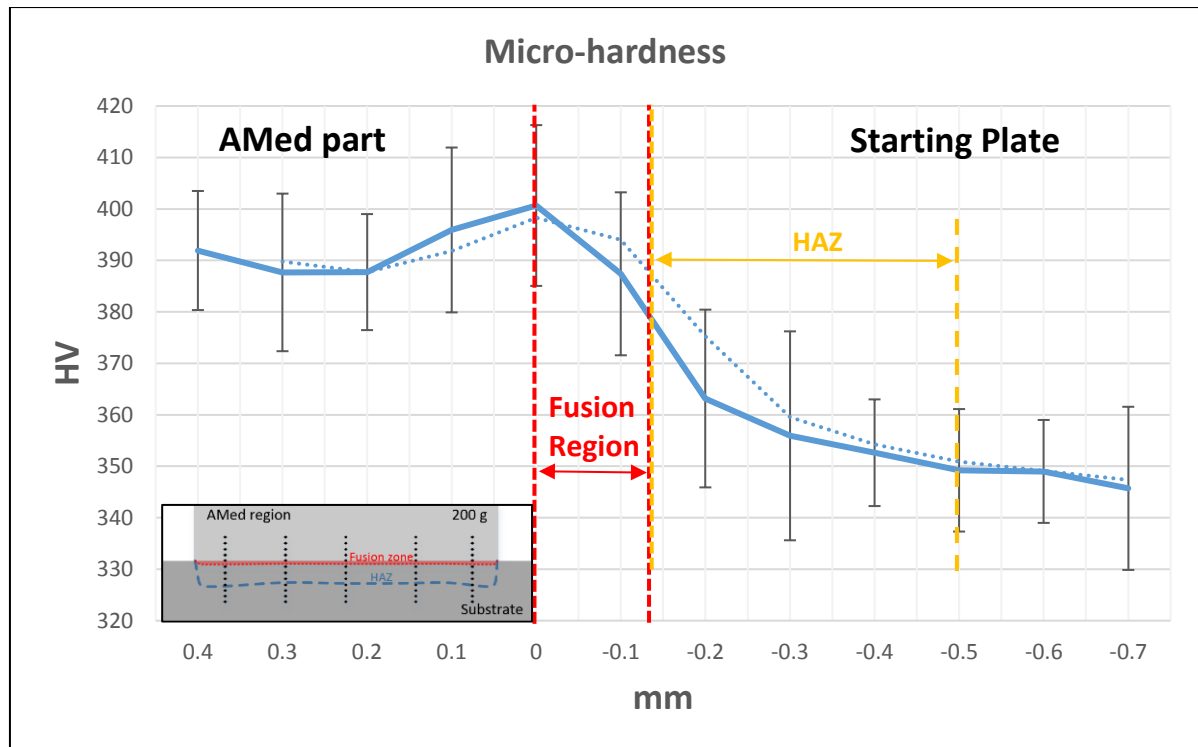
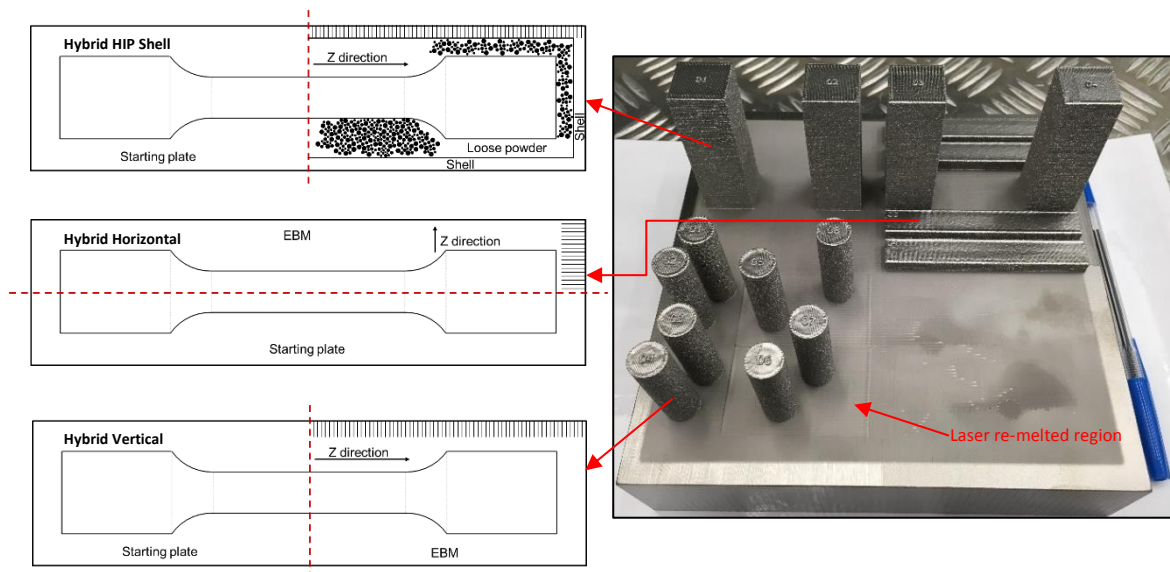


Figure 7. 12: 200 g HV micro-hardness indentation average value and trend line captured from the AMed region to the substrate.

### 7.3.6 Tensile Properties

A starting plate 40 mm thick was used as a substrate to build tensile bars during DOE 2. Four equally divided surface conditions were maintained as the first 10 mm thick starting plate experiment, as Figure 7. 1 (a) shows. Four tensile bar samples for each orientation and condition were designed to better understand the bonding between the AMed part and the substrate.

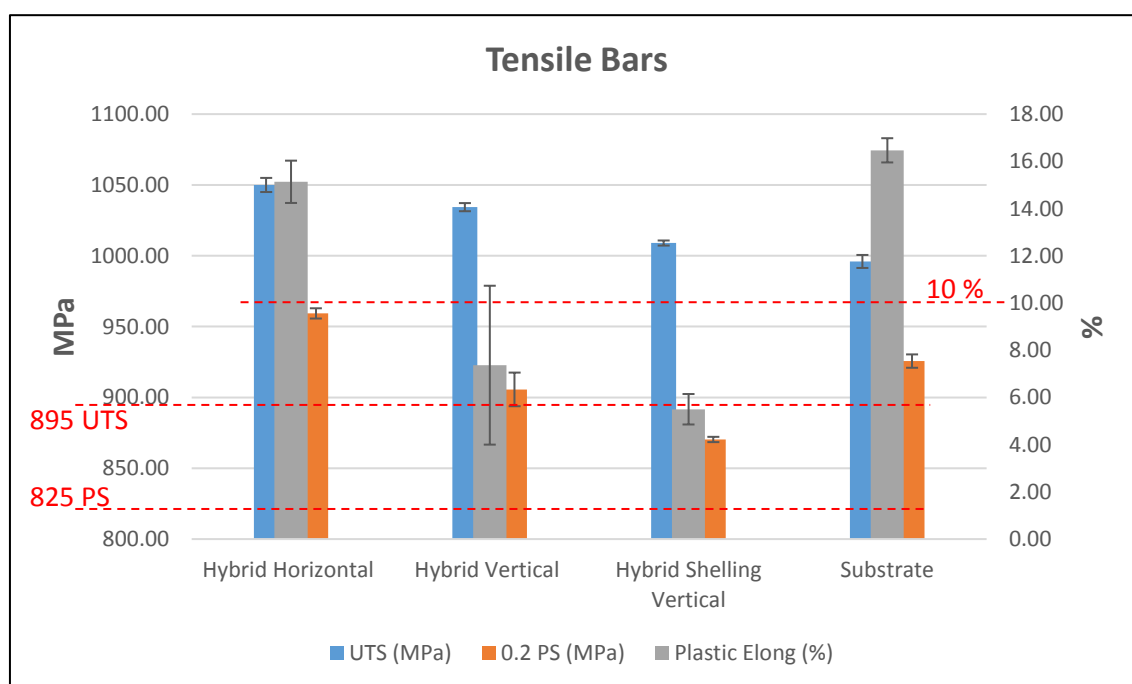


*Figure 7. 13: Schematic of the tensile bars and their characteristics manufactured (left); DOE 2 completed build with all tensile specimens manufactured on 40 mm thick Ti - 6Al - 4V starting plate (right).*

Figure 7. 13 shows the tensile strategies adopted during the manufacturing of the tensile bars and a representation of the completed build. Horizontal and vertical oriented bars were manufactured from the starting plate. The scope of the tests were focused on keeping the interface in the middle region of the gauge length in order to better understand the strength of the bonding and its mechanical properties. Two batches of four vertical tensile bars were manufactured to capture the tensile properties with conventional and laser re-melted substrates in order to understand potential mechanical differences in the bonding region. Horizontal tensile specimens were built in a cuboid shape with the aim of maintaining the bonding region along the tensile bar length. Four vertical shells with trapped, loose, pre-sintered powder were manufactured with the intention of solidifying the enclosing powder through a post HIPping treatment that enabled the complete the solidification of the powder encapsulated in the shell. This method allows bonding between the substrate, the powder solidified, and the E-PBF shell after the completion of the HIP treatment. Pictures of the manufactured raw and machined samples are shown in Figure 7. 14. After shaping the 16 tensile specimens out of the Ti - 6Al - 4V starting plate, they were sent to Westmoreland Ltd. for machining and final tensile testing. Each three of the four samples were tested for mechanical properties comparison. One sample of each condition was kept for metallurgical analysis without being tested. ASTM E8 standards were followed for the manufacture of the specimens tested (see chapter 3.12 for technical details).

Table 7. 4: Tensile bar results. \* Indicates if the specimen broke outside the middle 50 % of the gauge length. + Indicates if the specimen broke outside of the gauge length.

	UTS (MPa)	0.2 PS (MPa)	Plastic Elong (%)	
Hybrid Horizontal #1	1045	960	15.2	
Hybrid Horizontal #2	1056	955	14.1	*
Hybrid Horizontal #3	1049	963	16.1	
Hybrid Vertical #1	1030	892	14.4	
Hybrid Vertical #2	1037	923	6.4	+
Hybrid Vertical #3	1032	907	6.1	+
Hybrid Vertical #4	1035	917	6.7	+
Hybrid Vertical #5	1038	901	4.5	+
Hybrid Vertical #6	1034	894	6.1	+
Hybrid Shelling Vertical #1	1009	871	5.7	+
Hybrid Shelling Vertical #2	1011	872	6.1	+
Hybrid Shelling Vertical #3	1007	868	4.7	+
Substrate #1	991	924	16.6	+
Substrate #2	1000	922	15.9	+
Substrate #3	997	931	16.9	+



A



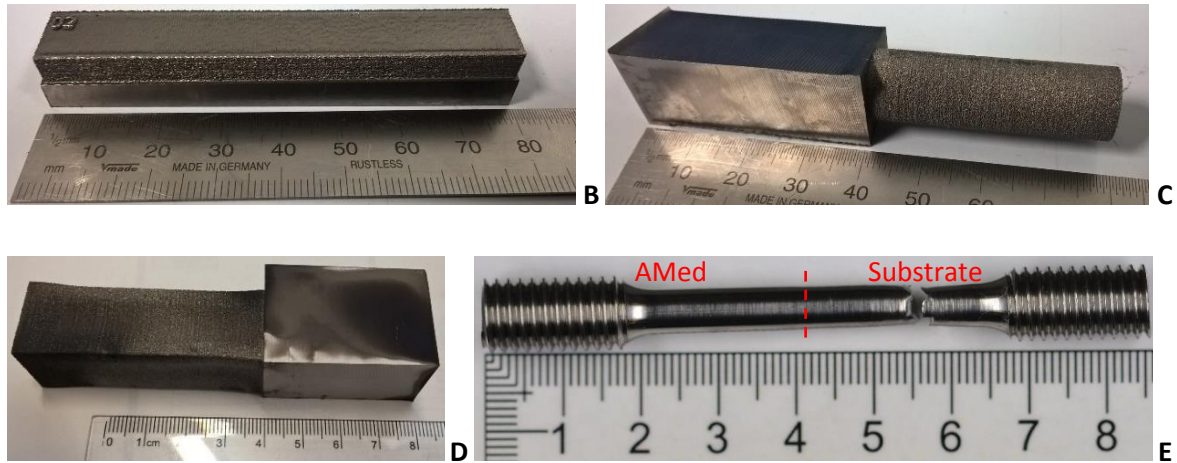


*Figure 7. 14: Tensile bars values compared to ASTM F2924 – 14 standard [106] (a). Horizontal (b), vertical (c), and vertical in-situ shelling HIPped (d) tensile bars before being machined. Hybrid vertical #3 tensile bar machined and tested (e).*

Figure 7. 14 summarises all the mechanical properties completed during the mechanical tests. All the results obtained for tensile and yield strength were classified above the standard required in AM Ti - 6Al - 4V [106], and elongation showed different results between specimens. The Hybrid horizontal tensile bars achieved superb mechanical properties. The elongation measured was above 14% for all specimens which is comparable with literature [129, 202] and considered good properties using an E-PBF system. However, some specimens showed ductility below the ASTM standard of 10 % and >15 % obtained with forged material [127]. Figure 7. 15 shows the surface fracture captured with SEM at low resolution, where it is possible to distinguish the bonding line between the AMed region and the substrate (a). This was identified through the circular gas porosity, shown with arrows (b), which are residual powder particle gas pores trapped into the layers. No porosity should be found in the substrate as previously inspected. Ductile behaviour was observed from the typical dimples ductile fracture across all surface fractures of the specimen. The crack initiation site is located inside the starting plate region (which resulted with lower UTS, PS, and micro-hardness compared to the E-PBFed region), then it gradually propagates through the middle region of the specimens in both AMed and substrate material. All the specimens inspected had similar characteristics to each other. No hybrid horizontal tensile bar studies in E-PBF were found in literature. Nevertheless, as reported by Qui et al. [225] in Figure 7. 15 (c), when the axial load is normal to the interface, it is likely to have poor elongation properties as favourable crack initiation sites tend to initiate and propagate perpendicularly to the load direction.

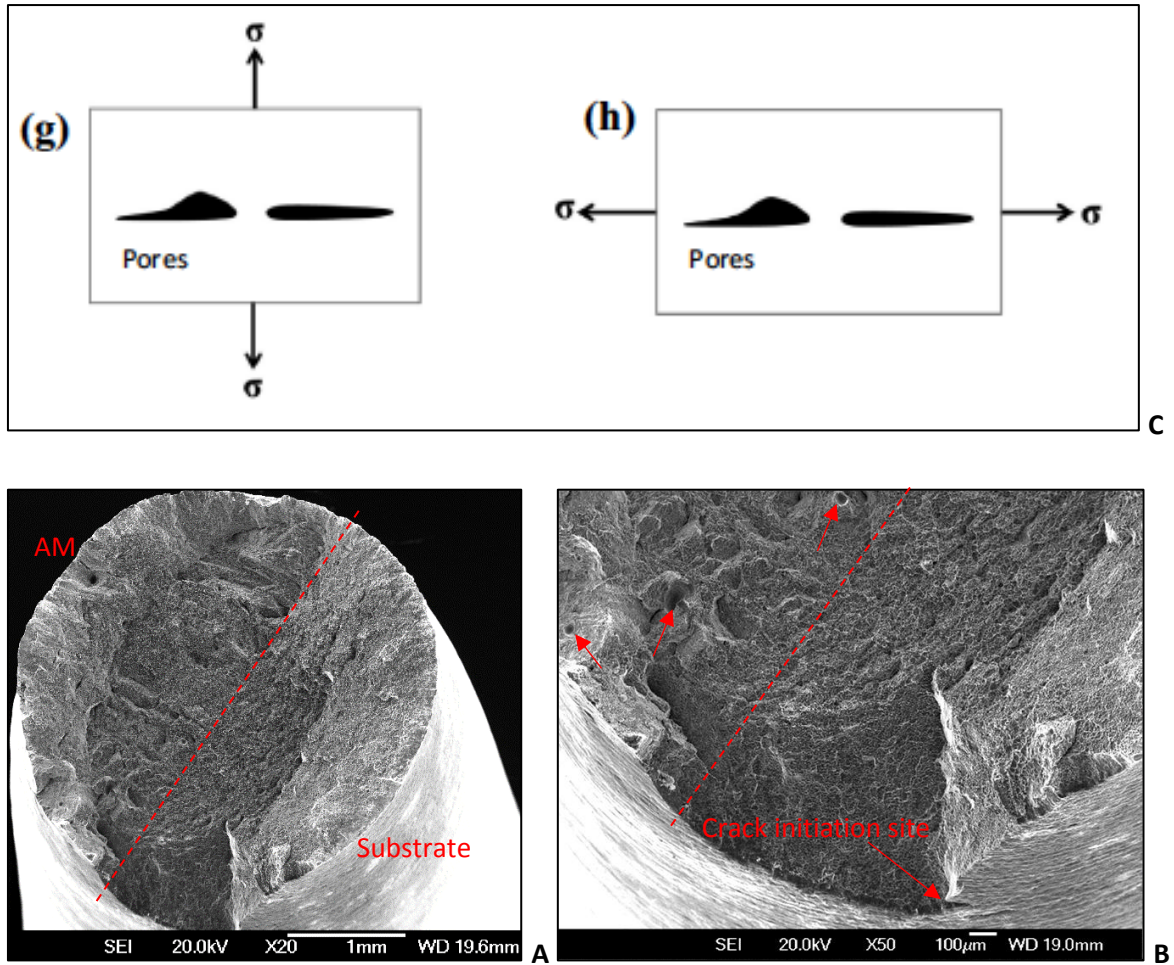
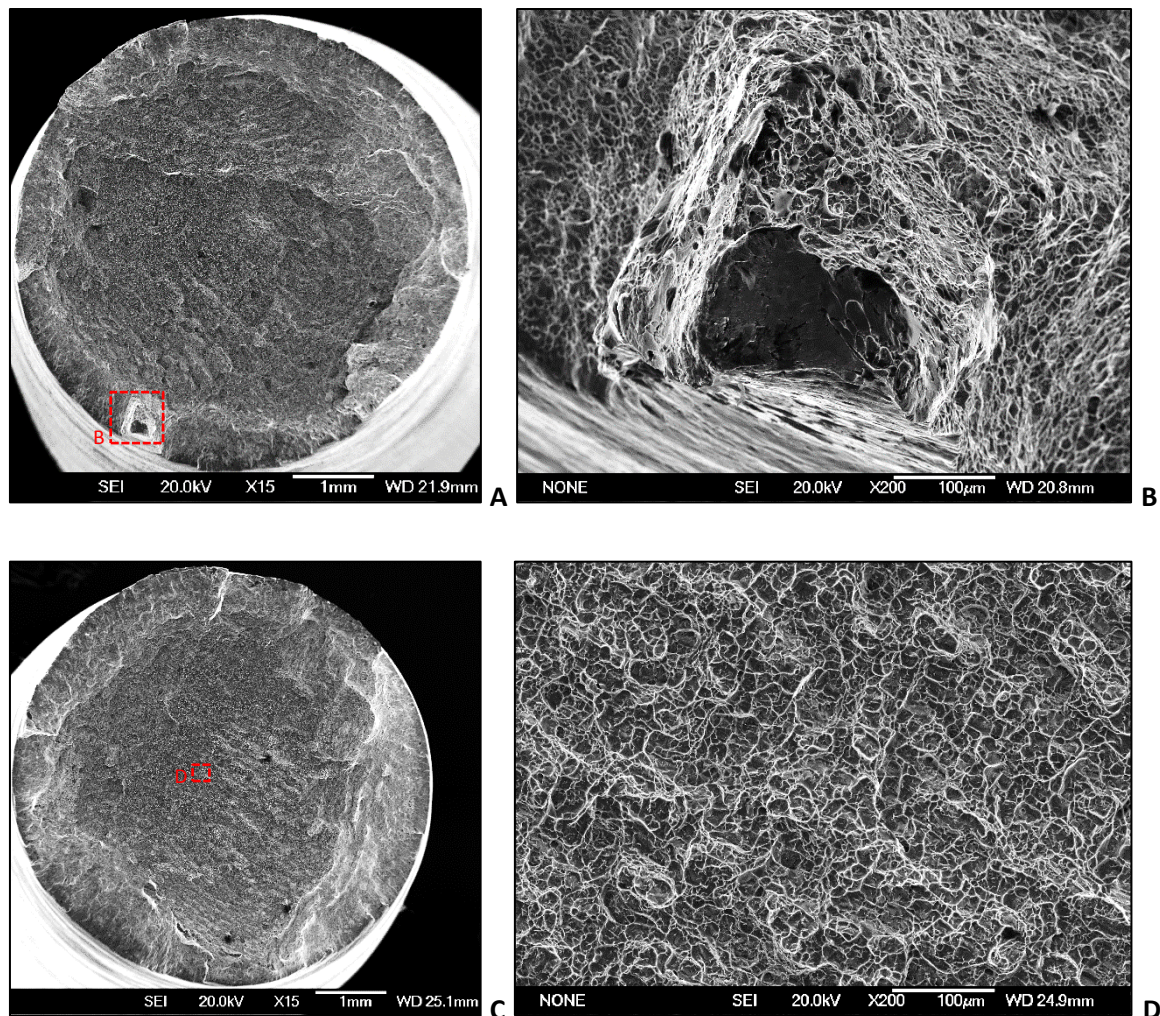


Figure 7. 15: SEM tensile surface fracture analysis of hybrid horizontal #1 sample. Full image of the AMed part on the substrate (a). Allows show the porosity generated during the AMing of the material and the crack initiation of the specimens (b). Different axial load relative to the pores (c).

The hybrid vertical tensile samples show a ductile fracture with a good tensile and yield strength, and an elongation around or below 6 % excluding sample # 1 (see



Table 7. 4), which are less than the 10% required by the ASTM E8 standards. Sample # 1 was the only specimen which broke in the middle region of the gauge length, with an elongation of 14.4%. Figure 7. 16 shows the ductile surface fracture (a) and its crack initiation site. It is probably initiated from a pore located in the AMed area close to the surface (b) which then propagated across the starting plate material, observed in the absence of porosity normally seen with AMed parts. However, tensile and yield strength is very similar to the other five vertical samples, which could be related to similar mechanical properties with better elongation. The other vertical samples broken outside the gauge length region of the specimen, as shown in Figure 7. 14 (c - d), all show a failure in the starting plate region. Figure 7. 16 shows an example of an SEM fractography analysis of the specimen failure in the substrate area, which has ductile behaviour across the entire crack propagation. All the samples analysed had a crack initiation site starting from the specimen surface and all had similar fracture properties to each other. No differences were noticed between samples built on the normal substrate and on the laser re-melted region. The different starting plate surface conditions did not influence the tensile specimens.



*Figure 7. 16: SEM fractography of hybrid vertical # 1 surface fracture sample (a) and its crack initiation pore (b). Hybrid vertical # 2 surface fracture sample (c) and its ductile dimpled surface (d).*

In-situ shelling hybrid tensile bars were also performed after HIP treatment to consolidate the powder trapped inside the shell before being machined to the final tensile geometry. Before HIPping, shrinkage estimations were considered to allow enough material to generate half of the tensile bar from the AMed region. The bonding region between the three areas can be observed in Figure 7. 17, where all the bonding regions seem to be well established and no relevant porosity was observed. Bended prior  $\beta$ -grains are observed in the AMed region (Figure 7. 17 (a - b)) caused by the shrinkage that took place during the HIPping process. No cracks or defects were observed in the bonding and join interfaces which allowed for a successful HIPping cycle. The HIPping cycle, as described in chapter 3.13, generated a fully equiaxed structure in the loose powder region, and an increase in alpha lath in the E-PBF solidified region. Surface fracture analysis shown in Figure 7. 18 (a) represent surface fracture and ductile breaking behaviour outside the gauge length (as observed in Figure 7. 14 (b)) region achieved from sample #1. The homogeneity of the dimples noticed along the entire surface fracture (b) do not clarify which region of the specimens failed, even if an optimised powder HIP cycle can achieve better properties than the conventional casting and forging route [226]. The reduction in mechanical properties shown in

Table 7. 4 could be attributed to the post HIPping treatment performed on the samples which reduced the mechanical properties of the starting plate, lowering the mechanical values observed with the vertical tensile specimens. A cross section investigation could be performed to better understand the breaking region and its properties.



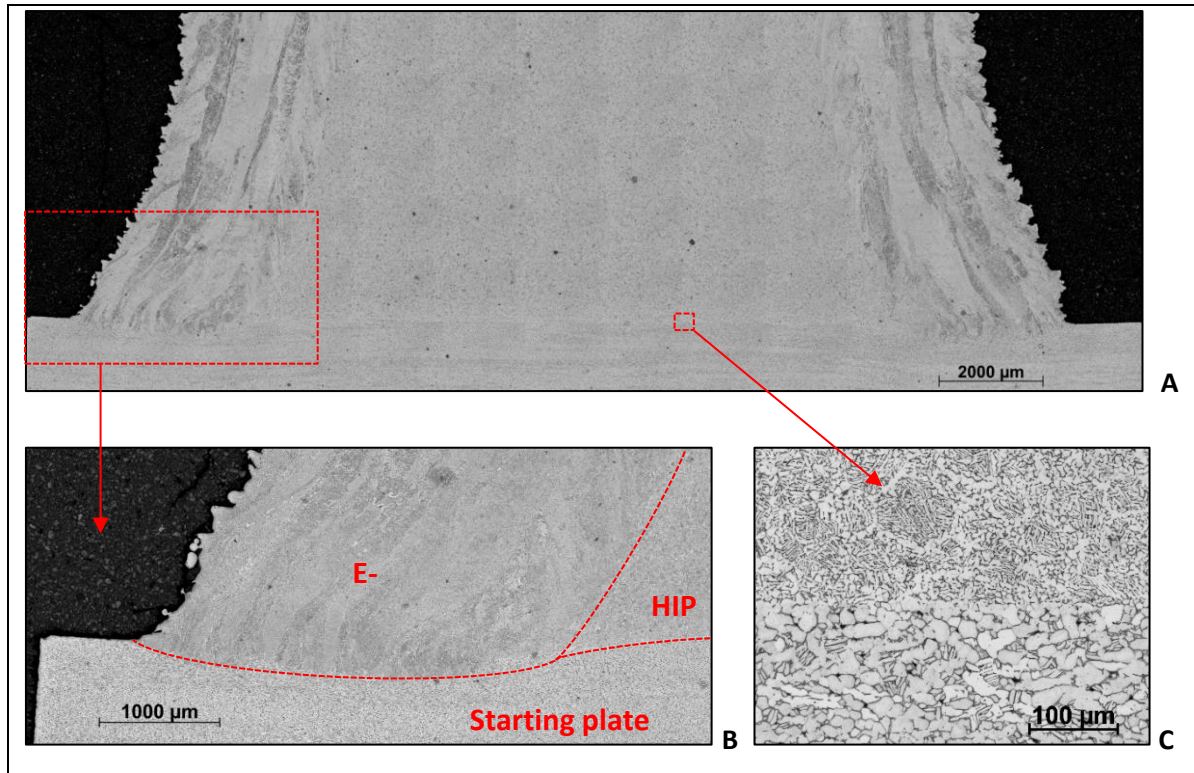


Figure 7. 17: OM X - Z cross section of #4 (a), intersection lines between the solidify E-PBF and HIP areas and the substrate (b), microstructure at the interface region between the consolidated powder and the substrate (c).

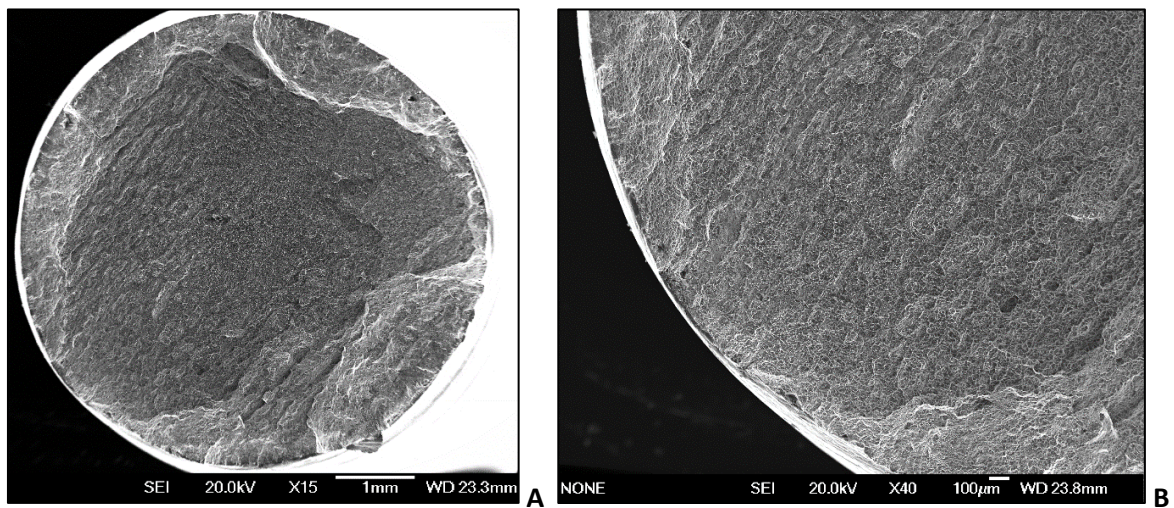


Figure 7. 18: SEM fractography of hybrid in-situ vertical # 1 surface fracture sample (a) and its ductile behaviour (b).



## 7.4 Conclusion

This chapter investigates a hybrid manufacturing solution using the substrate as an integrated part of the final component, as a feasibility study. Literature was used to guide the experiment, where the standard parameters were kept as a guideline for the experiment. Two experiments with different Ti - 6Al - 4V starting plate thickness (10 mm and 40 mm respectively) were used to understand the dilution and metallurgical properties in the bonding region using different BF and surface treatment. The second experiment was developed to better understand the mechanical properties of the bonding interface using different manufacturing approaches and orientations. Four different substrate conditions were used to better understand potential influences on the interface between the starting plate and the first few bonded layers.

- During the DOE 1 investigation, it was understood that by keeping the substrate T up to 720 °C for a long time, just the laser re-melted surface kept the initial properties as a fused region. The peened region and the Krolls' etched area were stress relieved and cleaned up from the electrons shot on the surface and the maintained high T.
- It is possible to assume that just the laser re-melted region had a different bonding impact with the first AMed layers.
- During the pre-treatment of the substrates, compressive stresses were generated and consequentially relieved during the cooling phase, generating a substantial distortion at the end of the build. This issue may result in distortions which are able to deform or bend the final manufactured component if not planned in advance. To avoid potential distortions after the build, a prior stress relieving treatment for the starting plate should be considered.
- Problems in DOE 2 pre-heating were observed due the thick 40 mm Ti - 6Al - 4V starting plate and its thermocouple located at the bottom of the substrate. It caused an inaccurate reading and consequent issues in defining the top starting plate surface T, where the electrons were impacting.
- No difficulties in bonding the first substrate into the starting plate were noticed and standard E-PBF settings were sufficiently good to perform the mentioned preliminary studies.
- A linear dilution region was noticed in all conditions tried in DOE 1, which generated a good bonding interface between the first E-PBFed layer and the starting plate. Small differences in dilution across the different BF were observed due to differing energy distribution.

- The shell region demonstrated a deeper penetration compared to the hatch scanning due to the highest energy density delivered in that phase.
- In the HAZ region prior  $\beta$ -grains were growing from the substrate to the AMed region, which demonstrated excellent bonding between the substrate and the first few layers.
- A finer superficial microstructure was observed between the laser re-melted substrate region and the edge of the AMed area (Figure 7. 8 (b)). The high strength bonding may help reduce interface cracks in the welding toe region, but more studies are needed to better understand its properties and potential benefits.
- BF influence analysis exposed different behaviour in the beam between 19 mA and 0 – 9 mA, where the refined 0 and 9 mA had a higher energy density and a consequent increment in melt pool compared to the 19 mA ones. No relevant differences in bonding, porosity or HAZ were noticed between the samples. A small improvement in top surface roughness was observed defocusing the BF.
- Micro-hardness and tensile properties demonstrated that the hot rolled and annealed starting plate had lower mechanical properties compared to the additive regions. For this reason, most of the mechanical specimens broke outside the gauge length area in the substrate region, apart from the horizontal bars which had a failure across the bonding region as explained in paragraph 7.2.6. Some of the ductility results were below the Ti - 6Al - 4V forged values of >15 %.
- The hybrid shell technique proved that it is possible to generate an enclosed shell with the substrate to be HIPped afterwards. Good bonding properties were observed between the E-PBF, starting plate and powder HIPped interface. However, the elongation properties did not reach the level required for aerospace standards of 10%.
- The hybrid investigation has the potential to improve the knowledge of the hybrid technique and give some basic understanding to this approach.

## **Chapter 8: Conclusion and Future Work**

### **8.1 Conclusion**

Several topics were discussed and analysed in this thesis. The literature review explored the current state of the E-PBF field, which was useful to understand different approaches and strategies employed to improve productivity in E-PBF. The four experimental chapters in this thesis give insight into the microstructure of components manufactured in different locations, the

volume reduction of the build chamber and investigations into advanced building techniques for in-situ shelling and hybrid manufacturing.

Key assumptions stated in the experimental chapters have highlighted the current status and limitations of the technology, their drivers, potential improvements and techniques to be further investigated. The main observations are summarised below.

#### **Software and Hardware:**

- Limitations in software changes were observed. The modification in the pre-heat area along Z axis was tweaked manually during the manufacturing of the parts. Little flexibility was observed in the Arcam software in changing the pre-heating condition actively along the build.
- The starting plate T measurement created an issue due the location of the thermocouple and the low Ti - 6Al - 4V T conductivity. An alternative solution to monitor the substrate T should be considered for example, by using a thermal imaging camera or a built-in or screwed T sensor into the substrate, an accurate measurement could be achieved before building the first layers.
- The adaptronic chamber using modified hardware parts demonstrated flexibility during the build. Flexibility in changing the machine settings, such as control of powder sensors and number of rake moves, allowed for successful builds using the reduced kit. Customised chambers, or different dimension chambers, can be manufactured to reduce the powder required for a build, manufacturing time, and machine turnaround.

#### **Microstructure Evolution:**

- No significant changes in microstructure were observed in building components in different locations of the chamber. The cooling rate achieved in the substrate and in the edges of the build can cause changes to mechanical properties. Similar microstructural and mechanical behaviour were observed in parts manufactured using a reduced chamber and with the use of GA powder which were aligned with results of other studies. All the components manufactured using standard settings demonstrated mechanical properties similar to the values found in literature. The hybrid manufacturing method showed limitation in elongation, where vertically built specimens had ductility below forged materials and ASTM standards. More investigation is needed to better understand microstructural and mechanical differences between experiments.

- Good bonding interface was overserved between the E-PBFed surface and the powder solidified through HIP treatment. In these particular cases, both microstructural and mechanical properties showed conditions above the standards required in industry.

#### **Productivity:**

- Several aspects of improving productivity in different areas have been explored. The reduction in time and flexibility in production can impact on the strategies defined before production. The solutions identified can result in an overall reduction in time which creates potential cost benefits. However, the settings conventionally used for the manufacture of parts had the higher production time.
- A custom manufacturing approach could be considered to improve the productivity of specific batches of parts. Customised solutions can contribute to reducing the time and cost involved in manufacturing the parts if planned in advance.

## **8.2 Future Work**

The investigations analysed in this thesis established a number of potential areas to be further explored in more detail. To move the abovementioned topics to a manufacturing level, analysis needs to be performed to better understand the impact of the process at a production level. In order to achieve greater understanding, a number of key areas for investigation are summarised below:

- Modelling and simulation investigations should be considered to predict mechanical properties, metallurgical behaviour, and changes taking place after HIP treatment. Existing studies can be used to predict the final components.
- Manufacturing and mechanical tests have been analysed in this study however, fatigue investigation should be performed to understand the real properties of the material manufactured with an unconventional method.
- Demonstration parts need to be manufactured using the approaches above mentioned so that part performance and behaviour can be explored.
- Pre and post machine investigation could be improved. A better understanding of the limitations of the system should bring about greater understanding of manufacturing time in a production chain. It will allow for a broader analysis of the manufacturing cost over the entire process of manufacturing parts in E-PBF.

- Different powder and substrate material should be investigated to explore potential benefits of having a different manufacturing approach as demonstrated in this thesis.
- Deep microstructural investigations should be achieved in the bonding region of the manufactured parts. Both in-situ shelling and hybrid manufacturing processes need a detailed microstructural investigation at micron and submicron level.
- The limit of bottom thermocouples for live T measurement can be mitigated using an IR in-situ camera, or an external IR T gun. Improvements in T control (both substrate and components themselves) inside the chamber should be improved. Not many solutions are currently available from manufacturers or within literature.
- Better understanding of building time and manufacturing variations need to be implemented during the process planning happened beforehand. An optimisation of time and cost need to be added during the evaluation of build strategies. This approach can impact the productivity of future batches.

#### **Chapter 4 Future Work:**

This current work requires further investigation to fully understand the characteristic of the samples and the properties that connect the preheating strategy to the microstructure observed inside the specimens. Further analysis using other methods will be considered to complete the investigation.

1. More grains investigation is required to understand the relationship between them and the micro-hardness. Further boundary lines and lamellar structure studies can be conducted using a high resolution SEM or OM, in order to generate a correlation between hardness and microstructure. The study should include pictures in different parts of the specimens in order to improve the understanding of size and alignment of  $\alpha$  and  $\beta$  phases, which will also allow us to define in detail the growing characteristics of the specimens.
2. Electron Backscatter Diffraction will be utilised to perform quantitative microstructural analysis of the grains, to gain a better understanding of the size of the grains, grain growth route, orientation of the grains, and phase identity of the sample. Mechanical behaviour can be connected to the orientation and size of the grains in order to understand if a tailored structure can be achieved. Different tests should be done at different Z heights in order to capture the heat distribution along the build direction.
3. FEA, investigation using a thermal camera, surface roughness, and tensile tests are continuously observed in papers and journals and can be used in order to improve the

knowledge of the E-PBF technology, method settings, as can new discoveries and developments achieved for other manufacturing applications. Results achieved after the studies should allow for the generation of new parameter settings to improve the configuration used during the tests.

## **Chapter 5 Future Work:**

Having successfully achieved the development of the reducing kit 190 x 190 mm, it is worth thinking about the additional advantages of decreasing the chamber size and consequently optimising the build envelope and reducing the cost can benefit the Arcam or other AM systems.

1. Some key points of new development can be summarised as:
  - Reducing time and cost in a production environment;
  - Customising the build to speed up the manufacturing and turnaround process during production;
  - Less material needed – development of new powder and parameters;
  - Potential reduction on environmental impact.
2. An ad-hoc chamber can be designed around a production part in order to fully optimise the chamber volume reducing time and cost. Resulting metallurgical and mechanical behaviour should be analysed.
3. More validation tests can be performed to better understand the microstructural issues related to the mechanical properties described. Metallurgical defects can be tolerated up to a point, which is not well defined yet. X - CT or  $\mu$  - CT can help to validate the process of inspection and mechanical behaviour.

## **Chapter 6 Future Work:**

More studies need to be performed to exploit this technique where different settings and geometries can be used to better understand the limits of the in-situ shelling approach. Considering the shell as a fundamental part of this method, more tests should be conducted. Details of which are as follows:

1. Simulation should be used to predict the shrinkage taking place during the post HIP process, which will help to predict final net shape geometries. A study conducted by Qiu et al. [215] shows a comparison between the predicted FEA shape and final AMed



component. Advanced microstructure and mechanical properties should also be considered during FEA prediction. A real component should be manufactured, inspected, and tested.

2. Investigation into material properties and microstructure of manufactured parts needs to be explored. An interstitial content analysis should be performed to better understand potential (oxygen) excesses which may influence mechanical properties.
3. A better microstructural comparison of columnar grains, mixed columnar and equiaxed grains, and equiaxed grains should be carried out. Tensile and fatigue tests in different manufacturing orientations should be considered to explore the structure achieved using the in-situ shelling technique. The components to be manufactured can be strategically oriented depending on the characteristic of the build and final mechanical behaviour of the part. Similar studies, such as Seifi et al. [37], should be used as a guideline for preliminary fracture toughness and fatigue behaviour studies.
4. More metallurgical investigation into low energy density samples with high void volume percentage needs to be performed. Technique such as EBSD should be used to capture the texture of the solidified, partially consolidated, and loosed powder regions.
5. Time and cost calculation can be better validated using real case studies. The saving in time during the optimisation of settings, and the full compaction after post HIP treatment, can reduce the manufacturing time of the build and the cost of the component. Full exploitation of the in-situ shelling technique should be explored in order to improve productivity and deliver consequent reduction in cost of manufacturing.

## **Chapter 7 Future Work:**

Several fundamental studies were explored using a hybrid manufacturing approach. The concept captured in this chapter allows further advanced developments of the topic. Bearing in mind that the starting plate can be manufactured with different material and shapes, other solutions using the analysed method can be explored:

1. Use different material for the starting plate. It allows different material properties between the added part and the substrate which could have benefit in multi-purpose materials. This solution can also be an advantage compared to the vacuum and heated bed condition found in E-PBF.
2. The traditional starting plate, if optimised, can be replaced by a real component. This technique could be suitable for worn parts that need to be repaired, by adding 3D

geometries on existing components, or to improve the characteristics of an existing component (as surface coatings or hardening).

3. Explore the real benefits of integrating the starting plate as a final part. End users could be interested in reducing usage of scrap material, lowering the environmental footprint, and reducing time and cost of manufacturing. An example can be found in mould industries; the clamping plate can be part of the final mould, where additional features with cooling channels can be added to it via E-PBF.
4. Post treatment can be considered to improve the current elongation properties of the tensile bars performed during the tests. By increasing the elongation characteristics, the parts would be suitable for the aerospace market. Other markets and end users can be targeted based on the mechanical properties currently achieved.
5. Potential investigations into crack propagation using the in-situ shelling technique can be explored.

## References

- [1] W. Associates, "Wohlers Report 2016," Wohlers Associates, Inc., Colorado, 2016.
- [2] E. Sivertsen, "A Brief History of Additive Manufacturing," Type a Machines, 30 September 2016. [Online]. Available: <https://www.typeamachines.com/blog/a-brief-history-of-additive-manufacturing>. [Accessed 07 August 2017].
- [3] M. Abrams, "3D Printing for Mass Production," ASME Setting the Standards, February 2015. [Online]. Available: <https://www.asme.org/engineering-topics/articles/manufacturing-processing/3d-printing-for-mass-production>. [Accessed 07 August 2017].
- [4] S. Mellor, L. Hao, D. Zhang, "Additive manufacturing: A framework for implementation," *International Journal of Production Economics*, vol. 149, pp. 194-201, 2014.
- [5] B. S. I. Gibson, "Additive Manufacturing Technologies, Rapid Prototyping to Direct Digital Manufacturing,," New York, Springer, 2010.
- [6] P. Heintz, L. Müller, C. Körner, R. F. Singer, F. A. Müller, "Cellular Ti-6Al-4V Structures With Interconnected Macro Porosity For Bone Implants Fabricated by Selective Electron Beam Melting," *Acta Biomater*, 2008, p. 1536-44.
- [7] G. P. Dinda, L. Song, J. Mazumder, "Fabrication of Ti-6Al-4V scaffolds by direct metal deposition,," Michigan, Springer, 2008, pp. 2914-22.
- [8] V. Weißmann, P. Drescher, R. Bader, H. Seitz, H. Hansmann, N. Laufer, "Comparison of Single Ti6Al4V Struts Made Using Selective Laser Melting and Electron Beam Melting Subject to Part Orientation," *Metals*, vol. 7, no. 91, pp. 1-22, 2017.
- [9] Arcam, "EBM, Electron Beam Melting – in the forefront of Additive Manufacturing," Arcam, [Online]. Available: <http://www.arcam.com/technology/electron-beam-melting/>. [Accessed 09 October 2017].
- [10] Q. Li, I. Kucukkoc, D.Z. Zhang, "Production planning in additive manufacturing and 3D printing," *Computers & Operations Research*, vol. 83, pp. 157-172, 2017.
- [11] K. Steigerwald, Germany Patent 2,746,420, 1952.
- [12] Arcam, "Arcam History," Arcam, [Online]. Available: <http://www.arcam.com/company/about-arcam/history/>. [Accessed 15 August 2017].
- [13] Arcam, "Arcam EBM," Arcam, a GE Additive Company, [Online]. Available: <http://www.arcam.com/wp-content/uploads/arcamebm-corp.pdf>. [Accessed 15 August 2017].
- [14] Arcam, "http://www.arcam.com/," Arcam, [Online]. Available: <http://www.arcam.com/technology/products/>. [Accessed 15 August 2017].
- [15] Arcam, "Metal Powders," Arcam, [Online]. Available: <http://www.arcam.com/technology/products/metal-powders/>. [Accessed 15 August 2017].
- [16] Arcam, "EBM Overview," Arcam, 2010.
- [17] F. K. M. Jamshidinia, "Numerical Modeling of Heat Distribution in the Electron Beam Melting of Ti-6Al-4V," *Journal of Manufacturing Science and Engineering*, vol. 135, 2013.
- [18] X. Gong, T. Anderson, K. Chou, "Review on powder-based electron beam additive manufacturing review," *manufacturing Review*, vol. 1, no. 2, 2014.
- [19] Arcam, "Beam Quality\_ Training Level 2," Arcam, 2015.

- [20] I. Gibson, *Additive Manufacturing Technologies: Rapid Prototyping to Direct Digital Manufacturing*, London, New York: Springer, 2010.
- [21] C. Korner, "Additive manufacturing of metallic components by selective electron beam melting — a review," *International Materials Reviews*, pp. 1-17, 09 May 2016.
- [22] M. Kahnert, S. Lutzmann, M.F. Zaeh, "Layer formations in electron beam sintering," in *Solid Free Form Symposium*, Austin, 2007.
- [23] B. S. S. Association, "Magnetic Properties of Stainless Steel," British Stainless Steel Association, [Online]. Available: <http://www.bssa.org.uk/publications.php?id=12>. [Accessed 12 September 2017].
- [24] Arcam, "Electron Beam melting Theory," Arcam, 2010.
- [25] C. H. A. Leung, R. Tosi, E. Muzangaza, S. Nonni, P. J. Withers, P. D. Lee, "Effect of preheating on the thermal, microstructural and mechanical properties of selective electron beam melted Ti-6Al-4V components," *Material & Design*, vol. 174, 2019.
- [26] M. Svensson, "EBM Heat Theory," Arcam, 2012.
- [27] Arcam, "EBM Heat Theory\_ Arcam Training Level 1," Arcam, 2015.
- [28] P. Drescher, H. Seitz, "Processability of an amorphous metal alloy powder by electron beam melting," *Rapid Technologies e-Journal*, 2015. [Online]. Available: <https://www.rtejournal.de/ausgabe12/4236>. [Accessed 12 September 2017].
- [29] Arcam, "Process setting\_ Training Level 2," Arcam, 2015.
- [30] M. Galati, L. Iuliano, A. Salmi, E. Atzeni, "Modelling energy source and powder properties for the development of a thermal FE model of the EBM additive manufacturing process," *Additive Manufacturing*, vol. 14, pp. 49-59, 2017.
- [31] W. Yan, Y. Qian, W. Ma, B. Zhou, Y. Shen, F. Lin, "Modeling and Experimental Validation of the Electron Beam Selective Melting Process," *Engineering*, vol. 3, pp. 701-707, 2017.
- [32] H. Weiwei, J. Wenpeng, L. Haiyan, T. Huiping, K. Xinting, H. Yu, "Research on Preheating of Titanium Alloy Powder in Electron Beam melting Technology," *Rare Metal Materials and Engineering*, vol. 40, no. 12, pp. 2072-2075, 2011.
- [33] H. Gong, K. Rafi, H. Guc, G.D.J. Ram, T. Starr, B. Stucker, "Influence of defects on mechanical properties of Ti-6Al-4 V components produced by selective laser melting and electron beam melting," *Materials and Design*, vol. 86, pp. 545-554, 2015.
- [34] S. Hou, E. Muzangaza, M. Bombardiere, A. Okioga, M. Rahman, D. Brackett, "Optimising the Dynamic Process Parameters in Electron Beam Melting (EBM) to Achieve Internal Defect Quality Control," in *European Powder Metallurgy Association*, Milan, 2017.
- [35] P. Edwards, A. O'Conner, M. Ramulu, "Electron Beam Additive Manufacturing of Titanium Components: Properties and Performance," *Journal of Manufacturing Science and Engineering*, vol. 135, pp. 1-7, 2013.
- [36] M. Grasso, B.M. Colosimo, "Process defects and in situ monitoring methods in metal powder bed fusion: a review," *Measurement Science and Technology*, vol. 28, pp. 1-25, 2017.
- [37] M. Seifi, A. Salem, D. Satko, J. Shaffer, J.J. Lewandowski, "Defect distribution and microstructure heterogeneity effects on fracture resistance and fatigue behavior of EBM Ti-6Al-4V," *International Journal of Fatigue*, vol. 94, pp. 263-287, 2017.
- [38] B. Liu, R. Wildman, C. Tuck, I. Ashcroft, R. Hague, "Investigation the effect of particle size distribution on processing parameters optimisation in selective laser melting process," in *Solid Freeform Fabrication Symposium*, Austin, 2011.

- [39] W.J. Sames, F.A. List, S. Pannala, R.R. Dehoff, S.S. Babu, "The metallurgy and processing science of metal additive manufacturing," *International Materials Reviews*, vol. 61, no. 5, pp. 315-360, 2016.
- [40] R.B. Dinwiddie, R.R. Dehoff, P.D. Lloyd, L.E. Lowe, J.B. Ulrich, "Thermographic In-Situ Process Monitoring of the Electron Beam Melting Technology used in Additive Manufacturing," *SPIE*, vol. 8705, 2013.
- [41] Q. Huang, N. Hu, X. Yang, R. Zhang, Q. Feng, "Microstructure and inclusion of Ti-6Al-4V fabricated by selective laser melting," *Frontiers of Materials Science*, vol. 10, no. 4, pp. 428-431, 2016.
- [42] S.K. Everton, M. Hirsch, P. Stravroulakis, R.K. Leach, A.T. Clare, "Review of in-situ process monitoring and in-situ metrology for metal additive manufacturing," *Materials & Design*, vol. 95, pp. 431-445, 2016.
- [43] K. F. Martin, "A Review by Discussion of Condition Monitoring and Fault Diagnosis in Machine Tools," *International Journal of Machine Tools and Manufacture*, vol. 34, no. 4, pp. 527-551, 1994.
- [44] E. Incorporated, "Measurement science roadmap for metal-based additive manufacturing," National Institute of Standards and Technology, Gaithersburg, 2013.
- [45] D.D. Baere, M. Strantza, M. Hinderdael, W. Devesse, P. Guillaume, "Effective Structural Health Monitoring with Additive Manufacturing," in *7th European Workshop on Structural Health Monitoring*, Nantes, 2014.
- [46] "AMAZE," AMAZE, 2016. [Online]. Available: <http://amazeproject.eu/>. [Accessed 19 September 2017].
- [47] Arcam, "Arcam EBM Q20plus," Arcam, [Online]. Available: <http://www.arcam.com/technology/products/arcam-q20/>. [Accessed 9 September 2017].
- [48] E. Rodriguez, F. Medina, D. Espalin, C. Terrazas, D. Muse, C. Henry, E. MacDonald, R.B. Wicker, "Integration of a Thermal Imaging Feedback Control System in Electron Beam Melting," in *Solid Free Form Symposium*, Austin, 2012.
- [49] B. Cheng, S. Price, J. Lydon, K. Cooper, K. Chou, "On Process Temperature in Powder-Bed Electron Beam Additive Manufacturing: Model Development and Validation," *Journal of Manufacturing Science and Engineering*, vol. 136, pp. 1-12, 2014.
- [50] M. V. Technology, "Softare Systems," Machine Vision Technology, [Online]. Available: <http://www.machine-vision-technology.co.uk/applications/softwareystems.html>. [Accessed 2 October 2017].
- [51] ImageJ, "ImageJ," ImageJ, [Online]. Available: <https://imagej.net/ImageJ>. [Accessed 09 October 2017].
- [52] J.A. Slotwinski, E.J. Garboczi, "Porosity of Additive Manufacturing Parts for Process Monitoring," in *National Institute of Standards and Technology*, Baltimore, 2013.
- [53] T. L. Depot, "ARCHIMEDES' PRINCIPLE AND DENSITY DETERMINATION," The Lab Depot, [Online]. Available: <http://www.labdepotinc.com/articles/archimedes-principles.html>. [Accessed 2 October 2017].
- [54] M. Strantza, D.G. Aggelis, D. Baere, P. Guillaume, D. Hemelrijck, "Evaluation of SHM System Produced by Additive Manufacturing via Acoustic Emission and Other NDT Methods," *Sensors*, vol. 15, pp. 26709-26725, 2015.
- [55] T.B. Kim, S. Yue, Z. Zhang, E. Jones, J.R. Jones, P.D. Lee, "Additive manufactured porous titanium structures: Through-process quantification of pore and strut networks," *Journal of Materials Processing Technology*, vol. 214, pp. 2706-2715, 2014.

- [56] O.B. Olurin, M. Arnold, C. Korner, R.F. Singer, "The investigation of morphometric parameters of aluminium The investigation of morphometric parameters of aluminium," *Materials Science and Engineering A*, vol. 328, pp. 334-343, 2002.
- [57] S. Tamas-Williams, H. Zhao, F. Léonard, F. Derguti, I. Todd, P.B. Prangnell, "XCT analysis of the influence of melt strategies on defect population in Ti-6Al-4V components manufactured by Selective Electron Beam Melting," *Materials Characterization*, vol. 102, pp. 47-61, 2015.
- [58] G. Ziółkowski, E.Chlebus, P.Szymczyk, J. Kurzac, "Application of X-ray CT method for discontinuity and porosity detection in 316L stainless steel parts produced with SLM technology," *Archives of Civil and Mechanical Engineering*, vol. 14, no. 5, pp. 608-614, 2014.
- [59] H. Hasib, O.L.A. Harrysson, H.A. West, "Powder Removal from Ti-6Al-4V Cellular Structures Fabricated via Electron Beam Melting," *The Minerals, Metals & Materials Society*, vol. 67, no. 3, pp. 639-646, 2015.
- [60] P. Drescher, T. Reimann, H. Seitz, "Investigation of powder removal of net-structured titanium parts made from electron beam melting," *International Journal of Rapid Manufacturing*, vol. 4, no. 2, 2014.
- [61] F. Hashimoto, H. Yamaguchi, P. Krajnik, K. Wegener, R. Chaudhari, H. Hoffmeister, F. Kuster, "Abrasive fine-finishing technology," *CIRP Annals - Manufacturing Technology*, vol. 65, pp. 597-620, 2016.
- [62] J. Karlsson, A. Snis, H. Engqvist, J. Lausmaa, "Characterization and comparison of materials produced by Electron Beam Melting (EBM) of two different Ti-6Al-4V powder fractions," *Journal of Materials Processing Technology*, vol. 213, pp. 2019-2118, 2013.
- [63] S.S. Al-Bermani, M.L. Blackmore, W. Zhang, I. Todd, "The Origin of Microstructural Diversity, Texture, and Mechanical Properties in Electron Beam Melted Ti-6Al-4V," *METALLURGICAL AND MATERIALS TRANSACTIONS A*, vol. 41A, pp. 3422-3434, December 2010.
- [64] Q. Technologies, "Hot Isostatic Pressing," Quintus Technologies, [Online]. Available: <http://quintustechnologies.com/hot-isostatic-pressing/applications/additive-manufacturing/>. [Accessed 06 October 2017].
- [65] P. Homporová, C. Poletti, M. Stockinger, F. Warchomicka, "Dynamic phase evolution in titanium alloy Ti-6Al-4V," in *Proceedings of the 12th World Conference on Titanium, Volume: 1*, Beijin, 2012.
- [66] A. Kirchner<sup>1</sup>, B. Klöden, T. Weißgärber, B. Kieback, A. Schoberth, S. Bagehorn, D. Greitemeier, "Mechanical Properties of Ti-6Al-4V Additively Manufactured by Electron Beam Melting," in *Euro PM2015 - AM - Electron Beam Melting*, Turin, 2015.
- [67] F. Bahbou, U. Ackelid, "Improved Parameters for Hot Isostatic Pressing (HIP) of Ti-6Al-4V Additively Manufactured by EBM," in *EBAM*, Nuremberg, 2016.
- [68] H.Galarraga, R.J. Warren, D.A. Lados, R.R. Dehoff, M.M. Kirkab, P. Nandwana, "Effects of heat treatments on microstructure and properties of Ti-6Al-4V ELI alloy fabricated by electron beam melting (EBM)," *Materials Science & Engineering A*, vol. 685, pp. 417-428, 2017.
- [69] J. Vaithilingam, R.D.Goodridge, R.J.M. Hague, S.D.R. Christie, S. Edmondson, "The effect of laser remelting on the surface chemistry of Ti-6Al-4V components fabricated by selective laser melting," *Journal of Materials Processing Technology*, vol. 232, pp. 1-8, 2016.
- [70] X. Zhou, X. Liu, Zhang, Z. Shen, W. Liu, "Balling phenomena in selective laser melted tungsten," *Journal of Materials Processing Technology*, vol. 222, pp. 33-42, 2015.
- [71] C.P. Ma, Y.C. Guan, W. Zhou, "Laser polishing of additive manufactured Ti alloys," *Optics and Lasers in Engineering*, vol. 93, pp. 171-177, 2017.



- [72] B.A. Mangour, J.M. Yang, "Improving the surface quality and mechanical properties by shot-peening of 17-4 stainless steel fabricated by additive manufacturing," *Materials & Design*, vol. 110, pp. 914-924, 2016.
- [73] A. O. M. R. P. Edwards, "Electron Beam Additive Manufacturing of Titanium Components: Properties and Performance," *Journal of Manufacturing Science and Engineering*, vol. 135, no. 6, p. 7, 18 November 2013.
- [74] A.S. Iquebal, S. El Amrib, S. Shrestha, Z. Wanga, G.P. Manogharand, S. Bukkapatnam, "Longitudinal Milling and Fine Abrasive Finishing Operations to Improve Surface Integrity of Metal AM Components," in *45th SME North American Manufacturing Research Conference*, Los Angeles, 2017.
- [75] A. Fatemi R. Molaei, S. Sharifimehr, N. Phan, N. Shamsaei, "Multiaxial fatigue behavior of wrought and additive manufactured Ti-6Al-4V including surface finish effect," *International Journal of Fatigue*, vol. 100, pp. 347-366, 2017.
- [76] M. AM, "Secondary finishing processes in metal Additive Manufacturing," Metal AM, [Online]. Available: <http://www.metal-am.com/introduction-to-metal-additive-manufacturing-and-3d-printing/secondary-finishing-processes/>. [Accessed 18 September 2017].
- [77] P. Sun, Z.Z. Fang, Y. Xia, Y. Zhang, C. Zhoua, "A novel method for production of spherical Ti-6Al-4V powder for additive manufacturing," *Powder Technology*, vol. 301, pp. 331-335, 2016.
- [78] Y.Y. Sun, S. Gulizia, C.H. Oh, C. Doblin, Y. F. Yang, M. Qian, "Manipulation and Characterization of a Novel Titanium Powder Precursor for Additive Manufacturing Applications," *The Minerals, Metals & Materials Society*, vol. 67, no. 3, pp. 564-572, 2015.
- [79] A. F. E. M. Tsantrizos P. G., "Methof of Production of Metal and Ceramic Powders by Plasma Atomisation". Patent 5,707,419, 13 January 1998.
- [80] L.V.M. Antony, R.G. Reddy, "Processes for Production of High-Purity Metal Powders," *Journal of Materials*, pp. 14-18, 2003.
- [81] AP&C, "<http://advancedpowders.com/plasma-atomization-technology/our-technology/>," [Online].
- [82] J. Dawes, R. Bowerman, R. Trepleton, "Introduction to the Additive Manufacturing Powder Metallurgy Supply Chain," *Johnson Matthey Technology Review*, vol. 59, no. 3, pp. 243-256, 2015.
- [83] J. Clayton, D. Millington-Smith, B. Armstrong, "The Application of Powder Rheology in Additive Manufacturing," *The Minerals, Metals & Materials Society*, vol. 67, no. 3, pp. 544-548, 2015.
- [84] A.B. Spierings, M. Voegtlin, T. Bauer, K. Wegener, "Powder flowability characterisation methodology for powder-bed-based metal additive manufacturing," *Progress in Additive Manufacturing*, vol. 1, no. 1-2, pp. 9-20, 2016.
- [85] V. Seyda, N. Kaufmann, C. Emmelmann, "Investigation of aging processes of Ti-6Al-4V powder material in laser melting," *Physics Procedia*, vol. 39, pp. 425-431, 2012.
- [86] Z.C. Cordero, H.M. Meyer, P. Nandwana, R.R. Dehoff, "Powder bed charging during electron-beam additive manufacturing," *Acta Materialia*, vol. 124, pp. 437-445, 2017.
- [87] P. Kilburn, "Disruptive Magazine," 17 March 2017. [Online]. Available: <http://www.disruptivemagazine.com/opinion/traceability-and-costs-powders-additive-manufacturing>. [Accessed 28 September 2017].
- [88] J. Dawes, "Introduction to the Additive Manufacturing Powder Metallurgy Supply Chain," *Johnson Matthey Technology Review*, vol. 59, no. 3, p. 243, 2015.

- [89] A. Aero, "Additive Manufacturing," Avio Aero, [Online]. Available: <http://www.avioaero.com/Where/Contacts-Plants/ITALY-CAMERI-NOVARA-Additive-Manufacturing>. [Accessed 10 October 2017].
- [90] LPW, "PowderLab," LPW, 2016. [Online]. Available: <http://www.lpwtechnology.com/what-we-do/powderlab/>. [Accessed 10 August 2017].
- [91] M. Laterza, "AVIO AERO: Piedmont witnesses the birth of 3D printing for the aeronautics industry of the future," 14 December 2013. [Online]. Available: <https://www.avioaero.com/Press-releases/AVIO-AERO-Piedmont-witnesses-the-birth-of-3D-printing-for-the-aeronautics-industry-of-the-future>. [Accessed 28 September 2017].
- [92] R. Kennedy, "GE Plans to Invest \$1.4B to Acquire Additive Manufacturing Companies Arcam and SLM; Accelerates Efforts in Important Digital Industrial Space," Eastern Daylight Time, 6 September 2016. [Online]. Available: <http://www.businesswire.com/news/home/20160905005631/en/GE-Plans-Invest-1.4B-Acquire-Additive-Manufacturing>. [Accessed 28 September 2017].
- [93] C. Körner, "Additive manufacturing of metallic components by selective electron beam melting — a review," *International Materials Reviews*, 16 May 2016.
- [94] O.L.A. Harrysson, O. Cansizoglu, D.J. Marcellin-Little, D.R. Cormier, H.A. West, "Direct metal fabrication of titanium implants with tailored materials and mechanical properties using electron beam melting technology," *Materials Science and Engineering: C*, pp. 366-373, 1 April 2008.
- [95] L.E. Murr, S.M. Gaytan, F. Medina, E. Martinez, J.L. Martinez, D.H. Hernandez, B.I. Machado, D.A. Ramirez, R.B. Wicker, "Characterization of Ti-6Al-4V open cellular foams fabricated by additive manufacturing using electron beam melting," *Materials Science and Engineering: A*, pp. 1861-1868, 25 March 2010.
- [96] P. Heinel, L. Muller, C. Korner, R.F. Singer, F.A. Muller, "Cellular Ti-6Al-4V structures with interconnected macro porosity for bone implants fabricated by selective electron beam melting," *Acta Biomaterialia*, vol. 4, no. 5, pp. 1536-1544, September 2008.
- [97] I. J. Polmear, *Light Alloys: Metallurgy of the Light Alloys*, 2nd Edition, 2. edition, Ed., London: Edward Arnold, 1989.
- [98] X. Tan, Y. Kok, Y.J. Tan, M. Descoins, D. Mangelinck, S.B. Tor, K.F. Leong, C.K. Chua, "Graded microstructure and mechanical properties of additive manufactured Ti-6Al-4V via electron beam melting," *Acta Materialia*, vol. 97, pp. 1-16, 2015.
- [99] Lütjering G., Williams J. C., *Titanium*, Columbus: Springer, 2003.
- [100] R. Pederson, O. Babushkin, R. Warren, "The Use of High Temperature X-Ray Diffractometry to Study Phase Transition in Ti-6Al-4V," May 2002. [Online]. Available: <https://www.diva-portal.org/smash/get/diva2:991369/FULLTEXT01.pdf>. [Accessed 02 November 2017].
- [101] D. J., *Titanium - A Technical Guide*, ASM International, 1988.
- [102] J. Donachie, *Titanium - A Technical Guide*, ASM International, 1988.
- [103] J. Sieniawski, W. Ziaja, K. Kubiak, M. Motyka, "Microstructure and Mechanical Properties of High Strength Two-Phase Titanium Alloys," in *Titanium Alloys - Advances in Properties Control*, Intech, 2013, p. Chapter 4.
- [104] T. Ahmed, H. J. Rack, "Phase transformations during cooling in  $\alpha+\beta$  titanium alloys," *Material Science Engineering*, vol. 243, pp. 206-211, 1998.
- [105] M. Donachie, *Titanium, a Technical Guide*, Ohio: ASM International, 1988.
- [106] A. Compass, "Standard Specification for Additive Manufacturing Titanium-6 Aluminum-4 Vanadium with Powder Bed Fusion," ASTM International, [Online]. Available:

[https://compass.astm.org/EDIT/html\\_annot.cgi?F2924+14#s00026](https://compass.astm.org/EDIT/html_annot.cgi?F2924+14#s00026). [Accessed 04 September 2017].

- [107] Kobryn P., Semiatin S., "The laser additive manufacture of Ti-6Al-4V.," *JOM Journal of the Minerals, Metals and Materials Society*, pp. 42-44, 2001.
- [108] Kobryn P.A., Semiatin S.L., "Microstructure and texture evolution during solidification processing of Ti-6Al-4V.," *Journal of Materials Processing Technology*, pp. 330-339, 2003.
- [109] David A., Vitek J.M. , "Solidification and Weld Microstructures.," *International Materials Reviews*, pp. 213-245, 1989.
- [110] Bontha S., Klingbeil N.W., Kobryn P.A., Fraser H. L., "Thermal process maps for predicting solidification microstructure in laser fabrication of thin-wall structures.," *Journal of Materials Processing Technology*, pp. 135-142, 2006.
- [111] T. Scharowsky, V. Juechter, R.F. Singer, C. Korner, "Influence of the Scanning Strategy on the Microstructure and Mechanical Properties in Selective Electron Beam Melting of Ti-6Al-4V," *Advance Engineering Materials*, vol. 17, no. 11, pp. 1573-1578, 2017.
- [112] P. Drescher, M. Sarhan, H. Seitz, "An Investigation of Sintering Parameters on Titanium Powder for Electron Beam Melting Processing Optimization," *Materials*, vol. 9, no. 974, pp. 1-8, 2016.
- [113] Porter D.A., Easterling K.E., Sherif M.Y., "Phase transformations in metals and alloys.," *CRC Press*. xix, vol. 3rd edition, p. 500, 2009.
- [114] A. A., "Microstructure, Texture and Mechanical Property Evolution during Additive Manufacturing of Ti6Al4V Alloy for Aerospace Applications," University of Birmingham, Birmingham, 2012.
- [115] A. Klassen, V. E. Forster, V. Juechter, C. Körner, "Numerical simulation of multi-component evaporation during selective electron beam melting of TiAl," *Journal of Materials Processing Tech.*, vol. 247, pp. 280-288, 2017.
- [116] A.M. Rausch, V.E. Küng, C. Pobel, M. Markl, C. Korner, "Predictive Simulation of ProcessWindows for Powder Bed Fusion Additive Manufacturing: Influence of the Powder Bulk Density," *Materials*, vol. 10, no. 1117, pp. 1-14, 2017.
- [117] A.M. Rausch, V.E. Küng, C. Pobel, M. Markl, C. Korner, "Predictive Simulation of Process Windows for Powder Bed Fusion Additive Manufacturing: Influence of the Powder Bulk Density," *Materials*, vol. 10, no. 1117, pp. 1-14, 2017.
- [118] C. Guo, W. Ge, F. Lin, "Effects of scanning parameters on material deposition during ElectronBeam Selective Melting of Ti-6Al-4V powder," *Journal of Materials Processing Technology*, vol. 217, pp. 148-157, 2015.
- [119] A. Mohammad, A.M. Alahmari, M.K. Mohammed, R.K. Renganayagalu, K. Moiduddin, "Effect of Energy Input on Microstructure and Mechanical Properties of Titanium Aluminide Alloy Fabricated by the Additive Manufacturing Process of Electron Beam Melting," *Materials*, vol. 10, no. 211, pp. 1-16, 2017.
- [120] D. Herzog, V. Seyda, E. Wycisk, C. Emmelmann, "Additive manufacturing of metals," *Acta Materialia*, vol. 117, pp. 371-392, 2016.
- [121] A. Antonysamy, J. Meyer , P.B. Prangnellc,, "Effect of build geometry on the  $\beta$ -grain structure and," *Material Characterisation*, pp. 153-168, 19 July 2013.
- [122] S.L. Lu, M. Qian, H.P. Tang, M. Yan, J. Wang, D.H. StJohn, "Massive transformation in Ti-6Al-4V additively manufactured by selective electron beam melting," *Acta Materialia*, vol. 104, pp. 303-311, 2016.
- [123] F.X. Gil Mur, D. Rodriguez, J.A. Planell, "Influence of tempering temperature and time on the  $\alpha'$ -Ti-6Al-4V martensite," *Journal of Alloys and Compounds*, vol. 234, pp. 287-289, 1996.

- [124] A. Kirchner, B. Klöden, J. Luft, T. Weißgärber, B. Kieback, "Process Window for Electron Beam Melting of Ti-6Al-4V," in *Euro PM2014 – AM: Technologies*, Salzburg, 2014.
- [125] C. Körner, "Additive manufacturing of metallic components by selective electron beam melting — a review," *International Materials Reviews*, pp. 1-17, 2016.
- [126] X. Wang, X. Gong, K. Chou, "Scanning Speed Effect on Mechanical Properties of Ti-6Al-4V Alloy Processed by Electron Beam Additive Manufacturing," *Procedia Manufacturing*, vol. 1, pp. 278-295, 2015.
- [127] B. Dutta, F.H. Froes, "The Additive Manufacturing (AM) of titanium alloys," *Metal Powder Report*, vol. 72, no. 2, pp. 96-106, 2017.
- [128] H.P. Tang, M. Qian, N. Liu, X.Z. Zhang, G.Y. Yang, J. Wang, "Effect of Powder Reuse Times on Additive Manufacturing of Ti-6Al-4V by Selective Electron Beam Melting," *Journal of Materials*, vol. 67, no. 3, pp. 555-563, 2015.
- [129] N. Hrahe, T. Quinn, "Effects of processing on microstructure and mechanical properties of a titanium alloy (Ti-6Al-4V) fabricated using electron beam melting (EBM), part1: Distance from build plate and part size.," *Materials Science & Engineering A*, vol. 573, pp. 264-270, 2013.
- [130] T. Horn, "Material Development for Electron Beam Melting," October 2013. [Online]. Available: <https://camal.ncsu.edu/wp-content/uploads/2013/10/Tim-Horn-2013CAMAL.pdf> . [Accessed 21 August 21].
- [131] TMS, "Conference Tools for 2013 TMS Annual Meeting & Exhibition," TMS, 2013. [Online]. Available: <http://www.programmaster.org/PM/PM.nsf/ApprovedAbstracts/9CC7CEAD1CE3833485257A4D00158B39?OpenDocument> . [Accessed 21 August 2017].
- [132] T. Horn, "Material Development for Electron Beam Melting," [Online]. Available: <https://camal.ncsu.edu/wp-content/uploads/2013/10/Tim-Horn-2013CAMAL.pdf>. [Accessed 23 August 23].
- [133] J. Wright, "Development of a Tungsten EBM Theme," August, Sheffield, 2016.
- [134] G. Lütjering, J.C. Williams, *Titanium 2nd edition*, Berlin: Springer, 2007.
- [135] R. Knight, J. Wright, J. Beaman, D. Freitag, "Metal Processing Using Selective Laser Sintering and Hot Isostatic Pressing (SLS/HIP)," 1995.
- [136] C. Qiu, N.J.E. Adkins, H. Hassanin, M.M. Attallah, K. Essa, "In-situ shelling via selective laser melting: Modelling and microstructural characterisation," *Materials and Design*, vol. 87, pp. 845-853, 2015.
- [137] N. Adkins, L. Carter, C. Qiu, K. Essa, M. Attallah, "Selective laser melting of components with thick section through in-situ shelling," Salt Lake City, 2016.
- [138] K. Essa, C. Qiu, N. Adkins, H. Hassanin, A.M. Abdelhafeez, M. Attallah, "Net-Shape Manufacturing using Hybrid Selective Laser Melting/Hot Isostatic Pressing," *Rapid Prototyping Journal*, vol. 23, no. 4, 2017.
- [139] A. Leicht, Sundaram M.V., Hryha E., Nyborg L., Rännar L., Koptioug A., Frisk K., Ahlfors M., "As-HIP Microstructure of EBM Fabricated Shell Components," in *World PM2016*, Hamburg, 2016.
- [140] Frisk, K.; Rännar, L.E.; Koptioug, A.; Petterson, N.; Persson, D.; Leicht, A.; Sundaram, M.V.; Hryha, E.; Nyborg, L.; Ahlfors, M., "Characterisation of EBM-Built Shelled Samples of Ti6Al4V Compacted by HIP," in *World PM2016*, Hamburg, 2016.
- [141] K.A. Lorenz, J.B. Jones, D.I. Wimpenny, M.R. Jackson, "A Review of Hibrid Manufacturing," in *Solid Freeform Fabrication*, 2015.

- [142] A. Hinojos, J. Mireles, A. Reichardt, P. Frigola, P. Hosemann, L.E. Murr, R.B. Wicker, "Joining of Inconel 718 and 316 Stainless Steel using electron beam melting additive manufacturing technology," *Materials and Design*, vol. 94, pp. 17-27, 2016.
- [143] X. Shia, S. Maa, C. Liua, Q. Wua, J. Lua, Y. Liub, W. Shib, "Selective laser melting-wire arc additive manufacturing hybrid fabrication of Ti-6Al-4V alloy: Microstructure and mechanical properties," *Materials Science & Engineering A*, vol. 684, pp. 196-204, 2017.
- [144] M. Merklein, D. Junker, A. Schaub, F. Neubauer, "Hybrid additive manufacturing technologies - An analysis regarding potentials and applications," in *9th International Conference in Photonic Technologies - LANE 2016*, Erlangen-Nurnberg, 2016.
- [145] F. Scherillo, M. Liberini, A. Astarita, S. Franchitti, C. Pirozzi, R. Borrelli, P. Cirillo, A. Caraviello, A. Squillace, L. Carrino, "On The Microstructural Analysis of LFW Joints Of Ti6Al4V Components Made Via Electron Beam Melting," *Procedia Engineering*, vol. 183, pp. 264-269, 2017.
- [146] C. Fuges, "Rebuild, Don't Replace," Additive Manufacturing, 8 August 2014. [Online]. Available: <https://www.additivemanufacturing.media/articles/rebuild-dont-replace>. [Accessed 2017 November 13].
- [147] L. Portolés, O. Jordá, L. Jordá, A. Uriondo, M. Esperon-Miguez, S. Perinpanayagam, "A qualification procedure to manufacture and repair aerospace part with electron beam melting," *Journal of Manufacturing Systems*, vol. 41, pp. 65-75, 2016.
- [148] C.A. Terrazas, S.M. Gaytan, E. Rogriguez, D. Espalin, L.E. Murr, F. Medina, R.B. Wicker, "Multi-material metallic structure fabrication using electron beam melting," *Advanced Manufacturing Technology*, vol. 71, pp. 33-45, 2014.
- [149] M.S. Hossain, J.A. Gonzalez, R.M. Hernandez, M.A.I. Shuvo, J. Mireles, A. Choudhuri, Y. Lin, "Fabrication of smart parts using powder bed fusion additivemanufacturing technology," *Additive Manufacturing*, vol. 10, pp. 58-66, 2016.
- [150] G. Mandil, V.T. Le, H. Paris, M. Suard, "Building new entities from existing titanium part by electron beam melting: microstructures and mechanical properties," *International Journal of Advanced Manufacturing Technology*, vol. 85, no. 5, pp. 1835-1846, 2016.
- [151] H. Smith, "GE Aviation to grow better fuel nozzles using 3D Printing," 3D Printing Reviews, 17 June 2013. [Online]. Available: <http://3dprintingreviews.blogspot.co.uk/2013/06/ge-aviation-to-grow-better-fuel-nozzles.html>. [Accessed 25 August 2017].
- [152] T. Kellner, "This Electron Gun Builds Jet Engines," GE Reports, 18 August 2014. [Online]. Available: <http://www.ge.com/reports/post/94658699280/this-electron-gun-builds-jet-engines/>. [Accessed 18 August 2017].
- [153] A. EBM, "Order for 10 Arcam EBM systems from Avio Aero," Arcam EBM, 22 December 2015. [Online]. Available: <http://www.arcam.com/order-for-10-arcam-ebm-systems-from-avio-aero/>. [Accessed 24 August 2017].
- [154] T. Kellner, "Fit to Print: New Plant Will Assemble World's First Passenger Jet Engine With 3D Printed Fuel Nozzles, Next-Gen Materials," GE Reports, 23 June 2014. [Online]. Available: <http://www.ge.com/reports/post/80701924024/fit-to-print/>. [Accessed 15 November 2017].
- [155] "Rolls-Royce breaks additive record with printed Trent-XWB bearing," Centaur Communications Ltd, 16 June 2015. [Online]. Available: <https://www.theengineer.co.uk/issues/june-2015-digi-issue/rolls-royce-breaks-additive-record-with-printed-trent-xwb-bearing/>. [Accessed 24 September 2018].
- [156] I. Gibson, D.W. Rosen, B. Stucker, "Rapid Prototyping to Direct Manufacturing," in *Additive Manufacturing Technologies*, New York, Springer Science, 2010, p. 368.

- [157] A. Ortho, "Custom make implants," Adler Ortho, [Online]. Available: [http://www.adlerortho.com/adlerortho\\_download/index.php?route=product/category&path=101](http://www.adlerortho.com/adlerortho_download/index.php?route=product/category&path=101). [Accessed 24 August 2017].
- [158] A. Medical, "3D printed HIP prosthesis formally approved by China's Food and Drug Administration," AK Medical, 18 September 2015. [Online]. Available: <http://www.ak-medical.net/English/3D/Printing/2015/0918/501.html>. [Accessed 18 October 2017].
- [159] M. Cotteleer, J. Holdowsky, M. Mahto, J. Coykendall, "3D opportunity for aerospace and defense. Additive manufacturing takes flight," Deloitte Insights, 2 June 2014. [Online]. Available: <https://dupress.deloitte.com/dup-us-en/focus/3d-opportunity/additive-manufacturing-3d-opportunity-in-aerospace.html>. [Accessed 2017 October 13].
- [160] M.K. Thompson, G. Moroni, T. Vaneker, G. Fadel, R.I. Campbell, I. Gibson, A. Bernard, J. Schulz, P. Graf, B. Ahuja, F. Martina, "Design for Additive Manufacturing: Trends, opportunities, considerations, and constraints," *CIRP Annals - Manufacturing Technology*, vol. 65, pp. 737-760, 2016.
- [161] T. Grimm, "Voxeljet Introduces Continuous 3D Printer," Engineering.com, 21 January 2013. [Online]. Available: <http://www.engineering.com/3DPrinting/3DPrintingArticles/ArticleID/5105/Voxeljet-Introduces-Continuous-3D-Printer.aspx>. [Accessed 21 August 2017].
- [162] A. International, "Committee F42 on Additive Manufacturing Technologies," ASTM International, 2017. [Online]. Available: <https://www.astm.org/COMMITTEE/F42.htm>. [Accessed 21 August 2017].
- [163] ISO, "International Organization for Standardization," ISO, 2011. [Online]. Available: <https://www.iso.org/committee/629086.html>. [Accessed 21 August 2017].
- [164] B. Vayre, F. Vignat, F. Villeneuve, "Designing for Additive Manufacturing," *Procedia CIRP*, vol. 3, pp. 632-637, 2012.
- [165] M. Baumer, P. Dickens, C. Tuck, R. Hague, "The cost of additive manufacturing: machine productivity, economies of scale and technology-push," *Technological Forecasting & Social Change*, vol. 102, pp. 193-201, 2016.
- [166] B.P. Conner, G.P. Manogharan, A.N. Martof, L.M. Rodomsky, C.M. Rodomsky, D.C. Jordan, J.W. Limperos, "Making sense of 3-D printing: Creating a map of additive manufacturing products and services," *Additive Manufacturing*, vol. 1, no. 4, pp. 64-76, 2014.
- [167] S.H. Huang, P. Liu, A. Mokasdar, L. Hou, "Additive Manufacturing and its Social Impact: a Literature Review," *Advance Manufacturing and Technology*, vol. 67, pp. 1191-1203, 2013.
- [168] C. Weller, R. Kleer, F.T. Piller, "Economic implications of 3D printing: Market structure models in light of additive manufacturing revisited," *Int. J. Production Economics*, vol. 164, pp. 43-56, 2015.
- [169] M. Gebler, A.J.M.S. Uiterkamp, C. Visser, "A global Sustainability Perspective on 3D Printing Technologies," *Energy Policy*, vol. 74, pp. 159-167, 2014.
- [170] F. Le Bourhis, O. Kerbrat, L. Dembinski, J. Hascoet, P. Mognol, "Predictive model for environmental assessment in additive manufacturing process," *Procedia CIRP*, vol. 2014, no. 15, pp. 26-31, 2014.
- [171] N. Bérauda, F. Vignat, F. Villeneuve, R. Dendievel, "New trajectories in Electron Beam Melting manufacturing to reduce curling effect," *Procedia CIRP*, vol. 17, pp. 738-743, 2014.
- [172] T. F. Scientific, "iCAP™ 7400 ICP-OES Analyzer," Thermo Fisher Scientific, [Online]. Available: <https://www.thermofisher.com/order/catalog/product/842320074081>. [Accessed 06 December 2017].



- [173] A. International, *Standard Terminology of Powder Metallurgy*, West Conshohocken: ASTM International, 2017.
- [174] LPW, "Quantitative Shape Analysis of Metal Powder Samples by Morphology," [Online]. Available: <http://www.lpwtechnology.com/wp-content/uploads/2017/05/Lab-Services-Morphology-Final.pdf>. [Accessed 04 December 2017].
- [175] Malvern, "Laser Diffraction," Malvern, [Online]. Available: <https://www.malvern.com/en/products/technology/laser-diffraction>. [Accessed 19 December 2017].
- [176] A. International, "Standard Practice for Microetching Metals and Alloys," ASTM Compass, 01 January 2016. [Online]. Available: <https://compass.astm.org/download/E407.34825.pdf>. [Accessed 01 December 2017].
- [177] E. Store, "Kroll's Reagent, 250 mL," ES Laboratory, LLC, 2017. [Online]. Available: <http://www.etchantstore.com/Krolls-Reagent-250-mL-171.htm>. [Accessed 01 December 2017].
- [178] BUEHLER, "MicroMet® 6000 Series," BUEHLER, [Online]. Available: <http://photos.labwrench.com/equipmentManuals/10781-4288.pdf>. [Accessed 20 December 2017].
- [179] M. Kahlin, H. Ansell, J.J. Moverare, "Fatigue behaviour of notched additive manufactured Ti6Al4V with as-built surfaces," *International Journal of Fatigue*, vol. 101, pp. 51-60, 2017.
- [180] T. L. Depot, "Archimede's Principle and Density Determination," The Lab Depot, 2018. [Online]. Available: <http://www.labdepotinc.com/articles/archimedes-principles.html>. [Accessed 18 January 2018].
- [181] Sartorius, "Sartorius YDK03," January 2015. [Online]. Available: [https://www.sartorius.com/\\_ui/images/h2a/h89/8869650890782.pdf](https://www.sartorius.com/_ui/images/h2a/h89/8869650890782.pdf). [Accessed 18 January 2018].
- [182] Zeiss, "Axio Imager 2," Zeiss, 2017. [Online]. Available: <https://www.zeiss.com/microscopy/us/products/light-microscopes/axio-imager-2-for-materials.html>. [Accessed 01 December 2017].
- [183] A. Townsend, N. Senin, L. Blunt, R.K. Leach, J.S. Taylor, "Surface texture metrology for metal additive manufacturing: a review," *Precision Engineering*, vol. 46, pp. 34-47, 2016.
- [184] S. Swapp, "Scanning Electron Microscopy," Geochemical Instrumentation and Analysis, [Online]. Available: [https://serc.carleton.edu/research\\_education/geochemsheets/techniques/SEM.html](https://serc.carleton.edu/research_education/geochemsheets/techniques/SEM.html). [Accessed 20 December 2017].
- [185] A. Vagnon, J.P. Riviere, J.M. Missiaen, D. Bellet a, M. Di Michiel, C. Josserond, D. Bouvard, "3D statistical analysis of a copper powder sintering observed in situ by synchrotron microtomography," *Acta Materialia*, vol. 56, pp. 1084-1093, 2008.
- [186] Nikon, "Software," Nikon, [Online]. Available: <https://www.nikonmetrology.com/en-gb/products/x-ray-and-ct-inspection/software-x-ray-and-ct-inspection>. [Accessed 05 December 2017].
- [187] ResearchGate, "Schematic of the HIPpig cycle," [Online]. Available: [https://www.researchgate.net/figure/Schematic-of-the-HIPing-Cycle-I-under-which-the-temperature-and-pressure-are-elevated-at\\_fig4\\_296692495?\\_sg=6P9L1vi3PAwhYQAJZ2Si1ECv7U22PiyBnxmBX\\_snI4iyS\\_JEdSpRLE0m\\_2KqcPBFWMo-y-bKgaEiazxMsqScBg](https://www.researchgate.net/figure/Schematic-of-the-HIPing-Cycle-I-under-which-the-temperature-and-pressure-are-elevated-at_fig4_296692495?_sg=6P9L1vi3PAwhYQAJZ2Si1ECv7U22PiyBnxmBX_snI4iyS_JEdSpRLE0m_2KqcPBFWMo-y-bKgaEiazxMsqScBg). [Accessed 16 June 2018].
- [188] Sandwell, "Shot Peening," Sandwell, 2014. [Online]. Available: <http://www.sandwell-uk.com/shot-peening/shot-peening>. [Accessed 28 November 2017].

- [189] H. Geduld, "Impact Blasting with Glass Beads," in *Sinc Plating*, Tarrytown, ASM International, 1988, pp. 101-106.
- [190] M. Neikter, P. Akerfeldt, R. Pederson, M.L. Antti, "Microstructure characterisation of Ti-6Al-4V from different additive manufacturing processes," *IOP Conference Series: Materials Science and Engineering*, vol. 258, no. 1, 2017.
- [191] S.P. Narra, R. Cunningham, J. Beuth, A.D. Rollett, "Location Specific Solidification Microstructure Control in Electron Beam Melting of Ti-6Al-4V," *Additive Manufacturing*, vol. 19, pp. 160-166, 2018.
- [192] N. Hrabea, R. Kircher, T. Quinn, "Effects of Processing on Microstructure and Mechanical Properties of Ti-6Al-4V Fabricated using Electron Beam Melting (EBM): Orientation and Location," in *Solid Freeform Fabrication Symposium*, Austin, 2012.
- [193] S.P. Narra, R. Cunningham, J. Beuth, A.D. Rollett, "Location Specific Solidification Microstructure Control in Electron Beam Melting of Ti-6Al-4V," *Additive Manufacturing*, 2017.
- [194] X. Wang, X. Gong, K. Chou, "Scanning Speed Effect on Mechanical Properties of Ti-6Al-4V Alloy Processed by Electron Beam Additive Manufacturing," *Procedia Manufacturing*, vol. 1, pp. 278-295, 2015.
- [195] A. International, "Apparent Density of Free-Flowing Metal Powders Using the Hall Flowmeter Funnel," 11 January 2018. [Online]. Available: <https://compass.astm.org/download/B212-12.35191.pdf>. [Accessed 11 January 2018].
- [196] AMAZE, "Publications," AMAZE, 21 June 2017. [Online]. Available: <http://amazeproject.eu/publications/>. [Accessed 11 January 2018].
- [197] C. Formanoir, S. Michotte, O. Rigo, L. Germain, S. Godet, "Electron beam melted Ti-6Al-4V: Microstructure, texture and mechanical behavior of the as-built and heat-treated material," *Materials Science & Engineering A*, vol. 652, pp. 109-119, 2016.
- [198] P. Li, D.H. Warner, A. Fatemi, N. Phan, "Critical assessment of the fatigue performance of additively manufactured Ti-6Al-4V and perspective for future research," *International Journal of Fatigue*, vol. 85, pp. 130-143, 2016.
- [199] N. Hrabec, T. Gnäupel-Herold, T. Quinn, "Fatigue properties of a titanium alloy (Ti-6Al-4V) fabricated via electron beam melting (EBM): Effects of internal defects and residual stress," *International Journal of Fatigue*, vol. 94, pp. 202-210, 2017.
- [200] J.J. Lewandowski, M. Seifi, "Metal Additive Manufacturing: A Review of Mechanical properties," in *Annual Review of Materials Research*, Ohio, 2016.
- [201] B. Cheng, S. Price, J. Lydon, K. Cooper, K. Chou, "On Process Temperature in Powder-Bed Electron Beam Additive Manufacturing: Model Development and Validation," *Journal of Manufacturing Science and Engineering*, vol. 136, 2014.
- [202] X. Shui, K. Yamanaka, M. Mori, Y. Nagata, K. Kurita, A. Chiba, "Effects of post-processing on cyclic fatigue response of a titanium alloy additively manufactured by electron beam melting," *Materials Science & Engineering A*, vol. 680, pp. 239-248, 2017.
- [203] A. Boccacini, "Influence of Stress Concentrations on the Mechanical Property-Porosity Correlation in Porous Materials," *Journal of Material Science Letters*, vol. 17, pp. 1273-1275, 1998.
- [204] H. Nakajima, "Ultimate Tensile Strength," in *Porous Metals with Directional Pores*, Springer, 2013, pp. 138-140.
- [205] J. Günther, D. Krewerth, T. Lippmann, S. Leuders, T. Tröster, A. Weidner, H. Biermann, T. Niendorf, "Fatigue life of additively manufactured Ti-6Al-4V in the very high cycle fatigue regime," *International Journal of Fatigue*, vol. 94, 2017.

- [206] M. Kahlin, H. Ansell, J.J. Moverare, "Fatigue behaviour of notched additive manufactured Ti6Al4V with as-built surfaces," *International Journal of Fatigue*, vol. 101, pp. 51-60, 2017.
- [207] J. Günther, D. Krewerth, T. Lippmann, S. Leuders, T. Tröster, A. Weidner, H. Biermann, T. Niendorf, "Fatigue life of additively manufactured Ti-6Al-4V in the very high cycle fatigue regime," *International Journal of Fatigue*, vol. 94, pp. 236-245, 2017.
- [208] K.S. Chan, M. Koike, R.L. Mason, T. Okabe, "Fatigue Life of Titanium Alloys Fabricated by Additive Layer Manufacturing Techniques for Dental Implants," *METALLURGICAL AND MATERIALS TRANSACTIONS A*, vol. 44A, pp. 1010-1022, 2013.
- [209] D. Greitemeier, F. Palm, F. Syassen, T. Melz, "Fatigue performance of additive manufactured TiAl6V4 using electron and laser beam melting," *International Journal of Fatigue*, vol. 94, pp. 211-217, 2017.
- [210] J. Wright, "Development of a Tungsten EBM Theme," August, Sheffield, 2016.
- [211] B. Vayre, F. Vignat, F. Villeneuve, "Identification on some design key parameters for additive manufacturing: application on Electron Beam Melting," in *Forty Sixth CIRP Conference on Manufacturing Systems*, Setubal, 2013.
- [212] S.P. Narra, R. Cunningham, J. Beuth, A.D. Rollett, "Location specific solidification microstructure control in electron beam melting of Ti-6Al-4V," *Additive Manufacturing*, vol. 19, pp. 160-166, 2018.
- [213] H. Gong, K. Rafi, T. Starr, B. Stucker, "The Effects of Processing Parameters on Defect Regularity in Ti-6Al-4V Parts Fabricated By Selective Laser Melting and Electron Beam Melting," in *Solid Free Form Fabrication*, Austin, 2013.
- [214] T. DebRoy, H.L. Wei, J.S. Zuback, T. Mukherjee, J.W. Elmer, J.O. Milewski, A.M. Beese, A. Wilson-Heid, A. De, W. Zhang, "Additive manufacturing of metallic components – Process, structure and properties," *Progress in Materials Science*, vol. 92, pp. 112-224, 2018.
- [215] C. Qiu, Adkins, N.J.E.; Hassanin, H.; Attallah, M.M.; Essa, K., "In-situ shelling via selective laser melting: Modelling and microstructural characterisation," *Materials and Design*, vol. 87, pp. 845-853, 2015.
- [216] A. Leicht, Sundaram, M.V.; Y, Y.; Hryha, E.; Nyborg, L.; Rännar, L.; Koptioug, A.; Frisk, K.; Ahlfors, M., "Characterisation of EBM-Built Shelled Samples of Ti6Al4V Compacted by HIP," in *World PM2016*, Hamburg, 2016.
- [217] S.S. Al-Bermani, M.L. Blackmore, W. Zhang, I. Todd, "The Origin of Microstructural Diversity, Texture, and Mechanical Properties in Electron Beam Melted Ti-6Al-4V," 2010.
- [218] P. Homporová, C. Poletti, M. Stockinger, F. Warchomicka, "Dynamic phase evolution in titanium alloy Ti-6Al-4V," Beijing, 2012.
- [219] S.S. Rocha, G.L. Abado, G.E. Henriques, M.A. Nobilo, "Vickers Hardness of Cast Commercially Pure Titanium and Ti-6Al-4V Alloy Submitted to Heat Treatments," *Brazilian Dental Journal*, vol. 17, no. 2, pp. 126-129, 2006.
- [220] L. Delaey, H. Tas, Hot Isostatic Pressing '93, Antwerp: Elsevier, 1993.
- [221] K. Zhang, The Microstructure and Properties of HIPped Powder Ti Alloys, Birmingham: University of Birmingham, 2009.
- [222] "Influence of Shot Peening on the Fatigue Behaviour of Titanium Alloys," 1981. [Online]. Available: <https://www.shotpeener.com/library/pdf/1981036.pdf>. [Accessed 13 February 2018].
- [223] M. Galati, L. Iuliano, "A literature review of powder-based electron beam melting focusing on numerical simulation," *Additive Manufacturing*, vol. 19, pp. 1-20, 2018.
- [224] A. Sidambe, "Three dimensional surface topography characterization of the electron beam melted Ti-6Al-4V," *Metal Powder Report*, vol. 72, no. 3, pp. 200-208, 2017.

- [225] C. Qiu, G. A. Ravi, M. Attallah, "Microstructural control during direct laser deposition of a  $\beta$ -titanium alloy," *Materials & Design*, vol. 81, pp. 21-30, 2015.
- [226] K. Zhang, "The microstructure and properties of HIPped powder Ti alloys," April 2009. [Online]. Available: <http://etheses.bham.ac.uk/856/1/Zhang10PhD.pdf>. [Accessed 12 February 2018].
- [227] A. a. J. V. David, "Solidification and Weld Microstructures.," *International Materials Reviews.*, pp. 213-245, 1989.
- [228] P. Y. M. Yan, "An Overview of Densification, Microstructure and Mechanical Property of Additively Manufactured Ti-6Al-4V — Comparison among Selective Laser Melting, Electron Beam Melting, Laser Metal Deposition and Selective Laser Sintering, and with Conventional Powder," 1 April 2015. [Online]. Available: <http://dx.doi.org/10.5772/59275>. [Accessed 30 October 2017].
- [229] Q. Technologies, "Hot Isostatic Pressing," [Online]. Available: <http://quintustechnologies.com/hot-isostatic-pressing/applications/additive-manufacturing/>. [Accessed 16 August 2018].
- [230] F. Bahbou, U. Ackelid, "Improved Parameters for Hot Isostatic Pressing (HIP) of Ti-6Al-4V Additively Manufactured by EBM," Nuremberg, 2016.